Modelling and reduction of the LOx-Methane chemical kinetics for rocket engine applications

Antoine Mouze-Mornettas

UNIVERSITÉ D'ORLÉANS

ÉCOLE DOCTORALE EMSTU (Energie, Matériaux, Sciences de la Terre et de l'Univers)

Laboratoires ICARE (Institut de Combustion, Aérothermique, Réactivité et Environnement) et CERFACS (Centre Européen de Recherche et de Formation Avancée en Calcul Scientifique)

THÈSE présentée par

Antoine MOUZE-MORNETTAS

soutenue le : **10 octobre 2023**

pour obtenir le grade de : **Docteur de l'Université d'Orléans**

Discipline/ Spécialité : Energétique

Modelling and reduction of the LOx-Methane chemical kinetics for rocket engine applications

THÈSE dirigée par :

Bénédicte CUENOT	Chercheur Senior, CERFACS
Fabien HALTER	Professeur, CNRS ICARE, Université d'Orléans

RAPPORTEURS :

Frédérique BATTIN-LECLERC	Directeur de Recherche, CNRS LRGP, Université de Lorraine (présidente de jury)
Guillaume RIBERT	Professeur, CNRS CORIA, INSA Rouen Normandie

---

JURY :

Aurélie NICOLE	Chercheur, ONERA
Annafederica URBANO	Maître de Conférences, ISAE SUPAERO
Guillaume DAYMA	Professeur, CNRS ICARE, Université d'Orléans

INVITÉS :

Miguel MARTIN-BENITO	Ingénieur, CNES
Florian MONNIER	Ingénieur, ArianeGroup

Page intentionnally left blank

“It is difficult to say what is impossible, for the dream of yesterday is the hope of today and the reality of tomorrow.”

Robert H. Goddard

“Now it is clear that anyone working with rocket fuels is outstandingly mad. I don’t mean garden-variety crazy or a merely raving lunatic. I mean a record-shattering exponent of far-out insanity.”

John D. Clark, *Ignition ! An informal history of liquid rocket propellants*

“Don’t panic.”

Douglas Adams, *The Hitchhiker's Guide to the Galaxy*

Abstract

The space market being more and more competitive, reusable launch vehicles are envisioned as a key technology to significantly decrease the cost of access to space. As it positions as the best cost-performance tradeoff, multiple international players of the space sector consider methane as a solution for future reusable engines. However, the operating conditions of the rocket engines are extreme in terms of temperature (from cryogenics fluids to a turbulent flame) and pressure (up to 100 bar or more). Hence, there is a fundamental lack of knowledge of the methane oxycombustion kinetics for those conditions. The current context and particularly the project to develop the European PROMETHEUS MethaLOx rocket engine with adjustable thrust, makes the development of kinetic schemes compatible with the treatment of high-pressure methane oxycombustion a top priority subject.

In order to obtain such a model, an experimental database representative of the application conditions is required. Hence, the OPTIPRIME isochoric combustion chamber developed at CNRS ICARE is used to acquire flame speed data at high pressure and temperature. Challenging high levels of pressure variation and flame front propagation speed required adaptations of the acquisition and post-treatment processes and development of new methods. Nevertheless, measurement campaigns allowed to build a wide CH_4/O_2 flame speed database for a various range of equivalence ratios and never reached before pressure and temperature for those conditions. A selection of different recent chemical mechanisms is then compared to the experimental results in order to assess their performances. This study shows that the model fails to capture the correct levels of flame speed as they were initially derived for less extreme conditions. Indeed, all models tend to widely underestimate the flame speed for lean and stoichiometric mixtures, while they tend to overestimate it for rich ones. However, a best-performing mechanism (POLIMI C1-C3) is identified.

This model is used as the starting point of an optimization process on the experimental database. Various sensitivity analyses are made for the investigated conditions in order to identify the key reactions and species involved. Once identified, the parameters of the key reactions are then tuned to fit the flame speed experimental data along with ignition delay times in extreme conditions from the literature. In order to do so, the OPTISMOKE++ tool developed by ULB and POLIMI is used. At the end of the process a mechanism tailored for CH_4/O_2 combustion in rocket engine conditions is obtained.

Finally, the model is tested in a high-fidelity 3D LES simulation of a simplified rocket engine mono-injector configuration at 100 bar (REST HF-10 test case) using the AVBP code developed at CERFACS. In order to be compact and cost effective, the chemical scheme is preliminarily reduced on representative targets thanks to CERFACS's ARCANE tool. Obtain results are compared to previously used chemistry. It recovers the main flame features but exhibits a more complex flame structure than the reference, highlighting the interest of an optimized chemistry.

Keywords: Liquid Rocket Engine, Methane oxycombustion, High pressure, Flame speed acquisition, Chemical Kinetics, Optimization, Reduction, LES

Résumé

Le marché de l'espace étant de plus en plus compétitif, les lanceurs réutilisables sont considérés comme une technologie clé pour réduire de manière significative le coût de l'accès à l'orbite. Comme il représente le meilleur compromis coût-performance, de nombreux acteurs internationaux du secteur spatial considèrent le méthane comme une solution pour de futurs moteurs réutilisables. Cependant, les conditions de fonctionnement des moteur-fusée sont extrêmes en termes de température (du fluide cryogénique à une flamme turbulente) et de pression (jusqu'à 100 bars ou plus). Il y a donc un manque fondamental de connaissances sur la cinétique de l'oxycombustion du méthane dans ces conditions. Le contexte actuel et notamment le projet de développement du moteur-fusée européen MethaLOx PROMETHEUS, fait du développement de schémas cinétiques compatibles avec le traitement de l'oxycombustion du méthane à haute pression un sujet prioritaire.

Pour obtenir un tel modèle, une base de données expérimentale représentative des conditions d'application est nécessaire. Ainsi, la chambre de combustion isochore OPTIPRIME développée à ICARE (CNRS) est utilisée pour acquérir des données de vitesse de flamme S_u à haute pression et température. Les niveaux élevés de variation de pression et de vitesse de propagation du front de flamme ont nécessité des adaptations des processus d'acquisition et de post-traitement. Néanmoins, les campagnes de mesures ont permis de construire une large base de données de vitesses de flamme CH_4/O_2 pour une gamme variée de richesses des pressions et températures jamais atteintes auparavant pour ces mélanges. Une sélection de différents mécanismes chimiques récents est ensuite comparée aux résultats expérimentaux afin d'évaluer leurs performances. Cette étude montre que le modèle ne parvient pas à capturer correctement les données expérimentales car initialement développés pour des conditions moins extrêmes. En effet, tous les modèles ont tendance à largement sous-estimer S_u pour les mélanges pauvres et stœchiométriques et la surestimer pour les mélanges riches. Le processus permet d'identifier le mécanisme ayant l'écart le plus faible avec l'expérience (POLIMI C1-C3). Ce modèle est utilisé comme point de départ d'un processus d'optimisation sur la base de données expérimentale. Diverses analyses de sensibilité sont effectuées pour les conditions étudiées afin d'identifier les réactions clés et les espèces impliquées. Une fois identifiés, les paramètres de ces réactions sont alors ajustés pour correspondre aux données expérimentales de vitesse de flamme ainsi qu'à des délais d'auto-allumage dans des conditions extrêmes de la littérature. Pour ce faire, l'outil OPTISMOKE++ développé par l'ULB et POLIMI est utilisé. A la fin du processus, un mécanisme adapté à la combustion de CH_4/O_2 dans les conditions d'un moteur de fusée est obtenu.

Enfin, le modèle est testé dans une simulation LES 3D haute-fidélité d'une configuration mono-injecteur simplifiée d'un moteur de fusée à 100 bar (cas test REST HF-10) en utilisant le code AVBP développé au CERFACS. Afin d'être compact et rentable, le schéma chimique est réduit de façon préliminaire sur des cibles représentatives grâce à l'outil ARCANE du CERFACS. Les résultats obtenus sont comparés à la chimie utilisée précédemment. Les principales caractéristiques de la flamme sont retrouvées mais la structure de la flamme est plus complexe que celle de la référence, ce qui souligne l'intérêt d'une chimie optimisée.

Mots clés : Moteur fusées à ergols liquides, Oxycombustion du méthane, Haute pression, Mesures de vitesse de flamme, Cinétique chimique, Optimisation, Réduction, LES

Remerciements

Je tiens à remercier en premier lieu le jury de cette thèse pour avoir accepté de l'évaluer et avoir fait le déplacement pour la soutenance. Merci à tous pour vos questions et remarques. Ce temps d'échange a été à la fois intéressant et précieux. Je tiens à tout particulièrement remercier les rapporteurs Frédérique Battin-Leclerc et Guillaume Ribert pour leur lecture attentive du manuscrit et les remarques et questions qui en ont découlées, toujours avisées et constructives.

Ce travail de thèse n'aurait avant tout jamais été possible sans un encadrement efficace, et on peut dire que j'ai été gâté de ce côté-là ! Bénédicte, Fabien, Guillaume, Miguel, tout d'abord merci de m'avoir fait confiance et de m'avoir recruté sur ce projet de recherche. J'ai pu grâce à vous travailler pendant trois ans sur un sujet, les moteurs-fusée, qui me passionne depuis très longtemps. J'en ai savouré chaque instant, même quand c'était difficile. Merci également de m'avoir permis de travailler au sein de deux laboratoires (à Orléans puis Toulouse) sur deux aspects de la recherche (expérimental et numérique). C'est une chance rare, j'en suis conscient. Merci aussi pour m'avoir donné l'opportunité magique de présenter mes travaux à l'étranger, parfois loin de l'Europe (San Diego, Vancouver) et de m'avoir permis de travailler et d'échanger avec d'autres équipes de recherche (Bruxelles, Pékin). Ces années de thèse, qui ont au final passé très vite, auront été riches d'expériences dans tous les domaines.

Bénédicte, merci pour tes conseils toujours avisés qu'ils soient techniques, qu'ils concernent l'orientation de la thèse ou la relecture de papiers. Je tiens aussi à te remercier pour ta disponibilité, tu as toujours su trouver du temps pour répondre à mes interrogations (même parfois quand tu étais à l'autre bout du monde !) malgré un planning pour le moins chargé.

Fabien, Guillaume, je ne saurais jamais vous remercier assez pour votre encadrement sans faille, votre disponibilité, votre humour légendaire et les moments passés au labo ou en conférence et en déplacement. On ne peut rêver meilleurs encadrants. Merci pour vos conseils et plus généralement les échanges qu'on a pu avoir qu'ils aient trait au travail ou même au domaine personnel. Vous avez su m'aider et me redonner la motivation et le sourire lors de moment difficiles, alors encore une fois merci beaucoup, vous êtes les meilleurs !

Miguel, merci également à toi pour les conseils et remarques à chaque point d'avancement, pour l'opportunité d'avoir pu visiter la direction lanceurs à Daumesnil et le soutien pour mes projets professionnels. Ce fut un immense plaisir de travailler avec toi, et j'espère qu'on se recroisera régulièrement !

Je tiens également à remercier Christian, la légende, grand maître de l'équipe CT pour tous ses conseils, son aide, sa disponibilité et les discussions toujours très intéressantes que l'on a pu avoir. C'était génial d'avoir pu travailler avec toi !

Merci au passage à mes professeurs d'Ecole d'ingénieur et de classe prépa' pour m'avoir donné le goût de la recherche, guidé et permis d'en arriver là. Je pense plus particulièrement à Jacky Winne, Ivan Fedioun et Pierre Brequigny.

Je tiens maintenant à remercier mes collègues et amis thésards, qu'ils soient maintenant docteurs ou sur le point de le devenir.

Je commence chronologiquement par mes camarades expérimentateurs Orléanais d'ICARE avec qui j'ai passé deux ans et avec qui on a réussi à oublier le Covid notamment grâce aux nombreuses sorties

en bord de Loire. Merci tout d'abord à ma première co-bureau Deniz Kaya, maintenant experte du vol 0G, grande prêtresse du système unix CentOS, sans toi je n'aurais pas réussi mes premiers pas dans le monde numérique ! Merci aussi pour l'apprentissage du Turc, je crois que mon niveau a un peu stagné, ce sera un prétexte pour se revoir, en France ou ailleurs ! Merci à mon second cobureau Samsam Jeanjean pour les bons moments passés ensemble (mention spéciale au ranking des avis google maps sur les mers et océans du monde).

Un immense merci à Giorgia, l'ambassadrice d'Italie, pour tous les bons moments et les délires partagés entre Orléans, la coloc' de Vancouver et Toulouse ! Et ce n'est pas fini, à défaut de terminer en « héros » avec une cérémonie officielle aux invalides comme on le voulait (ce n'est pas faute d'avoir essayé entre la rando hardcore à *Garibaldi Lake*, la sortie *whale watching* dans une baie de Vancouver plutôt agitée et la canicule toulousaine). Que d'expériences inoubliables ! Pour tous ces moments et nos nombreuses discussions existentielles, *grazie mille* Gio.

Merci aussi à Léo pour les discussions « fusée » matinales, Maxence « maître Chemkin » pour ses enseignements en matière de cinétique chimique et de bière, Nesrine notre maman à tous, Vincente ma voisine de couloir et d'immeuble (coucou Suricate), Hugo N. « the waverider » ainsi qu'à Nico, Valentin, Alka, Laura, Hugo C., Camille, Fabian et Brian. Mention spéciale à mes anciens stagiaires Hugo K. et Mehdi ! ça a été un réel plaisir de bosser avec vous.

Un immense merci maintenant aux collègues et amis numériciens toulousains du CERFACS ! Pas facile de devoir se relocaliser en cours de thèse, mais vous avez su accueillir un expérimentateur (une espèce plutôt exotique dans les murs de ce labo) sans trop de difficulté et accepté de répondre sans rechigner à mes questions élémentaires sur le monde étrange, mais également fascinant (il faut bien l'avouer) de la simulation numérique. Merci aussi pour toutes les activités en dehors du labo, afterworks, apéros, sorties ciné et soirées cuisine, sorties rando dans les Pyrénées, etc. Maintenant je suis content de pouvoir dire « chocolatine » (ça va en irriter plus d'un mais tant pis c'est comme ça). Un immense merci tous ceux qui ont pu faire le déplacement pour ma soutenance, cela me touche énormément.

Pour commencer je tiens à remercier « Guigui » Bogopolsky mon cobureau cerfacien spécialiste de la brosse à dents et accessoirement du HPC, à moins que ce ne soit l'inverse. Grâce à toi nous formons le duo infernal qui fait que le bureau J15 est un haut lieu de la culture toulousaine entre Appa, « l'expérience chicorée » et « Carton Musk ». Guillaume, merci pour ton expertise poussée sur les problèmes numériques, pour les (nombreuses) discussions sur une multitude de sujets (au bureau et en sortie à l'extérieur) et les fous rires partagés (et ceux à venir car il y en aura). Je n'ai aucun doute sur le fait que tu vas surmonter cette satanée rédaction et travailler sur des sujets qui te passionnent par la suite (n'oublie pas au passage qu'on a un article à publier en rhéologie !). *Never give up* !

Un immense merci à Herr Lukas Gaipl ! D'abord surpris par le « manque d'organisation » français, tu t'y es très rapidement adapté. Te voilà maintenant en train de jurer avec l'accent du sud-ouest et de mettre tes talents innés d'organisateur à contribution en tant que *Beer Happiness Manager* officiel du labo (mais pas que) ! Merci pour les échanges culturels, de la pratique de l'Allemand à l'apprentissage de proverbes et hookup lines douteuses. Merci beaucoup pour l'opportunité du voyage de l'autre côté du Rhin, de Berlin à Aachen en passant par Köln, c'était génial, à refaire. Toujours là pour rigoler, pour aider sur des problèmes techniques complexes mais aussi pour parler et échanger à propos des problèmes de la vie, avec toi on trouve toujours une solution, et on y va *Vollgas* ! *Vielen Dank mein Freund*, ton amitié m'est précieuse.

Msieur Coudray c'est votre tour ! Côtoyer un ancien de *SpaceTech* (devenu maintenant expert en éoliennes et en suie), ça fait plaisir ! On aura vécu de sacrées aventures à San Diego (partir à la recherche de jus d'orange sans additif et de phoques sur la côte, échapper à des Mormons, la rencontre

épique avec *Jose*), que de souvenirs qui resteront. On forme un duo de choc pour implémenter la résolution implicite dans AVBP mais aussi pour les afterworks et faire les trajets retour *Biergarten* – *Patte d'Oie* avec le vélo… mais à pieds. Ne change rien mon Pouik-Pouik ! Hâte de voir l'éolienne en Ardèche !

Merci aussi à Susanne, la *queen* Munichoise du geoengineering ! (j'écris en français mais je sais parfaitement que tu pourras tout comprendre :P) Merci pour les soirées cuisine, film, et balades à La Ramée, on est maintenant devenus les experts du gâteau au matcha sous toutes ses formes ! Merci également pour les longues discussions sur de vastes sujets (parfois juste pour trouver des noms à des plantes) et tes précieux avis sur les lettres de motivation et les entretiens d'embauche *in English*. Merci également d'avoir été notre guide berlinoise, maintenant il va falloir que je visite la Bavière pour comparer ! *Viel Glück* pour la fin de la thèse, qui se terminera sans problème sans aucun doute. En attendant, je commence à mettre de côté pour acheter des Wombats pour *Weirdotopia* !

Merci à Thomas Naess, viking-rugbyman-bricoleur, tout d'abord pour l'aide précieuse que tu m'as apportée à mon arrivée au CERFACS, les riches échanges qu'on a pu avoir notamment sur l'optimisation de mécanismes cinétiques, ton expertise indéniable en sartorialisme, mais aussi et avant tout pour les bons moments passer à rire ensemble au labo et à l'extérieur. Le bureau J15 te servant de source de distraction infinie, je me demande comment tu peux être aussi productif, machine va !

Merci également à Eloïse pour les discussions geek (mais pas que) et les soirées en ville ou en appart (atelier cuisine ou casque VR c'est au choix) maintenant qu'on est voisins (coucou Axell au passage !) c'est toujours un plaisir. Merci à JJ « l'empereur du Tarn » mais aussi grand naturaliste-cruciverbiste du CERFACS pour les randos, les super soirées, les nombreuses discussions toujours intéressantes et ta gentillesse, ne change pas tu es génial ! (coucou Clo' au passage !). Merci à Félix pour les discussions moteur-fusée, Malouines et Pucara, son aide et expertise précieuse sur différents problèmes rencontrés (des instabilités de combustion au design des injecteurs de GG) mais surtout pour ses citations légendaires et sa bonté. *Amigo*, *to space, carajo* ! Merci à Francís pour sa culture internetique et de la royauté inégalée, ses cours d'espagnol et surtout nos conversation passionnantes (sérieuses ou non). Merci à Mehdi pour les discussions avion et l'expertise unique au monde que l'on a développé dans le text-to-speech japonais (ギュスターヴ・フローベール通り). Merci à Jessica pour les pauses café – midi, tantôt sérieuses tantôt déconne, c'est toujours un super moment ! Merci à Raphaël pour les discussions cinéma et la découverte du stadium (on ne sait toujours pas qui est le plus fort entre Reims et Toulouse). Merci à la team toulousaine du sympo de Vancouver (Thomas M., Nico, Varun et Kim) on n'aura peut-être pas réussi à attraper le petit chien devant *Waterfront Station* ou à manger beaucoup de bananes mais on déchire tout (surtout les karaokés improvisés dans les bus vides en retour de gala) !! Merci également à Arthur « Frigolem » Berthelot, Nath', Patoriku Sama Strempfl, PA, Ben, Justin, Hector, Yann, Carlos, Jean et Alex D. pour tous les bons moments passés ensemble durant cette thèse et après. Merci aussi aux « anciens » pour leurs nombreux conseils clés : John, Quentin, Antoine et Simon.

Merci également à mes amis de prépa connus dans les couloirs et les salles de classe du lycée Roosevelt que je continue à voir, comme quoi ça soude ! Un merci particulier à Antoine Lair, double ingénieur lieutenant de la cosmoforce ! Tonio, merci d'avoir fait le déplacement pour la soutenance, merci pour les aprèms jeu, les coups de téléphone et nos bavardages infinis sur les meilleures strats à avoir dans *Shogun* et *Wargame* mais aussi sur l'avenir de l'industrie spatiale. On est loin de s'arrêter ! Merci à Paulo (air et couscouuuus), Pauline (ma p'tite fille), P-H (le roi du process chimique), Toto (l'homme au chapeau) et Clément (*Delbar, l'avenir de la France !*) ainsi qu'à Léa (pour tout le chemin parcouru ensemble).

Merci au passage à mes amis d'enfance, Dr. Gab le *king* de la physique théorique et Benji l'expert sécu numérique : à quand le prochain court métrage ? ça sera une superproduction avec un casting pareil !

Enfin, je tiens à adresser un immense merci à toute ma famille. Merci tout d'abord à tous ceux qui n'ont pas pu être présents et dont je sais qu'ils pensent à moi, je pense à eux également.

Merci à mes grands-parents agenais qui auraient été si fiers, mais je ne doute pas qu'ils le sont là où ils sont. Vous avez vu naître ma passion et su me transmettre des valeurs humaines qui ont fait que j'en suis là actuellement.

Un merci spécial à ma grand-mère qui a toujours cru en moi, m'a toujours encouragé et suivi avec attention, de mon enfance à la thèse, en passant par l'école d'ingénieur. Merci à mon tonton Do' pour le suivi scientifique et les discussions sur la propulsion et d'autres sujets. Merci à Leti, Jules, Azalée et Zeïa, la team toulousaine. Vous êtes géniaux. C'est toujours un immense plaisir de passer du temps au havre de paix de la rue Mirepoix. Que ce soit pour discuter, prendre un thé, le dîner, regarder un film ou jouer à des jeux de société, vous m'avez beaucoup aidé dans les moments difficiles et je vous en remercie.

Un merci spécial à mon frère. Mon Benbenj, c'est en partie à cause de toi que j'ai choppé le virus de l'aérospatial, je me souviens encore des sessions *flight simulator* sur tes genoux quand j'étais petit, des séances de montage de maquettes et visionnage de films de SF !

Pour finir, je voudrais adresser un remerciement tout particulier à mes parents. Papa, maman, merci pour tout. Si j'en suis là actuellement, c'est aussi en grande partie grâce à vous. Vous m'avez appris à la fois à rêver mais aussi à persévérer, sans ça je ne serai jamais arrivé jusque-là, jusqu'à réaliser mon rêve d'Espace. Je vous dois tout. Merci.

Contents

Nomenclature 15

Introduction 18

Methalox Liquid Rocket Engines, context and objectives 18

1.1 Past and present context of the space industry 18

1.2 Reusable space launchers 21

1.3 A brief introduction to liquid rocket engines (LRE) 22

1.3.1 General principle and architecture 23

1.3.2 LRE performances 25

1.4 MethaLox liquid rocket engines 27

1.4.1 Advantages of MethaLOx LREs 27

1.4.2 Current MethaLox LREs under development 29

1.5 Means of research and development for LREs 31

1.6 Thesis motivations 31

Chapter 2 33

Fundamentals and global strategy 33

2.1 Fundamentals of chemical kinetics 33

2.1.1 Definitions 33

2.1.2 Third body and pressure dependent reactions 35

2.2 Fundamentals of flame structures 36

2.2.1 Laminar Premixed flames 36

2.2.2 Laminar Diffusion flames 37

2.2.3 Turbulent Diffusion flames 39

2.3 Chemical schemes for methane oxycombustion 40

2.3.1 Chemical schemes and CFD 40

2.3.2 State of the art of chemical schemes for methane oxycombustion 42

2.4 Global strategy 45

2.4.1 Pathway analysis 46

2.4.2 Contribution of reactions to the heat release 48

2.4.3 Organization of the manuscript 48

Chapter 3 50
Measuring $CH4/O2$ flame speeds at high pressure and temperature 50
3.1 State of the art of Su experimental determination, isochoric method advantages and limits 50
3.1.1 State of the art of Su determination for methane in extreme conditions 50
3.1.2 The isochoric method 52
3.2 The OPTIPRIME experimental setup 53
3.2.2 Flame stability limits, Lewis number and pressure effect 56
3.2.3 Su determination limits 58
3.3 High-pressure limit for Su extraction in SEF-CONV experiments: definition of a new criterion (extract from the paper published in *Thermal Science and Engineering Progress)* .. 59
3.4 Global overview of Su evaluation with OPTIPRIME, method to compare with kinetic schemes 71
3.4.1 Global overview of Su evaluation with OPTIPRIME 71
3.4.2 Building the numerical Su to be compared with the experimental data 71
3.5 Building the $CH4/O2$ Su database at high pressure and temperature (Paper published in *Proceedings of the Combustion Institute*) 72
3.6 Complementary diluted targets at stoichiometry 82
3.6.1 Global strategy: dilution effect parametric study 82
3.6.2 Diluted targets at stoichiometry: experimental results 84
3.7 Conclusion 85
Chapter 4 86
Kinetic mechanism optimization on experimental targets 86
4.1 Experimental vs numerical results: initial situation 86
4.2 Kinetic mechanisms optimization methods 87
4.2.1 Surrogate models 88
4.2.2 Genetic Algorithms 89
4.2.3 DIRECT algorithm 91
4.3 The OPTISMOKE++ optimization code 91
4.3.1 Reaction rate uncertainty propagation 92
4.3.2 Third-body efficiency optimization 92

4.3.3 Pressure dependent reactions optimization 93
4.3.4 Code structure and workflow 93
4.4 Optimization strategy 95
4.4.1 Flame speed targets 95
4.4.2 Ignition delay time targets 96
4.4.3 Target reactions selection 97
4.4.4 POLIMI C1-C3 reduction 99
4.5 Optimization results 101
4.5.1 Flame speed results 104
4.5.2 Ignition delay time results 106
Chapter 5 111
Application – the REST HF-10 case 111
5.1 Large Eddy Simulation (LES) 112
5.1.1 CFD and turbulence modelling 112
5.1.2 Filtered governing equations in LES 114
5.1.3 Turbulent viscosity models 118
5.1.4 AVBP solver numerical parameters 119
5.2 Application case description: the REST HF-10 configuration 123
5.2.1 Geometry 124
5.2.2 Operating conditions 125
5.2.3 Boundary conditions and mesh 126
5.3 Polimi Opti reduction for REST HF-10 conditions 127
5.3.1 Reduction targets 127
5.3.2 Reduced mechanism 128
5.3.3 Reduced mechanism validation 129
5.3.4 Compressibility factor 132
5.3.5 1D comparison with the RAMEC ARC mechanism 133
5.3.6 Validation on pseudo 1D AVBP calculations 134
5.4 The chemical stiffness issue 139
5.4.1 Chemical timescale 139
5.4.2 How to deal with chemical stiffness: state of the art 141

5.4.3 Implicit solving of the chemical source terms 143
5.4.4 CVODE solver coupling with AVBP 143
5.4.5 1D validation of the CVODE coupling 144
5.4.6 Implicit integration applied to 3D LES 146
5.5 REST HF-10 calculation results and analysis 148
5.5.1 Calculation parameters 148
5.5.2 Convective scheme, LAD activation and flame topology 149
5.5.3 Averaged longitudinal profiles per cross section 155
5.5.4 Analysis of chemical species average fields and profiles 156
5.5.5 Power budget and equilibrium 163
General conclusion and perspectives 167
Appendices 169
Appendix A – Reaction contributions to the heat release 169
1- 1D diffusion flame – 100 bar, χ=1000 $s-1$ 169
2- 1D premixed flames – 100 bar 170
Appendix B – Supplementary data of the OPTIPRIME $\boldsymbol{CH4/O2}$ campaign 172
1- Raw data treatment example 172
2- Flame images examples 173
3- $\boldsymbol{CH4/O2}$ OPTIPRIME campaign results - $\boldsymbol{Su = f(P,T)}$ vs mechanisms 175
4- $\boldsymbol{CH4/O2}$ OPTIPRIME campaign results - $\boldsymbol{P, T, Su}$ experimental traces 176
5- $\boldsymbol{CH4/O2}$ OPTIPRIME diluted targets at stoichiometry campaign results - $\boldsymbol{Su = f(P,T)}$ vs mechanisms 180
6- $\boldsymbol{CH4/O2}$ OPTIPRIME diluted targets at stoichiometry - $\boldsymbol{P, T, Su}$ experimental traces 181
Appendix C – Optimization results 187
1- Genetic algorithm trials 187
2- Complete results of the optimization process with the DIRECT method 188
A. Laminar flame speed results 188
B. Ignition delay times results 190
Appendix D – ARC Reduced mechanisms 192
Appendix E – Averaged longitudinal profiles per cross section of the REST HF-10 test case 200
1. Introduction et objectifs 218

2. Mesures expérimentales de vitesses de flamme laminaires pour des mélanges $CH4/O2$ à haute pression et température 219
3. Optimisation du schéma cinétique POLIMI C1-C3 sur les données expérimentales OPTIPRIME 222
4. Application du modèle sur un calcul LES 3D (REST HF-10) 225
5. Conclusion 228
Sources bibliographiques 230

Nomenclature

Roman symbols

Symbol	Meaning	SI unit
$\boldsymbol{A}$	pre-exponential factor	Variable
$\boldsymbol{a}$	strain rate	s^{-1}
$\boldsymbol{b}$	temperature exponent	-
$\boldsymbol{C_p}$	heat capacity	$J\ mol^{-1}\ K^{-1}$
$\boldsymbol{Da}$	Damkholer number	-
$\boldsymbol{D_m}$	diffusion coefficient	$m^2\ s^{-1}$
$\boldsymbol{D_{th}}$	thermal diffusivity	$m^2\ s^{-1}$
$\boldsymbol{Ea}$	activation energy	$J\ mol^{-1}$
$\boldsymbol{Eff}$	third body efficiency	-
$\boldsymbol{fr}$	uncertainty factor on k	-
$\boldsymbol{h}$	enthalpy	$J\ kg^{-1}$
$\boldsymbol{HR}$	heat release	$W\ m^{-3}$
$\boldsymbol{Isp}$	specific impulse	s
$\boldsymbol{k}$	rate constant	Variable
$\boldsymbol{L_b}$	Markstein length	m
$\boldsymbol{Le}$	Lewis number	$-$
$\boldsymbol{m}$	mass	kg
$\dot{\boldsymbol{m}}$	mass flow rate	$kg\ s^{-1}$
$\boldsymbol{MR}$	mixture ratio	$-$
$\boldsymbol{P}$	pressure	Pa
$\boldsymbol{Pr}$	Prandtl number	-
$\boldsymbol{R}$	universal gas constant	$J\ K^{-1}\ mol^{-1}$
$\boldsymbol{R_f}$	flame radius	m
$\boldsymbol{S_b}$	laminar flame speed relative to the burnt mixture	$m\ s^{-1}$
$\boldsymbol{S_b^0}$	unstretched laminar flame speed relative to the burnt mixture	$m\ s^{-1}$
$\boldsymbol{Sch}$	Schmidt number	-
$\boldsymbol{S_u}$	laminar flame speed relative to the unburnt mixture	$m\ s^{-1}$
$\boldsymbol{Tr}$	thrust	N
$\boldsymbol{u}$	speed	$m\ s^{-1}$
$\boldsymbol{W}$	molar mass	$kg\ mol^{-1}$
$\boldsymbol{X}$	molar fraction	-
$\boldsymbol{Y}$	mass fraction	-
$\boldsymbol{Z}$	mixture fraction	-
$\boldsymbol{z}$	compressibility factor	-
$[\boldsymbol{S}]$	Concentration of species S	$moles\ m^{-3}$

Greek symbols

$\boldsymbol{\chi}$	Scalar dissipation rate	s^{-1}
$\boldsymbol{\delta_f}$	flame thickness	m
$\boldsymbol{\delta_{PH}}$	pre-heat zone thickness	m
$\boldsymbol{\Delta t_{CFL}}$	simulation time step	s
$\boldsymbol{\gamma}$	heat capacity ratio	-
$\boldsymbol{\kappa}$	strech	s^{-1}
$\boldsymbol{\lambda}$	thermal conductivity	$W\ m^{-1}K^{-1}$
$\boldsymbol{\mu}$	dynamic viscosity	$Pa\ s^{-1}$
$\boldsymbol{\nu}$	kinematic viscosity	$m^2\ s$
$\boldsymbol{\dot{\omega}}$	reaction rate	$mol\ m^{-3}\ s^{-1}$
$\boldsymbol{\varphi}$	equivalence ratio	-
$\boldsymbol{\rho}$	density	$kg\ m^{-3}$
$\boldsymbol{\sigma}$	standard deviation	Variable
$\boldsymbol{\tau_c}$	chemical timescale	s
$\boldsymbol{\tau_f}$	turbulent flow timescale	s

Acronyms

Acronyms	Meaning
ARCANE	Analytical Reduced Chemistry: Automatic Nice and Efficient
AVBP	A Very Big Project
CERFACS	Centre Européen de Recherche et de Formation Avancée en Calcul Scientifique
CFD	Computational Fluid Dynamics
CFL	Courant–Friedrichs–Lewy Number
CIRA	Centro Italiano Ricerche Aerospaziali
CNES	Centre National d'Etudes Spatiales
CNRS	Centre National de la Recherche Scientifique
CRECK	Chemical Reaction Engineering and Chemical Kinetics Lab
DIRECT	Dividing RECtangles optimization method
DLR	Deutsches Zentrum für Luft und Raumfahrt
DNS	Direct Numerical Simulation
GA	Genetic Algorithm optimization method
GG	Gas Generator
HRE	Hybrid Rocket Engine
ICARE	Institut de Combustion, Aérothermique, Réactivité et Environnement
JAXA	Japan Aerospace Exploration Agency
LAD	Localized Artificial Diffusivity
LES	Large Eddy Simulation
LOx	Liquid Oxygen
LRE	Liquid Rocket Engine
LW	Lax-Wendroff scheme
NASA	National Aeronautics and Space Administration
ONERA	Office National d'Etudes et de Recherches Aérospatiales
POLIMI	Politecnico di Milano

QSSA	Quassi Steady State Approximation
RANS	Reynolds Averaged Navier Stokes
SC	Sub-Cycles
SRM	Solid Rocket Motor
TTGC	Two-step Taylor Galerkin scheme
TUM	Technische Universität München

Introduction

Methalox Liquid Rocket Engines, context and objectives

1.1 Past and present context of the space industry

After being theorized notably by the Russian scientist Konstantin Tsiolkovsky at the beginning of the 20th century, rocket propulsion principles were progressively applied and improved by several research groups and pioneers around the world. The American physicist Robert H. Goddard launched the first liquid fuel rocket in 1926, closely followed in 1931 by the German VFR research group led by Werner Von Braun. Almost simultaneously, in 1933, the GIRD research group of Soviet engineer Sergei Korolev also launched liquid fueled rockets. Despite being quickly used mainly for military applications, as illustrated by the German-made V2, rockets were progressively oriented toward space launch applications after World War 2. The development of nuclear deterrence systems (i.e. intercontinental ballistic missiles or ICBMs) during the cold war drove the creation of space launchers, which designs were mainly based on ICBMs. Hence, the first artificial satellite Sputnik 1 was launched from Soviet Union on October 4, 1957 starting what is known as the space race. The United States launched their first satellite in 1958, later followed by France in 1965. Since then, several countries also developed autonomous access to orbit. On April 12, 1961 Soviet cosmonaut Yuri Gagarin became the first man in space followed in 1962 by American astronaut John Glenn. The space race peaked in 1969 with the US manned moon landing of the Apollo 11 mission, Neil Armstrong becoming the first man to walk on Earth's natural satellite. Parallel to prestige activities, the space sector expanded with the appearance of commercial applications: science, exploration, telecommunication, meteorology, imaging and later global positioning. Commercial use of space (along with military applications) is one of the drivers of the development of several governmental and private-funded space activities and programs around the world. With an increasing demand on several markets, the number of orbital launches per year drastically increased (cf. Figure 1).

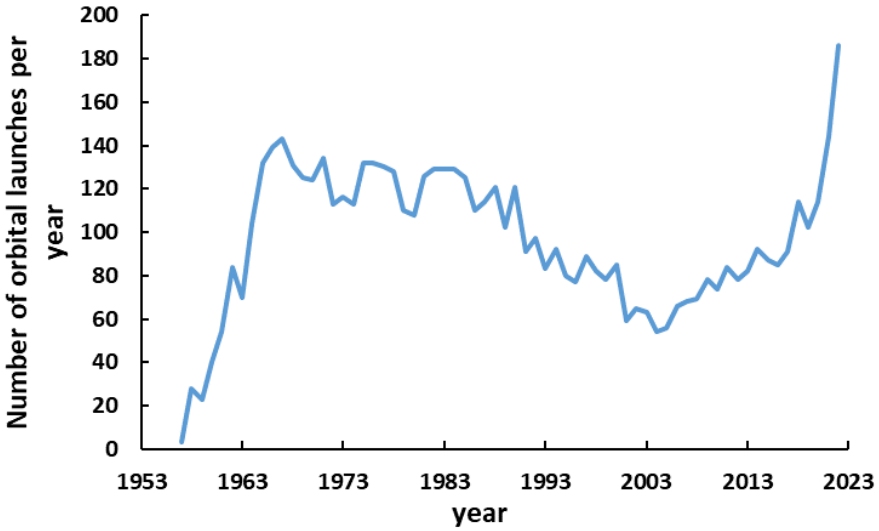

Figure 1: Number of orbital launches per year [1]

This increase also comes entangled with a paradigm shift in the space industry. Indeed, the beginning of the 2000s saw the appearance of what is now called the "New Space" [2], i.e. the massive involvement of private actors previously considered mainly as subcontractors for state-led programs (Apollo for example). This phenomenon, which first appeared in the US but is now worldwide, leads to an exponential growth of the space-related commercial sector as well on the upstream part (space launchers, satellites) as on the downstream one (space-related data use and its applications). This orientation change was dynamized by newly created actors, generally emerging as startups and completely unrelated to previously existing space industry entities. This is typically the case of SpaceX or BlueOrigin (respectively created in 2002 and 2000), which are now key players of the sector. With new actors, new methods appeared and continue to appear nowadays, driven by new available technologies (miniaturization of electronic components, digital revolution, additive manufacturing, etc.). New Space companies follow logics based on production and operating cost reduction with assembly line production for launchers and satellites with business models often based on the sector of digital technologies. Their financing processes are diversified. They are based on private and stock market investments but also still depends on public contracts (for example NASA's COTS and CCDev contracts [3] to produce vehicles for cargo and manned transport to and from the International Space Station (ISS)). This set of new methods and technologies led to a progressive decrease of the cost of access to space, encouraging actors for whom expenses had previously been prohibitive such as small companies or even universities and research laboratories. However, the costs remain high for classical size satellites. Hence, one of the current trends is to develop and launch small satellites (or SmallSats). They typically go from mass of the order of magnitude of 100 g (femtosatellite) to 150-500 kg (microsatellite-minisatellite) with the 10 kg nanosatellite in between [4]. These vehicles can be either build in a single exemplar by the manufacturer for a dedicated use or be deployed as a constellation (for example the ICEYE constellation of 18 micro satellites dedicated to real-time radar imaging of the Earth [5]). As their usage is becoming more and more widespread and reliable, they become attractive for deep space exploration missions (for example NASA's MarCO nanosats used as communication relay during the InSight probe landing on Mars [6]). SmallSats can be deployed as rideshare payloads (i.e. being embarked as secondary payloads on a classic satellite launch) or occupy entire dedicated launches for constellations. The most emblematic example being the Starlink satellite internet constellation deployed by SpaceX [7] which at present consists of 3580 satellites (12 000 are currently

planned). These factors explain the recent drastic increase in terms of objects launched into space as illustrated on Figure 2.

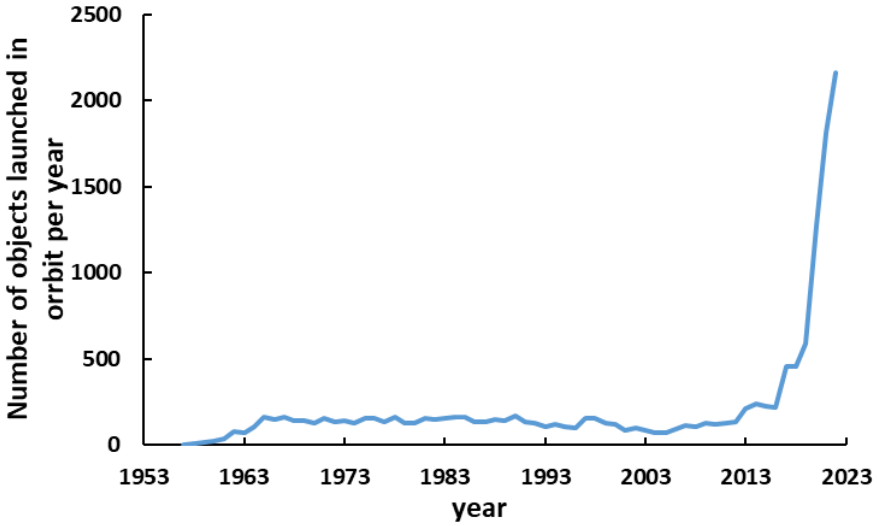

Figure 2: Number of objects launched in orbit per year [1]

In order to launch these SmallSats, classic launchers can be used for massive constellation-purposed grouped missions. However, for individual launches, small launch vehicles called nano or micro launchers can be used. This family of vehicles is typical of the New Space approach. Several companies around the world (mostly startups, sometimes spinoffs of existing space corporations) are currently working on their development. They exist in the US (for example Firefly with their Alpha rocket, ABL systems with RS1 or Rocket Lab with Electron), China (e.g. Landspace with Zhuque 2 or Galactic Energy with Ceres-1), Japan (e.g. Interstellar Technologies with Momo) and also in Europe (e.g. Latitude with Zephyr in France or Pangea Aerospace with Meso in Spain). Figure 3 illustrates the many existing projects of launch vehicles in Europe only (Ariane 5, Vega and Vega-C being the only current launchers in use on the figure).

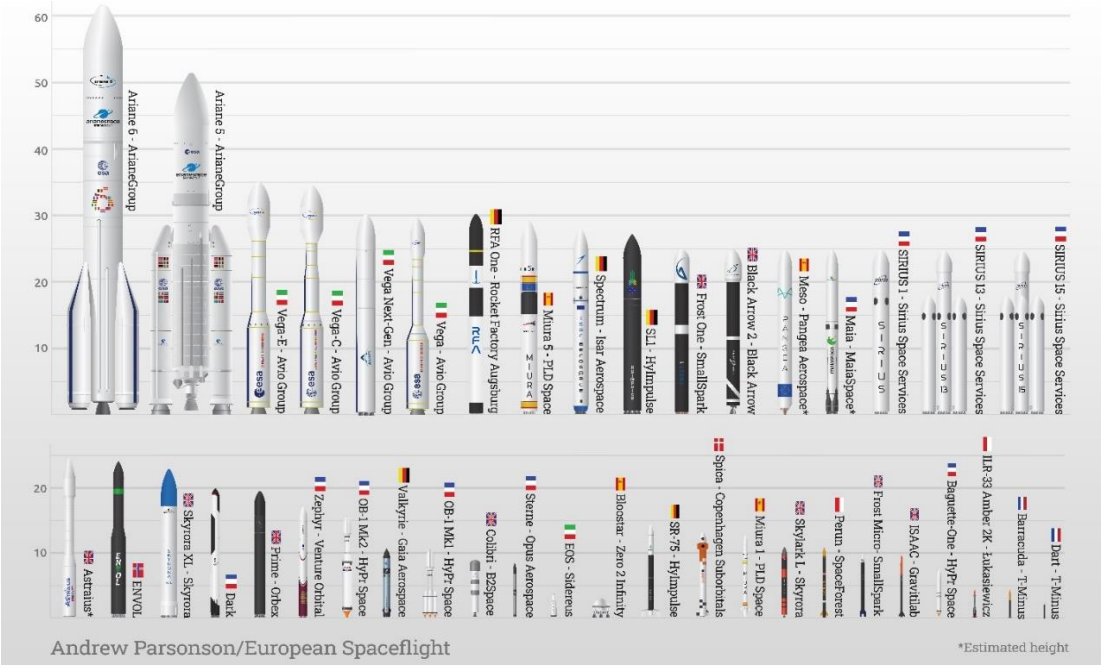

Figure 3: Current and future proposed European launch vehicles (height is indicated in m) [8]

1.2 Reusable space launchers

A strong solution to decrease the cost of access to space is the reusability of the launch vehicle. Indeed, a classical space launcher is fully expandable. As they are emptied, hence useless, the launcher stages are jettisoned and abandoned. By reusing the launcher, or at least parts of it, the realized savings are substantial [9]. Several approaches were examined and considered over time, with studies still continuing this day [10,11]. The challenge is hard to meet since the launch vehicle is subjected to particularly constraining conditions as it moves from sub to hypersonic speeds through different mediums. The first practical application of the concept was the crewed NASA's STS (Space Transportation System) also known as the Space Shuttle. On the shuttle, which first flew in 1981, only the orbiter part was recovered and reused. The central external tank burnt in the atmosphere, while the solid rocket boosters were recovered in the sea but never reused. The orbiter still required a significative amount of maintenance between flight, leading to significant extra costs. However, the main issue was that the launch rate per year never reached the amount needed to be cost-effective. Hence, after two deadly incidents, the STS was retired in 2011 at the completion of the International Space Station. As the market of space applications and the related demand increases since the beginning of Newspace, meeting what seemed to be an important number of launches during the shuttle era seems now manageable. Hence, several companies started reusable launch vehicles development in the early 2000s. After a bit more than 10 years of work and tests with different versions, the US company SpaceX proposed the Falcon 9 launch vehicle [12]. As of today, it is the only reusable orbital launch system in service, even qualified for manned flights. The vehicle is a two stages rocket using cost effective engines fueled by LOx/RP1 (which is a kerosene derivative). The first stage is fully recovered and reused (either on land or on a barge in the sea) as well as the payload fairings. There is no second stage recovery as it is still a big challenge as it cruises to higher speed than the main booster. However, future SpaceX vehicle Starship is developed with that purpose in mind [13]. As of today, the Falcon 9 flew more than 200 times with a total of around 140 1st stage recoveries and 120 reuses (a single stage being able to be reused several times). This success is illustrating the interest that other companies (and space agencies) have in order to develop their own reusable launch vehicle. There are currently many projects around the world, all in different phases of testing. Furthermore, the majority of the future potential European vehicles proposed of Figure 3 are initially designed to be reusable. CNES, DLR and JAXA are currently working on the small technological demonstrator CALLISTO [14] in order to validate key elements such as the navigation algorithms, critical for the recovery phase. ArianeGroup through its startup spinoff MaiaSpace is currently developing a reusable launcher based on the first stage full-scale demonstrator THEMIS [15] using the PROMETHEUS methane-fueled rocket engine (cf. next sections). These vehicles pave the way to a modular heavy reusable space launcher called ArianeNext which will come after Ariane 6 [16,17]. As it has a direct impact on performance, development and operating costs, the choice of the fuel used for the vehicle is a fundamental problem. Hence it will be addressed in the next sections.

Figure 4: THEMIS methalox demonstrator developped by ArianeGroup (left) and reusable launch vehicle based on THEMIS proposed by MaiaSpace (right) [18]

1.3 A brief introduction to liquid rocket engines (LRE)

In order to reach the escape velocity necessary to vanquish the earth's gravity and eventually reach orbit, launch vehicles need tremendous amount of energy. The movement of the rocket is achieved thanks to Newton's third law by ejecting large amount of hot gases at important speed. These gases are created by a combustion process taking place between a fuel and an oxidizer (generally O_2). Indeed, as the rocket quickly reaches space, no air is available to sustain combustion, hence all the reactants need to be embarked in the vehicle. When it comes to rocket propulsion, three families of engines exist. The first one, described in this section, is the liquid rocket engine (LRE). As indicated by its name, its propellants are stored in a liquid form and react only once mixed in the combustion chamber. It can be very complex in terms of design but remains a system capable of delivering important thrust that can also be finely tuned. Another type of engine is the solid rocket motor (SRM). It consists on a solid powder block of propellant composed of a mix of both oxidizer and fuel. These systems are able to deliver instantaneous and important thrust. However, thrust modulation can only be achieved in advance with variation of the solid grain design and once ignited, it is impossible to stop [19]. Hence it is principally used as a booster, cheap kick stage or for military applications. The last type of engine is the hybrid rocket engine (HRE). It is a crossover between LRE and SRM, the oxidizer being generally in the liquid form (or sometimes gaseous) as the fuel is solid. Hence, they are safer than SRM, and their thrust can be modulated as well as for LRE. However, the amount of thrust they can classically deliver is not enough for an orbital-class capable launch vehicle [19] but progresses have allowed to improve the design of these engines and envision them for launchers [20]. Hence, as they can both achieve high thrust and large modulation of the latter, LRE are indicated for reusable launch vehicles.

1.3.1 General principle and architecture

As mentioned above, LRE rely on oxidizer and fuel stored in the liquid form, then mixed in a combustion chamber to create thrust. The latter is achieved through the hot gas expansion through a nozzle. This section describes the global elements of the engine in a simplified way.

Tanks:

The tanks design depends on the type of propellants used for the vehicle. For example, RP-1 is liquid at ambient conditions (1 bar and 300 K) while H_2 requires temperature below 20 K at 1 bar, hence dedicated tanks with special insulation. For LRE, the oxidant is almost always liquid O_2 (as its combustion is more efficient than with the air without the unnecessary N_2 acting as a thermal ballast). Liquid O_2 is often written as LOx for Liquid Oxygen. Its boiling temperature is 191 K at atmospheric pressure, also requiring cryogenic insulation. However, some launch vehicles can use other specific oxidizers such as N_2O_4, for example used with the highly toxic UDMH hydrazine fuel in the Russian Proton rocket. Both of these propellants are liquid at ambient temperature.

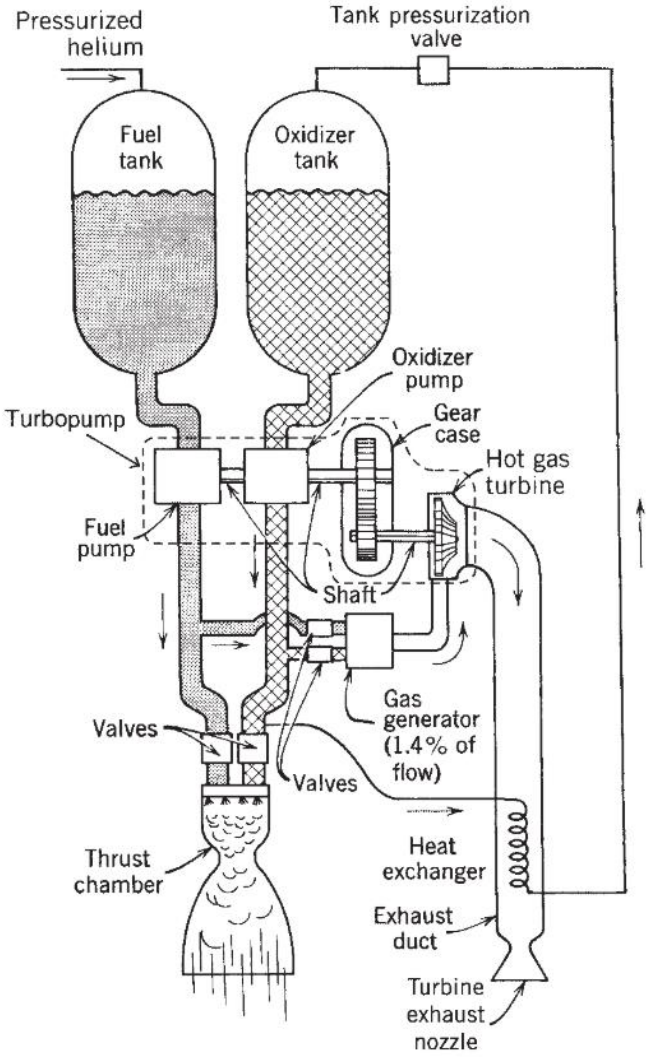

Figure 5: Simplified diagram of a gas generator cycle LRE taken from [21]

Turbopumps and engine cycles:
Fuel and oxidizer then need to be pumped at high pressure in the combustion chamber. The pressure value depends entirely on the desired operating point of the engine. Typically, it varies between 30 and 300 bar. To achieve such pressures, turbopumps are employed. Their rotation can be driven differently depending on the engine's architecture, also called thermodynamic cycle. Figure 5 illustrates a gas generator cycle which is for example employed on the Vulcain 2 engine propelling Ariane 5. In that case the turbopump is driven by a turbine alimented in hot gases by a dedicated auxiliary combustion chamber called the gas generator (GG) where small amounts of propellant are injected. Typically, the combustion conditions in GGs are fuel rich as O_2 rich mixture could create oxidation problems for the turbine, requiring special alloys to withstand the conditions. The hot gases coming from the GG are then expelled in the surrounding environment. This is what is called an "open cycle".

In order to take advantage of this potential supplementary energy supply, "close cycles" can be used. For example, staged combustion, where the GG exhaust gases are reinjected in the combustion chamber, was used on the RS25 SSME (Space Shuttle Main Engine). Various other cycles with several variants exist and allow to adapt to the different operating and cost constraints [21].

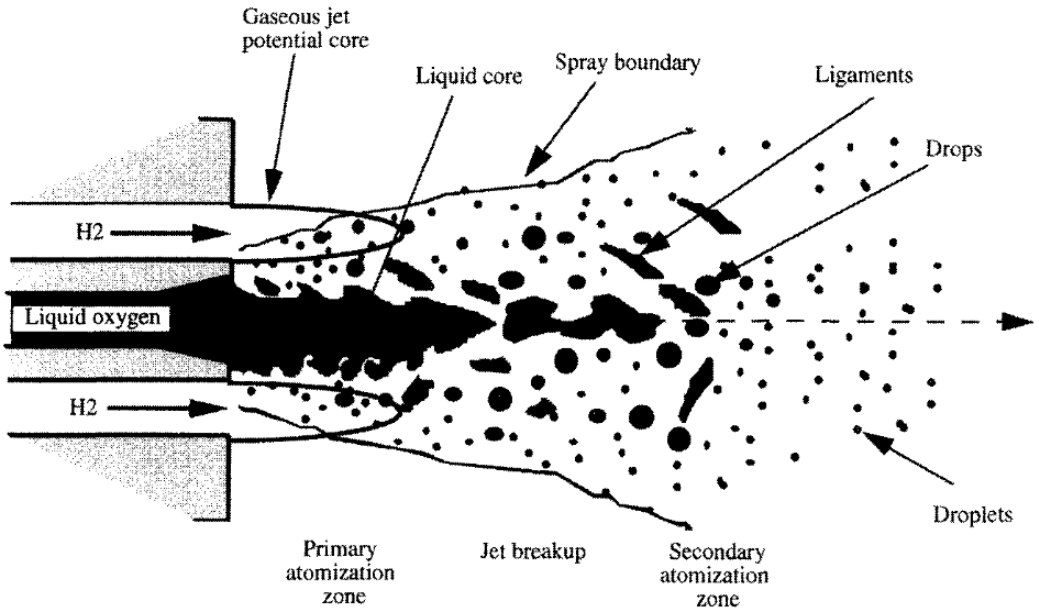

Figure 6: Illustration of coaxial injection of propellants for a GH2/LOx LRE in subcritical conditions. Taken from [22]

Injection in the combustion chamber, instabilities:
Once the propellant is pumped, it is injected in the combustion chamber and ignited. Ignition can be achieved through various systems like for example small electric-ignited torches, the injection of special additives (like TEA-TEB used in the Merlin engine) or even lasers [22]. As mentioned before, injection can happen at different pressures. Indeed, it depends both on the propellant thermodynamic properties and the engine operating point which can typically be found between 30 and 100 bar [21]. Hence, the propellant can either be found in 3 different main regimes. The first is the subcritical regime where the propellants are found in the liquid and/or gaseous form, the phases being separated by an interface. In these conditions, the flame characteristics are driven by atomization and evaporation phenomena (see example on Figure 6). The two other regimes are the trans and supercritical conditions. The first is reached when the pressure exceeds the critical conditions while the second one

is attained when the temperature is also above the critical point. Hence, in these extreme conditions the interface between liquid and gas disappears as well as the atomization phenomena [23]. Propellants can be injected through different types of injectors with specific designs that have their own advantages to improve atomization and mixing phenomena.

The injection process has a direct impact on the flame behavior. Hence the feed system can sometimes trigger hydro and thermoacoustic interactions with specific modes of the chamber [21]. Combustion instabilities can then occur and rapidly destroy the engine as it was the case for example with the Apollo era F1 engine [24]. The subject is widely studied to prevent such destructive phenomena to happen [25] with dedicated technic solutions such as baffles on the injector plate for example.

Thrust chamber cooling:

As the temperature reached by the hot gases is extremely important (3000 K being a typical order of magnitude), the combustion chamber and the nozzle need to be cooled down in order to prevent melting. This can be achieved through a technique called regenerative cooling. In that case, one of the liquid propellants circulate in a special jacket along the combustion chamber and nozzle walls before being fed to the injector plate [21]. Another less expensive method is called radiative cooling. In that case, the thrust chamber/nozzle ensemble is made of a special material (for example Niobium) that radiates the produced heat in the surrounding environment. Hence, wall heat flux predictions remain an important problematic when it comes to calculations during the engine sizing process [23].

When designing a LRE, all of these constraint and phenomena, often being inter-dependent, need to be taken into account making these engines very complex machines.

1.3.2 LRE performances

In order to assess the performances of LRE, different figures of merit require attention. The main ones are presented in this section.

Mixture and equivalence ratio:

In order to describe the mixture inside the combustion chamber, the oxidizer to fuel ratio, also called O/F or mixture ratio (MR) is used in the space industry. It is introduced as:

$$MR = \frac{\dot{m}_{Ox}}{\dot{m}_{fuel}} \tag{1}$$

$\dot{m}_{Ox}$ and $\dot{m}_{fuel}$ being respectively the mass flow rates of oxidizer and fuel. This definition yields a different value for the stoichiometric $(MR)_{St}$ as the considered propellant change. If $MR > (MR)_{St}$ the mixtures are oxidizer rich whereas $MR < (MR)_{St}$ lead to fuel rich mixtures. The mixture ratio is presented here in a mass form, but can also be expressed in volume. Another parameter describing the mixture can be used to generalize the MR definition. φ is the mixture ratio which is always equal to unity at stoichiometry. $\varphi > 1$ describes rich (fuel) mixtures and $\varphi < 1$ lean (fuel) ones. It is defined as:

$$\varphi = \frac{\frac{Y_{fuel}}{Y_{Ox}}}{\left(\frac{Y_{fuel}}{Y_{Ox}}\right)_{St}} = \frac{\frac{1}{MR}}{\left(\frac{1}{(MR)_{St}}\right)} \tag{2}$$

Thrust:

The thrust force Tr (measured in Newtons) is the direct output of the engine. This is what will principally drive the launch vehicle performances. It is defined as:

$$Tr = \dot{m}u_e + (P_e - P_a)A_e \tag{3}$$

Where $\dot{m}$ is the ejected mass flow rate of hot gases at speed u_e. A_e is the exhaust area of the nozzle, P_e the exit pressure and P_a the ambient pressure. This relation highlights the need to maximize the pressure, speed and amount of ejected hot gases. In the case of an optimum nozzle, the exhaust pressure is identical to the ambient one, canceling the second term of the equation.

Specific impulse:

Another key parameter that allow to evaluate and compare rocket engine performances is the specific impulse Isp (measured in seconds). By definition, the Isp is the time during which an engine can deliver 9.81 N (i.e. 1 kg) of thrust. Hence, it's a figure of merit of the engine's efficiency. Its definition is the following:

$$Isp = \frac{Tr}{\dot{m}g_0} \tag{4}$$

g_0 being the standard gravity (here the gravitational acceleration near the surface of the Earth). Hence, the Isp depends on the pressure. Consequently, it will vary during the rocket flight, the sea level specific impulse being different that the one in orbit. In the ideal case of an optimum nozzle, the specific impulse is only a function of the hot gases' exhaust speed u_e and g_0:

$$Isp = \frac{u_e}{g_0} \tag{5}$$

Exhaust speed:

The exhaust speed u_e is mainly a function of the thermochemical parameters such as the heat capacity ratio of the burnt gases γ_b as well as the unburnt ones γ_u, the flame temperature reached in the combustion chamber T_c (in K) at a given pressure P_c (in bar), the average molar mass of the species in the combustion chamber $\overline{W}$ (measured in kg.kmol^{-1}) and R the universal gas constant (in J.K^{-1}.mol^{-1}). The expression of u_e is the following:

$$u_e = \frac{1}{g_0}\sqrt{\frac{2\gamma_u}{\gamma_u - 1}\frac{R}{\overline{W}}\,T_c\left[1 - \left(\frac{P_e}{P_c}\right)^{\frac{\gamma_u - 1}{\gamma_u}}\right]}$$

This means that the ejection speed varies roughly as:

$$u_e \sim \sqrt{\frac{T_c}{\overline{W}}} \tag{6}$$

So roughly does the Isp. Hence, to maximize the engine's performances, the optimum is to find an operating point for which T_c is maximal while $\overline{W}$ is minimal. Hence, this explains why the optimal operating conditions of rocket engine combustion chambers is slightly rich mixtures (hence slightly above stoichiometry). However, one has to remember that this optimum is not the one desired for

GGs as one of the driving parameters is the output temperature that needs to be compatible with the turbine materials.

1.4 MethaLox liquid rocket engines

As mentioned in the section introducing the reusable launch vehicles, the choice of the propellant has a major impact on the development of the rocket and the missions it will be able to accomplish. Hence it is important to choose it carefully. Now that the key parameters describing the LRE performances were introduced, it is possible to compare the impact of different propellant combinations for a fixed nozzle geometry.

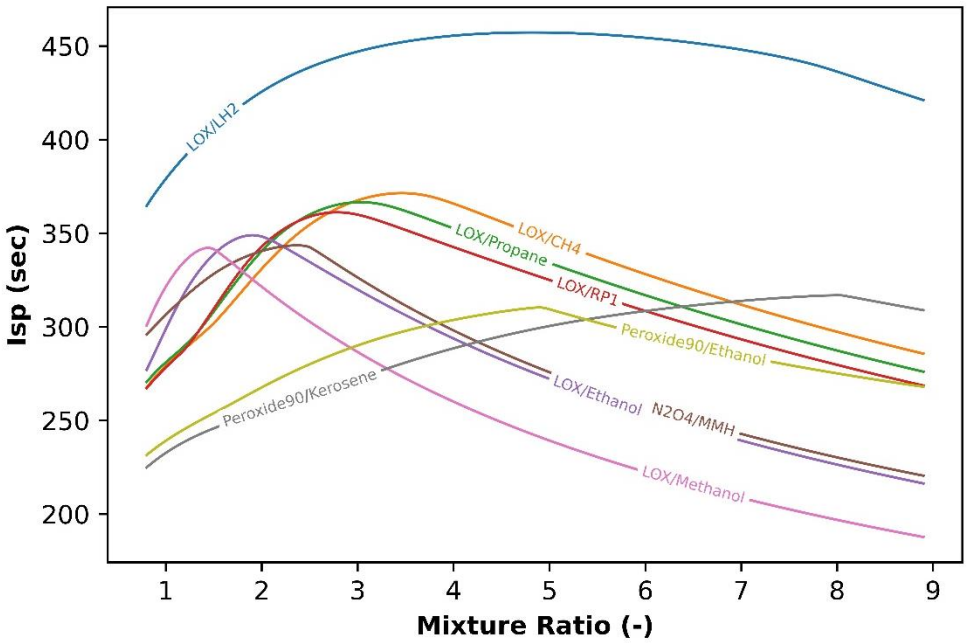

Figure 7: Isp in vacuum values over mixture ratio for different propellants for a fixed nozzle geometry (Eps=45), and operating conditions (chamber pressure Pc = 100 bar) - 0D calculations performed by the author with NASA CEA code [26,27]

1.4.1 Advantages of MethaLOx LREs

Figure 7 shows values of the specific impulse in vacuum over the mixture ratio for different couples of propellants. These results were obtained from 0D computations performed by the author with the NASA CEA (Chemical Equilibrium with Applications) code [26,27]. The nozzle geometry and operating conditions are fixed and identical for every studied case. The nozzle area ratio (noted Eps) being the ratio between the exhaust section A_e and the throat section A^* was fixed at 45 which is a typical value for upper stage engines [21]. The chamber pressure is fixed at 100 bar. The LOx/LH_2 propellant couple (one can talk about HydroLOx) yields by far the best performances for a large spectrum or RM with a max Isp of arount 450 s. The LOx/CH_4 couple (or MethaLOx) comes next in terms of performances with a max Isp of around 360 s. It is closely followed by propane and RP1 fuels with LOx while Ethanol and Methanol are far behind, their performances being really low on the lean side. As mentioned before, other oxidizers than LOx can be used, for example hydrogen peroxide H_2O_2 (labeled Peroxide90 on the graph, meaning that the oxidizer is composed of a aqueous solution of 90% H_2O_2). The H_2O_2/Kerosene couple shows interesting performances but requires highly oxidizer rich mixtures to yield its best performances and remains behind most of the hydrocarbon species. Finally, the already

mentioned toxic N_2O_4/MMH mixture gives performances comparable to ethanol (with the advantage of having non-cryogenic propellants storable at ambient temperature).

Hence, the Isp is not the only criterion to consider when sizing a launch vehicle and its engine. Indeed, the thermodynamic properties are also interesting to investigate. As they yield the best performances, H_2, CH_4 and RP1 properties are compared.

		Fuels		**Oxidizer**
	RP1	$\boldsymbol{LCH_4}$	$\boldsymbol{LH_2}$	$\boldsymbol{LOx}$
$\boldsymbol{\rho}$ **(kg/m³)**	813	422	70	1141
$\boldsymbol{T_{vap}}$ **(K) (at 1 bar)**	490	111	20	191
max $\boldsymbol{Isp}$ **(s) (with** $\boldsymbol{LOx}$**)**	300	360	430	-
Optimum mass MR	2.77	3.45	4.83	-
Optimum volume MR	1.97	1.28	0.30	-

Table 1: Thermodynamic and performance properties of different fuels with LOx. Optimum values extracted from [28]

Density:
The first interesting point is density. RP1 is two times denser in mass than LCH_4 and eleven times denser than LH_2. Hence, the kerosene derivative propellant has a clear advantage, allowing to store far more fuel in a tank than H_2. The latter requiring bigger tanks, which means more mass, hence more performance penalties for the payload. CH_4 is an interesting tradeoff, placing itself in between RP1 and hydrogen.

Boiling temperature T_{vap}:
The main advantage of RP1 is that it is storable at ambient temperature and atmospheric pressure whereas LCH_4 and LH_2 are cryogenic. However, LH_2 Boiling temperature is far lower than the one of methane, requiring additional thermal insulations to keep the fuel at optimum conditions. H_2 being a small molecule, leaks can easily happen, requiring again special systems, hence more mass for the launch vehicle. Methane, on the other side, has an interesting advantage: its T_{vap} is close to the one of LOx. Hence, as LCH_4 tanks already require less thermal insulation than for LH_2, methane tanks can be built identical to the one of LOx, allowing to decrease the production cost.

Optimum mixture ratios:
Optimum values of MR were taken from [28], based on a tradeoff focused on specific impulse using the relations defined in the previous section. They are also compatible with Table 1. These values can also be expressed in terms of volume ratio starting from the massic definition of RM. It will hence pilot the tanks volumes. The obtain figures from Table 1 means that for a LOx/LH_2 launch vehicle, the required volume of the LOx tank is only 30% of the LH_2 one. Meaning the latter, being manufactured with augmented insulation as mentioned before, is far bigger than the oxidizer tank. For RP1, the LOx tank needs to be twice as large as the fuel one whereas for methane the ratio is closer to one, reinforcing the cost manufacturing advantage of methane.

Combustion products:

Another important point is the nature of the combustion products generated during combustion. It can change depending on the engine's operative point but is principally driven by the propellant nature. LOx/LH_2 engine will typically produce a majority of water whereas LOx/RP1 or LOx/LCH_4 will also produce CO_2. Another side product of hydrocarbon combustion are soots. They tend to form for rich mixtures, so typically in the gas generators. Soot can be a problem as it forms deposits on chamber walls, turbine parts and increases the amount of radiated heat [21], hence increasing the thermal load on the surrounding materials. However, methane only contains one carbon atom C in its formulation while kerosene derivatives like RP1 are composed of an important number of C, which leads to more soot formation as seen on Figure 8. Hence, from the combustion products point of view, CH_4 seems like an interesting tradeoff. Compared to RP1, Methane is sometimes referred as a "green" propellant [29].

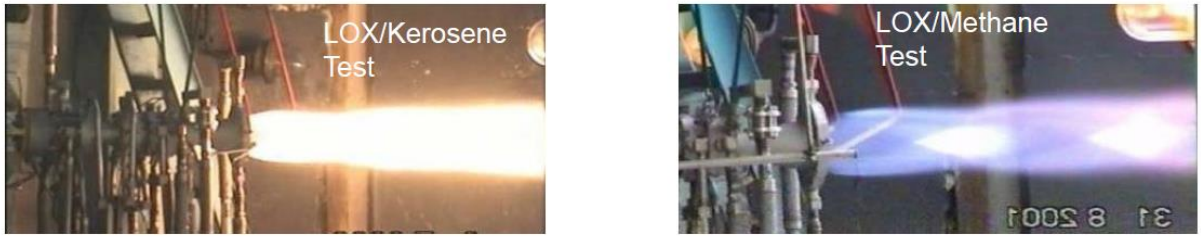

Figure 8: Gas Generator demonstrator tests in fuel rich conditions. Left picture shows a LOx/Kerosene test with a bright flame due to an important amount of soot-related radiation. Right picture shows a LOx/Methane test with far less radiation. Pictures extracted from [30]

Hence, as LH_2 is a fuel made for performance (used on expandable vehicles such as the European Ariane 5 or Japanese H-2), as RP1 is made for cost efficiency (used on expandable vehicles such as the Russian Soyuz and the American Falcon 9 and Atlas 5), CH_4 appears as the best tradeoff when sizing a reusable launch vehicle. Indeed, it presents good overall Isp performances and interesting density and storage temperature properties, making it also cost efficient. It produces less soots than its kerosene-derivative counterpart, hence reducing potential damage levels on the engine, increasing the duration of their lifespan which is a key point for reusability. Concerning its production, local processes based on biomethane deriving from plant decomposition directly at the launch base to avoid transport CO_2 emission are currently investigated [31]. Furthermore, in the perspective of future sample return or even manned mission to Mars, methane is envisioned as a key propellant as it can be produced from the large amounts of CO_2 found in the atmosphere [32] or even directly extracted [33] for the travel back to the Earth.

1.4.2 Current MethaLox LREs under development

As methane was quickly identified as the best candidate for reusable launch vehicles, several studies were conducted since the beginning of the 2000s with increasing complexity, from testing sub-parts to full engines [30,34,35]. Hence, MethaLox LREs started to be developed in parallel to the launchers. SpaceX, which as mentioned before manufactures the reusable Falcon 9 vehicle based on KeroLox for mainly development-cost-driven reasons, switches to methane for its massive Starship/SuperHeavy fully reusable launcher currently in development [13]. In order to do so, the company is currently testing its Raptor rocket engine. Other industrial actors are following this trend in the US, testing their own hardware in preparation of upcoming 2023 launches. This goes from heavy launchers with ULA's

Vulcan/Centaur equipped with BlueOrigin BE-4 engines [36] to small vehicles like the 85% in mass 3D printed Terran rocket from Relativity space using Aeon engines [37]. Numerous industrial players are also developing MethaLOx engines in Asia, with a majority of projects in China. Perhaps the most famous in 2023 is the Landspace company with its Zhuque 2 medium launch vehicle equipped with TQ-12 engines [38]. The rocket was the first orbital-class MethaLox vehicle to be ever launched. However, the flight ended with the second stage failure [39]. The 2nd launch attempt on July 2023 was successful, Zhuque 2 becoming the first MethaLox rocket to reach orbit. Europe is also intensively developing methane-based LRE. The Italian company AVIO is currently testing its MIRA LM-10 upper stage engine [40] which will equip the future Vega-E rocket. ArianeGroup, in partnership with CNES and ESA is currently working and testing the PROMETHEUS engine [41]. It is a gas-generator cycle 100-tons-of-thrust-class engine. In addition of being efficient, the idea is also to drastically reduce the production costs by simplifying the engine's design and by including additive manufacturing components. PROMETHEUS will equip the THEMIS demonstrator mentioned in this chapter as well as the future reusable launch vehicle developed by MaiaSpace and ultimately ArianeNext. Many other projects are currently at various development phase around the world [42]. Some statistics about the few above-mentioned MethaLox LRE are proposed on Table 2. It allows to appreciate the wide range of proposed performances, hence potential application of those engines. Some of these engines are also featured on Figure 9.

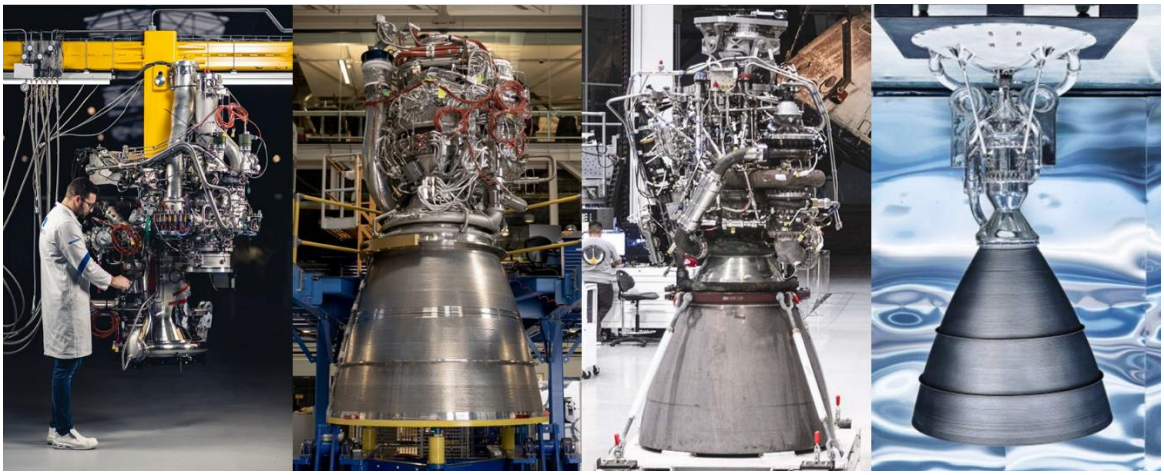

Figure 9: Currently developped and tested MethaLox LREs. From left to right: Prometheus (ArianeGroup), BE-4 (BlueOrigin), Raptor (SpaceX) and Aeon (Relativity Space) – Not to scale.

Engine	Raptor	BE-4	Prometheus	TQ-12	Aeon
Manufacturer	SpaceX (USA)	Blue Origin (USA)	ArianeGroup (Europe)	Landspace (China)	Relativity Space (USA)
Launch vehicle	Super Heavy/Starship	Vulcan/New Glenn	Themis/Ariane Next	Zhuque 2	Terran 1
Cycle	Full flow staged combustion	Staged combustion (oxygen rich)	Gas generator (fuel rich)	Gas generator (fuel rich)	Open expander
Chamber pressure (bar)	330	134	100	100	-
Thrust (kN)	2500 (SL)/3000 (Vac)	2400 (SL)	1000 (Vac)	667 (SL)/785(Vac)	100 (Vac)
***Isp* (s)**	327 (SL)/360 (Vac)	360 (Vac)	360 (Vac)	284.5 (SL)/337 (Vac)	360 (Vac)

Table 2: Comparison of a selection of currently tested MethaLOx LREs. SL indicates performances for sea level operations, Vac indicates performances for vacuum operation

1.5 Means of research and development for LREs

Before integrating a rocket engine on a launch vehicle, or even firing it on a test bench, sizing calculations and assessments need to be performed. Several potential issues must be tackled first. This is especially true when developing systems based on a relatively new fuel in the field such as methane. Hence, there are several means of study available to obtain a functional engine. Generally, sub-systems of the LRE are tested separately [30] (gas generator, injection head, turbopumps, etc.). These partial tests are generally conducted by the industrial and the partner governmental space agencies. They take place at a quite advanced state of the project. However, other capital studies are conducted beforehand (or in parallel to the development when focus is needed on a problematic aspect), on more fundamental phenomena. For combustion-related problematics, it can be for example injection behavior in certain conditions, flame structure analysis, soot production measurements etc.

These works can be carried out by experimental means. As the conditions at stake in LREs are extreme in terms of pressure (cf. Table 2) and temperature (cryogenic fluids followed by flames), dedicated test benches are as expensive as measurements are challenging. Hence there is not a lot of them. In France, the MASCOTTE test bench developed and operated by ONERA is used for multiple studies (carried out with CNES) and in particular methane combustion up to 60 bar [43].The injection plate can be equipped with either one or several injectors. Several systems can be plugged to the test rig. It can be for example equipped with optical access allowing PLIF and/or OH* profiles visualization to characterize atomization and flame behavior in transcritical and supercritical conditions [44,45], flame topology and soot characterization in GG operative conditions as the mixture ratio can be tuned [46]. Heat transfer at the wall is also studied [47], sometimes with additional setups such as the CONFORTH experiment [48]. In Germany, similar test benches are operated by the Technische Universität München (TUM) and co-operated by DLR. The single-injector combustion chamber developed by TUM operates at pressure comparable to MASCOTTE and is also equipped with various systems allowing to study flame topology [49] and wall temperature characterization [50,51]. Other setups allow, among other things, to study combustion instabilities in MethaLOx LREs such as the BKD test rig developed by DLR [52].

As experiments allow to observe and characterize key phenomena, numerical simulation comes as a support and complement. Indeed, computational fluid dynamics (CFD) allow to access data where no sensor can be placed (for example inside the main combustion chamber of a LRE operating at 100 bar) and are far cheaper than an engine test. Recent technological progresses in computational science allow to perform high fidelity simulations of LRE configurations in extreme conditions giving very interesting results (several examples will be cited in this manuscript). However, models used in CFD are initially based on experimental observations as accurate as possible. Hence, experiments and numerical simulations are inseparable complementary processes.

1.6 Thesis motivations

Even though experimental test rigs such as MASCOTTE and BKD allow to access to fundamental data and information, even more fundamental studies are sometimes required to understand all the phenomena involved. Indeed, sometimes hard-to-explain differences can be observed between experimental measured data and numerical prediction [45].

One of the issues with methane combustion in rocket engines is the understanding of the chemistry taking place in such extreme conditions. In order to describe the chemical transformations in CFD simulations, models called kinetic mechanisms (or schemes) are used (cf. next chapter for more details). Hence, detailed models based on experimental data and specifically dedicated to methane combustion already exist. However, as they have been developed to cover a wide range of academic and industrial applications, the vast majority of these kinetic mechanisms were validated against experimental data only at atmospheric pressure for methane reacting with air. Hence, the specific phenomena taking place at high pressure, and also high temperature (for combustion with pure O_2) are not recovered. This is an issue as chemistry is a key parameter in the combustion description. Indeed, in order to correctly predict the engine's performances, recovering the correct composition of the gases in the combustion chamber and their temperature is primordial. Those parameters directly pilot the heat release values, flame topology and by extension engine performances either in transient or steady state. To add a level of complexity, in certain regimes the turbulent flow directly interacts with the chemistry. Hence if some parameters such as reaction rates are miss predicted in those conditions, large error may ensue [53]. This highlights the need for having a correct chemistry description for MethaLOx LRE conditions based on representative experimental data. Obtaining such a model in order to perform accurate simulations is the aim of this research work. Experimental measurements should be performed in representative enough conditions before optimizing a kinetic mechanism on the obtained database. Moreover, as a highly detailed mechanism leads to more computational cost, the obtained model should be as compact as possible while keeping its precision. All the required steps toward these goals are detailed in the next chapter.

Chapter 2

Fundamentals and global strategy

2.1 Fundamentals of chemical kinetics

2.1.1 Definitions

In order to describe the behavior of chemical species in a reactive system, several basic parameters need to be defined.

For a system of N_s reactive species, the **mass fraction $\boldsymbol{Y_k}$** of the species k (for $k = 1$ to N_s) is defined as:

$$Y_k = \frac{m_k}{m_{tot}} \tag{7}$$

Where m_k is the mass of the species k and m_{tot} the total mass of the species in the system. In the same fashion, it is possible to define the **molar fraction $\boldsymbol{X_k}$** with n_k the number of moles of species k and n_{tot} the total number of moles in the system as:

$$X_k = \frac{n_k}{n_{tot}} \tag{8}$$

The system of N_s reactive species can be associated with N_R reactions defined as follows (for $j = 1$ to N_R):

$$\sum_{k=1}^{N_s} \nu'_{kj} S_k \leftrightarrow \sum_{k=1}^{N_s} \nu''_{kj} S_k \tag{9}$$

Where S_k is the symbol of the species k, and ν'_{kj} and ν''_{kj} the stoichiometric coefficients of species k for reaction j.

Each reaction j can be described by its **rate constant k_j** defined through the modified Arrhenius law as:

$$k_j = AT^b e^{-\frac{Ea}{RT}} \tag{10}$$

A being the pre-exponential factor, b the temperature exponent and Ea the activation energy. k_j unit depends on the reaction order. R is the universal gas constant.

For reversible reactions, there is a forward and a backward rate constant (respectively k_j^f and k_j^b). The **equilibrium constant K_j** of reaction j can be written as:

$$K_j = \frac{k_j^f}{k_j^b} \tag{11}$$

K_j can be computed using Gibb's free energy. Indeed, the expression of the **standard molar reaction Gibb's free energy $\Delta_r G^0$** (in $J\ mol^{-1}$) yields:

$$\Delta_r G^0 = -RTln(K_j) \tag{12}$$

$\Delta_r G^0$ can also be computed with the aid of the **standard molar reaction enthalpy $\Delta_r H^0$** (in $J\ mol^{-1}$) and **entropy $\Delta_r S^0$** (in $J\ mol^{-1}K^{-1}$) at a given temperature thanks to thermodynamics tables using the NASA polynomials [54]

$$\Delta_r G^0 = \Delta_r H^0 - T\Delta_r S^0 \tag{13}$$

All these parameters can be used to compute the **progress rate Q_j** for each reaction as:

$$Q_j = k_j^f \prod_{k=1}^{N_s} [X_k]^{\nu'_{kj}} - k_j^b \prod_{k=1}^{N_s} [X_k]^{\nu''_{kj}} \tag{14}$$

Where $[X_k]$ is the molar concentration of the species k (in $moles\, m^{-3}$). Q_j is measured in $moles\ m^{-3}\ s^{-1}$.

It is now possible to define the **reaction rate** of a given species k for a given reaction j as:

$$\dot{\omega}_{kj} = W_k Q_j (\nu''_{kj} - \nu'_{kj}) \tag{15}$$

W_k being the molar mass of species k. $\dot{\omega}_{kj}$ describes the contribution of reaction j to the production of species k. It is measured in $kg\ m^{-3}\ s^{-1}$.

Reaction rates are useful to define the **production rate** of a given species k for all the M reactions as:

$$\dot{\omega}_k = \sum_{j=1}^{M} \dot{\omega_{kJ}} = \sum_{j=1}^{M} W_k Q_j (\nu''_{kj} - \nu'_{kj}) \tag{16}$$

The production rate $\dot{\omega}_k$ describes the global contributions of all the reactions to the production of species k. It is also measured in $kg\ m^{-3}\ s^{-1}$. According to the mass conservation law, the sum of all the production rates is equal to 0.

It is now possible to define the **heat release rate $\dot{\omega}_T$** (also written HR) as:

$$\dot{\omega}_T = -\sum_{k=1}^{N_s} \Delta h_{f,k}^0 \, \dot{\omega}_k \tag{17}$$

$\dot{\omega}_T$ is expressed in $J\ m^{-3}\ s^{-1}$ with $\Delta h_{f,k}^0$ the standard formation enthalpy of species k.

2.1.2 Third body and pressure dependent reactions

Third bodies, also called collision partners and noted M, are species that are sometimes necessary for a reaction to happen. Indeed, M can either give or absorb energy, thus allowing other chemical species breakup or stabilization. Hence, the concentration of the collision partner directly appears in the progress rate of the concerned reactions as follows:

$$Q_j = [M_j](k_j^f \prod_{k=1}^{N_s} [X_k]^{\nu'_{kj}} - k_j^b \prod_{k=1}^{N_s} [X_k]^{\nu''_{kj}}) \tag{18}$$

$[M_j]$ being the concentration of the collision partner for reaction j. M represents all the different species that can be taken as third body. Hence all their potential contributions need to be accounted for in the progress rate. In order to do so, each species has a different collision efficiency E_{ff}. This leads to the following expression of $[M_j]$ with i being the subscript of all the possible collision partner species of concentration $[X_i]$:

$$[M_j] = \sum_i E_{ff_i} [X_i] \tag{19}$$

$[M_j]$ can also be computed as a function of the pressure and temperature.

Some rate constants may also display a pressure dependency. Hence, their behavior changes with P. This is for example the case of the C_2H_6 formation reaction. At low pressure, a third body is critical to initiate the reaction. Hence, the reaction can be written as $2CH_3 + M = C_2H_6 + M$. However, at high pressure, where $[M_j]$ is high, the collision partners are no longer critical to the reaction completion. Hence the reaction can now be written as $2CH_3 = C_2H_6$. Each of these two behaviors can be described with an Arrhenius law. k_0 being the low-pressure one while k_∞ stands for the high-pressure part. However, in between the low- and high-pressure limit, the rate constant behavior is difficult to describe. This is called the fall-off region. To make this pressure dependency clear, the reaction is written as $2CH_3(+M) = C_2H_6(+M)$. Several methods are available to match at the best the correct k_j behavior in this zone. A global expression of k is given as:

$$k = k_\infty \left(\frac{P_r}{1 + \mathrm{P_r}}\right) F(P_r, T) \tag{20}$$

Where P_r is the reduced pressure, expressed as:

$$P_r = \frac{k_0[M_j]}{k_\infty} \tag{21}$$

$F(P_r, T)$ is called the fall-off function. Several definitions exist, as the Lindemann [55,56] or Troe [56,57] formulations.

A more recent way to reproduce the pressure dependency of rate constants, without using a third body approach, is the PLOG formalism [58]. The idea is to describe the behavior of a given reaction through several Arrhenius laws defined at different pressures. In order to get k_j at a given pressure, a logarithmic interpolation is performed in between the already defined functions. Both fall-off reactions or PLOG can simultaneously be encountered in chemical mechanisms.

2.2 Fundamentals of flame structures

The two main existing combustion modes are premixed or diffusion. In the first case, the fuel and oxidizer are mixed before the ignition. In the second one, the fuel and oxidizer are injected separately and the flame develops at the stoichiometric interface between the two streams. Both of these combustion modes can be either laminar or turbulent. As premixed and diffusion flames will be encountered during this work, they are described in this section.

2.2.1 Laminar Premixed flames

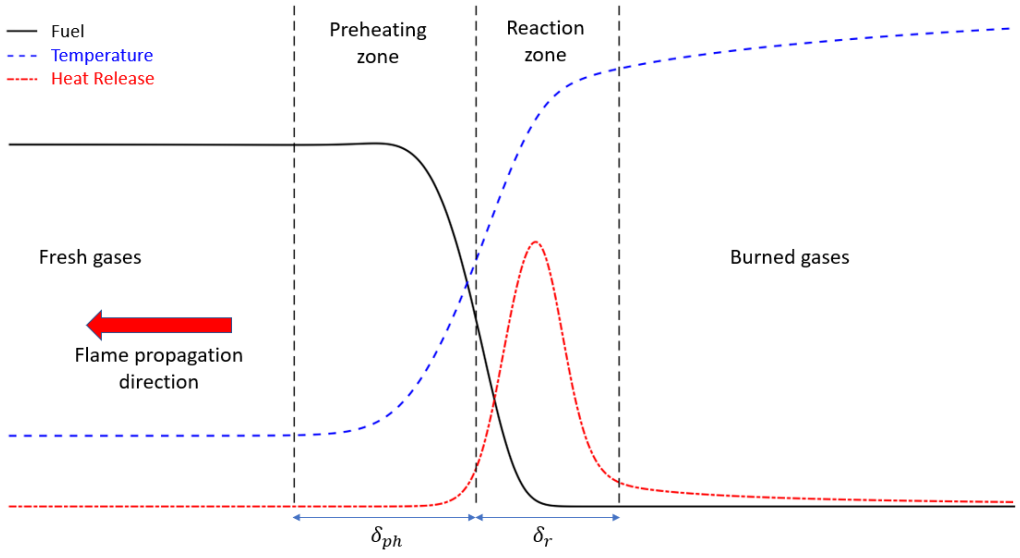

Figure 10: Premixed flame structure (adapted from [59]*)*

Laminar premixed flames can be divided in two characteristic zones as illustrated on Figure 10. First a preheating zone (of thickness δ_{ph}) where the fresh gases near the flame front are heated until they reach the ignition temperature. Its thickness is mainly piloted by thermal diffusion effects (see next chapter for its detailed definition). In the reaction zone (of thickness δ_r), chemical effects are

predominant. This is where the maximum of heat release is located. Molecular and thermal exchanges between the two zones lead to the flame self-propagation in the mixture.

Planar laminar premixed flames are an ideal case. For premixed spherical expanding flames, which are widely used in experimental setups, the flame front geometry directly impacts the propagation speed. This is true in particular for small radii. The evolution of the flame's geometry is affected by stretch κ (measured in s^{-1}), which describes the temporal variation of the flame surface A:

$$\kappa = \frac{1}{A}\frac{dA}{dt} \tag{22}$$

For a spherical flame, κ yields:

$$\kappa = \frac{2}{R_f}\frac{dR_f}{dt} \tag{23}$$

Hence, when measuring the flame radius evolution over time, the obtain speed is the stretched flame speed in the laboratory reference frame (or speed relative to the burn gas) S_b, defined as:

$$S_b = \frac{dR_f}{dt} \tag{24}$$

In order to extract the unstretched flame speed value for isobaric conditions (i.e. during the early stages of the flame propagation), a relation between stretched and unstretched flame speeds needs to be used. Several approaches were proposed, suggesting linear [60,61] and non-linear [62,63] relations. The linear relation suggests that S_b and S_b^0 are related through a parameter called the Markstein length L_b (measured in m). It yields:

$$S_b = S_b^0 - L_b\,\kappa \tag{25}$$

S_b^0 is obtained by plotting the relation over stretch, and then by performing a zero-stretch extrapolation. Hence, it is possible to deduce the unstretched laminar flame speed relative to the fresh gases S_u^0 thanks to the mass conservation equation and the density expansion ratio:

$$S_u^0 = \frac{\rho_b}{\rho_u} S_b^0 \tag{26}$$

Moreover, several instability phenomena can affect the premixed flame during its propagation. They are discussed in depth in the next chapter referring to the experimental study of spherical expanding flames in extreme pressure and temperature conditions.

2.2.2 Laminar Diffusion flames

Diffusion flames appear when flows of oxidizer and fuel diffuse toward each other. Once the mixture is ignited, a reaction zone is found along the stoichiometric line near which the heat release is maximum. Hence, the position of the flame mainly depends on the oxidizer/fuel couple. As the diffusion flame does not propagate toward the rich or lean side of the domain where it would not be

sustained anymore, it has no intrinsic speed. Moreover, the reaction zone thickness along the stoichiometric line is very small compared to premixed flames [64].

Z formalism:

An easier way to describe diffusion flames is to work in the mixture fraction Z space and not in the physical space x. This transformation leads to simplified 1D formulations of the mass and energy conservation equations as described in [64]. However, certain hypotheses are needed:

- Small Mach number and constant thermodynamic pressure
- Unity Lewis number: thermal and mass diffusivity are supposed equal
- Diffusion coefficients D are identical for each species
- The heat capacities of the species C_{p_k} are all equal and independent of the temperature

Derivation of laminar diffusion flames in Z space is used in this work for 1D CANTERA computations or mechanisms reductions using the ARCANE [65] tool. It allows to be computationally efficient by creating a "natural scaling" on the reaction zone, ensuring the use of far less grid points than in the physical space to solve the flame [23]. Even if the previously mentioned assumptions are not valid in a real case, there are considered acceptable for 1D calculations, allowing valid chemical scheme reductions [23,66].

This work uses the Bilger definition of Z [67] :

$$Z = \frac{\beta - \beta_0}{\beta_1 - \beta_0} \tag{27}$$

With

$$\beta = \sum_{e=1}^{N_e} \gamma_e \sum_{k=1}^{N_s} N_{e,k}\, W_e \left(\frac{Y_k}{W_k}\right) \tag{28}$$

$N_{e,k}$ being the number of elements e present in species k ans N_e the number of elements in the whole chemical system. The γ_e are weighting coefficients defined by Bilger for C,H and O atoms [67]. Z being normalized, its minimum value $Z = 0$ represent pure oxidizer while $Z = 1$ means pure fuel. Hence, the stoichiometric value, written as Z_{St} depends on the fuel/oxidizer couple. In our case, for CH_4/O_2 mixtures, $Z_{St} = 0.2$. Figure 11 describes the structure of a diffusion flame in the Z space, showing its different characteristic zones.

It is now possible to define the scalar dissipation rate χ (measured in s^{-1} and given here in the 1D case) that directly quantifies the mixing level as:

$$\chi = 2D_m \left(\frac{\partial Z}{\partial x}\right)^2 \tag{29}$$

Strain rate:

When studying a counter-flow diffusion flame in the physical space x, playing on the injection speed (hence on the mass flow rates) of oxidizer and fuel while keeping the distance between the two injectors constant increases the strain rate a of the flame (measured in s^{-1}). The higher the strain rate, the higher the mixing speed, hence increasing the heat release. At a certain point, combustion is

not fast enough to allow the proper chemical reactions to take place, leading to flame extinction. High strain rates are typically encountered in the combustion chamber of rocket engines. However, the use of pure O_2 as oxidizer ensures very reactive mixtures, hence pushing away the extinction limit [23].

The link between the strain rate and the scalar dissipation rate can be defined as a proportional relation [64]:

$$\chi = \frac{a}{\pi}(-2[\mathrm{erf}^{-1}(1-2Z)]^2) \tag{30}$$

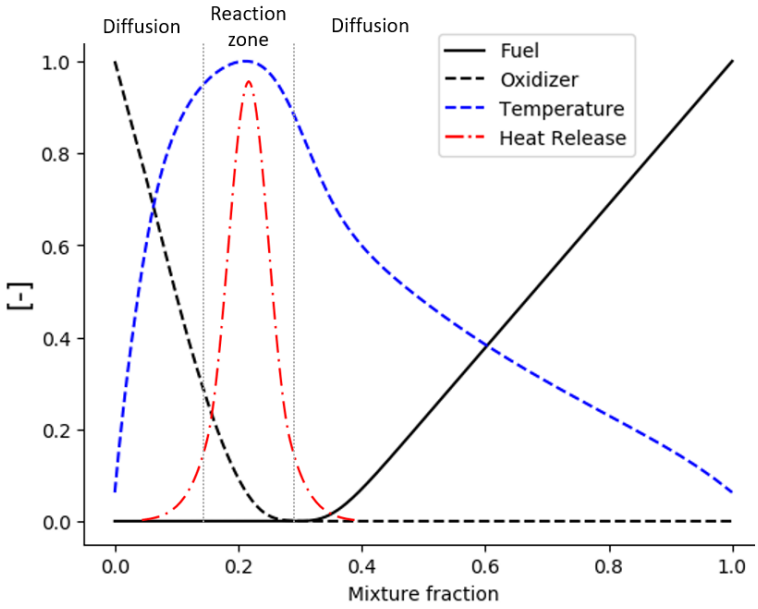

Figure 11: Example of diffusion flame structure

2.2.3 Turbulent Diffusion flames

1D laminar diffusion flames are interesting configurations to validate chemistry models. However, rocket engine combustion chambers feature turbulent combustion. Turbulent diffusion flames can be characterized with different regimes. These zones can be described with the aid of the Reynolds number Re characterizing the turbulence, and the Damköhler number Da. The latter is defined as the ratio between the turbulent flow and the chemical characteristical timescales, respectively τ_f and τ_c. Figure 12 representing the Damköhler of the flow Da^{fl} over the turbulent Reynolds Re_t illustrates these different regimes.

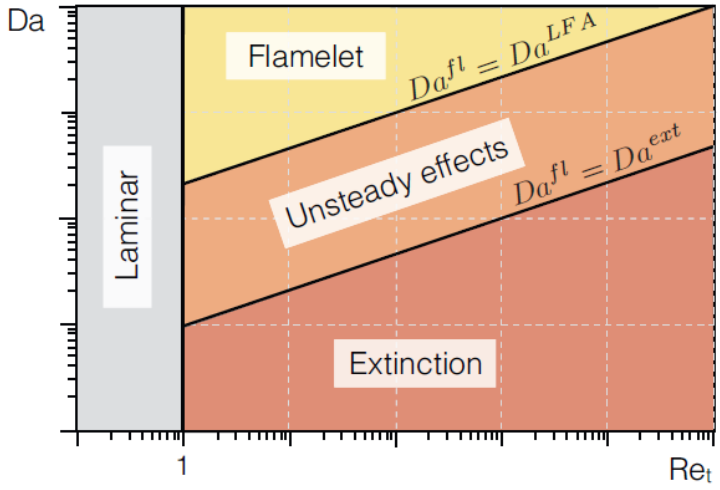

Figure 12: Diffusion flame regimes map (from [68] *adapted from* [69]*)*

Three characteristic zones are visible on the graph for turbulent flows (i.e. $Re_t > 1$).

- For high Da values, the chemistry is very fast compared to the flow characteristic time scale. Hence the flame is not affected by turbulence and keeps a laminar structure. This regime is called LFA regime for *Laminar Flamelet Assumption*. It can also be called the infinitely fast chemistry regime. The lower limit of this zone is the critical Da^{LFA}.

- For $Da^{LFA} < Da^{fl} < Da^{ext}$, unsteady effects predominate. Indeed, turbulence and chemistry are in close interaction.

- For low Da values, the chemical time scale is too important compared to the flow timescale. Hence the flame is fully affected by turbulence. And for $Da^{fl} < Da^{ext}$, the flame is quenched.

Da can be expressed as a function of the scalar dissipation rate. Supposing that $\tau_f \sim 1/\chi$:

$$Da \sim \frac{1}{\chi \tau_c} \tag{31}$$

This illustrates that at small Da, high strain values tend to quench the flames.

2.3 Chemical schemes for methane oxycombustion

2.3.1 Chemical schemes and CFD

In order to describe the evolution of a chemical system, the transformations at stake can be described through a kinetic mechanism (also called chemical scheme). These models are composed of several species interacting in different reactions described by their rate constants. Coupled with thermodynamics and transport properties, the mechanism can be used to perform 0D and 1D computations with CANTERA or CHEMKIN like solvers. They can also be used for 3D LES CFD computations.

The mechanisms can be of various sizes as illustrated by Figure 13. The detailed ones, composed of more than a hundred of species, are generally used for 0D and 1D computations only. For example, species profiles in PSR, or flame speed calculations. Indeed, their cost is prohibitive for CFD simulations. It is important to note that each added transported species corresponds to an additional conservation equation to solve.

Figure 13: Classification of chemical mechanisms

Hence, the so-called global mechanisms (4 to 6 species for an order of magnitude of 2 reactions) are often used in CFD because of their attractive computational cost. Several global models were developed to describe hydrocarbon combustion for LES applications [70,71] and even for CH_4 oxycombustion (*Glomec* approach by Blanchard and Strauss [23,72]). The selection of species is performed to correctly recover reference equilibrium values and kinetic properties are generally tuned to match flame speed targets for given conditions [71]. Hence, global mechanisms are able to correctly describe these conditions and key representative values like the heat release. However, the model has difficulties to reproduce a good flame structure and the interaction with turbulence [23]. Moreover, it tends to exhibit poor performances when outside the initially defined range on which is was optimized.

Another method called tabulated chemistry also allows to reduce the calculation cost. Values of density, temperature, species mass fractions and chemical source terms are pre-tabulated from diffusion and/or premixed 1D flames (depending on the case) as a function of scalar quantities (e.g., mixture fraction, scalar dissipation rate, and/or progress variable *c*). The latter are then computed and transported by the CFD solver, hence avoiding multiple resolutions of species conservation equations. The table can be generated with different chemical kinetics mechanisms, from detailed ones to global. Moreover, if the chemistry is supposed infinitely fast (as opposed to the detailed finite rate chemistry), equilibrium quantities can be used to build a manifold. Tabulated chemistry is often coupled with probability density function (PDF) models to account for turbulence-chemistry interaction effects. Such methods were successively applied to rocket engine combustion chamber simulations [73,74]. However, like every methods, tabulated chemistry has limitations. First, the shape of the PDF must be accurately presumed as it is going to impact the prediction in an a-posteriori manner. Finally, the generated manifold is dependent on the studied case, and consequently, the flame structure and turbulence regime, thereby requiring the generation of a new table when changing the operating conditions of the simulation.

Hence, an intermediary solution between global and detailed mechanisms without sacrificing too much accuracy on chemistry is proposed. As the computational power available for CFD computations rises, reduced mechanisms (composed on average of 10 up to 40 reactions) are more and more used for high fidelity LES. The method used at CERFACS is called ARC (*Analytical Reduced Chemistry*). The aim is to reduce a detailed mechanism without degrading its performance for specific conditions called reduction targets. These targets can be for example flame speeds, ignition delay times, heat release

profiles etc. At the end, only the most relevant species and reactions are conserved. Moreover, some fast species (typically the radicals) can be treated with the QSSA (*Quasy-Steady State Approximation*), removing stiffness from the system. At CERFACS, the reduction process is performed by a tool called ARCANE [65]. A detailed presentation of the tool as well as an application example is given in Chapter 4.

This method was successfully applied for CH_4/O_2 rocket engines combustion chamber calculations [66,75]. However, the generated reduced schemes are fully dependent on the detailed scheme that was initially used for the reduction process. This raises the issue of the validity of chemical mechanism in these extreme conditions. Hence, before deriving any ARC for an LES computation, it is important to possess a mechanism reliable enough for CH_4/O_2 combustion at high pressure and temperature, which is not an easy thing.

2.3.2 State of the art of chemical schemes for methane oxycombustion

Since the interest in methalox rocket engines appeared, the question of the validity of the chemical schemes in these extreme conditions has arisen. Several models and approaches were developed and are summed up in this section. Meanwhile, the potential of mechanisms not initially derived for these applications is also discussed.

RAMEC

The most famous and widely used model is the RAMEC mechanism proposed in 1999 by Petersen et al. [76]. It consists of 38 species and 190 reactions. The mechanism derivation was first motivated for *ram accelerator* applications [77], an innovative cost effective launch method for space or military payloads. In order to obtain a mechanism able to describe the kinetics of CH_4 oxycombustion at high pressure and temperature, the model derivation was made on experimental ignition delay times in extreme conditions obtained by the same team [78]. As CH_4/O_2 combustion releases a significant amount of energy (cf. Chapter 3), measures were performed for mixtures diluted with Ar or N_2. However, the dilution rates employed at the explored (P, T) of this study are among the lowest of the literature (<70% in volume). Pressure varies from 35 to 260 atm and temperature between 1040 to 1600 K. The mechanism species and reactions were mainly derived from the GRI-Mech 1.2 [79], though some particular reactions were added. The author emphasizes the importance of the HO_2, CH_3O_2 and H_2O_2 species and the reactions involving them, not sufficiently known at the time.

RAMEC-derived mechanisms

RAMEC being a reference model for CH_4/O_2 combustion, it is widely used as a basis for other models. Some key examples are listed in this section. Petersen first proposed a reduced version of the mechanism called REDRAM [80]. It is composed of 22 species and 34 reactions. The aim was to remove species and reactions that do not have a significant impact on the ignition delay times from [78]. Hence, REDRAM has the same performances as RAMEC on these targets with a 5% margin of error.

Natale et al. from CIRA derived the HPRB mechanism [81] from RAMEC in the framework of the HYPROB project [82]. The goal of HYPROB is to develop as small demonstrator of methalox combustion chamber to validate models and hardware designs like the injector head. HPRB is a 18 species 47 reactions model derived on the design point of the test engine, i.e. a stoichiometric mixture at 52.5 bar. The reduction method consists on a combination of reaction pathways and sensitivity analyses on a reference PSR 0D numerical computation. The mechanism was used to perform CFD RANS calculations on a domain composed of the injector plate, combustion chamber and nozzle. Other

simulations were performed with additional mechanisms from the literature and compared to experimental results (combustion chamber pressure, qualitative analysis of the density lines at nozzle outlet and a posteriori examination of the injector plate damages). On the overall, the mechanism performed well compared to other models and global 2 steps chemistries previously used. However, it is only valid for the reduction point it was derived on. Moreover, results near the injection plate where propellants are cold and exhibit non-ideal-gas behavior may not be valid.

More recently, Monnier et al. developed a mechanism also reduced from RAMEC composed of 17 species and 44 reactions [83]. Reduction targets were reference numerical calculations of auto ignition delay times, laminar premixed flames and counter-flow diffusion flames performed with RAMEC for a wide range of conditions. However, no experimental data was used as reference or for validation, the initial RAMEC derivation on Petersen ignition delay times being enough. The reduction process was performed with the ORCh tool [84]. After validation, DNS computations with the real-gas version of the SiTCom-B solver were performed. The calculations focused on a pocket of methane at 100 bar and a double transcritical injection in a splitter plate configuration at 54 bar.

Blanchard also proposed a mechanism derived from the RAMEC [23,66] using ARC chemistry. The ARCANE tool [65] previously mentioned and detailed in Chapter 4 was used for reduction. As the objective was a 3D LES computation of the CONFORTH test bench of ONERA [43], reduction targets where chosen for representative conditions. Hence, 1D strained diffusion flames were derived for pressure and strain values representative of the application case (respectively $49 < P < 59$ bar and $100 < \chi < 1500\ \mathrm{s}^{-1}$). The obtained mechanism is composed of 14 transported species, 4 QSS species which concentrations are computed analytically, and 68 reactions. The use of ARC chemistry makes detailed study of the chemical phenomena in the flame computationally affordable for 3D LES simulations of rocket engines configurations.

Zhukov-Kong

Another widely used mechanism is the model derived by Kong [29,85] from the Zhukov model [86,87]. The latter is a massive 549 species and 2518 reactions model for C1-C7 species. It is validated against experimental ignition delay times for a wide range of temperatures (850 to 1700 K) and pressures (1 to 537 bar). Kong reduced the mechanism into the Zhukov-Kong model of 23 species and 51 reactions. The reduction method is based on reaction pathways and sensitivity analysis. A posteriori validation is made against a mix of experimental and numerical targets. The experimental auto-ignition delay times from Zhukov study for lean conditions at 50 bar as well as numerical 0D ignition delay times at high pressure and 1D computations of counterflow flames at 60bar. The study allowed to identify the major oxidation pathways, mainly the *C2 mechanism* involving species from C_2H_6 to C_2H_3 for fuel rich conditions in particular. The author also highlights the fact that C3 and C4 species are not important for methane oxycombustion (also observed for RAMEC derivation). Due to its compactness, Zhukov-Kong mechanism is used for many CFD applications. It was used for example in the 3D RANS calculations by CIRA for the HYPROB project [81] as a benchmark comparison. Another example of application is the DLR URANS calculations performed by Horchler et al. with the TAU code on a 3D mono-injector test case at high pressure [88].

Slavinskaya

The Slavinskaya mechanism [89] was proposed as a reduced version of a DLR detailed C1-C2 model for soot precursors formation [90]. The reduction is performed with the in-house RedMaster code based on sensitivity analysis, allowing to obtain a 24 species and 100 reactions model. Highly diluted ignition delay times (from 1 to 50 bar) as well as laminar flame speeds from 1 to 60 bar for CH_4/air and highly He diluted mixtures (85% in molar fraction of the oxidizing mixture) were used as reduction

targets for a wide range of equivalence ratios. The mechanism was then validated against the corresponding experimental values of these targets. The overall performance is good, especially for CH_4/air mixtures. However the mechanism has difficulties to capture the experimental behavior at 60 bar, especially for rich mixtures (experimental data from [91]). The author also proposed other similar mechanisms for lower pressures [92].

Other mechanisms

Other mechanisms were used as a starting point to derive CH_4/O_2 kinetic models. For example, Saccone et al. from CIRA derived a model [93] from the Lu30 kinetic scheme [94] (itself deriving from GRI-Mech 3.0) for intermediate pressure (i.e. 20 bar) applications in the frame of the HYPROB project. A mechanism also derived from Lu was used by Maestro et al. for an ARC derivation then implemented for a 3D LES computation of a TUM methalox experimental test bench at 20 bar [75].

As explained above, mechanisms used to describe methane oxycombustion always initially derive from a more detailed model created for a broader range of applications. Kinetic schemes are then generally reduced using numerically computed 0D/1D targets representative of the application case. For example, ignition delay times and/or laminar counterflow diffusion flames at high pressure. However, since CH_4/O_2 mixtures lead to prohibitive conditions for most of the classical experimental setups (see Chapter 3), the datasets used for validation in the literature are always based on diluted conditions. It would be interesting to perform such a process on non-diluted CH_4/O_2 dataset studied with a dedicated setup for a broad spectrum of conditions. However, since the majority of mechanisms are not initially designed for high pressure and temperature applications, the reduced kinetic model might have difficulties to match the validation dataset. Hence, an optimization procedure of the starting mechanism on the oxycombustion experimental dataset could be a key approach to guarantee a good model behavior. It would be then possible to perform reductions of the obtained mechanism on targets representative of the CFD application case of interest. The latter process can be performed with ARCANE to obtain an ARC mechanism tailored for LES calculations. More recent kinetic mechanisms encompassing new experimental datasets, that did not exist at the time of the RAMEC derivation, are interesting candidates for such a procedure, along the other already existing models. Stanford's FFCM1 [95] and Polimi CRECK's POLIMI C1-C3 [96] present such characteristics. Figure 15 and Figure 14 provide an illustrated overview of the mechanisms mentioned in this section.

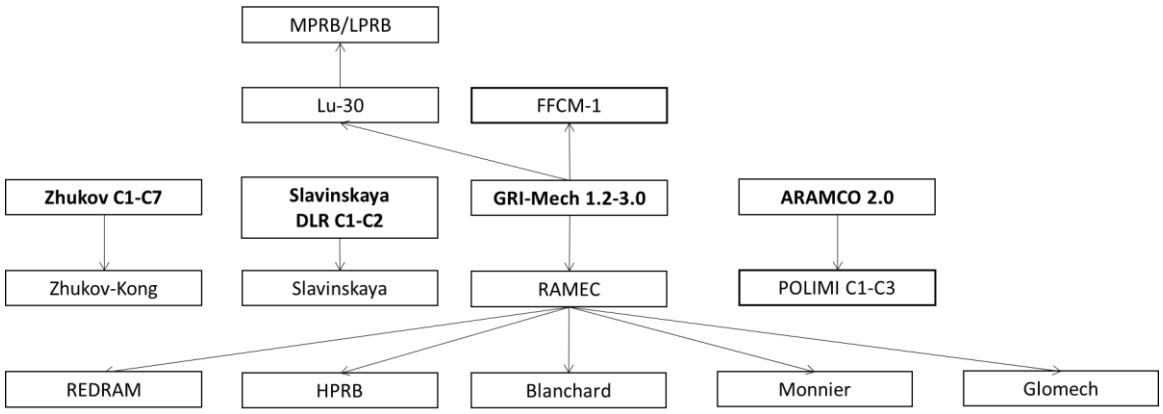

Figure 14: Family tree of the mechanisms involved or linked with CH_4/O_2 combustion

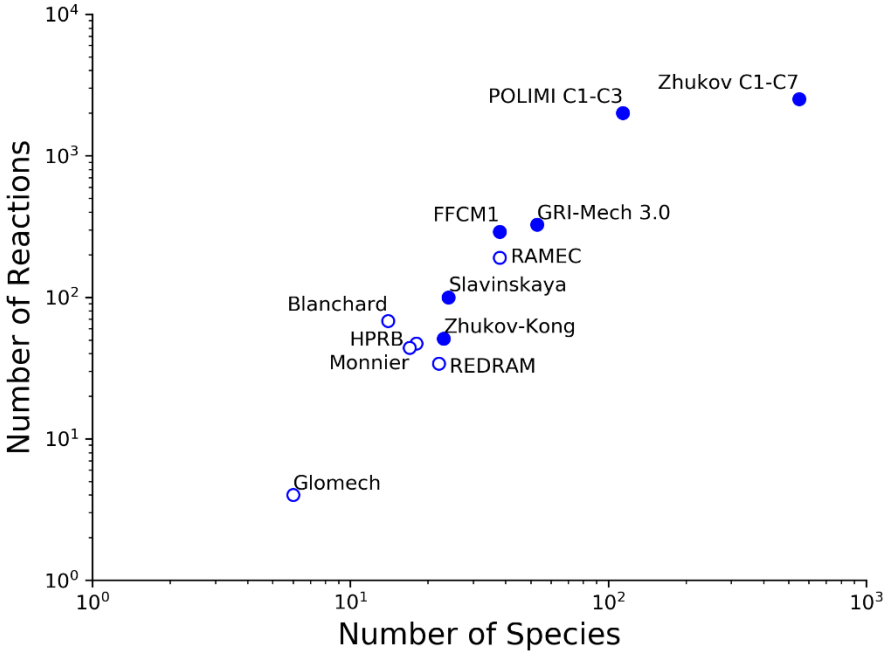

Figure 15: Sizes of the main mechanisms used or envisioned to be used for CH_4/O_2 combustion applications (empty marks are for RAMEC-derived mechanisms)

2.4 Global strategy

Diffusion flames are the main combustion mode in rocket engines. However, such flames for methane-oxygen mixtures at high strain and pressure are very challenging to study experimentally. Indeed, it requires dedicated expensive setups [43,51] and the parameters that can be measured are generally limited. Studies generally focus on combustion chamber pressure, temperature and heat flux at the walls [50,82] and OH* imaging [45,97]. If such flames are difficult to study at lab scale, a solution to the problem could be to use setups more dedicated to fundamental combustion phenomena. Spherical bombs, made for the measurement of premixed laminar flame speeds, are good candidates. Indeed, they allow to perform measurements for a wide range of mixtures conditions, pressure and temperature. The generated database can then be compared to kinetic mechanisms in order to evaluate their performances [98,99]. Hence, with hardware and post treatment methods adaptation as oxycombustion conditions remain challenging, such setups could be used for CH_4/O_2 flame speeds measurements at high pressure and temperature. A dedicated chemical mechanism could be then optimized on the created database.

Using kinetic mechanisms derived on premixed flames to apply them afterwards on diffusion flames was already performed with the Glomec approach [72]. Indeed, this global mechanism already mentioned in the previous section was tuned to match equilibrium conditions and numerical reference laminar flame speeds values. It was then used for 3D LES calculations and compared to the RAMEC-derived Blanchard scheme. Despite showing limitations, the approach exhibited encouraging results [23]. However, the CH_4/O_2 mechanism to be developed in this work is far more complex than a global model as it aims to describe the kinetics phenomena involved in a realistic way. Hence, it is important

to prove that the kinetic schemes behaviors are similar for both combustion modes (diffusion and premixed) in oxycombustion conditions. 2 types of investigations are performed in this section: pathway analyses to investigate the main ways of CH_4 oxidation and a study of the contribution of reactions to the global heat release.

2.4.1 Pathway analysis

The aim of such analysis is to study the flux between species of a single carbon atom coming from CH_4 down to the formation of CO_2, integrated on the computational domain. Two mechanisms were used: RAMEC as it is the current main reference for methane oxycombustion, and POLIMI C1-C3 as it is a recent promising detailed mechanism. Minor differences are noticed, however the two models lead to identical final conclusions detailed in this section regarding the premixed/diffusion paths.

The reference case for diffusion is a highly strained flame (χ=1000 s^{-1}) at 100 bar, representative of rocket engine conditions. This reference case is first compared to a 1 bar diffusion flame for similar strain values in order to assess the pressure effects. Results shown on Figure 16 were obtained with the POLIMI C1-C3 mechanism. Only the fluxes greater than 10% are shown to facilitate the analysis. Two main reaction pathways, identified with 2 colors and named C1 and C2, are identified.

C1: $CH_4 \rightarrow CH_3 \rightarrow CH_2OH \rightarrow CH_2O \rightarrow HCO \rightarrow CO \rightarrow CO_2$

C2: $CH_4 \rightarrow CH_3 \rightarrow (C_2H_6) \rightarrow C_2H_5 \rightarrow C_2H_4 \rightarrow C_2H_3 \rightarrow C_2H_2 \rightarrow HCCO \rightarrow CO \rightarrow CO_2$

C1 is composed of only C1 species progressively losing hydrogen atoms while C2 is mainly composed of C2 species losing carbon and hydrogen atoms. C_2H_5 is equally produced by pathways coming from C_2H_6 or even directly from methyl CH_3. At low pressure, it seems there is no preferred path of oxidation. When reaching the 100 bar pressure, the C1 pathway becomes clearly predominant. These conclusions are consistent with the ones of Zhukov and Kong [29,85]. Indeed, the same C1 and C2 paths were identified in the literature, as well as the shift to C1 when pressure and temperature increases. Hence, the involved C1 and C2 species are expected to be part of a detailed/reduced mechanism for methane oxycombustion. The same analysis on the RAMEC mechanism (not shown here) tends to show that C1 remains the main pathway at 1 and 100 bar.

A complementary analysis was carried out at different pressures (from 1 to 100 bar), this time varying the strain χ to characterize its impact (from 100 to 10000 s^{-1}). For pressures greater than 2 bar, no impact of the strain was observed on the main pathways.

The same investigation is then performed for premixed flames. As the fluxes presented on Figure 16 are integrated on all the 1D computational domain, and since diffusion flames cover the full spectrum of equivalence ratios depending on the position, several analyses at different φ are required for premixed flames in order to be comparable. Hence, different φ (from 0.5 to 2.5) are explored. The analyses are performed at 1 and 100 bar showing no critical difference on the displayed final result. The identified principal pathways for the tested conditions are listed in Table 3.

	φ=0.5	φ=1.0	φ=1.5	φ=2.5
POLIMI Opti	C1	C1	C1	C2
RAMEC	C1	C1	C1	C2

Table 3: Main pathways for premixed conditions at 100 bar

The key conclusion of this analysis is that the main pathways identified for premixed flames for a large spectrum of equivalence ratios are either C1 or C2. These are the same paths as those identified for diffusion flames in rocket engine representative conditions. Hence, it seems that the main species pathways proper to methane oxycombustion are the same for premixed flames and highly stretched diffusion flames. Another conclusion from Table 3 is that the C2 path is favored when it comes to rich mixtures. This is a feature also identified by Zhukov on the rich side of diffusion flames [85].

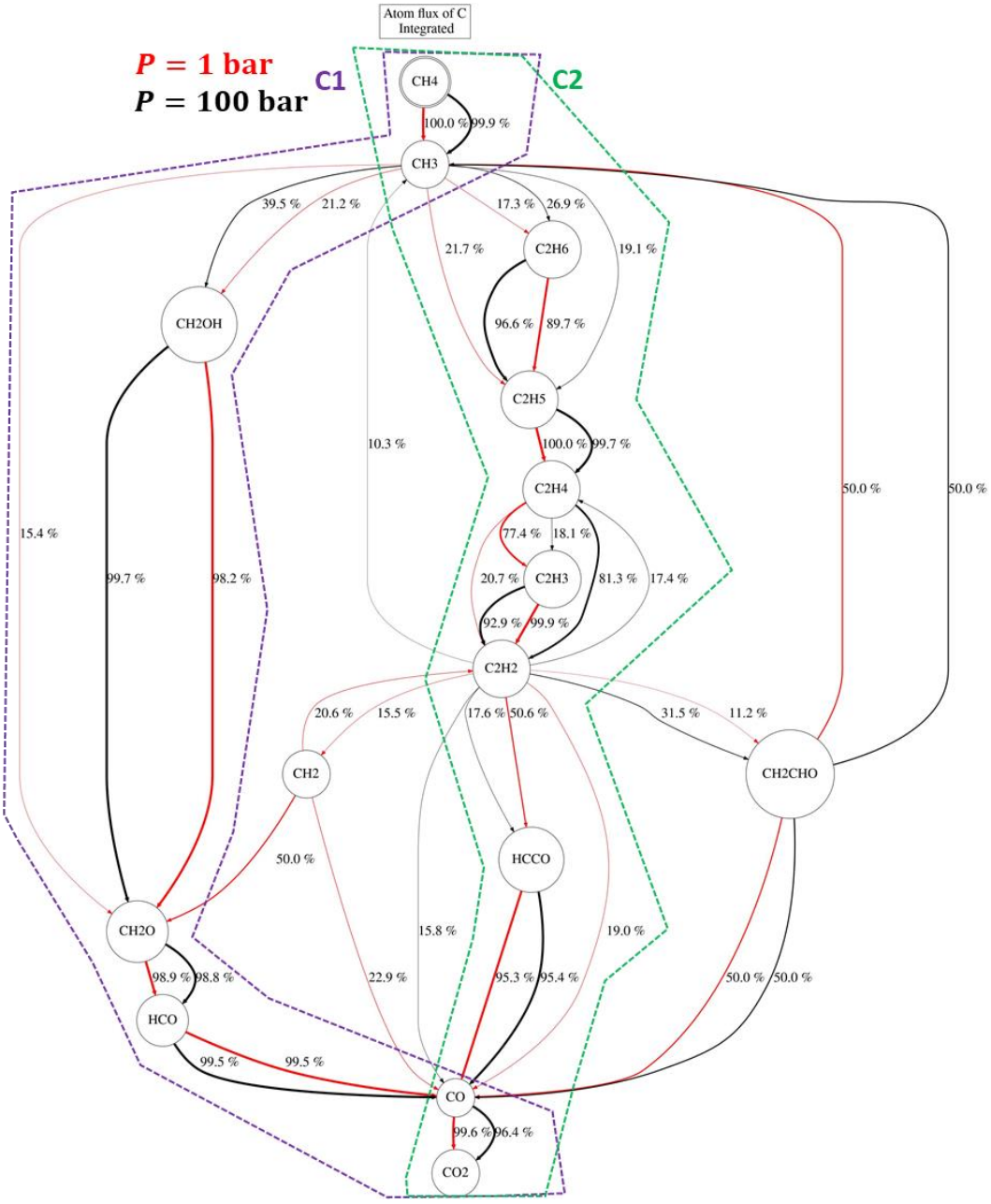

Figure 16: Integrated flux of a C atom starting from CH_4 for a highly strained flame at different pressures

2.4.2 Contribution of reactions to the heat release

One of the crucial parameters to characterize a kinetic model is the heat release. The idea of this section is to assess the contribution of each reactions of a chemical scheme to the global heat release for both laminar premixed and diffusion flames, and then compare it. The results displayed here come from the POLIMI C1-C3 mechanism, but once again, conclusions are identical with the RAMEC mechanism. Figure 17 illustrates the 10 most heat-release-contributing reactions for a highly stretched diffusion flame representative of rocket engine operating conditions (parameters similar to the previous section: χ=1000 s^{-1} and 100 bar). Reactions can contribute to the heat release HR in two ways: either exothermic (HR>0) like $H_2 + OH = H + H_2O$ or endothermic (HR<0) like $H + O_2 = O + OH$. The same analysis is then performed on premixed flames for the Table 3 conditions for different φ for the same reasons as the one mentioned in the previous section (the corresponding graphs are displayed in the Appendix section of Chapter 2). Several conclusions can be drawn from the comparison between the diffusion and the premixed cases. The endothermic reaction $H + O_2 = O + OH$ identified for diffusion flames appears as a major HR contributing reaction for all equivalence ratios tested for the premixed case. Some diffusion flames top HR-contributing reactions like $H + O_2(+M) = HO_2(+M)$ and $HO_2 + OH = H_2O + O_2$ also appear in the top 10 reactions contributing the most for lean premixed flames (φ=0.5 and 1 cases). Same conclusions for rich premixed mixtures where the reactions $H_2 + OH = H + H_2O$ and $H_2O + O = 2OH$ are non-negligible and can also be found in the top 10 for diffusion flames. Hence, it is clear that the main reactions involved in the heat release for methane oxycombustion conditions are the same for premixed and diffusion flames.

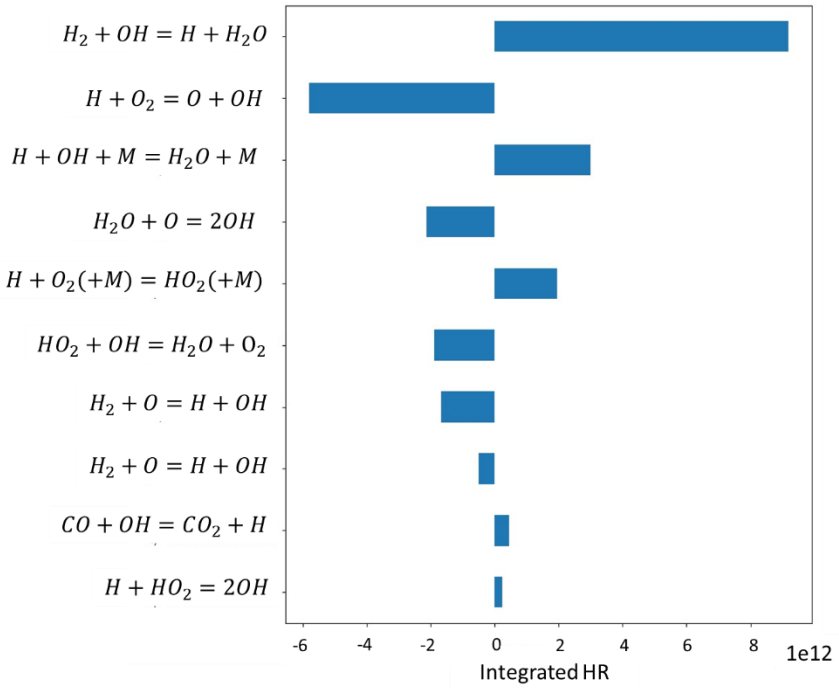

Figure 17: Reactions contributions to the integrated heat release for a diffusion flame at 100 bar, χ=1000s^{-1}

2.4.3 Organization of the manuscript

The performed analyses (pathways and heat release contribution) tend to validate the global strategy proposed at the beginning of this section. Indeed, as the same main chemical pathways and top heat

release contributing reactions are found in both premixed and diffusion flames representative of rocket engines conditions, premixed laminar flame speeds can be used as experimental reference targets for a kinetic mechanism that would be applied to diffusion flames. Consequently, the aim is now to build an experimental database of CH_4/O_2 laminar premixed flame speeds at high pressure and temperature for a wide range of equivalence ratios. Then, previously identified kinetic models will be evaluated against the experimental targets in order to assess their performances. The building of the experimental database as well as the kinetic models assessment are described in Chapter 3. After the best fitting mechanism is identified, an optimization procedure can be performed to match the experimental data acquired during this work but also from the literature. This optimization process is presented in Chapter 4. Once the kinetic model tailored for methane oxycombustion at high pressure and temperature is obtained, it is possible to use it for LES calculations in rocket engine conditions. This is described in the Chapter 5 of this manuscript. Finally, a conclusion and perspectives for future works are proposed.

Chapter 3

Measuring CH_4/O_2 flame speeds at high pressure and temperature

3.1 State of the art of S_u experimental determination, isochoric method advantages and limits

3.1.1 State of the art of S_u determination for methane in extreme conditions

Chapter 2 highlighted the need to build an experimental database of laminar flame speeds S_u at high pressure and temperature for CH_4/O_2 mixtures in order to correctly validate a mechanism.

Several methods have been developed to experimentally measure S_u at high pressure [100]. One of the most common is to track the evolution of an expanding spherical flame in a confined bomb. This technique allows the measurement of laminar flame speeds at relatively high pressure and temperature conditions. Indeed, exceeding 10 bar is possible, which is difficult for other methods using stationary flames such as Bunsen flame, counterflow flame or burner stabilized flat flames (cf. Figure 19 depicting the achievable range of different experimental systems in terms of pressure and temperature). Hence, a classical approach to measure S_u is to monitor the flame propagation in a combustion chamber at constant pressure [101–103]. This method will be referred here as SEF-CONP (*Spherical Expanding Flame at Constant Pressure*). In this case an optical access is used to monitor the flame radius over time. Flame speed acquisition is made during a short isobaric time for given unique initial pressure, temperature and mixture conditions. However, exploring high pressures raises different issues. One of them is the temperature limitation: sealing of the optical access is the weak point as it cannot endure extreme condition. A solutions for this problem is externally heated systems [104]. The other major issue is the pressure limitation, linked to the mechanical resistance of the chamber but also to the instabilities developing on the flame surface. Indeed, they tend to accelerate the flame propagation, hence the instantaneous pressure variation. One solution to delay these flame instabilities is to dilute the mixture in a neutral gas, such as He [105] . Therefore, building a S_u database for different conditions, especially at high pressure and temperature using the SEF-CONP method is time and money consuming. This is illustrated by showing an extensive listing (made by Egolfopoulos

et al. [105]) of different experiments using several methods to measure CH_4/air mixtures flame speed. The majority of studies were performed at atmospheric pressure.

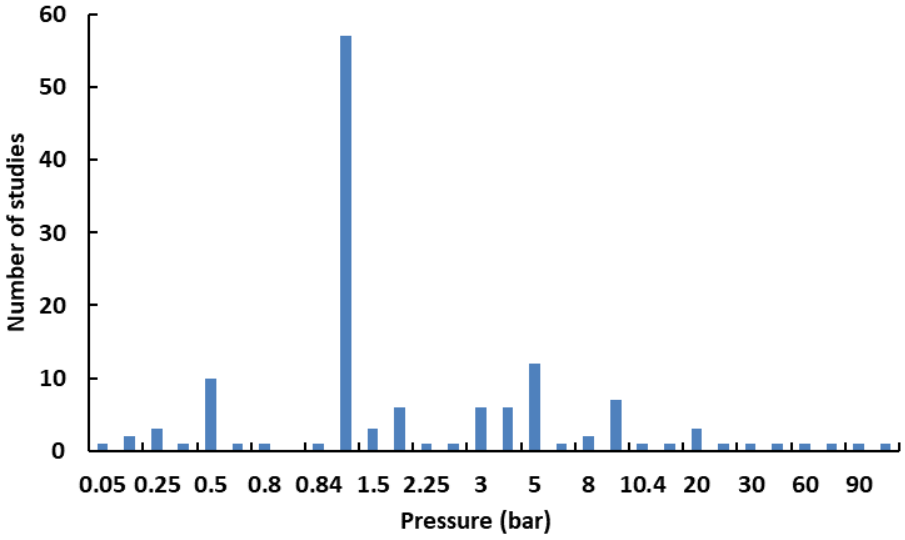

Figure 18: Litterature review of CH_4/air mixtures flame speed studies

Concerning CH_4/O_2 flame speeds, the few existing data were measured at atmospheric pressure [106–109] or lower [110]. Indeed, the high reactivity of methane with pure O_2 generally prevents its experimental study whether it is ignition delay, species profiles, or flame speed measurements. Such mixtures release a significant amount of energy compared to classically studied CH_4/air mixtures where nitrogen N_2 acts as a thermal ballast. Therefore, the resulting temperature of burnt gases is very high (greater than 3000 K against 2100 K in air at equivalence ratio φ = 1 and 1 bar). This leads to high laminar flame speeds (around 3 $m.s^{-1}$ against 0.3 $m.s^{-1}$ in air under the same T, P conditions). Therefore, bibliographical information on this topic is very scarce. The vast majority of the studies mentioned above used a Bunsen-type burner as experimental setup. The exception being the work of Fristrom et al. [110] which was performed in the 1950s on a flat burner. It allowed to characterize the flame structure at very low pressure (0.1 atm). Lewis and Von Elbe [108] then measured flame speeds at atmospheric pressure on a flat burner. More recently, Mazas et al. [106,107] performed a similar study, including additional measurements. A low diameter nozzle (3 mm) was used to reduce the turbulence effect on the flame as high flow rates were necessary to prevent any flashback issue. Flame speeds were measured thanks to a Schlieren technique for different equivalence ratios φ varying from 0.5 to 1.6 at atmospheric pressure and 298 K. Additional measurements were carried out at atmospheric pressure for lean, stoichiometric and rich mixtures, varying the initial temperature of the reactive mixture from 298 K to 500 K. A comparison with models was made, showing they tended to underpredict the flame speed. Another Bunsen-type burner study was performed by Oh et al. [109] for conditions close to Mazas'. Additional flame structure studies with CH^* filters were performed. However, no pressure variation was considered in this study, nor in the above-mentioned works. Therefore, extending the database to a wider range of temperatures and pressures is greatly valuable in order to develop a combustion model for CH_4/O_2 mixtures under rocket engine conditions.

3.1.2 The isochoric method

One of the solutions used to overcome the current limitation of experimental setups is to study the flame expansion at isochoric conditions. This method, initially proposed by Lewis and Von Elbe [111], is referred here as SEF-CONV (for *Spherical Expanding Flame at Constant Volume*). The general idea is to record the pressure evolution over time inside the combustion chamber in order to compute S_u. Conversion of the reactants to hot products across the flame front results in a rapid pressure increase and a corresponding temperature rise in unburnt and burnt gas.

The constant volume technique links the instantaneous evolution of the flame speed to the pressure history. In other words, in a single firing, flame speeds can be obtained for a range of higher pressures and temperatures [101,105,112]. An idea of the different P,T ranges achievable for each method is represented in the Figure 19.

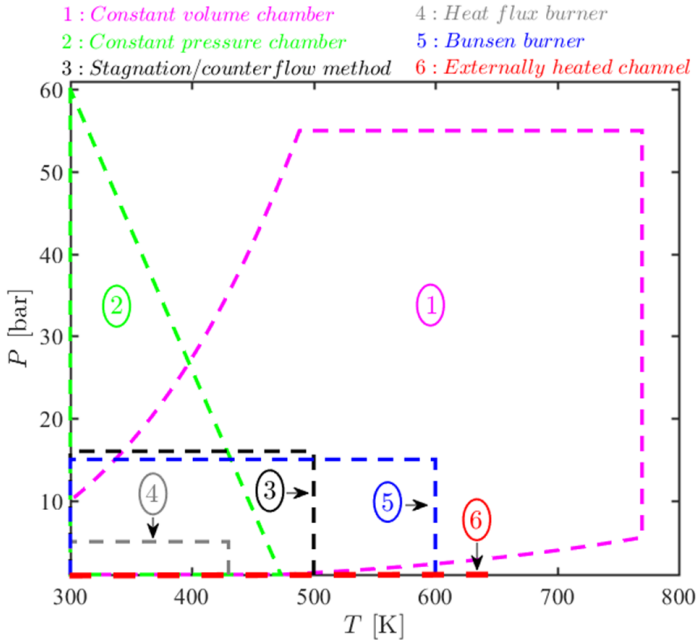

Figure 19: Map of achievable (P,T) range for S_u determination – from [112]

In order to compute the flame speed knowing the pressure evolution over time inside the chamber several assumptions need to be made:

- The pressure P is spatially uniform in the chamber
- Burnt and unburnt gases are considered as ideal gases
- There are no chemical reactions in the fresh gases
- The flame is perfectly spherical with an infinitesimally thin flame front
- The unburnt gas are compressed isentropically

Based on these assumptions, the following expression of the laminar flame speed S_u relative to the unburnt mixture can be derived [113]:

$$S_u = \frac{dR_f}{dt} - \frac{R_0^3 - R_F^3}{3\gamma_u R_f^2 P}\frac{dP}{dt} \tag{32}$$

It is defined as the difference between the flame speed in the lab reference frame and the fresh gases expansion speed. R_f and R_0 being respectively the flame and the inner chamber radius, and γ_u the heat capacity ratio of the unburnt gases. This relation supposes the knowledge of the simultaneous evolution of R_f and P. In order to overcome the lack of optical access, the following relation is generally used, introducing x as the burnt gases mass fraction:

$$\frac{R_f}{R_0} = \left[1 - (1 - x)\left(\frac{P_0}{P}\right)^{\frac{1}{\gamma_u}}\right]^{\frac{1}{3}} \tag{33}$$

Hence it is possible to deduce the flame radius and reinject its value into the S_u equation. The burnt gases mass fraction being not accessible experimentally, its evolution over pressure is unknown. Thus, it has to be computed either by numerical calculations, or using a model. Several relations exist [114] but the linear relation assumption between P and x proposed by Lewis and Von Elbe [111] is still widely used because of its simplicity (P_e being the adiabatic isochoric equilibrium combustion pressure):

$$x = \frac{P - P_0}{P_e - P_0} \tag{34}$$

Despite the fact of allowing the access to an important number of flame speed values for a single firing, the traditional SEF-CONV method needs to rely on a given model to compute x and does not allow the detection of any combustion instabilities on the flame front because of the lack of optical access. In order to overcome those issues, a special combustion chamber called OPTIPRIME was developed at ICARE.

3.2 The OPTIPRIME experimental setup

3.2.1 Hardware and firing procedure description

OPTIPRIME is a perfectly spherical isochoric combustion chamber with full (i.e. 360°) optical access. It is a unique setup, allowing to measure the flame radius, detect the development of instabilities and to reach high pressures (up to nearly 100 bar). The simultaneous access to the pressure and the radius allows to directly use equation (32) to compute S_u, thus avoiding a model for x. *Figure 20* depicts the setup, which has been described in details as well as the measurement procedures in two articles [112,115]. However, the main useful information is recalled in this manuscript.

Chamber:

The combustion chamber, made of stainless steel, has an internal radius R_0 of 60.85 mm. The optical access is made with a 360° fused silica ring designed to withstand pressures up to 100 bar. Pressure evolution inside OPTIPRIME is acquired thanks to 2 high sensitivity and frequency pressure sensors (AVL GU21D) flush with the wall while a type-K thermocouple allows to measure initial temperature of

the unburnt gases. The chamber is placed in a special furnace [112] allowing to heat up fresh gases up to 300°C if required.

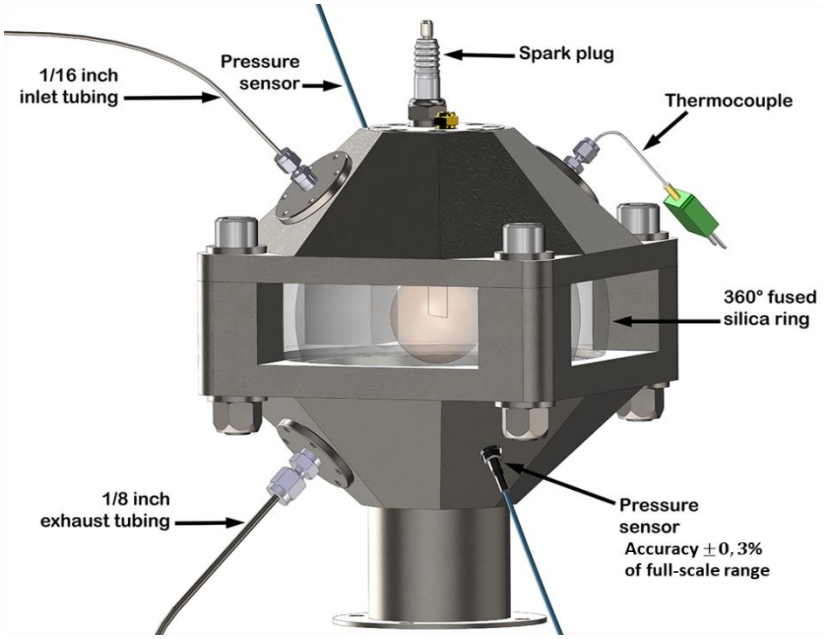

Figure 20: The OPTIPRIME setup [112]

Mixture preparation:

The studied mixture is prepared in a high-pressure buffer tank in order to conduct several experiments with the exact same parameters. The different components (fuel, oxidizer and sometimes diluent) are successively introduced in the tank, their respective amount being evaluated using Dalton's law of partial pressures. It is possible to sample the mixture for gas chromatography analysis in order to check precisely its composition.

Chamber filling and firing:

Before each firing, the combustion chamber is filled with air and then vacuumed to prevent any perturbations from the previously tested conditions through an outlet pipe of 1/8-inch. The tested mixture is then introduced at the desired initial pressure through a 1/16-inch tube. After this step, the chamber is totally isolated from the rest of the system and the mixture ready to be ignited. Ignition is ensured by an electric arc created between two extremely fine tungsten electrodes precisely positioned at the center of the chamber in order to produce a flame as perfectly spherical as possible.

At ignition, the electric arc generation is triggered at the same time as the pressure transducers and pictures acquisition of the flame with a high-speed camera (Phantom V2512). It is indeed essential to record the simultaneous evolution of P and R_f. A calibration was previously made in order to determine the relation between the apparent and real radius of the flame [112].

Post treatment:

During post treatment, flame radius detection on each frame is made with an algorithm which detects

the flame front by evaluating the maximum gradient of chemiluminescence in the visible spectrum [112]. The radius is then filtered to obtain a clear evolution over time. *Figure 21* presents example of frames captured by the camera, showing the flame propagation. *Figure 22* shows how the camera is arranged in relation to the rest of the experimental setup. Another algorithm treats the pressure signal, performing the conversion, filtering and re-sampling. Filtering is performed using zero-phase digital filters, which parameters (order and cut-off frequency) were adapted to get the best out of the raw data. It is then possible to compute the R_f and P derivatives in order to obtain S_u thanks to the relation introduced in the previous section. It has been evaluated that the uncertainty on S_u along the whole propagation process is $\pm 5\%$ [112]. At the end, a full trace of S_u as a function of both pressure and temperature is obtained for a given equivalence ratio φ.

As methane oxycombustion leads to high flame speed compared to CH_4/air mixtures, the camera sample rate is adapted (for example from 10 000 fps at φ=2.5 up to 110 000 fps at stoichiometry), as well as the image resolution (respectively 1024x768 to 1024x208 pixels) and the exposure time (10 μs at φ=2.5 to 6 μs at φ=1). The pressure temporal evolution is also greatly affected. At φ = 1.5 for example, there is a factor of 30 between the dP/dt encountered with CH_4/Air (400 $bar.s^{-1}$) and CH_4/O_2 (12000 $bar.s^{-1}$). As a consequence, the pressure transducers acquisition frequency is increased, from 20 to 60 kHz.

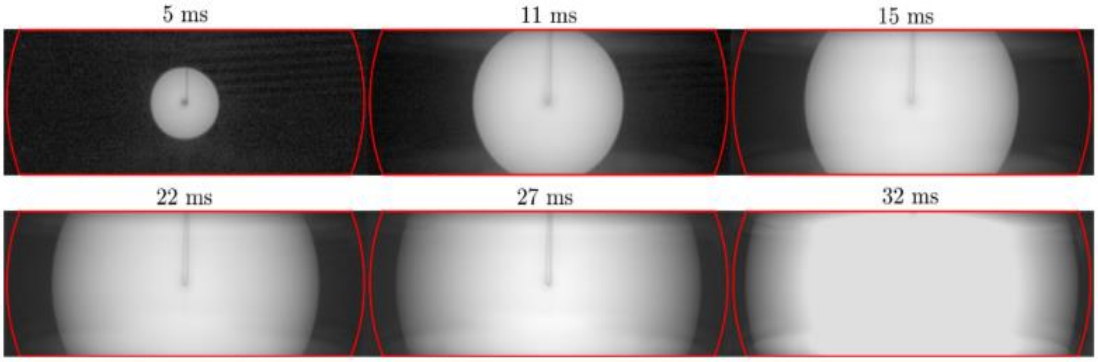

Figure 21: Example of flame radius evolution in OPTIPRIME for a methane/air mixture (chamber radius appears in red) [112]

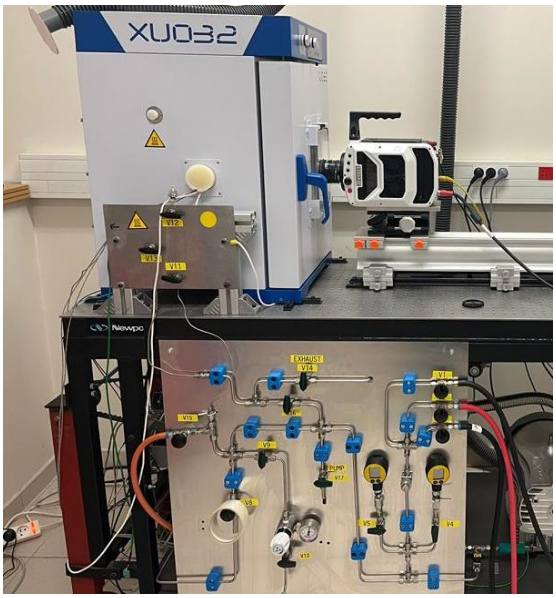

Figure 22: The complete OPTIPRIME experimental setup in its furnace with its filling system and high-speed camera

3.2.2 Flame stability limits, Lewis number and pressure effect

As the target conditions imply high speed flame propagation at high pressure, flame front stability issues need to be considered as they can directly affect the experimental measurements. However, since OPTIPRIME is equipped with an optical access, problems relative to flame front perturbation can be quickly detected, allowing to take corrective actions for the next firings. Three types of main instabilities generally arise for spherical expanding flames:

Gravity instabilities:

Figure 23 depicts the evolution of a numerically computed S_u as a function of φ at 1bar from 1D simulations conducted with CANTERA. The FFCM1 mechanism was used here to give an order of magnitude of the encountered S_u values. Gravity effects are encountered when the flame speed is not important enough to counter buoyancy effects. This generally happens when S_u is below 15 $cm.s^{-1}$ [112]. Since CH_4/O_2 induced S_u are far above this limit for a large spectrum of φ, this type of instability can be neglected.

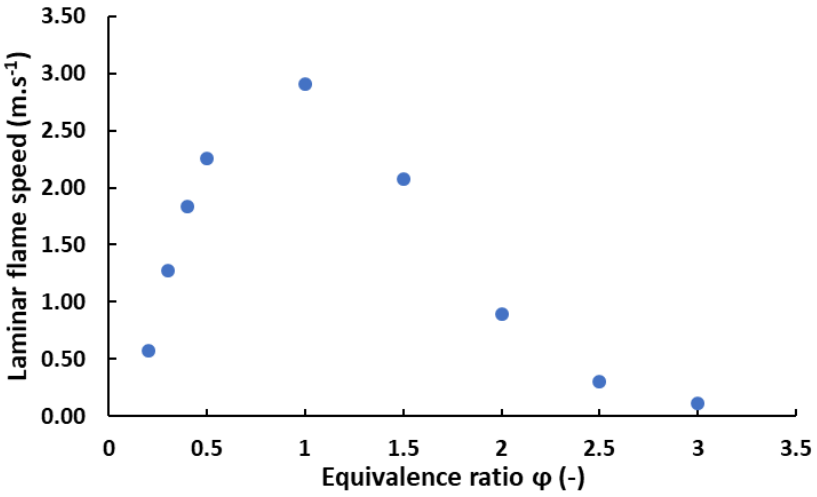

Figure 23: CH4/O2 Su over phi at 1 bar - numerical calculation with FFCM1 scheme

Thermo-diffusive instabilities:

An important phenomena to take into account are thermo-diffusive instabilities [61,116]. They are directly linked to the competition between molecular diffusion D_m (i.e. a mass flux) and thermal diffusion D_{th} (i.e. a heat flux), which can be characterized thanks to the Lewis number Le:

$$Le = \frac{D_{th}}{D_m} = \frac{\lambda_u}{\rho_u C_{p_u} D_m} \tag{35}$$

The molar diffusion considered for stabilities studies is the one from the minor species into the rest of the mixture. Hence Le evaluation at φ=1 is not trivial [116] and will not be discussed here. The components of D_{th} are average values computed for the whole mixture. The evaluation of this quantity is thus totally dependent on the equivalence ratio φ, hence on mixture composition.

The general idea is that the flame surface progressively wrinkles as Le decreases, leading to more and more important instabilities finally leading to a non-spherical flame propagation when $Le < 1$, hence preventing good S_u measurements. The transition from a stable to unstable flame front being not exactly sharp at $Le = 1$, the objective is to use mixtures leading to a Le greater than a critical Lewis number Le_c which was chosen to be greater than unity in order to guarantee a sufficient enough margin of error:

- **If $\boldsymbol{Le < Le_c}$,** $D_{th} < D_{m_{mino}}$ which means mass diffuses faster than heat in the fresh gases leading to flame front wrinkling and **instabilities**

- **If $\boldsymbol{Le > Le_c}$,** $D_{th} > D_{m_{mino}}$ which means heat diffuses faster than mass in the fresh gases, **stabilizing the flame front**

Hence, it is very important to preliminary evaluate the theoretical Lewis number of the mixtures to be tested in order to have an idea of the instabilities that might be encountered during the firing.

It is also imperative to keep in mind that pressure also has an effect on the flame front behavior. Indeed, the more the pressure increases, the more the flame thickness δ_f decreases (same for Le). Indeed, δ_f is defined as follows according to Zeldovich [117]:

$$\delta_f = \frac{\lambda_u}{\rho_u \cdot C_{p_u} \cdot S_u} \tag{36}$$

As the fresh gases are compressed during the flame propagation, λ_u and C_{p_u} do not vary much as ρ_u and S_u increase, hence leading to a decrease of δ_f. This leads to a thinner flame front, more prompt to be affected by thermo-diffusive instabilities. This observation is very important since the targeted experimental conditions for the firing are high pressure, to be compatible with rocket engines applications.

In order to overcome those problems and keep a stable flame front with correct S_u while increasing pressure, helium can be used as a diluent. This method has been widely depicted in the literature [105]. Indeed, this inert species allows to artificially increase the thermal diffusivity, He having a very high thermal conductivity. The drawback of this method being that mixture highly diluted in helium tend to diffuse the energy very fast which makes ignition more difficult.

Another method consists in starting the firing at sub-atmospheric (i.e. $P_0 < 1\ bar$) initial conditions. It allows a limitation of the final reached pressure, hence less instabilities, while still having an appreciable number of datapoints. Both methods were used for the experimental measurements with OPTIPRIME (cf. the next sections).

Darrieus-Landau instabilities:

The Darrieus-Landau instability (depicted in [118,119]) induces flame surface wrinkling, which increases the flame area. It consists on a hydrodynamic instability that results from the gas expansion caused by the heat released during combustion. As the flame thickness δ_f decreases at high pressure, the thermal gradient through it increases, leading to more instabilities. This phenomenon was generally observed on flames generated with OPTIPRIME just after the triggering of thermo-diffusive instabilities. Figure 24 illustrates the development of flame front instabilities for a CH_4/O_2 flame at rich conditions at the end of its propagation. The apparition of wrinkles on image (b) prevents a good

data exploitation as the flame is not perfectly spherical anymore and its propagation speed is modified. Hence, when theses phenomena are encountered, the concerned frames are not exploited.

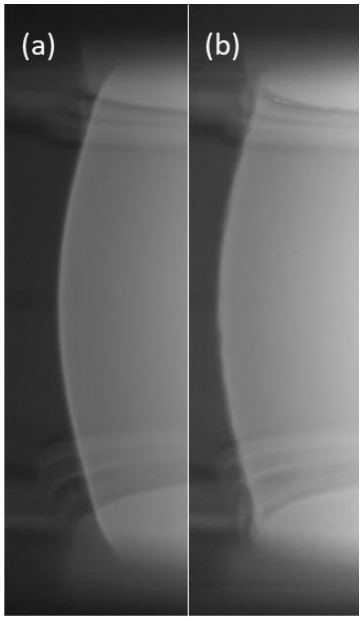

Figure 24: (a) stable flame front (b) unstable flame front - CH_4/O_2 at φ =2.5 - P =16 bar

3.2.3 S_u determination limits

One of the main difficulties in SEF-CONV experiments is to precisely identify the limits of the pressure range compatible with the hypotheses made in order to compute S_u. Indeed, at the beginning of propagation, the flame is affected by stretch effects (the low-pressure limit) whereas at the end, wall heat-loss impacts the isentropic compression hypothesis (the high-pressure limit). Being outside those limits means the main hypothesis allowing to derive the S_u relation presented at the beginning of the chapter are not valid anymore. Hence, a comprehension of these phenomena is critical for a good determination of S_u. Figure 25 represents the simultaneous evolution of R_f and P over time. The safe zone for S_u extraction is labelled as the "isochoric conditions" zone. It shows that the maximum measured pressure reached during a firing is more important than the final exploited pressure.

Low-pressure limit:

Concerning the low-pressure limit, as explained in the previous chapter, the stretch of the spherical flame is evaluated as $\kappa = \frac{2}{R_f}\left(\frac{dR_f}{dt}\right)$. It has been demonstrated in [112], by assessing the contribution of the different sources of inaccuracy and comparing the experimental results to DNS simulations performed by Chen et al. [120] and Xiouris et al. [121] for a wide range of conditions, that stretch effect can be neglected for pressures greater than 2 times the initial pressure P_0. However, as mentioned before, the OPTIPRIME optical access still allows to assess stretch over time such as the Markstein length L_u to compute the extrapolated unstreched flame speed S_u^0 . These computations will be shown in the next sections of this chapter as the $2P_0$ hypothesis is verified for CH_4/O_2 mixtures.

High-pressure limit:

Concerning the high-pressure limit, an initial criterion of 90% max($\frac{dP}{dt}$) was defined in [98,112]

according to the DNS calculations performed by Chen et al. for different CH_4/air mixtures [120,122]. A more versatile criterion for SEF-CONV enabling to access to higher pressures while being still valid in term of adiabaticity will be shown in the next section of this chapter.

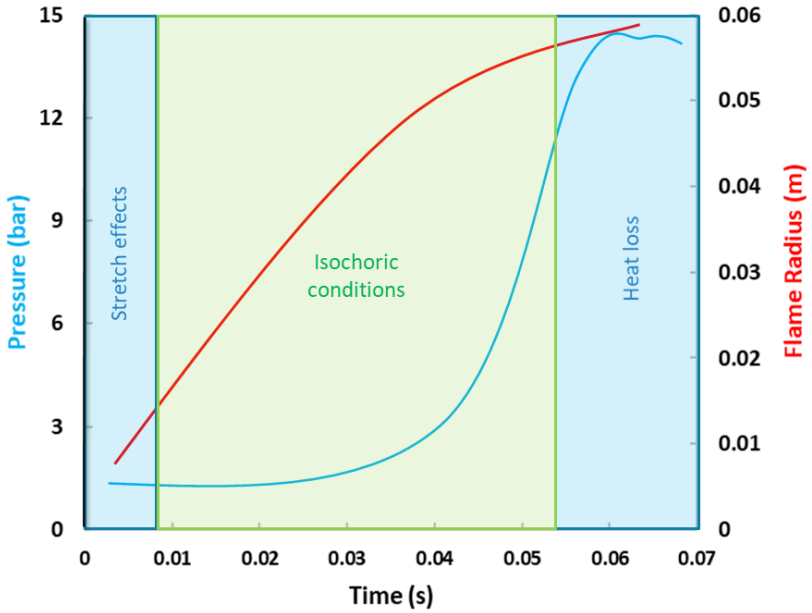

Figure 25: S_u determination limits

3.3 High-pressure limit for S_u extraction in SEF-CONV experiments: definition of a new criterion (extract from the paper published in *Thermal Science and Engineering Progress)*

The current section consists in an extract of a paper published in *Thermal Science and Engineering Progress* [122]. The aim of this publication is to establish a versatile criterion for the high-pressure limit of flame extraction in SEF-CONV experiments. The criterion (based on the evolution of the pre-heat thickness of the flame) is first defined, then validated against DNS simulations performed by Chen et al. with the A-SURF code [120,123,124]. Finally, its performances are compared to other criteria from the literature.

The objective of this paper is to revisit the criteria available to describe the heat exchanges of a premixed flame propagating perpendicular to a wall. In internal combustion systems, it is essential to evaluate heat losses as a function of the flame-wall distance [125,126]. Our specific objective is to develop a criterion to ensure that the flame speed evaluation in SEF-CONV is performed under adiabatic conditions.

To achieve these goals, 1D direct numerical simulations were performed to evaluate the effect of heat losses on the flame dynamics for a large range of mixture conditions.

The in-house code A-SURF [120,123,124] is used to simulate the 1D spherically expanding flame in a closed chamber with radius of 60.85 mm, which is the same as that of OPTIPRIME using in experiments. The computational domain was initially filled with static mixture at the specified initial pressure and temperature. The spherical flame propagation was initiated by a small hot spot at the center. Zero flow speed and zero gradients for temperature and mass fractions are enforced at both the center and the wall. In A-SURF, the fully compressible Navier-Stokes equations for a multi-component reactive mixture in 1D spherical coordinate are solved using the finite volume method. The detailed chemistry and transport are considered. The thermal diffusion and radiation are neglected. The FFCM-1 mechanism [95] are used for methane oxidation. The reaction rates as well as the thermodynamic and transport coefficients are evaluated by CHEMKIN [127] and TRANSPORT [128] packages. To accurately and efficiently resolve the moving flame front, the locally and dynamically adaptive mesh refinement (AMR) technique is also applied based on the gradient of temperature. A 6-level AMR with the finest mesh size of 9.5 μm is initially adopted, and the maximum mesh level will increase 1 level once the end gas pressure is doubled. In this way, the reaction front is well resolved and the gird convergence is ensured. A-SURF has been successively applied in previous studies on outwardly propagating spherical flame [99,120,123,129]. The details on numerical methods and schemes of A-SURF can be found in Refs [120,123,124]. and thereby are not repeated here.

3.3.1 Wall effects on the flame speed: definition of a new criterion

In order to validate the new criterion, DNS calculations were performed with the A-SURF code with either adiabatic or isothermal wall condition. In order to compare the new high-pressure limit, some criteria used by other teams on their own SEF-CONV experiments have been listed in the following table.

Table 4: high-pressure criteria from the literature

** P_{eq} corresponds to the adiabatic isochoric equilibrium combustion pressure.*

Source	Criterion
Halter [98,112]	90% max $(\frac{dP}{dt})$ – for safety margin 5 $\frac{P}{P_0}$
Omari/Tartakovsky [101]	max $(\frac{d^2P}{dt^2})$ – for safety margin $Pr = \frac{P-P_0}{P_{eq}-P_0}$ ~55% *
Burrell [130]	max $(\frac{d^2P}{dt^2})$
Razus [131]	max $(\frac{dP}{dt})$

Table 4 illustrates that pressure and its derivatives are the main indicators used for heat losses at the wall. Indeed, the evolution of $\frac{dP}{dt}$ over time follows a steep decrease when the heat losses happen.

However, it is still interesting to understand the underlying physical phenomena of the time heat losses appear and, if possible, define a criterion based on these observations. Then, obtained results will be compared to the ones from previous studies for different mixture conditions.

3.3.1.1 Laminar flame propagation dynamics and structure

The propagation of laminar flames observed in SEF-CONV experiments is made through the simultaneous compression of the fresh gases and the heating of those gases through thermal diffusion. Once the fresh gases near the flame front reach the ignition temperature, they react and will then heat the nearest fresh gases by diffusion, propagating the phenomenon. Only heat transfers by conduction are considered. Radiation effects can be neglected for several reasons:

- the characteristic time of the flame (i.e. the time taken by the flame to travel a distance equivalent to its own thickness δ_f) is negligible compared to the one of radiation heat transfer
- radiations emitted by the burnt gases do not impact the fresh gases which are considered as an optically thin environment
- the fuel used in this study (CH_4) does not lead to combustion products that radiate a lot considering its low number of carbon atoms

Neglecting radiative heat losses in classical SEF-CONV experiments could lead to errors in S_u evaluation (up to 15% according to [121]). However, the advantage of the OPTIPRIME is its optical access, allowing to directly measure R_f. Hence, the radiation effects are implicitly accounted for during S_u calculations. In addition, DNS calculations were performed with A-SURF to assess the importance of radiative heat losses [112]. Simulations show that the adiabatic model gives results very close to the *Statistical narrow band model* (SNB) accounting for radiation emission and reabsorption for conditions similar to the current study. Hence radiative heat losses can be neglected for the studied conditions, confirming the previously listed points.

An interesting aspect of the system composed by the laminar flame and the fresh gases is its structure, composed of three zones of interest illustrated on Figure 26. First, there is the reaction zone of a given width, δ_f. In front of it is a zone called the 'preheating zone' characterized by its thickness (δ_{ph}). This is the zone where the fresh gases near the flame front will be heated until they reach the ignition temperature (T_{ign}) and allow the flame to propagate further. The last zone is found near the wall. It is called the thermal boundary layer (δ_w). Here, the wall is considered as isothermal and acts as a heat sink. Therefore, a temperature gradient appears and develops over time between the gas and the surface of the combustion chamber.

From a phenomenological point of view, the time when the preheat zone (δ_{ph}) and the thermal boundary layer (δ_w) meet and overlap can be considered as the time when the flame starts to lose heat at the wall. Thus, it is interesting to study the evolution of the preheat zone thickness over time.

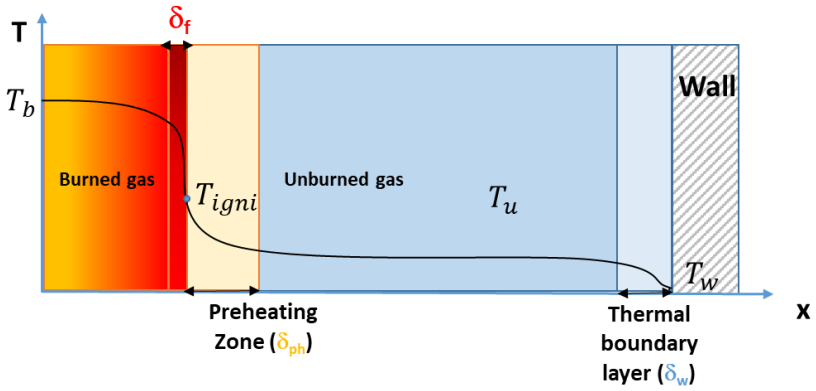

Figure 26 : Illustration of a premixed laminar flame structure

A power balance on the total power given by the flame $\dot{Q_{tot}}$, to the burnt gases, $\dot{Q_b}$, and to the fresh gases, $\dot{Q_u}$, can be made. It is important to notice that a fraction of $\dot{Q_u}$, noted $\dot{Q_{u_{eff}}}$, will effectively heat the fresh gases while the other part of the power, $\dot{Q_w}$, will be given to the wall. Hence, it is possible to write that the overall power given by the flame can be decomposed as follows, as illustrated in Figure 27:

$$\dot{Q_{tot}} = \dot{Q_u} + \dot{Q_b} = \dot{Q_{u_{eff}}} + \dot{Q_w} + \dot{Q_b} \tag{37}$$

This model supposing homogeneous properties in the unburnt gas and a very thin flame thickness, δ_f.

The power given to the fresh gases decomposes as the product of the gas density ρ_u, heat capacity C_{p_u}, the flame speed S_u and surface times the temperature difference between the unburnt mixture and the flame:

$$\dot{Q_u} = \rho_u \cdot C_{p_u} \cdot S_u \cdot (T_f - T_u) \cdot 4\pi R_f^2 \tag{38}$$

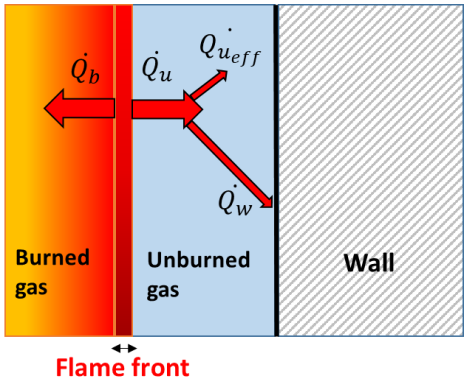

Figure 27: Illustration of the laminar flame power balance

The power given to the wall by conduction is expressed as follows:

$$\dot{Q_w} = \lambda_u \cdot \frac{dT}{dr} \cdot 4\pi R_{tot}^2 \tag{39}$$

A code has been developed to compute the fresh gas parameters over time knowing the pressure during the experiment and the initial conditions (mixture composition and initial P and T). This tool is based on all the above-mentioned hypotheses (ideal gas, isentropic compression, homogeneous

parameters in the gases) and the FFCM1 thermodynamic database [95]. Hence, it is possible to know the evolution of T_u, ρ_u, λ_u, C_{p_u} and thermal diffusivity $D_{th,u}$ over time. Knowing S_u, it is now possible to compute the power given to the fresh gases and to the wall, but these quantities do not lead to a viable criterion since they rely on the initial conditions.

3.3.1.2 Preheating zone thickness evolution and high-pressure limit criterion

In order to evaluate the preheating zone thickness, δ_{ph}, the definition given by Gaydon and Wolfhard was used. δ_{ph} is thus defined as the product between a scalar A (which numerical value will be discussed in the next section) and the flame thickness, δ_f, from Zeldovitch definition as shown in Eq. 6:

$$\delta_{ph} = A \cdot \frac{\lambda_u}{\rho_u \cdot C_{pu} \cdot S_u} \tag{40}$$

Eq. 6 was derived analytically, leading to a coefficient $A = 4.6$. The preheating zone was defined as the zone between the ignition temperature T_{igni} and the fresh gas temperature T_u plus 1 %. With the code mentioned in the previous section, the numerical evaluation of δ_{ph} over time can be performed.

During the combustion process, when the flame radius increases, so does the total power given by the flame, $\dot{Q_{tot}}$. This leads to an increase of P and ρ in the fresh gases, hence a decrease of δ_{ph} over time (λ_u and C_{pu} do not vary much with pressure). At some point, the flame will be close enough to the wall and will start to lose energy. At that moment, the flame speed, S_u, will decrease and δ_{ph} will start to increase. This behavior defines the exact moment when the flame starts to lose power at the wall, i.e. the point where the adiabatic hypothesis is not valid anymore. The criterion is defined as the minimum of δ_{ph} over time. This minimum indeed coincides with the moment when the preheating zone and the thermal boundary layer at the wall start to overlap according to numerical evaluations made thanks to the thermal properties code. This behavior is illustrated in Figure 28.

The computation of δ_{ph} supposes that the flame speed S_u has already been computed on a broad pressure domain. Therefore, the determination of the upper pressure criterion and the truncation are made afterwards. The computation of the thermodynamics parameters involved in the criterion definition is made with the help of the fresh gas parameters computation code described in the previous section.

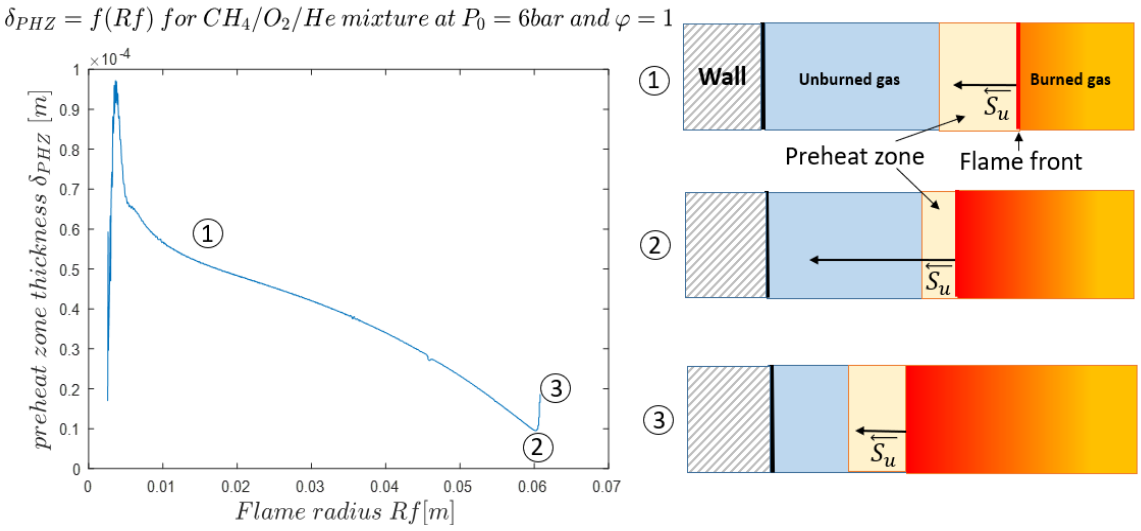

Figure 28: Preheating zone dynamics over time

3.3.1.3 Robustness of the new criterion

To test the criterion's robustness over a wide range of S_u (from 0.11 to 1.34 m s-1), δ_f (from 4.8x10^{-5} to 2.11x10^{-4}m) and D_{thu} (from 1.3x10^{-6} to 4.7x10^{-5} m². s-1), different mixtures for different initial conditions were considered (see Table 5):

Table 5: Tested mixtures

Mixtures	φ	P_0 (bar)	T_0 (K)
CH_4/air	1.1	1-3-6	300
	1.3	1-3-6	300
CH_4/ 15%O_2 85%He	1.1	1-3-6	300
	1.3	1-3-6	300

The new criterion is defined as the minimum of δ_{ph}. This definition relies on a constant value of A (the ratio between the preheating and the reaction zone) whatever the mixture conditions are during the flame propagation. This point needs to be assessed. In order to numerically evaluate A , the δ_{ph} over δ_f ratio has been computed for a large range of conditions. 1D flame speed calculations were performed using the PREMIX package from CHEMKIN. S_u was computed for the initial conditions of Table 2 and for each case, 3 successive *P* and *T* conditions along the isentropic compression were selected to evaluate the evolution of A during the flame propagation. On the average of the tested conditions, the A value was around 5.

As mentioned previously, δ_{ph} is defined between T_u+1% and T_{igni}, the latter being difficult to evaluate. The temperature corresponding to the position where 5% of the unburnt fuel mass fraction is consumed was arbitrary considered as T_{igni}.

The main conclusion of this evaluation is that the ratio between the thicknesses of the preheating zone and the reaction zone, even if not strictly equal to 4.6, does not vary quantitatively during the flame propagation for a given definition of T_{igni}, confirming that the proposed definition is a robust criterion of adiabaticity. Furthermore, since the method focuses on the minimalization of the δ_{ph} parameter

and that it has been proven that A is constant during flame propagation, the value of the coefficient does not matter much as it will not impact the position of min(δ_{PH}).

3.3.1.4 Evaluation of the new criterion performance

In this section, DNS using A-*SURF* are used to check how the proposed criterion (minimum of δ_{ph}) performs to indicate the time when the flame starts to lose power at the wall and that the isentropic compression hypothesis vanishes. Calculations of S_u were performed with either adiabatic ($S_{u\,adi}$) or isothermal ($S_{u\,isoth}$) wall for the conditions of Table 2. As mentioned before, radiative losses are not considered. The relative difference between $S_{u\,adi}$ and $S_{u\,isoth}$ was monitored during the flame propagation. At some point $S_{u\,isoth}$ drops while $S_{u\,adi}$ continues to increase, indicating the point where heat losses occur, as illustrated in Figure 29.

A relative difference of 5% on the DNS flame speeds, equivalent to the experimental uncertainty of OPTIPRIME [112], was chosen as the DNS criterion to point out this high-pressure limit. However, it is possible to be more accurate in terms of end of adiabaticity hypothesis, considering a lower relative difference on S_u. Nevertheless, the general idea of SEF-CONV setups is to obtain S_u data corresponding to the highest possible pressure. Indeed, as illustrated in Figure 30, the last instants of the flame propagation cover the higher pressure rise. This figure illustrates the flame-wall distance evolution as a function of pressure and clearly exhibits that the higher-pressure increase is achieved during the latest millimeters.

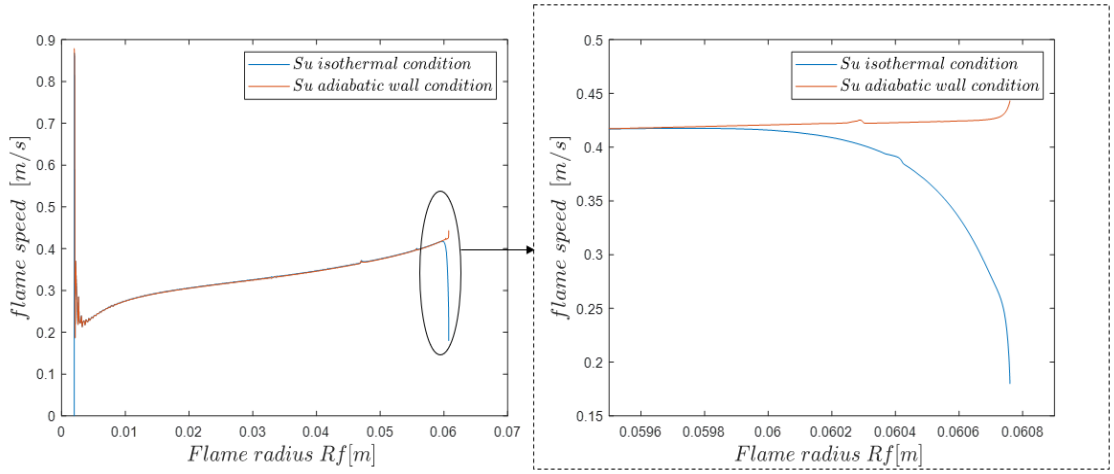

Figure 29: Flame speed evolution as a function of the flame radius. Adi wall in orange and isoT in blue. Mixture is CH_4/Air at φ=1.1 and P_0=1 bar

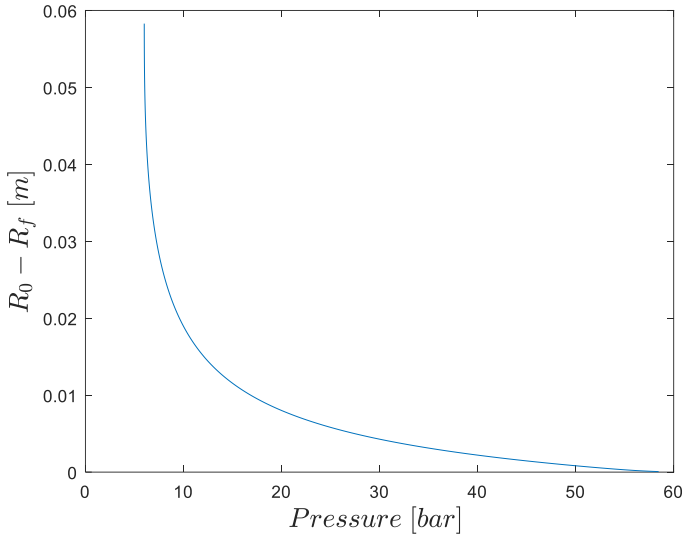

Figure 30: Variation of the flame-wall distance with pressure. Mixture is $CH_4/O_2/He$ at φ=1.1 and P_0=6 bar

Hence, in order to maximize the amount of high-pressure data considered at the end of the experiment while remaining in the setup margin of error, the 5% relative difference on the DNS flame speed was chosen as the numerical benchmark in this study. The balance between accuracy and maximal pressure reached is shown in Figure 31.

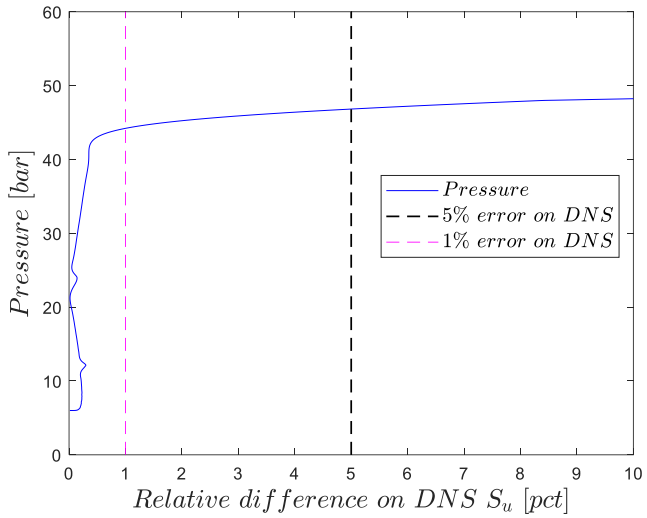

Figure 31: Pressure evolution over relative difference between $S_{u\,adi}$ and $S_{u\,isoth}$ numerical flame speeds. Mixture is methane/air at $\varphi = 1.3$, $P_0 = 6\ bar$

Figure 32 highlights the clear correlation between the DNS and the δ_{PH} criterion. Indeed, the 5% error on the numerical S_u and the minimum of the preheat zone are extremely close to each other (0.12% of relative difference in the case of Figure 31). This observation is valid for the scope of the tested conditions chosen to vary the S_u, D_{th} and δ_f parameters presented in Table 2. Indeed, on average, the relative difference between the two criteria is < 0.15%. Those values tend to confirm the validity of the δ_{ph} criterion from a physical point of view, at least for CH_4/air or $CH_4/O_2/He$ mixtures.

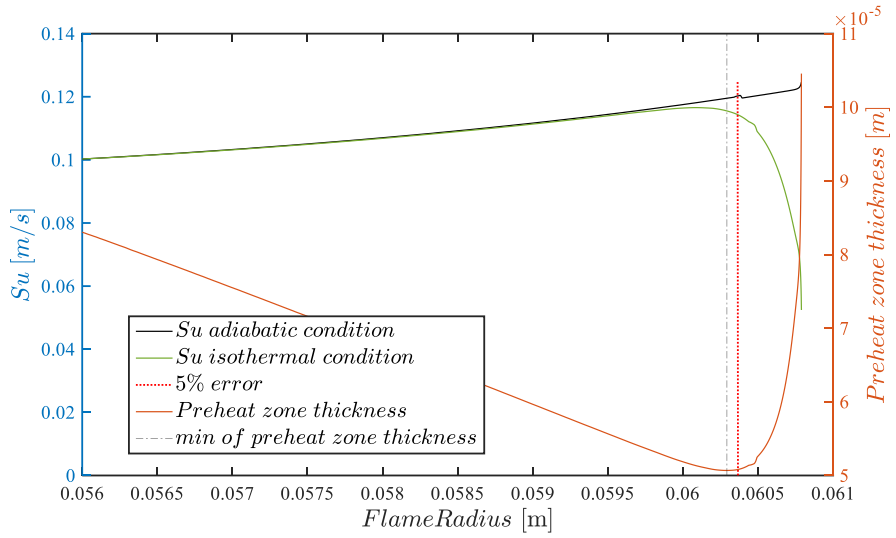

Figure 32: DNS criterion vs. preheat zone thickness criterion. Mixture is methane/air at $\varphi = 1.3$, $P_0 = 6\ bar$

3.3.2 Comparison with other criteria

As indicated in Table 4, the majority of the high-pressure limit criteria are based on the pressure evolution. It is now possible to compare the values used by those methods to our new proposed criterion and to test their performances using DNS results. Figure 33 shows the critical flame radii R_{crit} found by the criteria presented in Table 5 for methane/air mixture at φ = 1.3 and P_0 = 1 bar. It illustrates the fact that all the R_{crit} are relatively close to each other but that the critical radius can be over or underestimated depending on the conditions. This observation remains true regardless of the conditions listed in Table 5. This highlights the need for a robust and precise criterion allowing to reach the highest pressures while considering the physical phenomenology of the flame behavior.

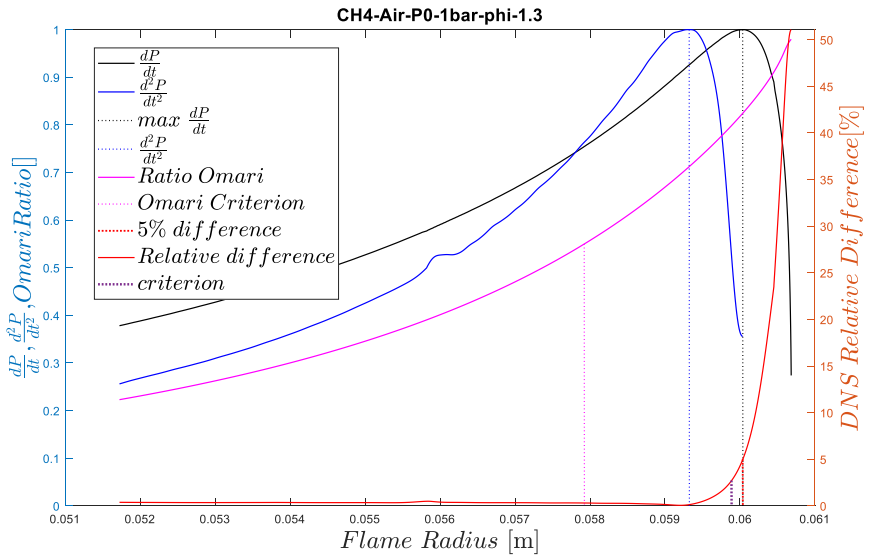

Figure 33: Critical radii of criterion from different studies. Mixture is methane/air at $\varphi = 1.3$, $P_0 = 1\ bar$

Knowing the R_{crit} from all criteria for the conditions of Table 5, it is possible to compare their relative differences with the set DNS criterion of 5% gap between $S_{u\ adi}$ and $S_{u\ isoth}$ in order to assess their

accuracy and robustness. It is important to notice that some conditions of Table 5 are missing because the DNS calculations did not converge.

Figure 34 allows drawing multiple conclusions:

- Among all the evaluated criteria, min (δ_{ph}) seems to be the most accurate compared to the set DNS criterion (indeed the relative difference is minimal in almost all conditions).
- Max ($\frac{\partial P}{\partial t}$) is sometimes even more accurate even though it seems to be the case only for CH_4/air mixtures. Indeed, the relative difference with DNS is far greater for CH_4/He mixtures. Hence min (δ_{ph}) seems to better consider the diluent effect (modification of D_{th}) on the flame dynamics.
- Max ($\frac{\partial^2 P}{\partial t^2}$) and *Omari* criteria seem both to systematically underestimate the critical radius. However, this observation is consistent with the aim of Omari and Tartakovsky study being a compromise between the limit accuracy and the available data range.

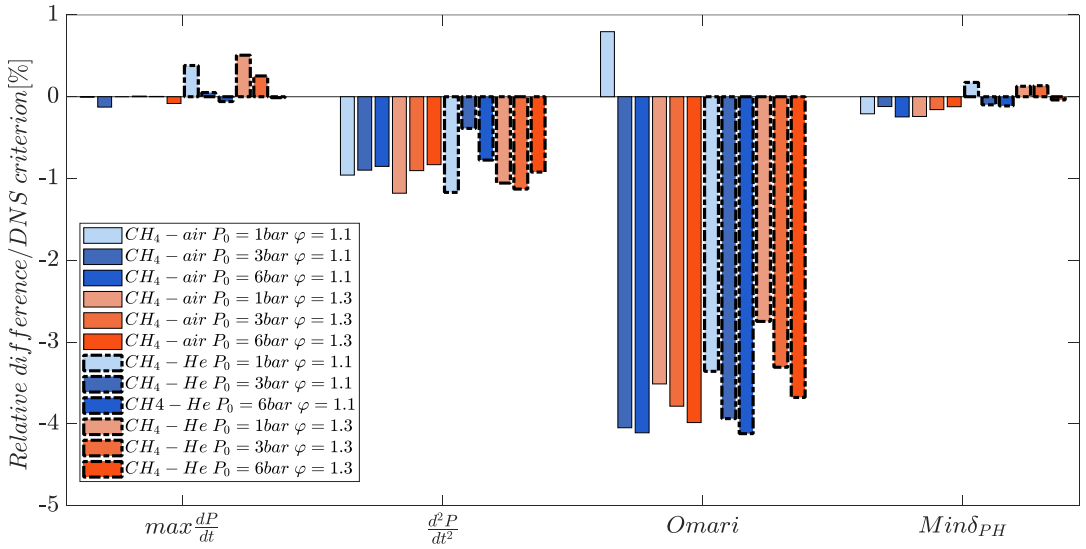

Figure 34 : Relative difference between critical radius criteria and DNS criterion (5% relative difference between $S_{u\ adi}$ and $S_{u\ isoth}$)

The evaluation of the standard deviation, σ, for each criterion compared to DNS gives additional information. Table 6 allows evaluating the criterion consistency for the scope of tested conditions regarding the set DNS criterion.

Table 6: Standard deviation of criteria for 5 %DNS criterion

$\sigma_{\frac{\partial P}{\partial t}}$	$\sigma_{\frac{\partial^2 P}{\partial t^2}}$	σ_{Omari}	$\sigma_{\delta_{PH}}$
0.1970	0.2157	1.3572	0.1469

Note that these observations are made for the chosen DNS criterion of 5% and could change if another percentage, for example lower than 5%, was chosen. The data reveals that max ($\frac{\partial^2 P}{\partial t^2}$) is as consistent as min (δ_{ph}). Two conclusions can be drawn from this observation:

- Min (δ_{ph}) criterion is comforted as a robust and precise criterion for the OPTIPRIME target conditions.
- Max ($\frac{\partial^2 P}{\partial t^2}$) is a secure and robust criterion that can be used as a good compromise between the accuracy of the end of adiabaticity limit and the available data range.

As mentioned in section 2d, it is possible to take a lower relative difference on the DNS flame speeds as a reference criterion for the end of adiabaticity regime in order to be more precise. This can be done assuming that the experimental measurements are accurate enough. Indeed, in the case of OPTIPRIME, the general idea of the 5% difference on DNS S_u is to stay in the setup margin of error while maximizing the amount of high-pressure data considered. If a DNS criterion of 1% relative difference between $S_{u\,adi}$ and $S_{u\,isoth}$ is now considered, the previous criteria comparison is also reevaluated as shown on the figure below, and several observations can be made.

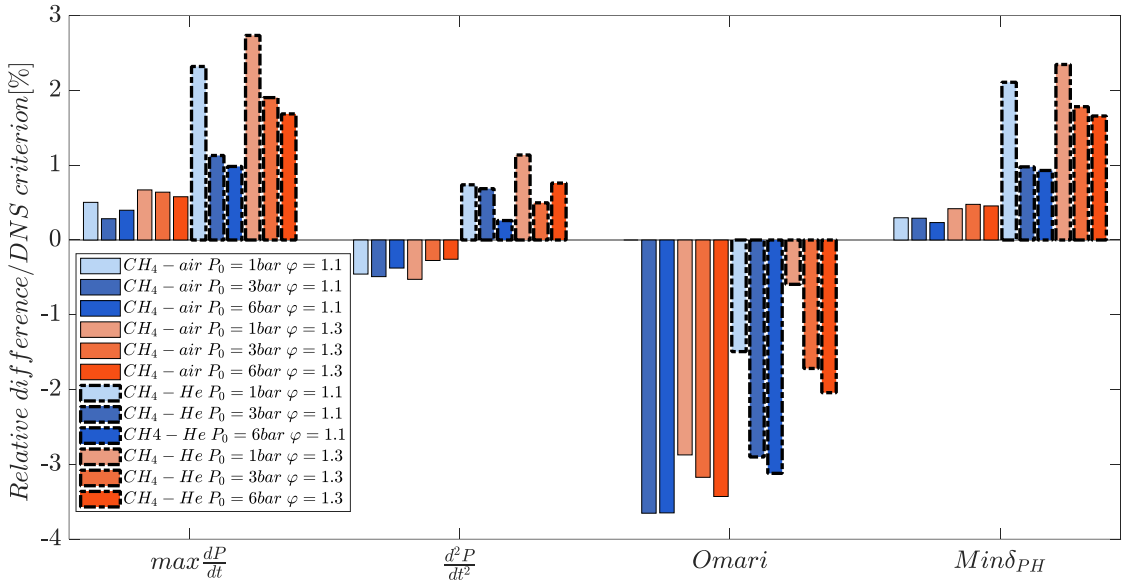

Figure 35 : Relative difference between critical radius criteria and DNS criterion (1% relative difference between $S_{u\,adi}$ and $S_{u\,isoth}$)

The standard deviation was also derived to give additional information concerning the robustness of the different criteria (Table 4):

Table 7: Standard deviation of criteria for 5%DNS criterion

$\boldsymbol{\sigma_{\frac{\partial P}{\partial t}}}$	$\boldsymbol{\sigma_{\frac{\partial^2 P}{\partial t^2}}}$	$\boldsymbol{\sigma_{Omari}}$	$\boldsymbol{\sigma_{\delta_{PH}}}$
0.8155	0.6005	1.4779	0.7738

- It appears that considering a lower percentage for the DNS criterion does not affect that much *Omari*'s behavior while the accuracy of the others is highly impacted. Hence, by always underestimating the critical radius for different reference criteria, *Omari* can be seen as a secure observation when a compromise between the accuracy limit and the available data range needs to be made. However, it remains the less stable criterion of this study, as far as standard deviation is concerned.

- Max ($\frac{\partial^2 P}{\partial t^2}$) does not seem to systematically underestimate the critical radius anymore since it overpredicts it principally for CH_4-He mixtures. It is, however, important to notice that it gives very accurate data in this case.
- Max ($\frac{\partial P}{\partial t}$) and min ($\delta_{ph}$) seem to have a similar behavior, as they both overestimate the critical radius globally by the same factor. It is interesting to notice that the overestimation is more important for CH_4- He cases. However, even if their global standard deviation is impacted, they still give accurate data for CH_4-Air mixtures with less than 1% relative difference with DNS.

Hence, it seems that, when considering a low percentage DNS criterion, the limit of adiabaticity regime is more difficult to evaluate for CH_4- He cases.

The choice of this reference criterion needs to be done accordingly to the studied mixture and to the main objective of the measurement, i.e. to find a balance between maximizing the number of high-pressure data and being secure enough on the available experimental data range.

Conclusion

The use of the Spherical Expanding Flame at Constant Volume method provides a large amount of accurate data for a wide range of pressure and temperature. One limitation relies on the perfect sphericity of the flame during the whole process. helium dilution is a solution to push back the limits of cellularity occurrence on the flame surface.

When the flame front approaches the wall, heat exchanges increase. They are favored when the thermal diffusivity of the mixture is high. The objective of this paper is to propose a model allowing to identify the conditions for which the propagation of the flame can be considered adiabatic.

A new criterion based on the minimization of the preheating zone thickness has been defined. Its robustness and its performance have been assessed.

It is possible to affirm that min (δ_{ph}) is a well-optimized criterion for the extraction of high-pressure S_u. Indeed, it has shown very good results with respect to the 5% difference reference criterion on DNS calculations. Considering the other criteria, the pressure first derivative and Omari criteria clearly have an inferior precision for the 5 and 1% difference reference criterion on DNS results. The max ($\frac{\partial^2 P}{\partial t^2}$) criterion, however, is the most precise for the latter reference condition. Hence, 2 criteria have been identified as robust and precise tools to identify the end of adiabaticity limit, relatively to its definition.

The other advantage of the min (δ_{ph}) criterion is that it is based on a phenomenological approach of the flame behavior directly accounting for the mixture composition. The results proved to be coherent with the overlap of the preheat and thermal boundary layer zones, confirming the physical interpretation of the end of adiabaticity. Hence, it is possible to have reliable data even for mixtures composed of high percentages of helium (increasing the D_{th} and thus decreasing the value of R_{crit} compared to CH_4/air conditions). It is also important to note that min (δ_{ph}) can be adapted to process data coming from every experimental SEF-CONV setup. Hence, it is possible to find a balance between the upper pressure limit accuracy and the range of available data.

3.4 Global overview of S_u evaluation with OPTIPRIME, method to compare with kinetic schemes

3.4.1 Global overview of S_u evaluation with OPTIPRIME

Figure 36 depicts the global procedure used to compute a complete full flame speed trace from raw data up to exploitable information. Several firings are conducted for one mixture condition thanks to the buffer tank. The pressure signal and flame pictures treatment procedures were presented in section 2.2. Properties of the fresh gases (T_u, ρ_u, λ_u and C_{p_u}) are then computed from the initial (P_0,T_0) conditions and from the pressure history of the firing thanks to the code mentioned in section 2.3.1.1 and in [122]. After the computation of the derivative terms, S_u is obtained from one firing. After several firings are completed for one given condition (their number depending on the buffer tank pressure and the targeted P_0), an average computation is performed to obtain the final S_u to which we apply the $\pm$5% margin of error. The overall procedure is described with *Figure 36*.

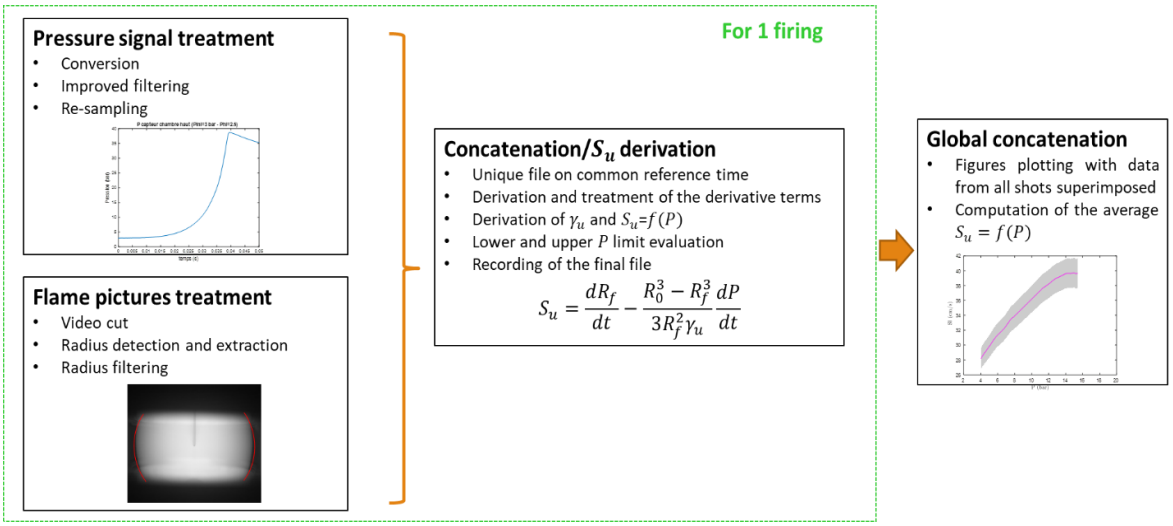

Figure 36: Global post-treatment strategy

3.4.2 Building the numerical S_u to be compared with the experimental data

In order to compare the experimental $S_u = f(P,T)$ trace to existing chemical schemes, it is important to detail the methodology of the corresponding numerical S_u computation. As described in the previous section and in [122], knowing the pressure history from the firing and the initial conditions, the computation of the corresponding fresh gases temperature T_u is possible. Hence The S_u trace is then discretized and (P, T_u) couples are obtained as inputs for S_u 1D flame computations with CANTERA. This procedure is illustrated by an example on Figure 37 showing the experimental $S_u = f(P,T)$ trace with its $\pm$5% uncertainty compared to the obtained corresponding numerical S_u.

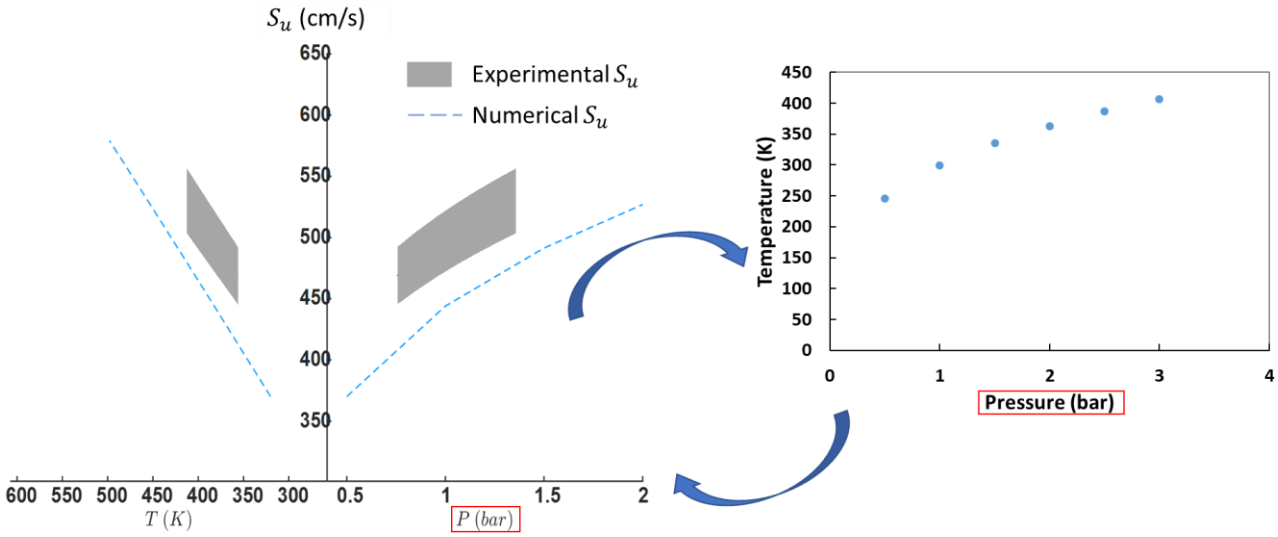

Figure 37: Schematic of the building process of the numerical S_u

3.5 Building the CH_4/O_2 S_u database at high pressure and temperature (Paper published in *Proceedings of the Combustion Institute*)

This section consists in a full paper published in *Proceedings of the Combustion Institute* [132]. Literature references were updated to be coherent with the one from the manuscript. After detailing the challenges of measuring S_u for oxycombustion at high pressure, the paper first investigates the initial stretch effects affecting the flames. Indeed, encountered stretch values are up to ten times more important than CH_4/air mixtures, hence the $2P_0$ criterion must be reevaluated. Once de database is built for a large spectrum of equivalence ratios and (P, T) conditions, the experimental results are compared to a panel of pre-selected chemical mechanisms. The best fitting mechanism (i.e. POLIMI C1-C3 [96]) is then analyzed through a sensitivity study on the reaction rate constants k for the tested conditions. The aim is to identify key sensitive reactions to be tuned during an optimization process to match the whole experimental database. Finally, a $S_u = f(P, T, \varphi)$ correlation fitted on the OPTIPRIME database and the existing literature sources is proposed. The full CH_4/O_2 $S_u = f(P, T)$ database produced with OPTIPRIME is available in Appendix B.

Laminar flame speed evaluation for CH_4/O_2 mixtures at high pressure and temperature for rocket engine applications

A. Mouze-Mornettas[a,b,c*], M. Martin Benito [a], G. Dayma[b,c], C. Chauveau[b], B. Cuenot[d], F. Halter[b,c]

[a] *CNES, Launcher directorate, 52 rue Jacques Hilairet, 75612 Paris Cedex, France*
[b] *CNRS ICARE, Avenue de la Recherche Scientifique, 45071 Orléans Cedex 2, France*
[c] *Université d'Orléans Cedex 2, France*
[d] *CERFACS, 42 avenue G. Coriolis, 31057 Toulouse Cedex 01, France*

Abstract

Pure methane-oxygen mixtures in liquid rocket engines lead to extreme pressure and temperature conditions that are prohibitive for most of the experimental setups. Hence, there is very little data on such flames in the literature, especially concerning the laminar flame speed S_u, often limited at atmospheric pressure. The recent development of methalox rocket engines, which design process often requires CFD calculations, brings this lack of data to the forefront. Indeed, the CFD simulations require valid chemical schemes in the real operating conditions. To address this problem, flame measurements have been performed in a special isochoric combustion chamber with full optical access (OPTIPRIME) developed at ICARE. An extensive database in conditions never tested before is generated for several equivalence ratios, temperature and pressure ranges. Multiple chemical mechanisms were then compared to those results, showing various levels of agreement. Hence, the best mechanism from the literature on OPTIPRIME results and other literature experimental data was selected. A sensitivity analysis was performed to identify key chemical reactions controlling the flame speed. These key reactions could later be tuned by an optimization process to perfectly match the experimental results. Finally, additional measurements were performed in order to develop a S_u=f(P,T) correlation to build a future flame speed database under rocket engines relevant conditions.

Keywords: Rocket engines; Methane-oxygen; High-Pressure; Laminar flame speed; Flame kinetics

*Corresponding author.

1. Introduction

With the space market being more and more competitive, reusable launchers are envisioned as a key technology to reduce the costs of access to orbit. Encompassed in this logic, methane (CH_4) has been identified as the best candidate fuel for the development of low-cost reusable space launch systems (high energy density, low operating cost, and good overall performances in terms of specific impulse [34]). As a consequence, several methane-based projects are currently being studied and developed around the world [41][23], making the understanding of pure methane/oxygen combustion (flame dynamics, kinetics, etc.) at high pressure and temperature a key problematic. Hence, available kinetic models need to be confronted to reliable experimental data.

However, the high reactivity of methane with pure oxygen (O_2) generally prevents its experimental study whether it is ignition delay, species profiles, or flame speed measurements. Indeed, such mixtures release a significant amount of energy compared to classically studied CH_4/air mixtures where nitrogen (N_2) acts as a thermal ballast. Therefore, the resulting temperature of burnt gases is very high (> 3000 K against 2100 K in air at equivalence ratio φ = 1 and 1 bar) leading to high laminar flame speeds S_u (around 3 m.s^{-1} against 0.3 m.s^{-1} in air under the same T, P conditions). Therefore, bibliographical information on this topic is very scarce.

As diffusion flames in rocket engine relevant conditions require very complex and expensive dedicated setups, premixed laminar flame speeds are more straightforward to measure. They are a fundamental parameter to study and can be used to assess the behavior of kinetic mechanisms [98]. Furthermore, it has been proven that a chemical mechanism valid for premixed flame configurations is generally also valid for stretched laminar diffusion flames. Indeed, simplified kinetic models validated at equilibrium and in premixed laminar flames show a similar behavior to diffusion-flames-derived chemistry in LES calculations of rocket engine configurations [23]**.** Nevertheless, as mentioned above, the extreme conditions of rocket engine combustion chambers are generally incompatible with most of the experimental devices used to measure flame speeds. Therefore, diluted mixtures using an inert gas as a thermal ballast (such as N_2, Ar or He) have been much more investigated. In order to study CH_4/O_2 flames, another option is to focus on very lean or very rich conditions where S_u values are lower.

To the best of our knowledge, very few studies were performed in CH_4/O_2 mixtures. The first are related by Lewis and Von Elbe [108]. More recently, measures were performed by Mazas et al.[106][107]. Both studies used a Bunsen-type burner as experimental setup. In Mazas case, a low diameter nozzle (3 mm) was used to reduce the turbulence effect on the flame. Flame speeds were measured thanks to a Schlieren technique for different equivalence ratios φ varying from 0.5 to 1.6 at atmospheric pressure and 298 K. Additional measurements were carried out at atmospheric pressure for lean, stoichiometric and rich mixtures, varying the initial temperature of the reactive mixture from 298 K to 500 K. However, no pressure variation was considered in this study, nor in the work of Lewis and Von Elbe. Therefore, extending the database to a wider range of temperatures and pressures is greatly valuable in order to develop a combustion model for CH_4/O_2 mixtures under rocket engine conditions.

The current study provides data acquired with the perfectly spherical and isochoric combustion chamber (OPTIPRIME) with full optical access developed at ICARE [112]. φ was varied from 1 to 2.5, with a pressure range depending on the tested conditions going from 0.3 to 18 bar while the fresh gases temperature vary between 298 and 603 K (and the burnt gases temperature from 2260 K to 3115 K). The obtained database, complemented with other measurements from the literature, is then used to build a valid kinetic model for methane oxycombustion at high pressure.

2. Experimental data acquisition

To be as close as possible to the conditions of interest, high pressures and temperatures are targeted. This is not straightforward as can be seen in the literature, where methane flame speeds are mostly studied around atmospheric pressure and low temperatures for technical reasons [105]. In order to go to higher pressures, the isochoric combustion method is used (also referred as spherically expanding flame at constant volume). The principle is to record the evolutions of pressure and flame radius over time and compute the fresh gases temperature assuming an isentropic compression, allowing to evaluate the flame speeds under these conditions. In OPTIPRIME, these simultaneous measurements are made possible thanks to an optical access with a 360° fused silica ring. The flame speed determination process has been detailed in previous publications [112][98]. Hence, the chamber allows to measure S_u values from ambient (or even sub-atmospheric) conditions up to 20 bar at high temperatures (up to 603 K in the fresh gases, 3115 K in the burnt gases). It is important to note that CH_4/O_2 mixtures lead in the studied conditions to very high flame speeds near stoichiometry (up to almost 6 m.s^{-1}), which is 10 times higher than the values encountered for diluted mixtures previously studied with OPTIPRIME. Such strong combustion induces an important mechanical and thermal stresses on the setup as well as challenging conditions for the data acquisition and post-treatment. These challenges require to perform several checks and adaptations which are detailed below.

2.1 Pressure effects

The pressure time-variation can be very steep for CH_4/O_2 mixtures. At φ = 1.5 for example, there is a factor of 30 between the dP/dt encountered with CH_4/Air (400 bar.s^{-1}) and CH_4/O_2 (12000 bar.s^{-1}). In order to withstand these brutal variations at each firing, the 360° silica ring used for optical access has a thickness of 11 mm. However, in order to avoid destructive levels at the end of the flame propagation where the pressure is at its maximum, the initial pressure P_0 was sub-atmospheric at 0.5 bar for most of the cases. This also allows to delay the occurrence of hydrodynamic instabilities (visually detectable) providing longer S_u recorded signals. On the other hand, lower initial pressure leads to slightly higher flame speed than at atmospheric pressure. Hence, the acquisition frequencies of the camera and pressure transducers need to be increased (up to respectively 110000 fps and 60 kHz). This requires an adaptation of the data filtering parameters for the post-treatment compared to what was previously used for CH_4/air mixtures.

2.2 Stretch effects

Another monitored parameter is the flame stretch. Numerical computations of flame speeds were performed for non-stretched flames. In order to compare the calculated values to the experimental ones, stretch dependence needs to be assessed. In spherical flames, the stretch is limited to curvature and writes as $\kappa = 2/R_f \, . \, dR_f/dt$. The high values of flame speed encountered for CH_4/O_2 mixtures then lead to high stretch values. Typically, in diluted cases, the initial κ is far lower than in non-diluted mixtures by a factor 10. In the present case, κ_{ini} is found around 400 s^{-1} for CH_4/air where it is 4000 s^{-1} for CH_4/O_2 at stoichiometry. These stretch levels were evaluated when R_f is large enough to start computing S_u. In practice in CH_4/air mixtures, the instant when the flame is considered not to be affected by stretch corresponds to the time when the pressure reaches 2 times its initial value P_0 [112]. This relation is based on the Markstein length in the burnt gases L_b, computed from experimental data, assuming the linear relation $S_b = S_b^0 - L_b\kappa$ (S_b^0 being the unstretched flame speed in the burnt gases). The criterion marks the time when $L_b\kappa \ll S_b^0$ (or very low values of the $L_b\kappa/S_b^0$ ratio), i.e. the stretch effects are negligible. In view of the observed high κ values, this evaluation needs to be conducted for CH_4/O_2 mixtures. In order to assess the evolution of the different parameters over the whole flame propagation process inside the chamber, the $L_b\kappa/S_b$ ratio is preferably used, while L_b is supposed constant over pressure and temperature [133]. In order to cover the whole range of studied equivalence ratios, $L_b\kappa/S_b$ is studied for φ=0.5, $\varphi = 1$ and φ=2.5. As illustrated in Table 1, κ_{ini} values for the first recorded R_f vary with

the equivalence ratio φ, κ strongly decreasing as φ tends toward richer mixtures since the flame speed diminishes. Concerning lean mixtures, the stretch progressively increases toward stoichiometry, following the flame speed evolution.

Table 1
Computed Markstein length and critical stretch values from experimental data at different φ for CH_4/O_2 mixtures

φ (−)	κ_{ini} (s^{-1})	L_b (m)
0.5	2000	2.72E-04
1	4000	1.60E-04
2.5	400	8.09E-04

Furthermore, it can be noticed that the Markstein length L_b is greater for rich and lean mixtures than for stoichiometric ones. Since this parameter roughly reflects the flame front response to an exterior perturbation, which is here the stretch κ, it means that rich and lean CH_4/O_2 flames tend to have a higher sensitivity to stretch than stoichiometric ones. This is indeed observed on Fig 1, illustrating the $L_b\kappa/S_b$ evolution over R_f for the studied cases.

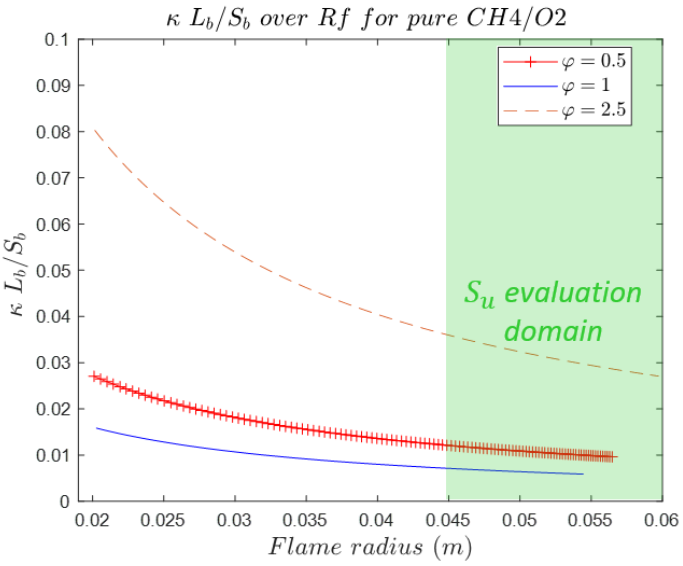

Fig. 1: *$\kappa L_b/S_b$ ratio over flame radius R_f for 2 different equivalence ratios (CH_4/O_2 mixture)*

The figure confirms that stretch effects are stronger for rich and lean mixtures, despite the lower κ values. However, as stated earlier, the evaluation of S_u starts when the pressure has reached $2P_0$ (region labelled as "evaluation domain" in Fig. 1). This threshold is reached for substantially similar flame radii for the studied conditions. It occurs at the end of flame propagation [112], i.e. at low stretch levels. Indeed, $L_b\kappa/S_b$ is lower than 5% for both studied mixtures in the measurement zone. Thus, the pressure criterion is still valid to determine the first R_f to be considered for flame speed calculation in CH_4/O_2 mixtures.

3. Comparison with numerical kinetic mechanisms

The chemical mechanisms investigated in this paper (cf. Table 2) are from various sources. Some were designed on purpose for high-pressure methane/oxygen applications such as RAMEC [80], Slavinskaya

[89] and Zhukov [85]. RAMEC and Zhukov are mainly validated on the basis of ignition delay times, the first one using low dilution ratios conditions at high pressure. Slavinskaya mechanism is validated on both high-pressure diluted ignition delay times and laminar flame speeds in the air at atmospheric pressure. The others selected models are multi-purpose mechanisms like GRI-Mech3.0 [79], FFCM1 [95] and POLIMI C1-C3 [134]. They were validated on various targets, including flame speeds, but at pressure and temperature far from rocket engine relevant conditions. FFCM1 and GRI-Mech 3.0 are compact mechanisms, allowing fast calculations. FFCM1 previously shown satisfactory results on OPTIPRIME CH_4/air experiments [115]. POLIMI C1-C3 requires more computation time but was validated on numerous experimental targets.

The mechanisms were used in 1D laminar flame computations performed with the PREMIX code from CHEMKIN Pro [135] at various P, T and φ conditions identical to the experiments.

Table 2
Tested chemical kinetic mechanisms

Mechanism	#Species	#Reactions
Slavinskaya[12]	22	97
Zhukov [13]	23	51
RAMEC [11]	38	190
FFCM1 [15]	38	291
GRI-Mech 3.0 [14]	53	325
POLIMI C1-C3 [16]	114	1999

First, an evaluation of these mechanisms against the experimental dataset of Mazas was performed at constant pressure (1 bar) and temperature (298 K). The overall agreement is good while some mechanisms (RAMEC in particular) underestimate S_u as φ increases. Others, like FFCM1, constantly underestimate the experimental values. When compared to Mazas parametrical study on initial temperature T_0 at 1 bar, all mechanisms except POLIMI C1-C3 show some discrepancies with the experiment as T_0 increases, for all tested φ (the figures can be found in the supplementary materials – Figs S2 to S4). Hence, it is now interesting to compare the mechanisms with the experiment at varying P and T.

Experimental results from φ = 0.5 to 2.5 are displayed in Fig 2. All tests started at P_0 = 0.4 bar except the case φ = 2.5 at P_0=2 bar for which S_u is lower. S_u is represented as a function of P (right side of each graph) and T (left side) with the associated experimental uncertainty of $\pm$5%. The flame speed increases with simultaneous augmentation of P and T as the fresh gases are compressed by the flame front. Maximum usable pressure goes from 1.5 to 18 bar depending on the considered equivalence ratio. All the experimental data can be found in the supplementary materials. Fresh gas temperature ranges between 300 and 603 K while the burnt gases temperature varies from 2260 to 3115 K. Unstretched laminar flame speeds S_u^0 (i.e. isobaric S_u) determined by using the zero-stretch extrapolation method described in section 2 are also indicated on Fig 2. The measured flame speed is maximum at stoichiometry between 450 and 550 cm.s^{-1} and then decreases with increasing φ.

Numerical results also reported in Fig 2 show that all tested mechanisms dramatically underestimate the experimental flame speed values for lean, stoichiometric and near-stoichiometric conditions. At φ = 2, most of the mechanisms are close to the measured values while they all over-estimate them at φ = 2.5. It is important to note that the last two equivalence ratios are beyond the range over which most of the mechanisms have been validated. However, all mechanisms well reproduce the evolution shape of S_u, i.e. its bending when P and T increase. This bending effect seems to be more important at low pressure (as seen at φ=2), confirming the trends suggested by the isobaric S_u^0 and the flame speed traces for most of the tested conditions. On average over all φ conditions, POLIMI C1-C3 is found to best predict experimental results, with a relative error varying between 26 and -10% depending on the tested conditions. Interestingly, FFCM1 behaves as an offset of POLIMI C1-C3, always underestimating S_u but mimicking well its evolution over P and T. All other mechanisms, apart from specific cases, remain in between POLIMI C1-C3 and FFCM1. Hence, it seems all the mechanisms initially tailored for

methane oxycombustion fail to capture the right S_u levels. For RAMEC and Zhukov, this may be due to the fact that their experimental validation is only based on ignition delay times. For Slavinskaya, the S_u targets in the air are too far from oxycombustion conditions. As for FFCM1 and GRI-Mech 3.0, although some of the numerous S_u validation targets are at high pressure, the important dilution rate leads to lower temperatures than CH_4/O_2 mixtures. Hence the observed discrepancies. Moreover, many of the sensitive (i.e. important) reactions depicted in the next section are defined differently from one mechanism to another.

Therefore, POLIMI C1-C3 seems to be the best starting point for a yet-to-be-optimized mechanism versatile for both CH_4/air and CH_4/O_2, as well as highly diluted mixtures. Indeed, other data acquired at high pressure (up to 20 bar) for stoichiometric highly diluted mixtures (up to 80% diluent in molar mass in the oxidizing mixture, diluent is composed of 70%He and 30%Ar, presented in the supplementary materials) confirm the rather good agreement obtained with POLIMI C1-C3 for these conditions. Overall a major outcome of this study is the lack of validity of existing mechanisms for CH_4/O_2 at high P due to the lack of data, which is partly overcome by the present OPTIPRIME measurements.

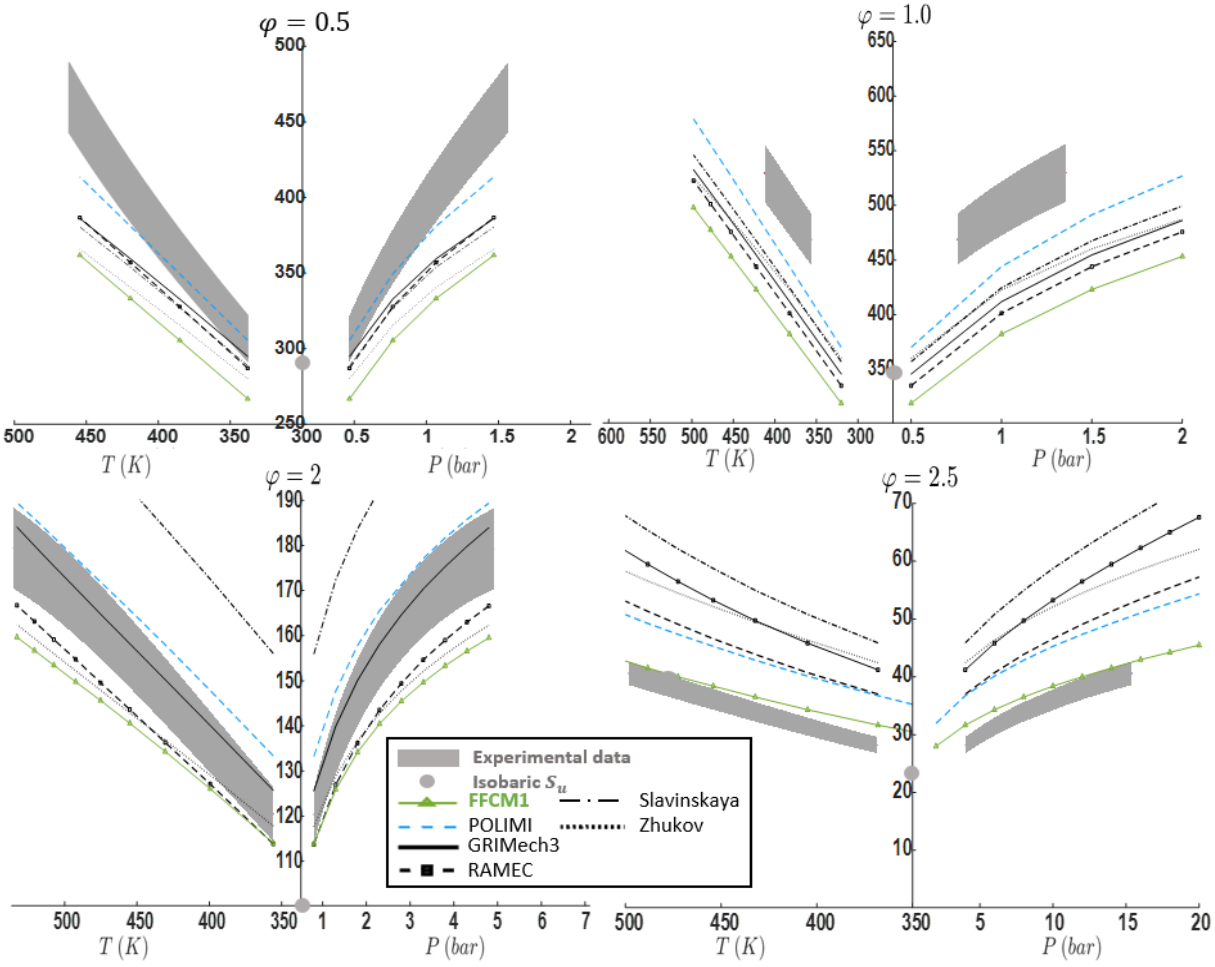

Fig. 2*: Flame speed S_u [cm.s^{-1}] for CH_4/O_2 mixtures at various equivalence ratios φ (thickened traces) as a function of T and P compared to several kinetic mechanisms (lines). Single symbols are for*

4. Sensitivity analysis of the POLIMI C1-C3 mechanism

As seen in the previous section, the calculations performed with POLIMI are in closest agreement with our experimental data. However, this mechanism is not able to fully reproduce the S_u behavior for CH_4/O_2 mixtures in the targeted (P,T,φ) conditions. In order to better understand the kinetics under these conditions and identify the rate constants, k, on which it would be possible to act to obtain a better agreement, a sensitivity analysis of S_u were performed for different φ (from 0.5 to 2.5) for the P and T range covered during the experiment. The sensitivity is defined as $S = \partial S_u/\partial k_j$ where k_j is the rate constant of reaction j. A panel of 13 most sensitive reactions was identified and displayed on Fig 3.

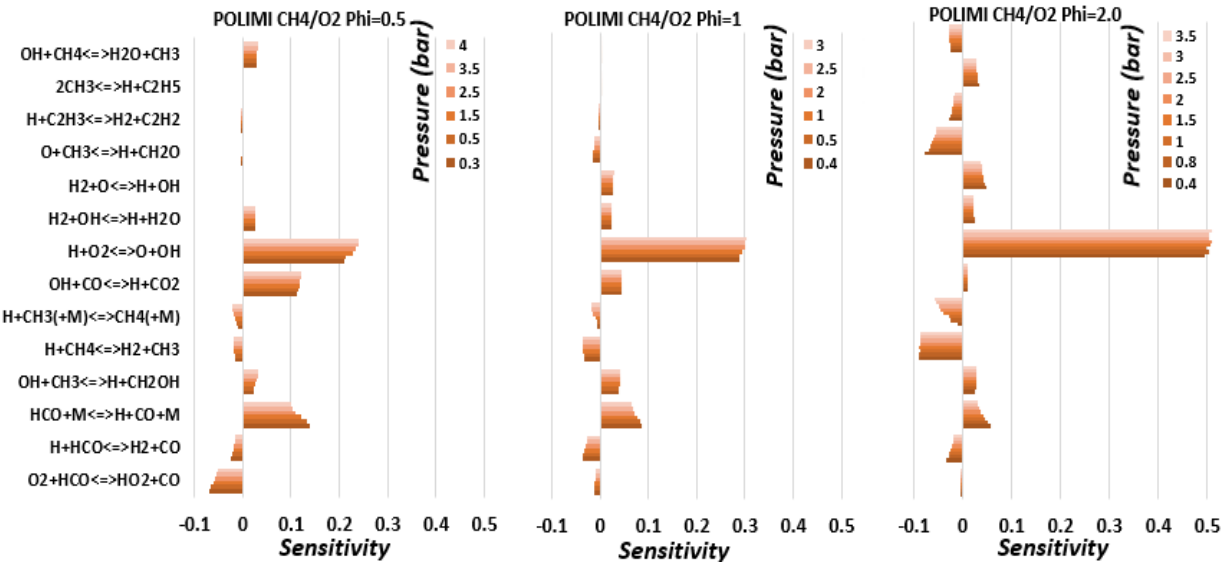

Fig. 3: *Sensitivity analysis on S_u of POLIMI C1-C3 for a CH_4/O_2 mixture at different equivalence ratios φ*

These driving reactions for the flame speed decompose in 2 families: those which have a promoting effect on S_u ($S > 0$) and those which have an inhibiting effect ($S < 0$). For all conditions, $H + O_2 = O + OH$ is by far the most sensitive reaction, its S increasing with φ. For other $S > 0$ reactions, $HCO + M = H + CO + M$ and $OH + CH_3 = H + CH_2OH$ seem non-negligible whatever the equivalence ratio. Interestingly $OH + CO = H + CO_2$ is quite sensitive at lean conditions while quickly becoming almost insensitive when φ increases. In addition, $H + CH_4 = H_2 + CH_3$ is the most important $S < 0$ reaction, with growing sensitivity as the equivalence ratio increases. Its value is only exceeded by $O_2 + HCO = HO_2 + CO$ for lean conditions only. $H + HCO = H_2 + CO$ also plays a significant role with a sensitivity not varying much which φ. The reaction $O + CH_3 = H + CH_2O$ however, has almost no impact at lean and stoichiometric conditions but becomes the second largest negative-sensitive reaction at φ = 2. Interestingly, the sensitivity sign of $OH + CH_4 = H_2O + CH_3$ changes with φ. Being positive for lean conditions (since it adds CH_3 in an environment where there is only a few), it gradually transits toward negative values for reach conditions.

All these reactions also play a role for the tested diluted mixtures mentioned before. On the other hand, $CH_3 + H(+M) = CH_4(+M)$, identified as a key reaction for CH_4/air flame speeds [98] is far less sensitive for oxy-combustion. Thus, it does not play an important (though not negligible) role here. However, complementary sensitivity analyses conducted at higher pressures for CH_4/O_2 tend to show that its S increases with P, which makes the additional role of high pressure diluted experimental measurements where this reaction is also sensitive more important for a future optimization process. This work is currently in progress, using the OptiSMOKE++ [136] code to tune the Arrhenius parameters of several sensitive reactions identified here.

5. Flame speed correlation

As seen in the previous sections, a single firing with the OPTIPRIME setup allows to access a full trace of flame speeds S_u over a variety of (P, T) conditions. Therefore, it is interesting to perform several firings, varying the initial pressure in order to have different traces allowing to explore other domains. It is then possible to fit a S_u= f(P, T) correlation on the obtained data, allowing to interpolate in between the traces and even extrapolate outside the measurement range, creating a full map limiting the number of experiments. This method would allow to progressively build a flame speed database for several mixtures, temperature and pressure conditions that could be used in a CFD combustion model. Such a work is currently underway at ICARE for CH_4/air mixtures.

In order to cover a broader range of conditions, additional firings are performed for the same set of equivalence ratios as previously tested at an initial pressure of 0.5 bar (P_0 = 3 bar for φ = 2.5). It is important to mention that the margin to choose the conditions to interpolate and extrapolate from is very thin for these extreme CH_4/O_2 mixtures compared to the diluted mixtures (for example with air), because of the limiting pressure derivatives values reached during the flame propagation in OPTIPRIME. Obtained experimental S_u traces are displayed in the supplementary materials in Fig S5. In order to enhance the model precision, data from Mazas at atmospheric pressure presented in the first section of the manuscript are added as target values for the correlation.

The first S_u= f(P, T) correlation used in this study to fit each equivalence ratio condition is described by Hu et al. [137][99]. It is based on the initial flame speed S_{u0} at reference conditions P_0, T_0. Two exponents, α_T and β_P, respectively functions of the temperature and the pressure contain five different coefficients that can be tuned to fit the experimental traces.

$$S_u = S_{u0}(T/T_0)^{\alpha_T}(P/P_0)^{\beta_P} \qquad (1)$$

Obtained numerical values of the function parameters are given in the supplementary materials. A different fit is generated for each φ conditions. Hence there is as many maps as tested equivalence ratios. Fig 4 illustrates an example of a correlation map for a CH_4/O_2 mixture at φ = 2.5. The experimental traces are represented in black, while the rest of the map is either interpolated or extrapolated within the range of the covered pressure and temperatures. This kind of map allows to predict the evolution of S_u over pressure and temperature, the map being more precise when new traces are added.

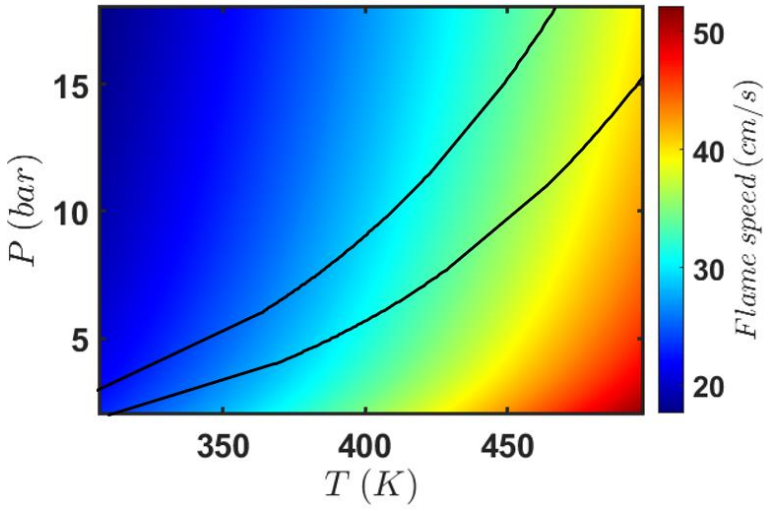

Fig. 4: S_u=f(P,T) *correlation map at* φ =2.5

Finally, the obtained correlation was compared to Mazas T_0 parametric database (graphs are available in the supplementary materials), showing satisfactory results. The models stay inside the range of experimental uncertainty for each φ condition tested by Mazas.

In order to simplify the modelling, another approach considering the equivalence ratio dependency was used. It consists of an expression similar to Equation 1, but with S_{u0}, α and β function of equivalence ratio φ. Such expression is described in the paper of Wu et al. [138]. This approach allows the use of a single correlation for all the range of applicable (P, T, φ). The results, also shown in the supplementary materials, were compared to Mazas $S_u = f(\varphi)$ study at 1 bar. Fitting is quite good for lean mixture and stoichiometry while it slightly overestimates the experience for rich conditions. The observation is identical on Mazas T_0 parametric database.

5. Conclusion

The development of methane-oxygen rocket engines for reusable launch vehicles requires an extensive knowledge of the chemical kinetics in extreme pressure and temperature conditions. However, it is precisely those hard-to-reach conditions that are prohibitive for experimental test benches, leading to very limited experimental flame speed datasets in the literature, often restricted to atmospheric pressure. In order to bring additional knowledge on the flame speed behavior at high P and T for those mixtures, the OPTIPRIME isochoric combustion chamber with full optical access was used. Measurements were performed for a variety of equivalence ratios (from 0.5 to 2.5) and a large range of pressures, depending on the tested cases (up to 1.5 to 18 bar). Kinetic mechanisms, for most of them traditionally used to describe CH_4/O_2 combustion are compared to OPTIPRIME and literature datasets. It allows to point out major discrepancies between the numerical and experimental results when it comes to extreme conditions. Finally, the POLIMI C1-C3 model seems to be the best candidate for a yet-to-be optimized mechanism to describe CH_4/O_2 combustion. Several reactions were identified as key ones that need to be better evaluated. In addition, S_u=f (P, T) correlations were built from OPTIPRIME results in order to create a full map of flame speed for diverse conditions. Additional experiments are still required to increase accuracy and extend the range of validity.

3.6 Complementary diluted targets at stoichiometry

3.6.1 Global strategy: dilution effect parametric study

As mentioned in the previous section, methane oxycombustion leads to extreme conditions in terms of flame speed, pressure evolution and flame front instabilities. The most challenging point being at stoichiometry. Hence, as explained in [132], a sub-atmospheric initial pressure of 0.4 bar was chosen for φ=1 measurements, allowing to reach a final exploitable pressure of 1.5 bar. However, the investigation of high pressures for a stoichiometric mixture (i.e. close to the one of a rocket engine) would be highly valuable in order to check the S_u behavior. Dilution is a simple solution in order to explore higher P for the stoichiometric conditions. Using an inert gas like He or Ar acts as a "thermal ballast". It allows to decrease the flame speed and the pressure temporal evolution, thus making the conditions less challenging for the hardware. He high thermal conductivity also delays the apparition of thermo-diffusive instabilities by increasing Le. However, as previously mentioned, it leads to fast energy dissipation, preventing the ignition system to operate well in highly diluted conditions. Consequently, after different experimentations, a hybrid diluent mixture of constant composition 70%He and 30%Ar in molar (or volume) fraction was chosen. This compensates the ignition issues created by He while keeping a stable flame front with S_u and final pressure levels compatible with OPTIPRIME.

He and Ar are both inert noble gases, thus they do not directly affect the chemical transformation at stake. However, the "thermal ballast" effect decreases the fresh gas temperature during compression, which might affect some reactions. Hence, to better understand these phenomena and explore higher pressures, an experimental parametric study is performed. The dilution ratio (i.e. molar fraction of diluent in the oxidizing mixture – the diluent composition being constant as mentioned above) is varied from 50 up to 82.5%.

In parallel with the measurements, a sensitivity analysis is performed in order to verify that diluted mixtures are still representative of pure CH_4/O_2 mixtures in term of major (or pilot) reactions. Indeed, the consistency of the latter is vital for the future optimization process of a mechanism on the OPTIPRIME experimental database. Figure 38 illustrates the sensitivity analysis performed on S_u with CANTERA for two different dilution ratios of 50% and 70% following the (P,T) trace of the experimental firings. The final pressure of the 50% diluent case is lower than the 70% one since thermo-diffusive instabilities are encountered sooner for less diluted cases. The analysis presented here was performed with the FFCM1 mechanism (the one performed with POLIMI C1-C3 giving similar trends). Axis values were arranged to focus on the main pilot reactions, hence $H + O_2 = O + OH$ is partially truncated, allowing to appreciate the 10 other most sensitive reactions.

Figure 38 shows that Sensitivity S on the flame speed tends to be more important for a majority of reactions when the percentage of diluent is high. Indeed, the methane recombination reaction $CH_3 + H(+M) = CH_4(+M)$, which is one of the key reaction piloting S_u close to stoichiometry is almost two times more sensitive at 70% diluent than 50%. This evolution seems coherent with the measured flame speed since its S is negative and that the global S_u is lower for higher dilution ratios.

However, even though the absolute sensitivity value is different, the key reactions (i.e. the most sensitive ones) are the same for the different diluted cases, from 50 to 82.5% diluent in the oxidizing mixture. Moreover, pathway analysis comparing diluted and non-diluted conditions show that the main pathways are only slightly affected by the dilution. Finally, flame speed sensitivity for a pure CH_4/O_2 mixture displayed on Figure 39 confirms that diluted mixtures are representative of the non-

diluted cases, hence validating the proposed experimental strategy for stoichiometric conditions at high pressure.

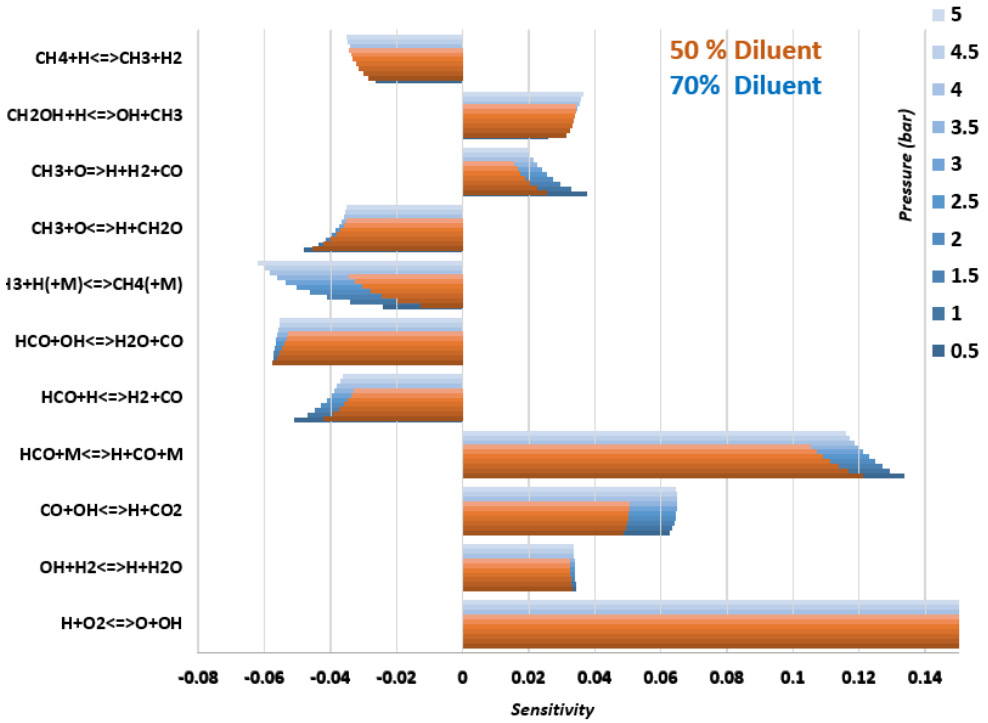

Figure 38: Sensitivity analysis for diluted CH_4/O_2 mixture

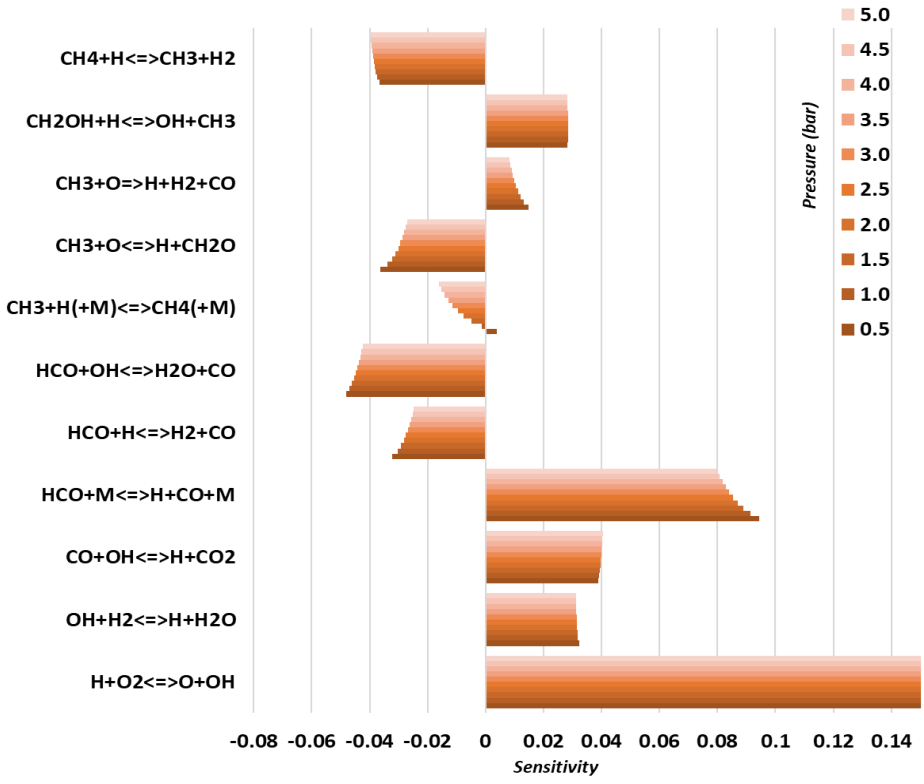

Figure 39: Sensitivity analysis for pure CH_4/O_2 mixture

3.6.2 Diluted targets at stoichiometry: experimental results

Figure 40 depicts the obtained experimental $S_u = f(P,T)$ for the dilution parametric study. As mentioned above, the dilution ratio was varied between 50 and 82.5% of the oxidizing mixture (the intermediary 70% case is not displayed here). Tested initial pressures for the 82.5% diluent case are P_0=2, 3 and 4 bar. P_0 was sub atmospheric at 0.5 bar for all other conditions. Consequently, the explored S_u range is quite large (from 60 $cm.s^{-1}$ to 5.5 $m.s^{-1}$). When comparing the 50% dilution case to the 0% displayed in the previous sections, the maximum encountered S_u are quite close (respectively 480 vs 530 $cm.s^{-1}$). The fresh gases temperature goes from 300 to roughly 650 K (depending on how much they are compressed) while the burnt gases temperature can go up to 3060 K for less diluted cases at high pressure. These levels are comparable to the non-diluted conditions. Hence, the stress levels on the combustion chamber and post treatments parameters employed for these conditions are globally similar. For this reason, the dilution effect was not explored further during this parametric study.

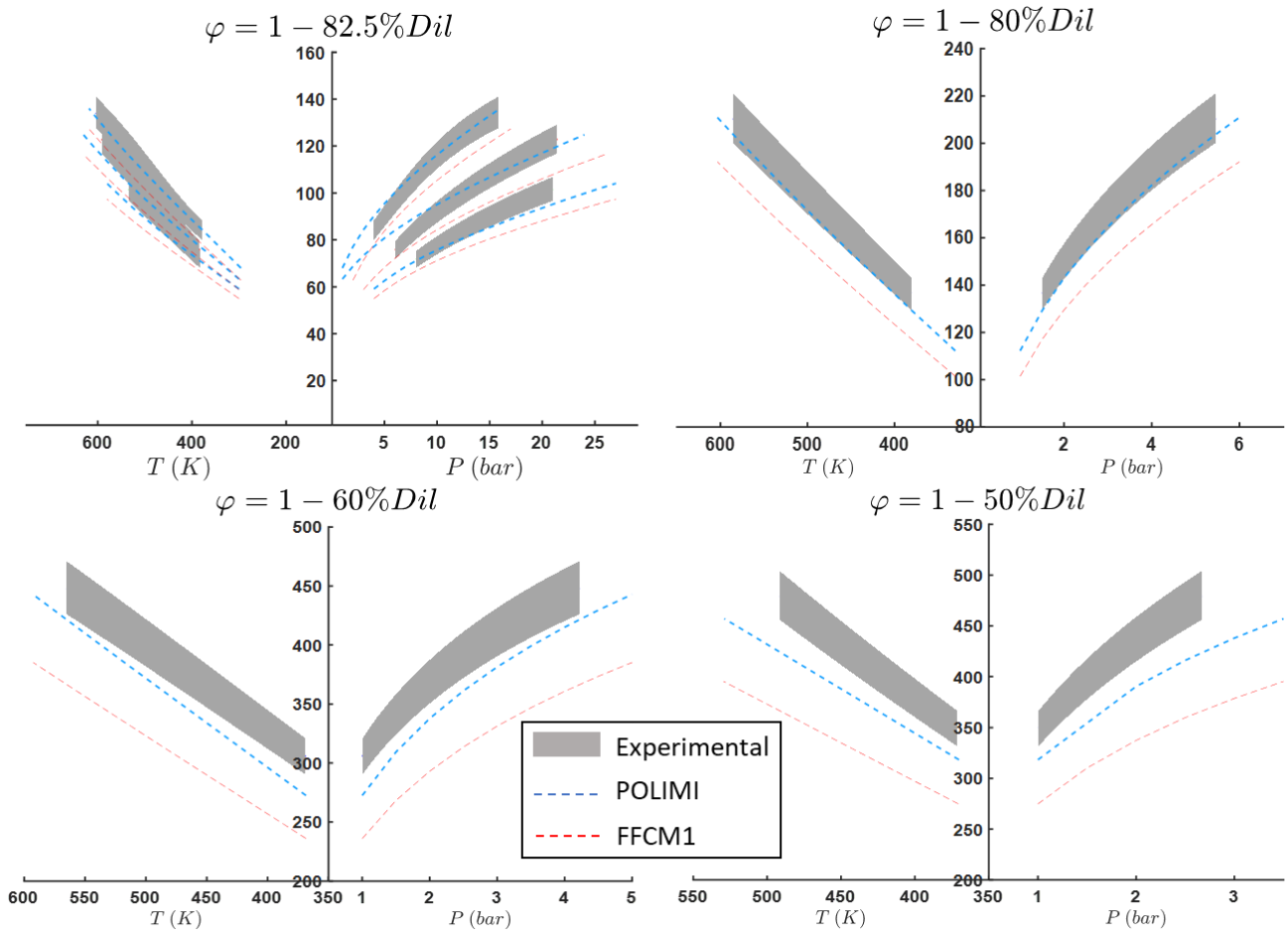

Figure 40: Diluted S_u=f(P,T) at stoichiometry

The FFCM1 and POLIMI C1-C3 mechanisms are confronted to the experimental results. As observed for CH_4/O_2 conditions, POLIMI tends to give higher S_u than FFCM1, with an almost constant relative difference. All the other studied mechanisms (not displayed here) fit in between. The trend over pressure or temperature of the displayed mechanisms is similar. As the dilution ratio decreases, the difference (absolute and relative) between the experimental and numerical S_u increases. This

observation is of course valid for both the evolution over pressure and temperature. It is consistent with the sensitivity analysis on S_u displayed on Figure 38 showing that an increase in dilution implies an increase of sensitivity for $S < 0$ key reactions such as CH_4 recombination. In conclusion, the behavior of this reaction, among others, needs to be corrected to fully capture the dilution effect with current mechanisms. These experimental conditions hence act as interesting additional targets for an optimization process. The full diluted CH_4/O_2 $S_u = f(P,T)$ database produced with OPTIPRIME is available in Appendix B.

3.7 Conclusion

This chapter highlights the lack of experimental data for CH_4/O_2 flames at high pressure and temperature which is highly problematic for rocket engine calculation applications. The summary of the state-of-the-art measurement techniques of flame speed in extreme conditions points out the advantages of the isochoric method. The OPTIPRIME experimental setup developed at ICARE is presented in terms of hardware, firing procedures and measurements methods and limitations inherent to spherical flames in closed vessels. Then a new high-pressure criterion for end-of-adiabaticity-regime detection is proposed to refine and increase the range of pressure explored during a firing. Once these new methods are established, the construction of the CH_4/O_2 experimental database for a large scope of equivalence ratio, pressure and temperature conditions is presented. This database is then compared to previously selected mechanisms, highlighting POLIMI C1-C3 being the one with less discrepancies with the experiment. Finally, the construction of a complementary database diluted flame speeds at stoichiometry in order to access higher pressures for this extreme condition is detailed.

Chapter 4

Kinetic mechanism optimization on experimental targets

4.1 Experimental vs numerical results: initial situation

The previous chapter presented the CH_4/O_2 flame speed database acquired with the OPTIPRIME setup for a large spectrum of equivalence ratios, pressure and temperature. The S_u traces were compared to a selection of different mechanisms as highlighted in the Chapter 3 sections based on [132]. On the overall, the POLIMI C1-C3 [134] mechanism was identified as the one presenting the less discrepancies with the experiments for the studied scope of experimental data. Hence, it is chosen as a starting point for the optimization process. The whole procedure was summarized in a publication of the EUCASS 2022 conference [139] and is presented in details in this chapter.

Figure 41 illustrates that the average relative difference between the experimental and numerical S_u is dependent on the equivalence ratio φ as illustrated in [132].

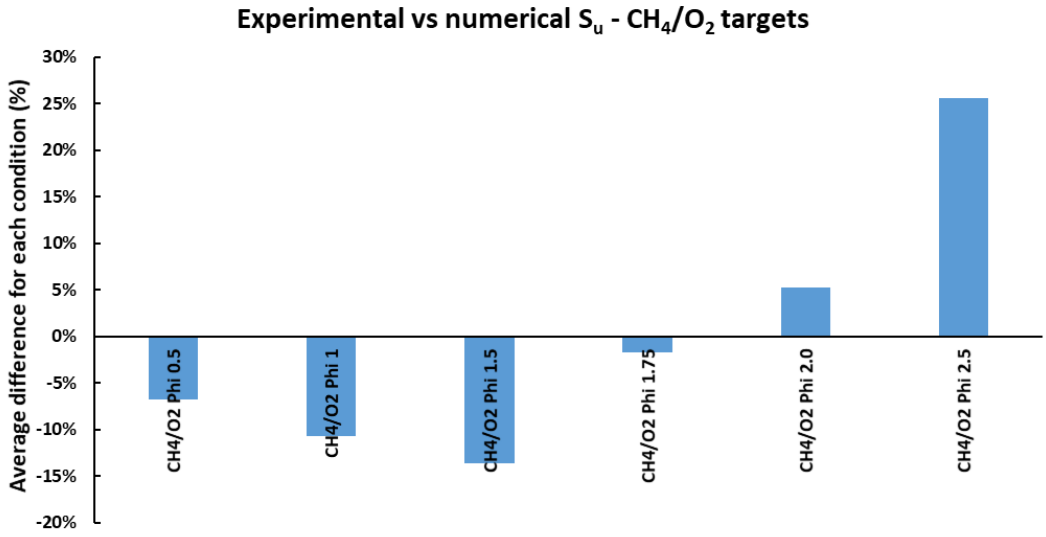

Figure 41: Average discrepancies between numerical and experimental S_u for CH_4/O_2 mixtures

For rich conditions at $\varphi = 2.5$ the absolute difference on S_u is 5 times less important with a 10 $cm\ s^{-1}$ gap on average. However, since flame speeds are quite low for these conditions, the relative difference becomes important. This leads to the 30% value displayed on Figure 41.

Figure 42 illustrates the diluted targets at stoichiometry. As detailed in the previous chapter, it is observed that the experimental/numerical discrepancy tends to increase while the percentage of diluent in the oxidizing mixture decreases. This observation is found to be coherent with the sensitivity analysis on flame speed. It indeed shows that the negative sensitivity of some key reactions (in particular the methane recombination) are much more important for diluted conditions, hence explaining lower flame speeds.

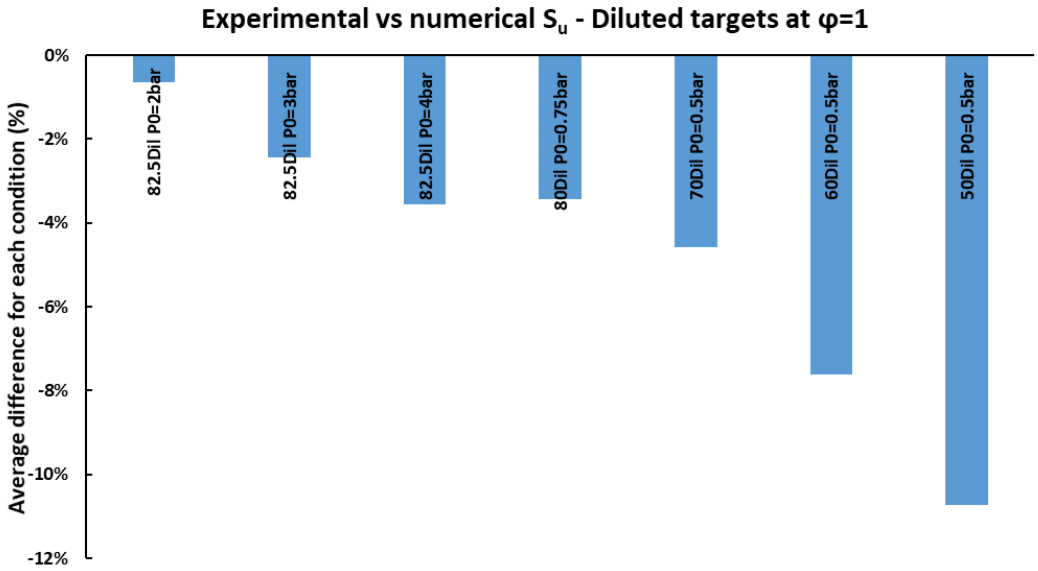

Figure 42: Average discrepancies between numerical and experimental S_u for diluted mixtures

It is important to recall that the relative experimental uncertainty on S_u is $\pm 5\%$, hence the 82.5 and 80% diluted conditions already match the experimental data. However, the gap is greater for all the other conditions (diluted and not diluted). Hence, the behavior of the POLIMI C1-C3 mechanism needs to be corrected via an optimization process.

4.2 Kinetic mechanisms optimization methods

Kinetic mechanism optimization consists in modifying key reaction parameters to correct the behavior of the numerical models so they can match the experimental datasets uncertainty zone. In other terms, the aim is to minimize an *objective function* describing the relative difference between the model and the experiment. The experimental targets can be ignition delay times, species profiles and laminar flame speeds S_u. In order to tune a mechanism, several *active parameters* can be modified during the process. First, key reactions having a non-negligible impact on the quantity we want to optimize need to be identified through sensitivity analyses or equivalent methods. The active parameters are generally the coefficients of the Arrhenius law, depicting the behavior of the reaction rate constants k.

$$k = AT^{b}e^{-\frac{Ea}{RT}} \tag{41}$$

An optimization procedure can be focused on A, b, Ea separately or simultaneously. In the case of pressure dependent reactions (see Chapter 2) both k_0 and k_∞ can be optimized, also alone or simultaneously. Figure 43 illustrates how the modification of each Arrhenius law parameter can affect the behavior of k as a function of temperature. Change in these parameters can result in drastic species profiles, ignition delay times or laminar flame speed variations.

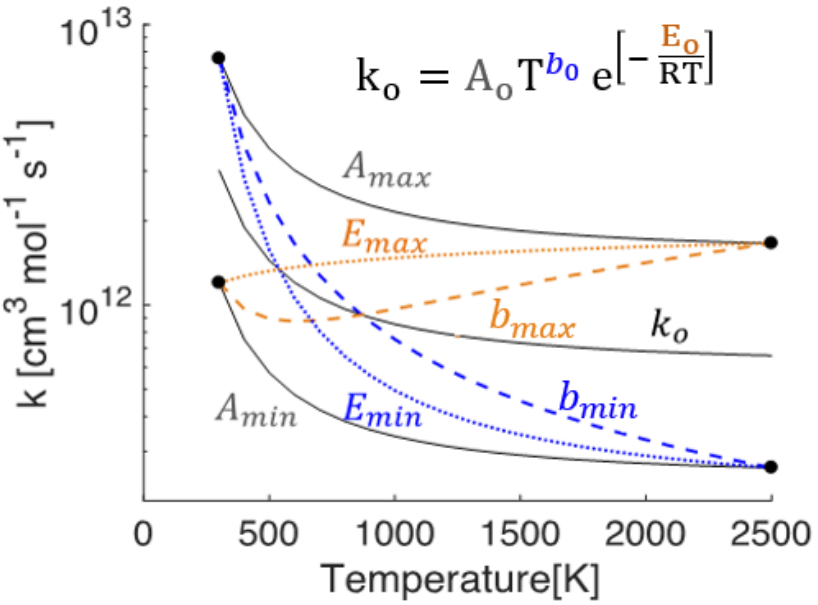

Figure 43: k=f(T) Arrhenius parameters modifications adapted from [140]

Other active parameters can be the third body efficiencies M, dependent on the species and the modified reactions.

In order for the optimization process to stay as physical as possible, the uncertainty on the active parameters needs to be considered when it exists. For example Baulch et al. [141,142] inventoried uncertainties values of rate constants k for a large panel of reactions for given temperature ranges. As for b and Ea parameters, the literature is scarce. As it will be explained in the following sections, the uncertainty on k is usually propagated to the other variables. Generally, the strategy is to target reactions that maximize the product of their sensitivity by the uncertainty on their Arrhenius parameters for the range of experimental targets.

When the number of experimental targets and the studied mechanism is quite small, a manual optimization of the Arrhenius parameter can be considered. However, as soon as the number of targets increases in term of equivalence ratio, pressure, temperature conditions, so will the number of key reactions to tune. Hence an optimization algorithm is necessary to complete the process. Several methods have been developed over time, the main ones being mentioned in this section.

4.2.1 Surrogate models

The use of response surfaces (or surrogate models) with a method called *solution mapping* was first proposed by Frenklach et al. [143] in 1992 in order to optimize a mechanism for methane combustion. Ignition delay times, species concentration profile and laminar flame speeds were used as experimental target. As every optimization procedure, it starts with an identification of key sensitive reactions for the targets. The method then consists in building response surfaces of the objective

function with the help of several computations modifying the pre-exponential factors A and following a design of experiment. Local values of the function are then interpolated in between to build a surrogate model. The same method was applied later to the initial version of the GRI-Mech mechanism [79].

The Method of Uncertainty Minimization using Polynomial Chaos Expansion (MUM-PCE) was then developed by Sheen and Wang in 2011 [144]. It is also based on response surfaces and was used to develop the FFCM1 mechanism [95]. Pre-exponential factors A and some third body efficiencies were modified during the process.

The same year, Turányi et al. [145] proposed a method tuning simultaneously A, b, Ea and third-body efficiencies. The process used a sum-of-squared-error minimization considering both direct rate parameters measurements (i.e. the uncertainty on k) and indirect measurements (ignition delay times, laminar flame speeds). It was used to improve the knowledge of some reaction's Arrhenius parameters. This method was also applied to H_2 combustion mechanisms [146] using surrogate models.

Despite a good efficiency, surrogate-model-based methods have some drawbacks. The addition of b and Ea parameters add a high non-linear behavior. This tends to decrease the response surface accuracy. Indeed, because of the high non-linear nature of Arrhenius laws, the right topology of the response surface presents a lot of local minima and can be very hard to correctly capture. A solution to that problem would be to increase the resolution of the surrogate model, thus drastically increasing the computational cost.

4.2.2 Genetic Algorithms

Hence, another strategy is to use dedicated algorithms that will eventually find the global minimum of the objective function based on information given by previous evaluations of the parameter space (modified parameters X objective function values). These methods would allow to eventually decrease the number of evaluations. Generally, the optimization methodologies can be gradient-based (meaning that the gradient of the parameter space is evaluated to sense the proximity with a local or global minima) or gradient-free. Due to the previously mentioned nonlinear nature of the parameter space induced by Arrhenius laws, gradient-free method are preferred for kinetic mechanisms optimization [147].

One of the most used methods are genetic algorithms (or GA). GA are part of the evolutionary algorithms' family inspired by the theory of evolution. They were first introduced in 1975 [148] to be used for the optimization of nonlinear problems. Polifke et al. [149] used this method in 1998 for a global 3 steps kinetic mechanism optimization in order to match a detailed reference model for lean premixed methane/air flames.

GA is based on the definition of *individuals* (the complete set of Arrhenius parameter of the mechanism to be tuned) composed of *genes* (each individual Arrhenius parameter) as illustrated on Figure 44. A *population* is then defined as a collection of randomly selected individuals.

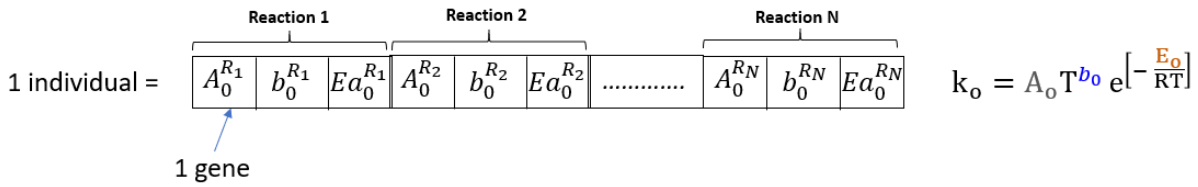

Figure 44: Definition of an individual for a genetic algorithm used for mechanism optimization with N reactions

The optimization process, based on the survival of the fittest individuals, is composed of the following steps:

Ranking of individuals

The first randomly selected population of N_{pop} individuals are ranked according to their objective function corresponding values. The best individuals are the one minimizing the objective function while the other are further away. Once the ranking is performed, a certain number of individuals are selected.

Crossover step

Random couples of individuals are selected among the best previously selected. Each couple, called parents, can exchange each of their genes (i.e. Arrhenius parameters of the same reaction) with a crossover probability p_c that can be tuned. The individuals resulting from this exchange are called children. There are 2 children per parents couples. Figure 45 below illustrates an example of crossover.

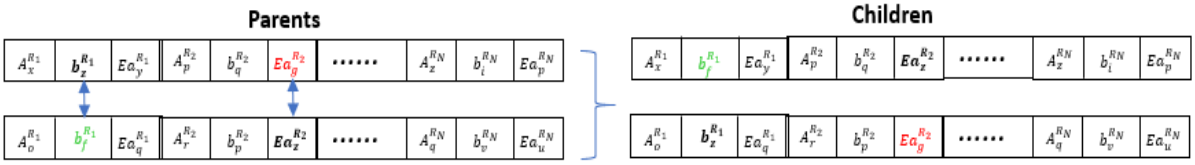

Figure 45: Crossover example

Mutation step

The obtained children can then mutate. Indeed, each of their genes can randomly vary with a probability p_m. Figure 46 below illustrates and example of mutation.

Figure 46: A mutation example

Selection

The last step is selection. The overall new population of individuals is once again ranked according to their objective function value. This new group is composed of a defined number the best individuals plus others randomly picked up in the remaining pool. Hence, a new initial population of N_{pop} individuals is built.

Elliot et al. [147] applied this method for H_2 and CH_4 combustion (with a reduced version of GRI), optimizing pre-exponential factors on experimental data of ignition delay times and species profiles. They also used genetic algorithm for an optimized reduction process [150] and proposed order of magnitude of p_c and p_m parameters. More recently, Matynia et al. [151,152] developed the *Brookesia* reduction and optimization tool based on GA, also focused on the A parameter. The tool allows to use the genetic algorithm method as well as *Particle Swarm* which is another kind of evolutionary algorithm. Performances were tested on a degraded version of the GRI-Mech 3.0 mechanism to try to re-capture the initial behavior of the model.

Another tool using GA (among other techniques) was developed by Fürst et al.[136,153,154]. *OPTISMOKE++* is a versatile code coupled with the *DAKOTA* [155] optimization library to allow the user to choose among different optimization algorithms. The 3 Arrhenius coefficients and third body efficiencies can be tuned to fit experimental data of different nature. The description of the code

structure is given in the following sections as it was chosen to be the tool used for the POLIMI C1-C3 optimization procedure on the OPTIPRIME experimental data.

4.2.3 DIRECT algorithm

As *OPTISMOKE++* proposes alternatives to genetic algorithms, in [136] Fürst highlights the interesting performances of the gradient-free *DIRECT* (Dividing RECtangles) [156] method as a good candidate for kinetic mechanisms optimization.

Figure 47 depicts the iterative process of the method:

- Parameter space (modified parameters X objective function values) is divided into rectangle zones. The objective function is evaluated at the center of each rectangle.
- According to the objective function value, regions are either designated as promising (low values) or non-promising (high values of the function)
- A local optimization method (only one parameter is changed at each iteration) is used in promising regions while a global method (several parameters are changed at each iteration) in non-promising regions
- The process is repeated several times till convergence is reached (the criterion is based on the minimum size a rectangle can take but the user can also stop the code at any time judging by the value of the objective function).

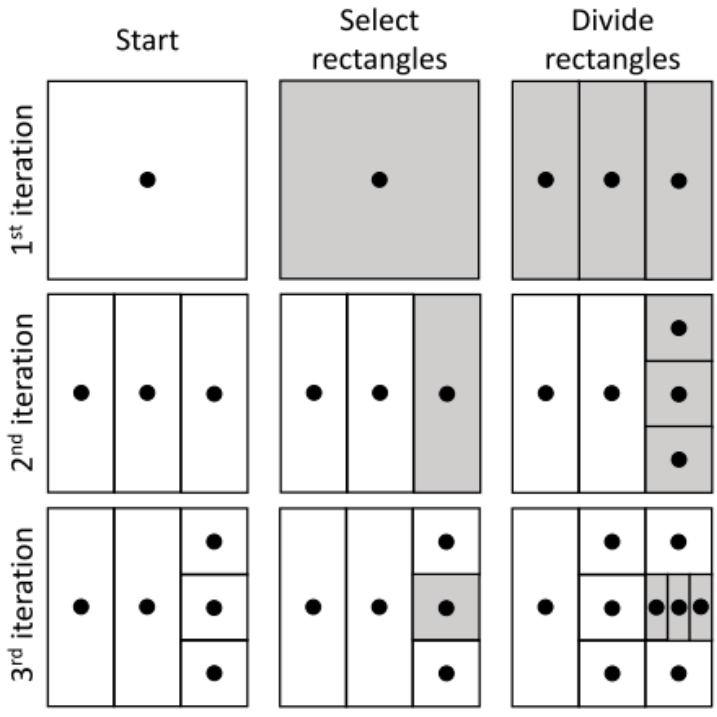

Figure 47: Schematics of the DIRECT optimization method, from [153]

4.3 The OPTISMOKE++ optimization code

As it offers the possibility to use different optimization algorithms and simultaneously tune the three

Arrhenius parameters as well as third-body efficiencies on a wide range of experimental targets (PSR species profiles, ignition delay times and laminar flame speeds), the *OPTISMOKE++ V1* [136] code was chosen for the optimization of the POLIMI C1-C3 mechanism on the OPTIPRIME CH_4/O_2 database. This section details the code structure.

4.3.1 Reaction rate uncertainty propagation

OPTISMOKE++ is capable of dealing with the three Arrhenius coefficients as active parameters. However, as mentioned in the previous section, the uncertainty on these parameters needs to be accounted for in order for the process to remain as physical as possible. Uncertainty on reaction rate constants k are generally well documented for methane chemistry. The data from Baulch et al. [141,142] is used in this work. It gives the uncertainty values fr on reaction rate constants as $\Delta logk = logk \pm fr$. However, to perform an optimization on all the active parameters, a propagation of this uncertainty on A, b and Ea is necessary. To facilitate this process, rate constants expressions are modified in the form of a linearized Arrhenius equation described below. According to [153,154], this re-parametrization minimizes the high correlation between the active parameters and make their computation more cost effective. Indeed, it avoids the use of two expensive functions (power and exponential). Hence the rate constants are rewritten as:

$$\ln(k) = \ln(A) + b\ln(T) - \frac{Ea}{RT} \tag{42}$$

This allows to evaluate k as:

$$k = e^{\ln(A)+b\ln(T)-\frac{Ea}{RT}} \tag{43}$$

Hence *OPTISMOKE++* directly works on the linearized parameters, expressed as α, β and ϵ. The uncertainty factor fr can then be propagated to this linear Arrhenius relation (see [154] for details), giving the following equations (the 0 subscript referring to the reference value):

$$\alpha_0 - ln\left(10^{fr}\right) \leq \alpha \leq \alpha_0 + ln\left(10^{fr}\right) \tag{44}$$

$$\beta_O - \frac{f_r}{log_{10}T} \leq \beta \leq \beta_O + \frac{f_r}{log_{10}T} \tag{45}$$

$$\epsilon_0 - Tf_r\, ln(10) \leq \epsilon \leq \epsilon_0 + Tf_r ln(10) \tag{46}$$

Hence, the code is informed of the authorized boundaries of each of the parameters to be optimized.

4.3.2 Third-body efficiency optimization

The third body efficiencies E_{ff} appearing on some reactions can also be considered as active parameters. They are defined as a coefficient, different for each species, directly proportional to the concentration of the concerned species, hence to the rate constant k. It can be described as the ability to either absorb or give energy during a reaction, thus allowing chemical species breakup or formation. A more complex presentation of third body reactions is proposed in Chapter 2. Their value come from different studies performed for each reaction. Hence, they can vary a lot in the same mechanism or

between mechanisms. E_{ff} generally has very little effect on the laminar flame speed (which is more diffusion controlled) while it tends to have more impact on ignition delay times. In this work, values of $E_{ff_{Ar}}$ and $E_{ff_{He}}$ are supposed correct and only E_{H_2O} and $E_{ff_{CO_2}}$ are optimized. In *OPTISMOKE++* the uncertainty on E_{ff} is defined as follows:

$$\begin{cases} E_{ff_{Max}} = 2\,E_{ff_{Baseline}} \\ E_{ff_{min}} = \dfrac{1}{2} E_{ff_{Baseline}} \end{cases} \tag{47}$$

4.3.3 Pressure dependent reactions optimization

As described in the previous sections, there are different ways to describe a rate constant dependence to pressure. In POLIMI C1-C3, both Troe and PLOG formulations can be encountered. Concerning the first, the k_0 and k_∞ rate constants can be separately or simultaneously optimized the same way the other reactions are. However, the centering function parameters are supposed correct, hence not seen as active parameters. Concerning the PLOG formalism, *OPTISMOKE++* in its first version is not able to deal with their optimization while the second version (which is not open-source yet) proposes solutions [154]. Consequently, if PLOG reactions are treated for the CH_4/O_2 optimization procedure, only the values corresponding to the average pressure of the experimental targets will be considered during the process.

4.3.4 Code structure and workflow

Figure 48 details the workflow of the *OPTISMOKE++* code. The global optimization procedure is described in this section. The code is mainly based on a coupling between the *OPENSMOKE++* solver [157] developed by the POLIMI CRECK team (comparable to CANTERA or CHEMKIN) with the *DAKOTA* [155] library developed by SANDIA.

Main inputs:

The initial kinetic mechanism is provided in *CHEMKIN* format. Then, experimental targets datasets (flame speed S_u , ignition delay times τ_{ign}, species profiles) are given to the code in the form of input files along with their uncertainty values. In parallel, input files for numerical evaluations describing the experimental targets conditions are set up using *OPENSMOKE++*. Hence *OPTISMOKE++* will be able to latter compare numerical results to experimental target values on these points. The main input file contains the list of the reactions to be optimized as well as their respective uncertainties on rate constants coming from the literature. The user can specify which Arrhenius parameters are considered active for each reaction. The file also contains the optimization method to be used (detailed below) and their parameters.

Objective function:

For the first iteration, *OPTISMOKE++* will numerically evaluate the target conditions thanks to *OPENSMOKE++* and then assess the relative difference between the results and the experimental data thanks to an objective function. The objective function is the parameter to minimize: indeed, the smaller it is, the smaller the distance between numerical and experimental points. The code allows the use of two definitions of the objective function: L1 and L2 norm [153]. Curve-Matching based objective

functions are also currently developed for future versions of the code [154]. The function choice is important when optimizing a kinetic mechanism on several kinds of experimental dataset that can be of different nature. Indeed, the user needs to choose an objective function that gives comparable values for all the datasets. Otherwise, the algorithm will first focus on the datasets presenting the maximum values. This of course tends to decrease the efficiency of the optimization process. The objective function chosen for this work is an L2 norm, defined as follows:

$$L_2 = \sum_i^N \frac{1}{N_i} \sum_j^{N_i} \left(\frac{Y_{ij}^{exp} - Y_{ij}^{sim}}{\sigma_{ij}} \right)^2 \tag{48}$$

Y^{exp} being the experimental points while Y^{sim} are the numerical ones computed by *OPENSMOKE++*. N is the total number of datasets and N_i the number of points in the dataset i. The relative difference $Y^{exp} - Y^{sim}$ is weighted by the standard deviation σ in order for the experimental data with larger uncertainties to have a lower importance.

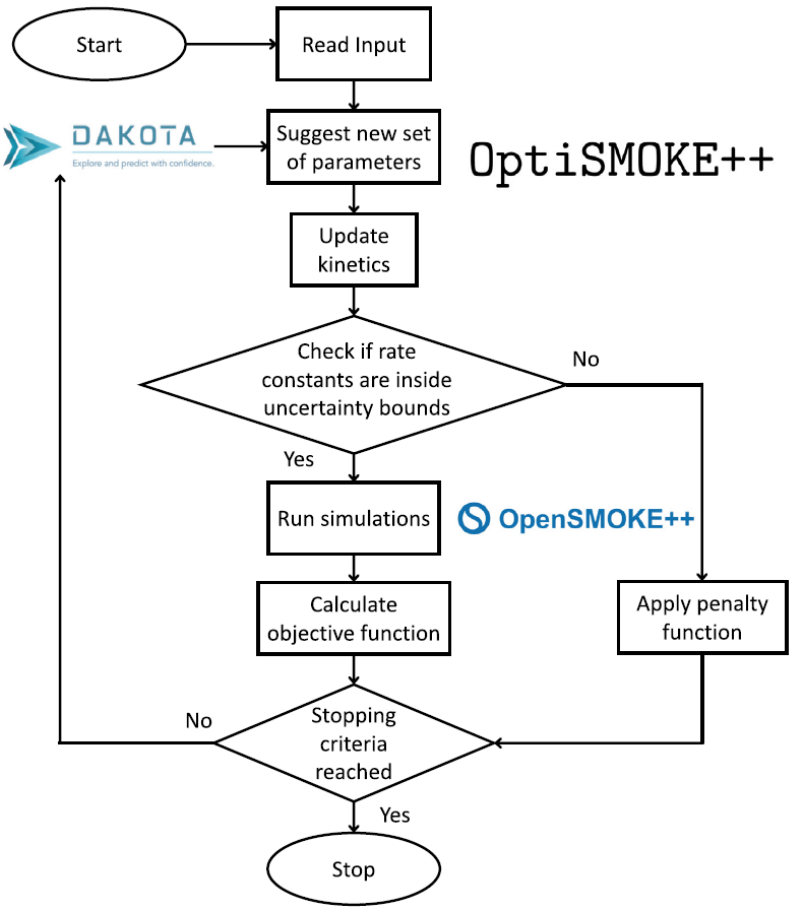

Figure 48: OPTISMOKE++ workflow [136]

Optimization algorithm:

After each run of the optimization algorithm, a new set of kinetic parameters is proposed. As *OPTISMOKE++* is coupled with the *DAKOTA* library, several optimization algorithms are available. As explained in the previous sections, gradient-free methods are preferred. Fürst [136] and Bertolino [154] compared the efficiency of different methods on different dataset (GA, DIRECT, MADS, etc.).

However, it is difficult to draw formal conclusions as each dataset is unique and each method can be parametrized in different ways. After several benchmark tests, and following the conclusions of Fürst, the DIRECT algorithm was preferred for this study.

Penalty function:

After the active parameters update, a check is then performed in order to confirm that they respect the boundaries previously defined. Indeed, because of the non-linear effects induced by the Arrhenius law, a change in the coefficients within their own uncertainty limits does not always guarantee that k satisfies its own uncertainty conditions for the whole temperature range (between 300 and 1500K) [153]. If the rate constant does not go out of bond, the iterative optimization process continues, otherwise a penalty function is applied. The latter artificially increases the objective function values (the order of magnitude is 10^{12} [153]) for kinetics parameters combinations not respecting the imposed boundaries. Hence, the optimizer will not go again in those regions for future iterations, decreasing the overall computation cost.

During the code iterations, the best (i.e. minimum) values of the objective function are recorded. Depending on the nature of the used optimization algorithm a maximum number of iterations (for DIRECT, MADS, etc.) or generations (for GA) can be imposed. The user can monitor the evolution of the objective function over time and can stop the calculation once it has reached a sufficient convergence level. At each iteration, *OPTISMOKE++* generates an optimized kinetic mechanism in *CHEMKIN* format.

4.4 Optimization strategy

In order to optimize POLIMI C1-C3 for CH_4/O_2 conditions at high pressure and temperature, several experimental target datasets need to be considered. Namely laminar flame speeds but also ignition delay times to give the mechanism more versatility. The OPTIPRIME laminar flame speed database for CH_4/O_2 mixtures in extreme conditions acquired for $0.5 \leq \varphi \leq 2.5$ and was presented in the previous chapter. The complementary diluted S_u at high pressure and stoichiometry are used as well since these reactions have been recognized as representative of undiluted conditions. Ignition delay times are extracted from the literature (cf. next sections). Once the pool of target dataset is selected, the sensitive reactions on these conditions need to be identified to serve as inputs for the optimization process.

4.4.1 Flame speed targets

As mentioned above, target flame speed values come from the OPTIPRIME experimental dataset. Since the optimization code will have to evaluate the objective function at each iteration, using the entirety of the S_u traces would lead to an important increase in calculation cost. Indeed, POLIMI C1-C3 is a large mechanism and flame speed convergence can take time. In order to avoid this problem but still match the S_u traces evolutions, only three points per tested conditions will be used. One at the initial pressure and temperature (low point), one at the final P,T conditions (high point) and an intermediary point in between. This brings the S_u dataset target number at 36 points for all the tested conditions.

Moreover, the targets are separated in two groups: effective optimization targets and control targets. The first group consists in the experimental conditions corresponding to CH_4/O_2 mixtures at φ=0.5-1.0-2.0-2.5 and diluted mixtures at stoichiometry (82.5 and 50% diluent in the oxidizing mixture) which allows to cover a wide range of conditions. The other group is used to assess the quality of the optimization process afterwards. Hence, there are in reality 18 S_u targets to be optimized

Figure 49 illustrates the initial situation of the two target groups in terms of relative difference between POLIMI C1-C3 and the experiment. The objective is to match the $\pm$5% uncertainty zone.

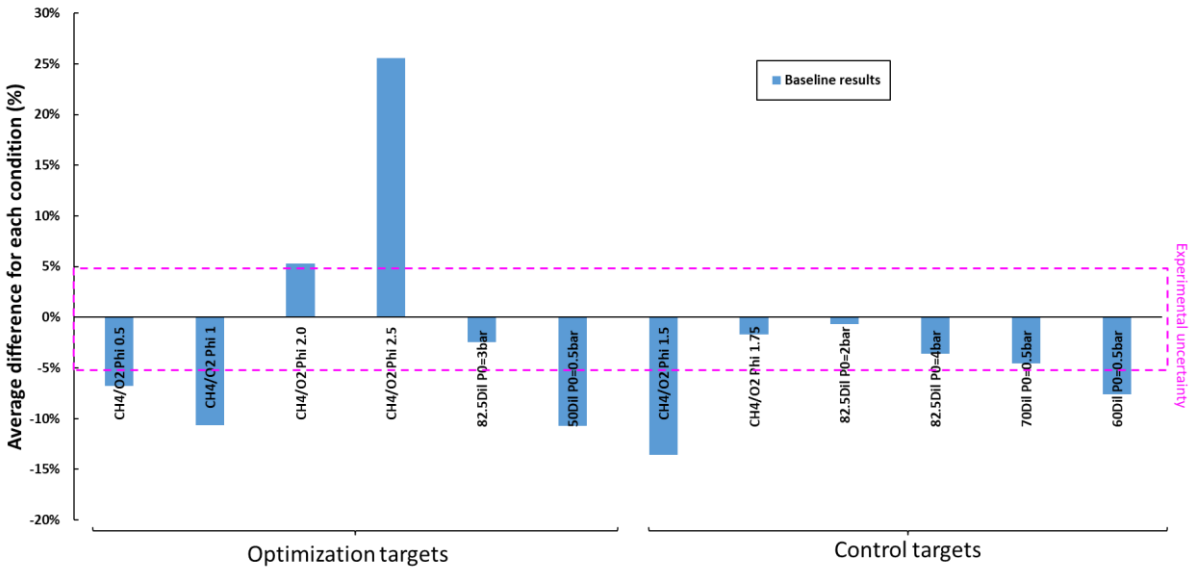

Figure 49: Initial situation of optimization and control targets

4.4.2 Ignition delay time targets

In order to consolidate the validity of the mechanism, auto-ignition delay times from the literature are added to the OPTIPRIME experimental targets. An extensive search shows that the data acquired for the creation of the RAMEC mechanism by Petersen et al.[76,78,80] consists, to the knowledge of the author, of the experimental data with the lowest dilution ratio of the reactive mixture in the literature. Indeed, the dilution percentages are comparable with the one tested with OPTIPRIME. They rank from 66% to 80% in molar mass (or volume) in the oxidizing mixture (or 33% to 77% for the total mixture). Moreover, the panel of tested pressures is quite large (from 41 to 263 bar), as well as the equivalence ratios φ (from 0.4 up to 6.0) covering rich mixtures compatible for example with the PROMETHEUS engine gas generator applications. The conditions tested by Petersen are detailed in Table 8. 5 different mixtures were tested for a total of 12 pressures conditions. For each pressure condition, 3 points are taken: low, intermediate and high temperature. It yields a total of 36 target values. The experimental uncertainty is $\pm$10%. Figure 50 shows the average discrepancies between POLIMI C1-C3 and the experiments for all the tested conditions. None of them initially satisfies the experimental uncertainty.

Mixture	φ	% diluent for the mixture (molar mass)
1	0.4	77.0% Ar
2	3.0	66.7% Ar
3	3.0	66.7% N_2
4	3.0	54.3% Ar
5	3.0	54.3% N_2

Table 8: Conditions tested by Petersen for ignition delay times

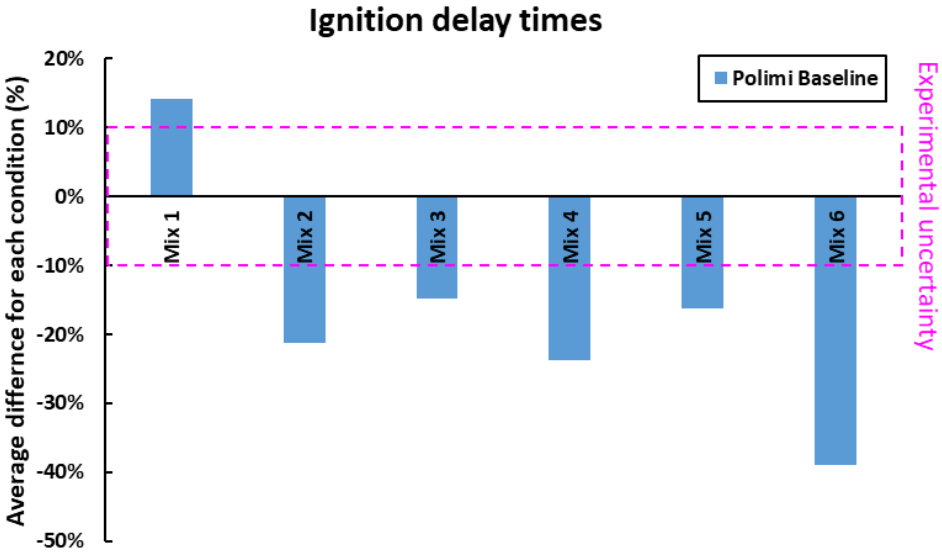

Figure 50: Average discrepancies between numerical and experimental ignition delay times – Petersen targets

Finally, counting the 18 laminar flame speeds experimental targets (CH_4/O_2 mixtures at different φ and the diluted measures at high pressure) as well as 36 ignition delay times from the literature, the total number of constraints for this optimization problem is 54.

4.4.3 Target reactions selection

As mentioned in the beginning of the chapter, different key reactions need to be identified in order to obtain the active parameters required for the optimization. The process is challenging in the sense that the equivalence ratios covered by the chosen experimental targets is broad (from 0.4 to 6 for all types of experiments). This implies that a large number of reactions need to be chosen to give the code enough margin for the process. The previous chapter, and [132] in particular, highlighted sensitivity analyses on laminar flame speed performed for the OPTIPRIME CH_4/O_2 conditions ($0.5 \leq \varphi \leq 2.5$). These analyses allow to identify the main pilot reactions. Their sensitivity varies a lot with φ conditions, some of them being predominant for rich mixtures (for example $CH_3 + H(+M) = CH_4(+M)$ or $H + CH_4 = H_2 + CH_3$) or lean ones (for example $O_2 + HCO = HO_2 + CO$ or $HCO + M = H + CO + M$). As specified before, the pilot reactions selection criterion is based on a combination of both the

sensitivity and the experimental uncertainty values when available. Hence, the process does not take the widely studied $H + O_2 = O + OH$ reaction into account despite its high values of sensitivity. Concerning the high pressure diluted S_u at φ=1, as mentioned in the previous chapter, the pilot reactions are the same as the one highlighted for the CH_4/O_2 data. It is also worth noticing that additional sensitivity analyses show that the key reactions (and their ranking) identified for the pressure conditions explored with OPTIPRIME remains unchanged for higher pressure (up to 100 bar).

The initial optimization attempt was based on 9 pilot reactions only, 2 of them being pressure dependent and described by two Arrhenius laws. For each reaction, A, b and Ea are considered as active parameters. This configuration led to a total 33 active parameters. However, it was not sufficient to match the 54 experimental constraints. Using the sensitivity analysis, the number of pilot reactions chosen was progressively increased to a total of 21 plus 6 third-body efficiencies (on H_2O and CO_2) leading to a total of 78 active parameters (some reactions have duplicate or are pressure dependent so the "real number of reactions" is 24). This combination gave satisfactory results for the flame speed targets but not for the ignition delay times. Indeed, some key reactions, in particular for rich conditions were required. As illustrated on Figure 51, complementary sensitivity analyses were performed for extreme equivalence ratios explored by Petersen et al. [78] in order to identify the additional pilot reactions.

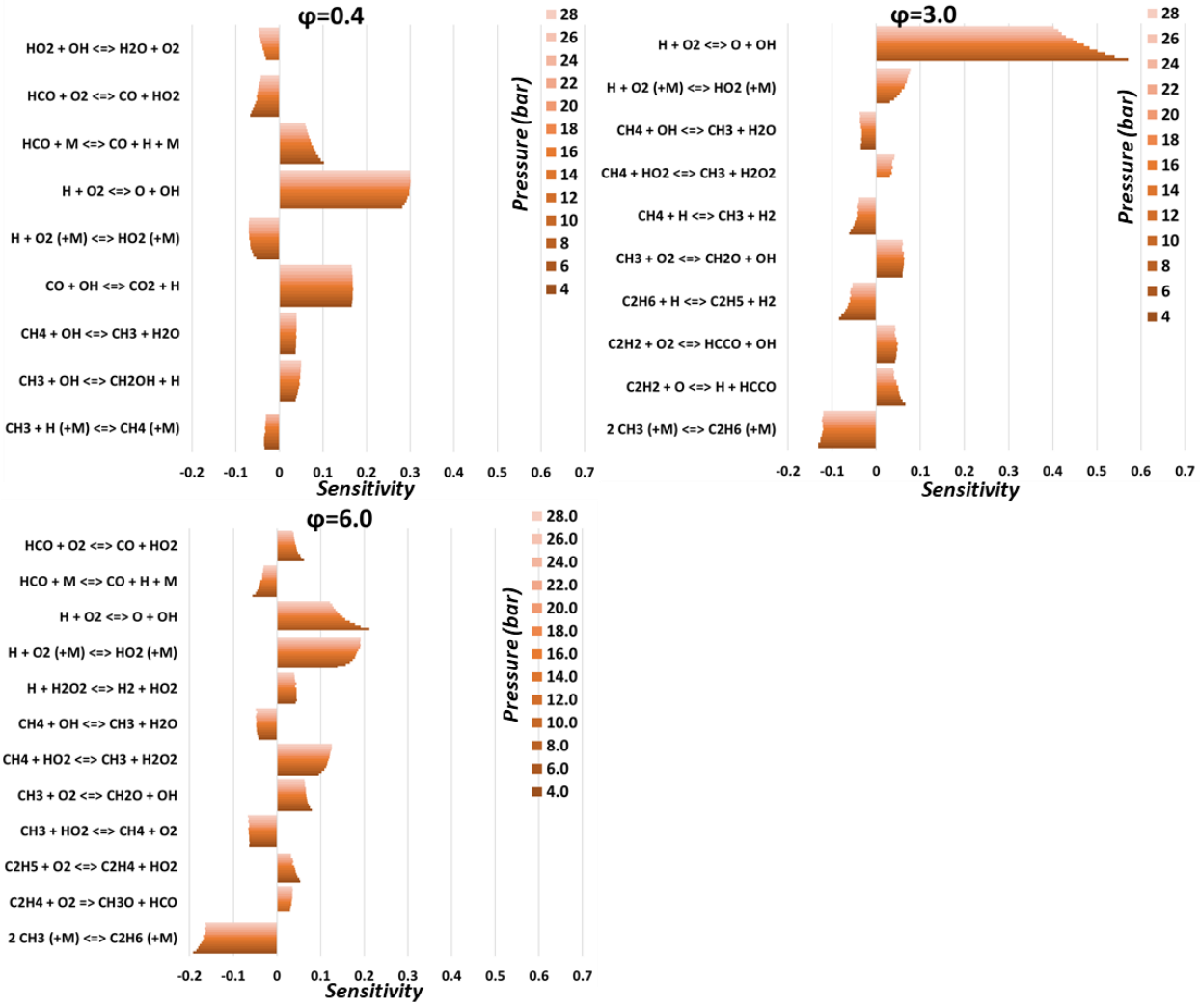

Figure 51: Complementary sensitivity analysis for Petersen conditions

As a consequence, 6 reactions were added (for example $O_2 + C_2H_2 = OH + HCCO$ and $O + C_2H_2 = H + HCCO$) leading to a total of 96 active parameters. The $2CH_3(+M) = C_2H_6(+M)$ reaction, which is non-negligible when it comes to rich mixtures, was already in the second set of parameters to tune.

Table 9 lists all the reactions that were used for the optimization of POLIMI C1-C3 on OPTIPRIME S_u and Petersen ignition delay times. For all the pressure dependent reactions involving a third body, E_{H_2O} and $E_{ff_{CO_2}}$ were optimized. As mentioned before, the PLOG reactions cannot be optimize with the current *OPTISMOKE++* version. Hence, the rate constant at an average pressure of 10 bar was chosen. The final number of active parameters to be optimized simultaneously is 96 against 54 constraints.

Main Action domain	Reaction	Sensitivity	Uncertainty $\frac{\Delta logk}{logk}$
Stoechio	H+CH3(+M)=CH4(+M)	<0	$\pm$0.3 (k_0)
		<0	$\pm$0.3 (k_∞)
Stoechio	H+CH4=H2+CH3	<0	$\pm$0.2
Stoechio	H+HCO=H2+CO	<0	$\pm$0.3
Stoechio	HCO+M=H+CO+M	>0	$\pm$0.2
Stoechio	OH+CH3=H+CH2OH	>0	$\pm$0.5 (PLOG)
Stoechio	OH+CO=H+CO2	>0	$\pm$0.5
		>0	$\pm$0.5 (duplicate)
Rich	2CH3(+M)=C2H6(+M)	<0	$\pm$0.3 (k_0)
		<0	$\pm$0.3 (k_∞)
Rich	H+C2H6=H2+C2H5	<0	$\pm$0.3
Rich	O+CH3=H+CH2O	<0	$\pm$0.1
Rich	2CH3=H+C2H5	>0	$\pm$0.3 (PLOG)
Rich	H+C2H3=H2+C2H2	<0	$\pm$0.3
Rich	OH+CH4=H2O+CH3	<0	$\pm$0.3
Rich	H+O2(+M)=HO2(+M)	>0	$\pm$0.3 (k_0)
	H+O2(+M)=HO2(+M)	>0	$\pm$0.5 (k_∞)
Rich	HO2+CH3=OH+CH3O	>0	$\pm$0.5
Rich	O2+CH3=OH+CH2O	>0	$\pm$0.3

Main Action domain	Reaction	Sensitivity	Uncertainty $\frac{\Delta logk}{logk}$
Stoechio	H2+O=H+OH	>0	$\pm$0.2
Stoechio	H2+OH=H+H2O	>0	$\pm$0.3
Stoechio	H+HO2=H2+O2	<0	$\pm$0.3
Stoechio	O+OH+M=HO2+M	>0	$\pm$0.3
Stoechio	H+CH2O=H2+HCO	>0	$\pm$0.5
Rich	O + C2H2=H + HCCO	>0	$\pm$0.4
Rich	O2 + C2H2=OH + HCCO	>0	$\pm$0.4
Rich	HO2 + CH4=H2O2 + CH3	>0	$\pm$0.4
Rich	HO2 + CH3=O2 + CH4	>0	$\pm$0.3
Rich	O2 + C2H5=HO2 + C2H4	<0	$\pm$0.4
Lean	O2 + HCO=HO2 + CO	<0	$\pm$0.3

Table 9: Reactions tuned for the optimization process

4.4.4 POLIMI C1-C3 reduction

One of the particularities of the current *OPTISMOKE++* version is that numerical calculations (flame speed or ignition delay times) does not support multi-threading. This feature is currently being developed by POLIMI CRECK/ULB team. In the meantime, calculations with the POLIMI C1-C3 mechanism are quite heavy for the flame speeds. Indeed, the mechanism contains a lot of species and reactions. This slows down the overall optimization process in a non-negligible way.

In order to overcome the problem, the POLIMI C1-C3 mechanism was reduced using the ARCANE [65,158] code before the optimization process. ARCANE (for *Analytical Reduction of Chemistry: Automatic, Nice and Efficient*) is a python tool developed at CERFACS for chemical mechanism reduction working with CANTERA. Reduction is useful for 3D CFD simulations with detailed chemistry. The methods used during the automatic reduction steps are explained in details in the literature by Pepiot et al. [159]. The process is described in a simplified way below:

- The detailed starting mechanism is the main input. Then, reduction targets and their pressure, temperature and φ conditions are given. Those are the conditions in which the reduced

mechanism will be used. The reduction targets values will be computed with CANTERA for the detailed mechanism and for each reduced mechanism at each step.

- The reduction step is fully automated and consists in the following of 3 different methods: DRGEP (*Direct Relation Graph with Error Propagation*) which allows to remove some species and reactions.
  Lumping, which allows to find and regroup similar species inside the same mechanism.
  QSS species determination, which identifies species which concentration does not vary much over time allowing to apply the *Quasi Steady State* hypothesis (these species are no longer transported and their concentration is solved analytically).

- At each reduction step, the current reduced mechanism is recorded and the reduction targets evaluated. Once the difference between the target values from the reduced mechanism and the ones from the detailed one exceeds a threshold value (i.e. maximum error allowed), the reduction is stopped.

- The last reduced scheme, including QSS species, is called an ARC (*Analytically Reduced Scheme*). If the QSS species part is skipped, the mechanism is called Skeletal.

The process is summarized by Figure 52.

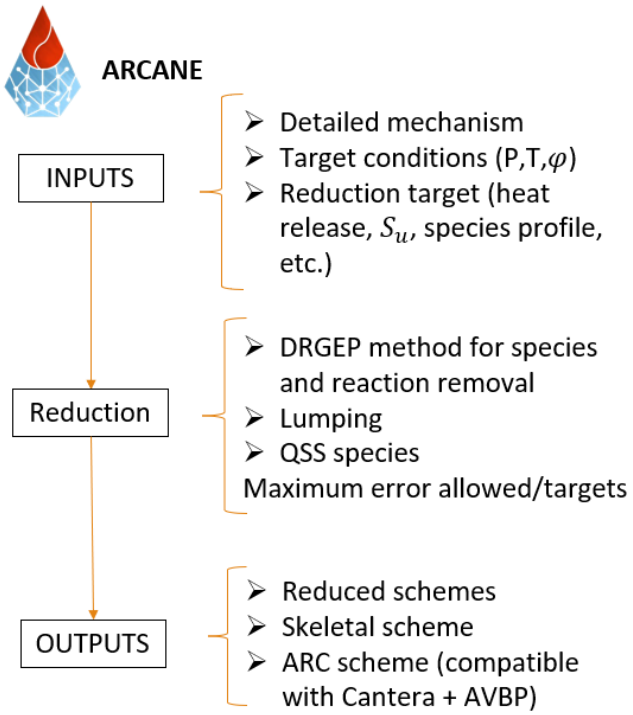

Figure 52: ARCANE flowchart (simplified)

For the pre-optimization reduction process, the QSS step was skipped as the aim is to obtain a skeletal mechanism. The reduction targets (on both S_u and ignition delay times) were chosen identical to the optimization ones with a 5% tolerance. Hence the reduced mechanism has the same properties as the reference one on the optimization targets. This behavior is checked at each step by *ARCANE*. The

obtained mechanism, called POLIMI C1-C3 RED, is much more compact than the original, significantly decreasing the computational cost of the optimization process.

	POLIMI C1-C3	POLIMI C1-C3 RED
#Species	114	30
#Reactions	1999	128

Figure 53: POLIMI C1-C3 reduction results

All the reactions identified as important and listed in Table 9 are still part of POLIMI C1-C3 RED after the reduction process. Sensitivity analyses show that their ranking in terms of absolute value is not affected by the reduction. This emphasizes the importance of their roles as the DRGEP procedure recognized them as significant to describe the mechanism behavior on the optimization/reduction targets. Post reduction sensitivity analysis show similar results to the original POLIMI C1-C3 mechanism. Hence, this legitimizes the optimization process on the reduced mechanism.

4.5 Optimization results

As mentioned in the previous sections, the genetic algorithm approach was first attempted. The GA parameters (probabilities of cross-over and mutation, population size, etc.) were chosen following the recommendations of [147,154] . However, despite several attempts for which the values were tuned, the algorithm remained blocked on a local minimum (cf. results in appendix). This solution does satisfy only a small part of all the experimental targets panel. Hence another method was evaluated in parallel. Following the recommendations of [136], the DIRECT algorithm described in the previous section was used. The values chosen for the parameters are described in Table 10.

Parameter	Value
Max iterations	10 000
Max function evaluations	10 000
Convergence tolerance	1e-8
Solution Target	1e-6
Seed	1000

Table 10: used parameters for the DIRECT algorithm

The maximum number of iterations is specific to the method used for the computation. It reflects the number of optimization loops conducted and considers the encountered penalties. Whereas the number of function evaluation exactly describes the number of evaluations of the objective function. It is important to emphasize that the number of maximum iterations/evaluations is strongly method

dependent. Indeed, for example the GA algorithm tends to have a more random aspect than DIRECT, hence giving more often parameters that end in penalties[153]. This must be anticipated when setting the optimization calculation. The solution target parameter specifies the objective function value for which the calculation is stopped if the tolerance is not reached before. The seed number guarantees that a stochastic optimization is repeatable [156]: for two identical studies, if the same seed is used, the same results will be generated.

The faster convergence of the DIRECT method compared to the GA method is highlighted by Fürst in [153]. As mentioned before, the GA keeps a slight random nature at each new generation while the DIRECT method determines the promising regions of the parameter space more efficiently. Non-promising regions are generally identified for parameters that have a non-negligible impact on k like the temperature exponent b or Ea. Indeed, a modification of these variables leads to an important k variation, potentially out of the imposed boundaries. It leads to a non-promising zone which will be less thoroughly explored, finally leading to a generally faster convergence. Instead, the more random nature of GA statistically ends with more combinations involving b and Ea that do not violate the uncertainties on k. Hence, an optimization with the DIRECT method will far less suggest changes in b and Ea than with a genetic algorithm.

The optimization calculations were performed on a single core of an Intel(R) Xeon(R) Gold 5118 CPU. Figure 54 shows the evolution of the objective function over its number of evaluations for the DIRECT method (curve labelled as Reference fr) parametrized as detailed in Table 10. However, after a consequent 1253 objective function evaluations during the 20 days run, the results are not fully satisfactory. Indeed, some S_u and ignition delay times are still far from the targeted experimental uncertainty zone. A solution could be to add supplementary reactions to increase the number of free parameters, but it would also increase the complexity of the parameter space topology, leading to a longer computation time. Another approach is to let the optimizer freer by artificially increasing the $fr = \Delta k/k$ uncertainty by a factor of 2. Once the optimization is performed, a thorough check on all the Arrhenius parameters of the modified reactions is performed. The behavior of $k = f(T)$ is evaluated in details for all reactions by comparing it to other data from the literature. If its behavior is still found to be aberrant, it is then manually corrected. The evolution of the objective function for this method is also illustrated on Figure 54 (curve labelled as Reference fr x2). The computation duration was 11 days.

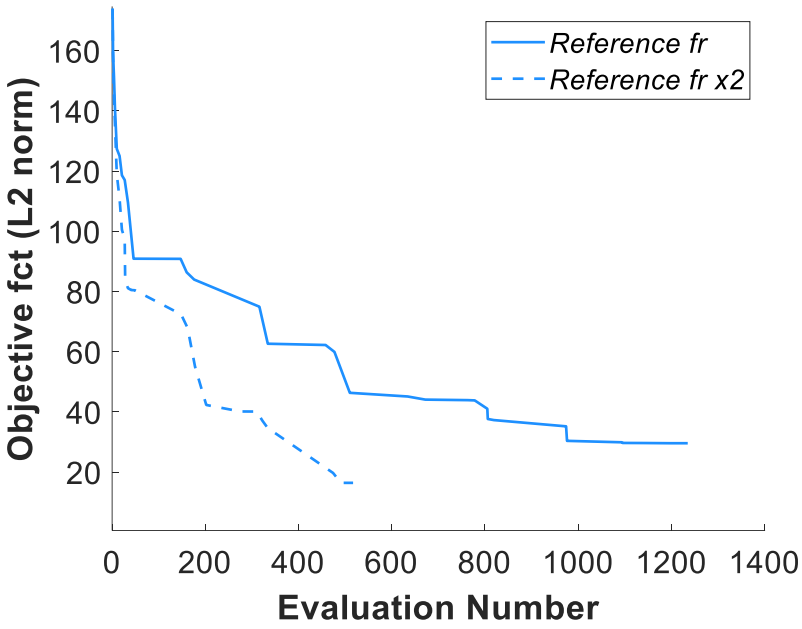

Figure 54: Evolution of the objective function with the DIRECT method

An evaluation of the objective function takes about the same time for the reference and doubled uncertainties cases. Indeed, since the experimental targets are the same for the two cases and that the S_u computational time is important, the DIRECT algorithm execution time is negligible. Finally, the final objective function value reached by the Reference fr x2 case is 1.8 times smaller than fr (respectively 16.43 and 29.59) for 2.38 times less evaluations (respectively 517 against 1235). It was checked that after evaluation number 517 the objective function value of the Reference fr x2 case do not vary anymore.

Figure 60 allow to directly appreciate the relative difference between the reference an optimized parameters. As expected, the reactions for which the flame speed is sensitive for rich mixtures were more modified, which is coherent with the observations made from the experimental versus numerical results. The OPTISMOKE++ code also mainly focused on the pre-exponential factor A rather than the temperature exponent b or the activation energy Ea (some of which were modified). The checking of the rate constants behavior before and after the optimization sometimes allow to put Baulch's uncertainties results [141,142] into perspective. This is for example the case with the methane recombination reaction $CH_3 + H(+M) = CH_4(+M)$ for which the A_0 parameter was modified more than the initial prescribed $\Delta k/k$ (cf. table at the end of the chapter). When plotting $k = f(T)$ from the original and optimized Reference fr x2 mechanism (labelled here as POLIMI C1-C3 Opti) versus other data from the literature, the optimized rate constant behavior does not seem aberrant (cf. Figure 55). Hence it is kept as it is.

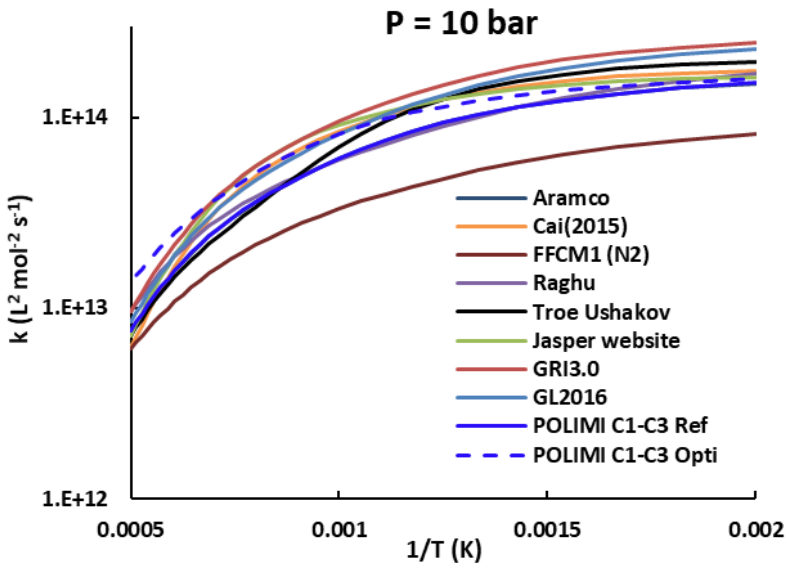

Figure 55: rate constant of $CH_3 + H(+M) = CH_4(+M)$ at 10 bar – different studies and ref/optim POLIMI C1-C3 mechanism

This checking is performed for every optimized reaction. Hence, at the end only 3 reaction rate constants required a manual post-optimization correction. The k of $OH + CH_4 = H_2O + CH_3$ was switched back to its POLIMI C1-C3 reference value, the optimized k of $CH_3 + OH = CH_2OH + H$ was decreased by half and was increased for $2CH_3(+M) = C_2H_6(+M)$. After these last modifications, the optimization process is considered complete. It is also interesting to note that 4 reactions were not modified at the final state of the optimization process. Indeed, the parameters of $CO + OH = CO2 + H, H + HO_2 = H_2 + O_2, CH_2O + H = H_2 + HCO$ and $CH_4 + OH = CH_3 + H_2O$ were left untouched. As the number of free parameters of the optimization process is higher than the number of constraint the solution mechanism is not unique, hence it does not mean that the original definitions of those rate constants are natively compatible with the description of methane oxycombustion at high pressure and temperature. The Arrhenius parameter values of the reference and optimized mechanism are listed in the Table 11 at the end of this chapter.

4.5.1 Flame speed results

Figure 56 illustrates the average relative difference between the numerical S_u and the experimental targets for the initial POLIMI C1-C3 mechanism and the optimized one (POLIMI C1-C3 Opti). The two target groups (optimization and control targets) are represented.

The majority of the average gaps were decreased inside the experimental uncertainty zone of $\pm$5%. Some conditions remain above, like CH_4/O_2 at φ=0.5 (optimization target), CH_4/O_2 at φ=1.5 and 82.5% diluent at stoichiometry (control targets). However, these average gaps are still acceptable. Finally, the lean condition is the only optimization target outside the experimental uncertainty range whereas the behavior of the others was greatly improved (in particular the rich conditions CH_4/O_2 at φ=2.5). Lean conditions are particularly difficult to optimize for CH_4/O_2 mixtures since there is not a lot of negative sensitivity key reactions specific to these mixture reactions. Indeed, in this specific case the numerical S_u needed to be decreased and most of the reactions action domains are quite broad. Moreover, the behavior of the control targets was not affected too much by the optimization process,

which can be taken as a sign of good optimization.

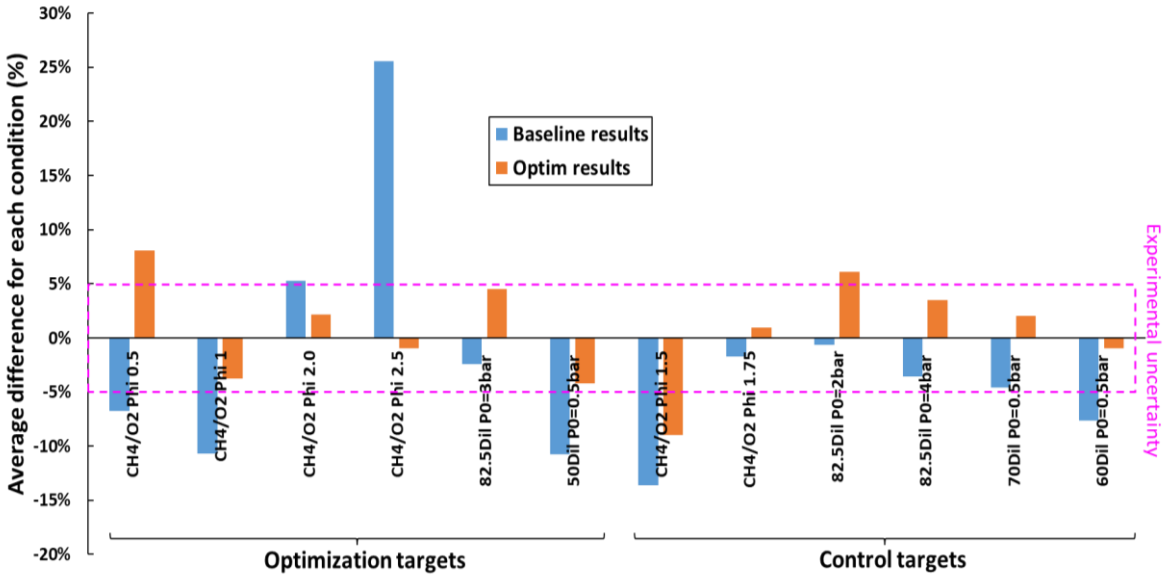

Figure 56: Optimization results on flame speed

Figure 57 illustrates as an example some of the targets in terms of flame speed evolution as a function of pressure for optimization target. It allows to check that the process respects the S_u trend, which is not visible on the average plots. The entire results are displayed in the appendix.

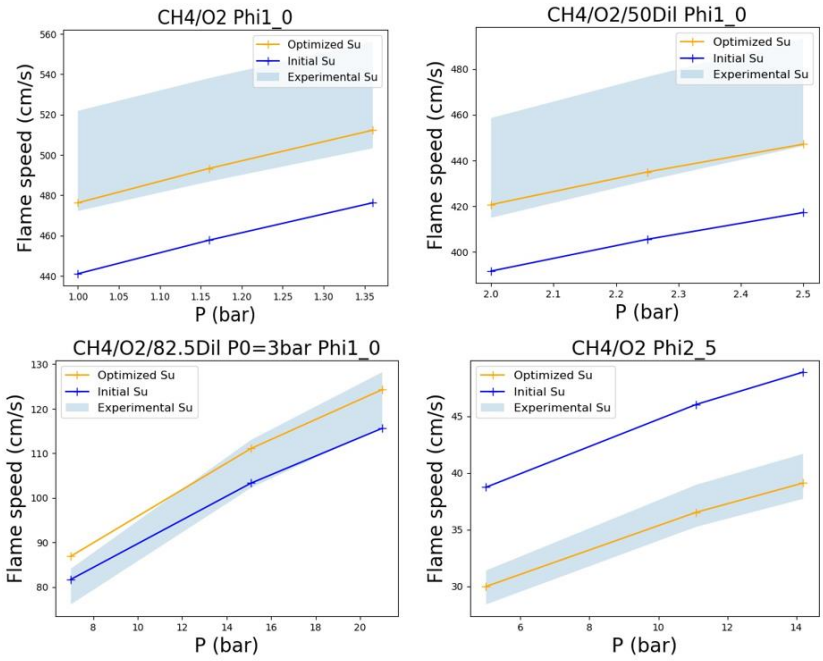

Figure 57: $S_u = f(P)$ optimization results at φ=1(pure CH_4/O_2, 50% diluent, 82.5% diluent) and φ=2.5 (pure CH_4/O_2)

4.5.2 Ignition delay time results

Ignition delay times optimization was a success as, on average, the discrepancy between the numerical and reference experimental data was reduced in the ±10% uncertainty domain as illustrated on Figure 58. The majority of the conditions (mix 2 to 5) concerns rich mixtures.

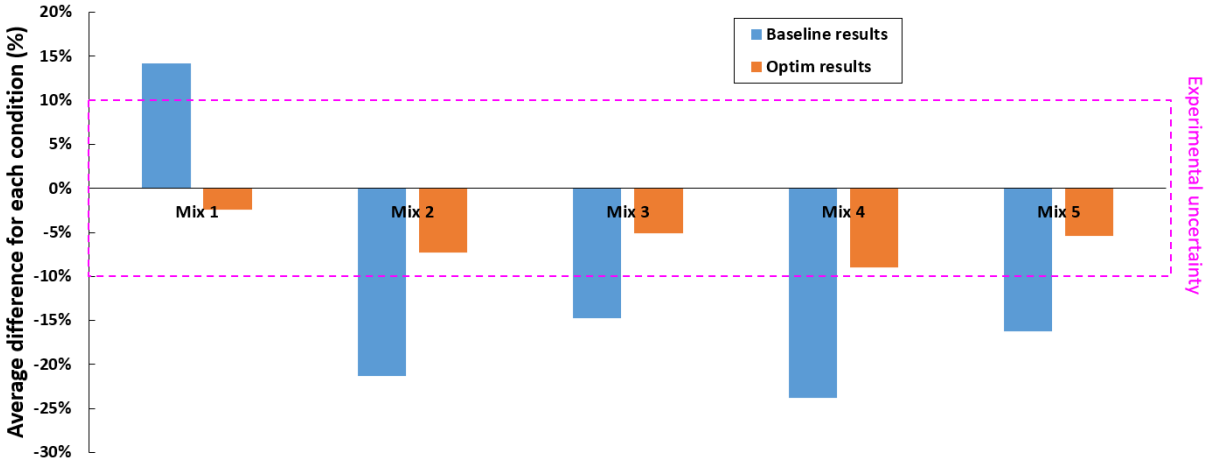

Figure 58: Optimization results on ignition delay times from Petersen et al.

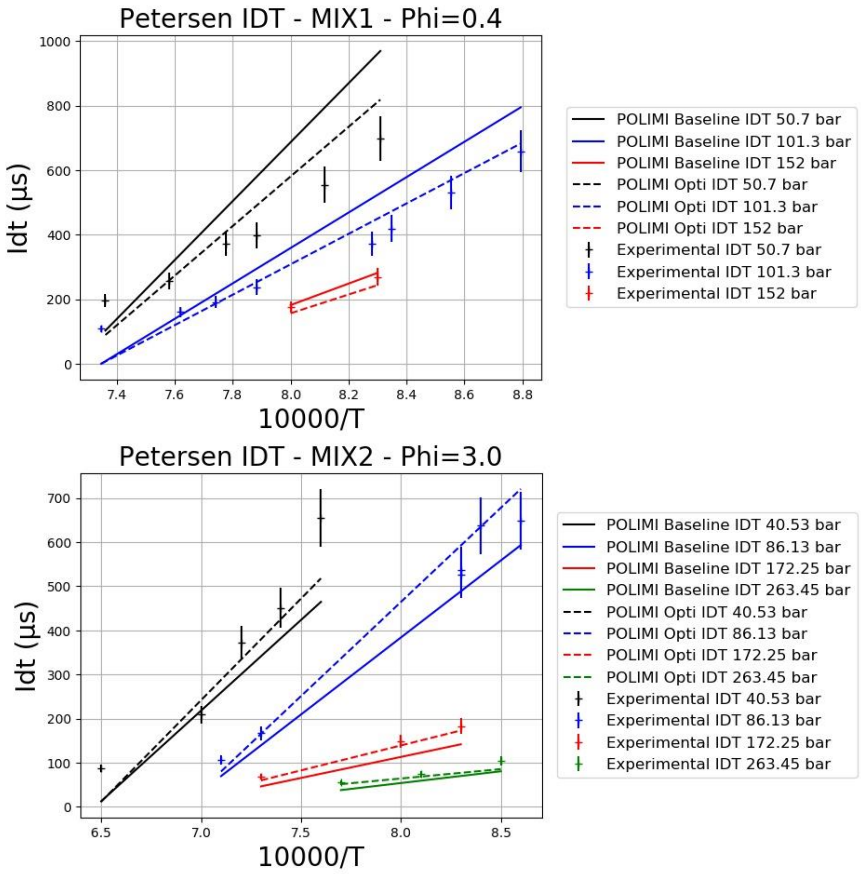

Figure 59: Examples of the Petersen et al. ignition delay times targets as a function of T

Once again, the average plots do not allow to confirm the full correct behavior of the ignition delay times as a function of temperature as errors can compensate. Hence, some results are presented on

Figure 59 while the full panel is displayed in the appendix, allowing to confirm the overall good behavior of the optimized mechanism. Same as for S_u, fitting for lean conditions is more difficult than for rich ones.

Finally, the global process described in this chapter yields a 29 species and 128 reactions mechanism, derived from POLIMI C1-C3 and fully optimized on high pressure and temperature CH_4/O_2 flame speed targets from the OPTIPRIME database as well as ignition delay times from the literature. This POLIMI C1-C3 Opti mechanism can be used for 0 or 1D computations with CANTERA like solvers. It is also possible to use it for 3D CFD computation of rocket engines configurations via another reduction step on targets representative of the studied case. This aspect is developed in the next chapter.

Table 11 shows all the values of the Arrhenius parameters (reference and optimized) of the modified reactions. A unit depends on the reaction order, b has no unit and Ea is in $cal\ mol^{-1}$.

Reaction	Parameter	Reference values	Optim values
$\boldsymbol{CH_3 + H(+M) <=> CH_4(+M)}$	A_0	2.48E+33	6.23E+33
	b_0	-4.76	-4.76
	Ea_0	2440	2440
	A_∞	1.27E+16	1.27E+16
	b_∞	-0.63	-0.63
	Ea_∞	383	383
$\boldsymbol{CH_4 + H <=> CH_3 + H_2}$	A	6.14E+05	1.13E+06
	b	2.5	2.5
	Ea	9587	10400.38
$\boldsymbol{H + HCO <=> CO + H_2}$	A	7.34E+13	7.34E+13
	b	0	0
	Ea	0	0
$\boldsymbol{HCO + M <=> CO + H + M}$	A	5.70E+11	1.43E+12
	b	0.66	0.66
	Ea	14870	14870
$\boldsymbol{CO + OH <=> CO2 + H}$	A	7.02E+04	7.02E+04
	b	2.053	2.053

	Ea	-355.7	-355.7
$\boldsymbol{CO + OH <=> CO_2 + H}$	A	5.76E+12	5.76E+12
	b	-0.664	-0.664
	Ea	331.8	331.8
$\boldsymbol{2CH_3(+M) <=> C_2H_6(+M)}$	A_0	8.05E+31	1.28E+32
	b_0	-3.75	-3.661
	Ea_0	981.6	1072
	A_∞	2.28E+15	4.54E+15
	b_∞	-0.69	-0.69
	Ea_∞	174.9	174.9
$\boldsymbol{C_2H_6 + H <=> C_2H_5 + H_2}$	A	1.15E+08	4.50E+08
	b	1.9	1.9
	Ea	7530	7530
$\boldsymbol{CH_3 + OH <=> H + CH_2OH}$	A	1.53E+13	4.40E+13
	b	0.134	0.134
	Ea	5641	5641
$\boldsymbol{CH_3 + O <=> CH_2O + H}$	A	5.54E+13	7.53E+13
	b	0.05	0.05
	Ea	-136	-136
$\boldsymbol{2CH_3 <=> C_2H_5 + H}$	A	2.15E+10	5.40E+10
	b	0.885	0.885
	Ea	13532.5	13532.5
$\boldsymbol{C_2H_3 + H <=> C_2H_2 + H_2}$	A	9.64E+13	3.84E+13
	b	0	0
	Ea	0	0
$\boldsymbol{CH_4 + OH <=> CH_3 + H_2O}$	A	5.83E+04	5.83E+04
	b	2.6	2.6
	Ea	2190	2190
$\boldsymbol{H + O_2(+M) <=> HO_2(+M)}$	A_0	1.74E+19	1.74E+19
	b_0	-1.23	-1.23

	Ea_0	0	0
	A_∞	4.65E+12	1.00E+12
	b_∞	0.44	0.44
	Ea_∞	0	0
$\boldsymbol{CH_3 + HO_2 <=> CH_3O + OH}$	A	1.00E+12	2.15E+11
	b	0.269	0.269
	Ea	-687.5	-687.5
$\boldsymbol{CH_3 + O_2 <=> CH_2O + OH}$	A	2.64E+00	6.63E+00
	b	3.283	3.283
	Ea	8105	8105
$\boldsymbol{H_2 + O <=> H + OH}$	A	5.08E+04	9.39E+04
	b	2.67	2.67
	Ea	6292	6292
$\boldsymbol{H_2 + OH <=> H + H_2O}$	A	4.38E+13	4.38E+13
	b	0	0
	Ea	15286	6990
$\boldsymbol{H + HO_2 <=> H_2 + O_2}$	A	1.14E+10	1.14E+10
	b	1.083	1.083
	Ea	553.78	553.78
$\boldsymbol{O + OH + M <=> HO_2 + M}$	A	1.00E+16	3.98E+15
	b	0	0
	Ea	0	0
$\boldsymbol{CH_2O + H <=> H_2 + HCO}$	A	5.74E+07	5.74E+07
	b	1.9	1.9
	Ea	2740	2740
$\boldsymbol{O + C_2H_2 <=> H + HCCO}$	A	2.96E+09	1.96E+09
	b	1.28	1.221
	Ea	2472	2562.38
$\boldsymbol{O_2 + C_2H_2 <=> OH + HCCO}$	A	2.00E+07	8.24E+06
	b	1.5	1.5

	Ea	30000	30000
$HO_2 + CH_4 <=> H_2O_2 + CH_3$	A	1.13E+01	2.74E+01
	b	3.74	3.74
	Ea	21010	21010
$HO_2 + CH_3 <=> O_2 + CH_4$	A	1.16E+05	5.96E+04
	b	2.23	2.23
	Ea	-3022	-3022
$O_2 + C_2H_5 <=> HO_2 + C_2H_4$	A	7.56E+14	5.76E+14
	b	-1.01	-1.069
	Ea	4749	4387.5
$O_2 + HCO <=> HO_2 + CO$	A	7.58E+12	3.90E+12
	b	0	0
	Ea	410	410

Table 11: List of the active parameters before and after the optimization process

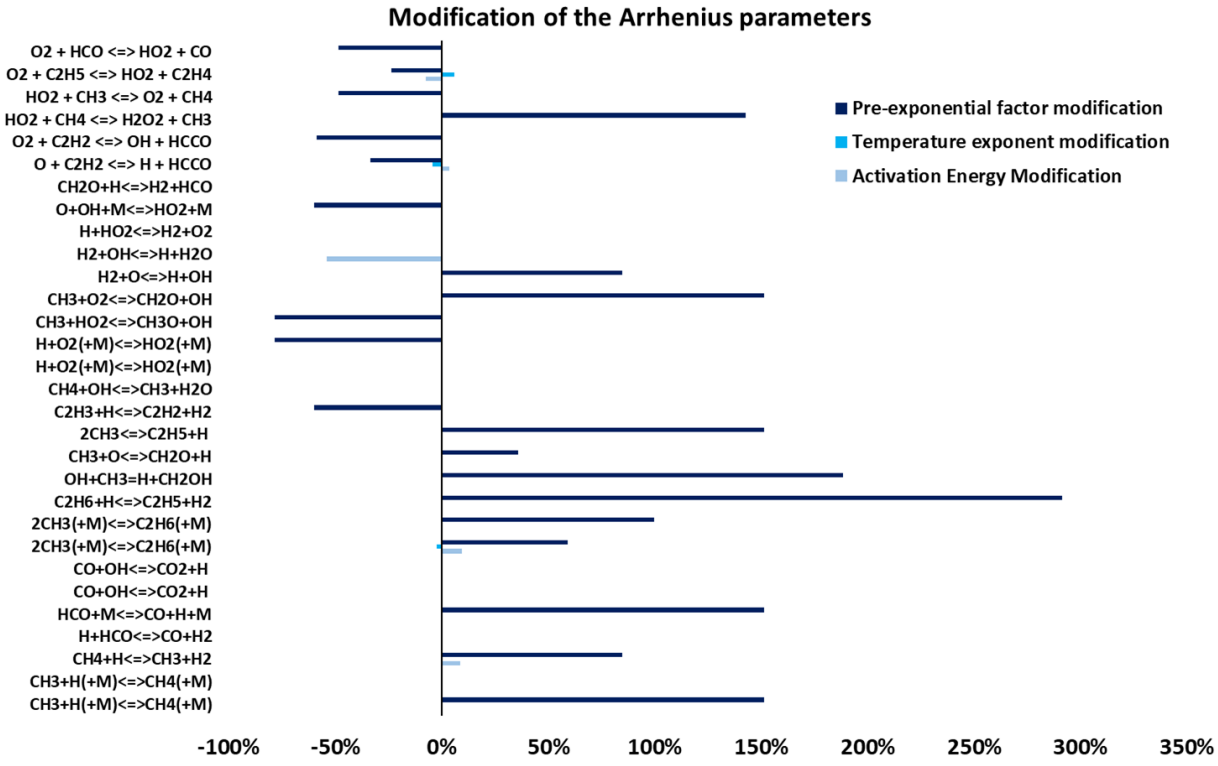

Figure 60: Modification of Arrhenius parameters of POLIMI during the optimization process

Chapter 5

Application – the REST HF-10 case

The previous chapters described the process used to obtain a kinetic mechanism able to describe methane oxycombustion in extreme pressure and temperature conditions. A benchmark study on the premixed flame speed database acquired with OPTIPRIME in CH_4/O_2 conditions led to the selection of POLIMI C1-C3 as a good starting point for optimization [132]. In order to reduce the computational cost of the optimization process, the mechanism was then reduced with the ARCANE tool on a database of experimental target points composed of the OPTIPRIME flame speeds and ignition delay times from the literature. The process ensures that the reduced POLIMI C1-C3 has the same behavior than the reference detailed mechanism on the target points. Key reactions to tune, previously identified through sensitivity analyses remain present in the reduced model. The latter was then optimized on the experimental database using the OPTISMOKE++ code, giving satisfactory results. The whole process hence leads to a POLIMI C1-C3 Opti of 30 species and 128 reactions mechanism tailored for CH_4/O_2 extreme conditions.

It is now possible to use the mechanism for CFD LES calculations representative of rocket engines configurations. Hence, the optimized mechanism can be reduced again in the form of an ARC mechanism, this time on targets representative of the chosen application case. This means that a new reduction process of POLIMI C1-C3 Opti is necessary for each new LES applications. Figure 61 describes the flow chart of the reduction/optimization procedure of POLIMI C1-C3 leading to a LES-compatible ARC mechanism. CERFACS' AVBP solver is used for the LES computations.

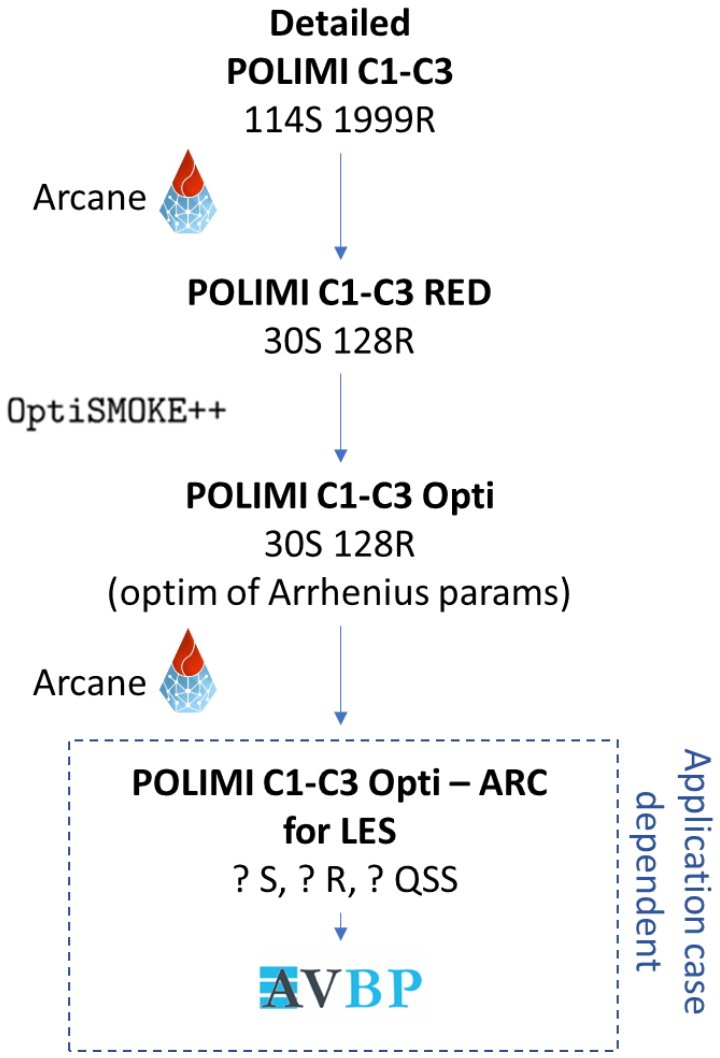

Figure 61: Flowchart of the reduction/optimization procedure

5.1 Large Eddy Simulation (LES)

5.1.1 CFD and turbulence modelling

In order to numerically reproduce the phenomena at stake in a rocket engine (or any other studied geometry) Computational Fluid Dynamics (CFD) is used. CFD is nowadays widely used in the industry to facilitate the design of parts and thus avoid expensive tests. It is also extensively used by research laboratories for model development or for example high-fidelity simulations to investigate a particular physical phenomenon. The method consists in discretizing the geometry with a mesh and solve the Navier-Stokes equations that describe the flow behavior. When performing these simulations, the main challenge is to describe turbulence. Indeed, this is a random and unsteady 3D phenomenon typically present in rocket engines where the flow exhibits high Reynolds numbers (10^4 to 10^7) [23]. The main issue is that turbulence covers a wide range of scales, from large eddies structures (the integral length scale noted l_t) to the smallest (the Kolmogorov scale noted η_κ). Hence, resolving all the turbulent scales is cost prohibitive. To tackle the issue, several methods are available:

- **Direct Numerical Simulation (DNS)**
  DNS consists in solving all the turbulent structures, from the integral length down to the Kolmogorov scale. As the latter is generally very small, a high level of discretization, hence a high computational cost is required. Consequently, this method cannot be used for calculations involving complex industrial geometries. Therefore, the method is for the moment mainly used by research laboratories working on fundamental phenomena. As mentioned before, DNS were already used to describe CH_4/O_2 combustion at small scale [83,160].

- **Large Eddy Simulation (LES)**
  LES consists in solving only part of the turbulent structures to optimize the computational costs while maintaining an accurate description of the flow. The result is obtained by filtering the Navier-Stokes equations. The main idea is to resolve the largest eddies (which are independently highly geometry dependent) while the smallest ones (having a more similar shape and behavior) are described with a sub-grid scale model. This allows to avoid the use of a heavily refined mesh. Hence it is still possible to describe unsteady phenomena in a detailed way which is interesting as it allows to capture the combustion-turbulence interaction. LES is widely used by researchers and is becoming more and more affordable for the industry. This is the method used in this work to test the methane oxycombustion mechanism on a rocket engine combustion chamber geometry (see next sections).

- **Reynolds Averaged Navier-Stokes (RANS)**
  RANS simulations are the most cost-effective CFD calculation methods. It consists of averaging the Navier-Stokes equations with the flow variables described as the sum of a mean and fluctuating component. This leads to a non-linear term known as the Reynolds stress tensor, requiring to be modelled in order to close the system of equations. The model (called "turbulence model") chosen for closure, accounts for the effect of turbulence on the mean flow. Hence, in RANS simulations all the turbulent scales are modelled. This allows to reduce the calculation cost in a drastic way. However, it prevents from capturing combustion-turbulence interaction which makes this method non-competitive for the study of unsteady phenomena. Unsteady-RANS (U-RANS) methods also exists, but they are not as precise as LES.

These three methods are summed up on Figure 62 representing the energy cascade of turbulence. The graph represents the turbulent energy as a function of the wavenumber. The latter is measured in m^{-1}, meaning that low wavenumber correspond to large turbulence structures. Figure 62 illustrates the fact that the largest turbulent structures contain most of the flow energy. Their size (the integral length scale l_t) is the same order of magnitude than the geometry. Then, as the eddies break up, the energy is transferred from large to small turbulent scales. Finally, when the eddies reach the Kolmogorov scale η_κ, the viscous forces overcome the inertia allowing the turbulent energy to be dissipated into heat by friction.

The filtered Navier-Stokes equations, diffusion fluxes and sub-grid-scale fluxes are extensively detailed in several theses [23,161,162] and books [64]. It is however recalled in the following section. As the smallest turbulent structures are filtered and modelled, various sub-grid scale models can be used. A quick overview of these models is also proposed in the following sections.

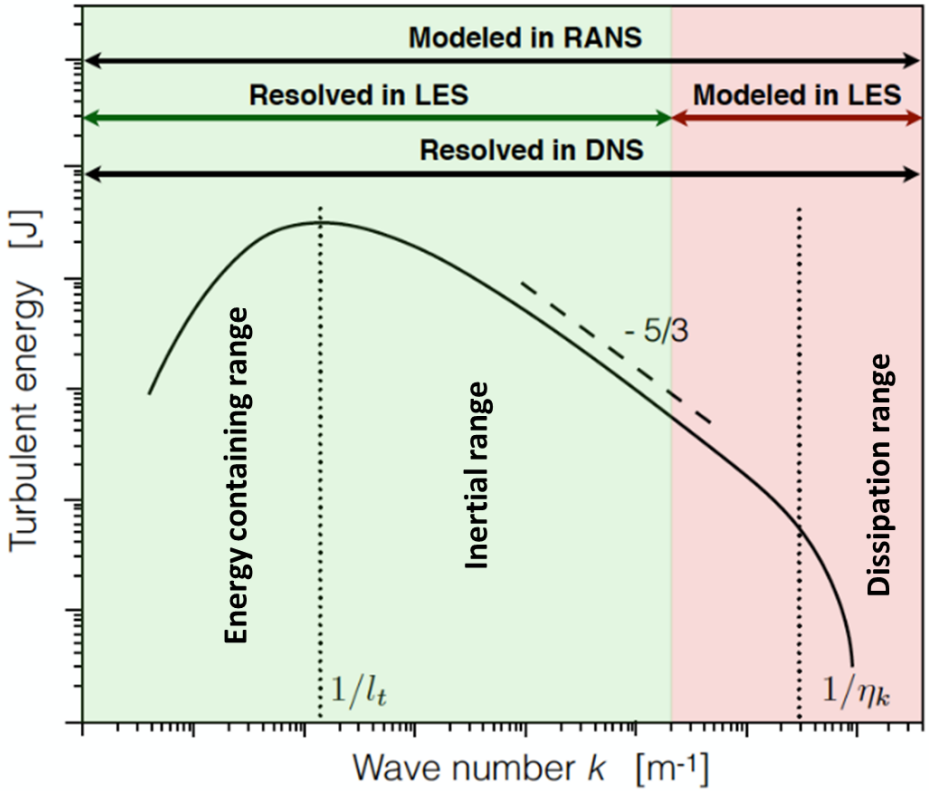

Figure 62: Energy distribution and scales in turbulence modeling, adapted from [68]

5.1.2 Filtered governing equations in LES

Governing equations

As mentioned in the previous section, Large Eddy Simulation governing equations are obtained by filtering the Navier-Stokes equations. The latter are defined as follows (respectively the equations for mass, momentum, energy and species conservation):

$$\frac{\partial \rho}{\partial t} + \frac{\partial}{\partial x_i}(\rho u_i) = 0 \tag{49}$$

$$\frac{\partial (\rho u_j)}{\partial t} + \frac{\partial (\rho u_i u_j)}{\partial x_i} + \frac{\partial P \delta_{ij}}{\partial x_i} = -\frac{\delta \tau_{ij}}{\partial x_i} \tag{50}$$

$$\frac{\partial \rho E}{\partial t} + \frac{\partial \rho u_i E}{\partial x_i} + \frac{\partial u_j P \delta_{ij}}{\partial x_i} = -\frac{\partial q_i}{\partial x_i} + \frac{\partial u_j \tau_{ij}}{\partial x_i} + \dot{\omega_T} \tag{51}$$

$$\frac{\partial \rho Y_k}{\partial t} + \frac{\partial \rho u_i Y_k}{\partial x_i} = \frac{\partial J_{k,i}}{\partial x_i} + \dot{\omega_k} \tag{52}$$

i represents the 3 spatial components and k the considered species among the N_S constituting the system. u is the velocity, τ_{ij} the viscous stress tensor, E the total energy, q the heat flux, $\dot{\omega_T}$ the energy source term (heat release rate), J the diffusive flux of species and $\dot{\omega_k}$ the species source term (production rate). δ_{ij} is the Kronecker symbol. It is equal to 1 if $i = j$ and to 0 otherwise.

The **viscous stress tensor $\boldsymbol{\tau_{ij}}$** is written as:

$$\tau_{ij} = 2\mu(S_{ij} - \frac{1}{3}\delta_{ij}S_{ll}) \tag{53}$$

With μ the dynamic viscosity and S_{ij} the deformation tensor written as:

$$S_{ij} = \frac{1}{2}(\frac{\partial u_j}{\partial x_i} + \frac{\partial u_i}{\partial x_j}) \tag{54}$$

The diffusive flux of the species $\boldsymbol{k}$ in the mixture $\boldsymbol{J_k}$ is computed thanks to the Hirschfelder and Curtiss approximation [163]:

$$J_{k,i} = \rho Y_k V_{k,i} = -\rho(D_k \frac{W_k}{W}\frac{\partial X_k}{\partial x_i} - Y_k V_i^c) \tag{55}$$

With D_k the diffusion coefficient of species k in the mixture and V_k the diffusion velocity of species k corrected by the V_i^c term to ensure global mass conservation expressed as:

$$V_i^c = \sum_{k=1}^{N_S} D_k \frac{W_k}{W}\frac{\partial X_k}{\partial x_i} \tag{56}$$

Finally, **the heat flux $\boldsymbol{q}$** is expressed as the sum of the Fourier and enthalpy flux induced by the species diffusion (λ being the heat conduction coefficient of the mixture):

$$q_i = -\lambda\frac{\partial T}{\partial x} + \sum_{k=1}^{N_S} J_{k,i}h_k$$

Filtering

As in LES the smallest eddies are filtered and modelled, the flow is described by the filtered Navier-Stokes equations. The modelled part of these equations are represented through sub-grid scale models. For any quantity of the flow noted f, the filtered values $\bar{f}$ is defined as:

$$\bar{f}(x,t) = \int f(x',t)F_\Delta(x-x')\,dx' \tag{57}$$

With F_Δ the LES filter of size Δ. Several types of filter are possible (cut-off, box, etc.). The unresolved sub-grid quantities are written f' and defined as:

$$f'(x,t) = f(x,t) - \bar{f}(x,t) \tag{58}$$

In order to avoid the appearance of undesirable terms in the filtered mass conservation equation, the Favre averaging definition is used:

$$\tilde{f} = \overline{\rho f}/\bar{\rho} \tag{59}$$

Hence the filtered values can be rewritten as:

$$\bar{\rho}\tilde{f}(x,t) = \int \rho f(x',t)F_\Delta(x-x')\,dx' = \overline{\rho f} \tag{60}$$

Note that it is important to distinguish between explicit and implicit LES. For the first one, the filter is explicitly built and applied to the Navier-Stokes conservation equations which are then solved numerically. For implicit LES, the conservation equations are implicitly filtered by the mesh, the latter acting like a low-pass filter. In this work, the implicit approach is used with CERFACS' AVBP solver.

Filtered governing equations

Applying the filtering operation to the Navier-Stokes equation yields:

$$\frac{\partial \bar{\rho}}{\partial t} + \frac{\partial}{\partial x_i}(\bar{\rho}\widetilde{u_\iota}) = 0 \tag{61}$$

$$\frac{\partial \bar{\rho}\tilde{u}_j}{\partial t} + \frac{\partial \bar{\rho}\tilde{u}_i\tilde{u}_j}{\partial x_i} + \frac{\partial \bar{P}\delta_{ij}}{\partial x_i} = \frac{\partial}{\partial x_i}\left[\overline{\tau_{\iota J}} - \bar{\rho}\left(\widetilde{u_\iota u_J} - \tilde{u}_i\tilde{u}_j\right)\right] \tag{62}$$

$$\frac{\partial \bar{\rho}\tilde{E}}{\partial t} + \frac{\partial \bar{\rho}\tilde{u}_i\tilde{E}}{\partial x_i} + \frac{\partial \overline{u_\iota P\delta_{\iota J}}}{\partial x_i} = \frac{\partial}{\partial x_i}\left[\bar{q}_\iota - \bar{\rho}\left(\widetilde{u_\iota E} - \tilde{u}_i\tilde{E}\right)\right] + \overline{\tau_{\iota J}\frac{\partial u_\iota}{\partial x_J}} + \overline{\dot{\omega}_T} \tag{63}$$

$$\frac{\partial \bar{\rho}\tilde{Y}_k}{\partial t} + \frac{\partial \bar{\rho}\tilde{u}_i\tilde{Y}_k}{\partial x_i} = \frac{\partial}{\partial x_i}\left[\bar{J}_{k,i} - \bar{\rho}\left(\widetilde{u_\iota Y_k} - \tilde{u}_i\tilde{Y}_k\right)\right] + \overline{\dot{\omega}_k} \tag{64}$$

The **filtered viscous stress tensor $\overline{\tau_{\iota J}}$** is expressed as:

$$\overline{\tau_{\iota J}} = \overline{2\mu(S_{\iota J} - \frac{1}{3}\delta_{\iota J}S_{ll})} \tag{65}$$

It can be approximated as:

$$\overline{\tau_{\iota J}} \sim 2\bar{\mu}(\widetilde{S_{\iota J}} - \frac{1}{3}\delta_{ij}\widetilde{S_{ll}}) \tag{66}$$

with:

$$\overline{S_{\iota J}} = \frac{1}{2}(\frac{\partial \widetilde{u_J}}{\partial x_i} + \frac{\partial \widetilde{u_\iota}}{\partial x_j}) \tag{67}$$

and:

$$\bar{\mu} \sim \mu(\tilde{T}) \tag{68}$$

The **filtered diffusive flux of the species k in the mixture $\overline{J_k}$** is expressed as:

$$\overline{J_{k,\iota}} = \overline{-\rho(D_k\frac{W_k}{W}\frac{\partial X_k}{\partial x_\iota} - Y_k V_\iota^c)} \tag{69}$$

It can be approximated as:

$$\overline{J_{k,\iota}} = -\bar{\rho}(\overline{D_k}\frac{W_k}{\overline{W}}\frac{\partial \widetilde{X_k}}{\partial x_i} - \widetilde{Y_k}\widetilde{V_\iota^c}) \tag{70}$$

with:

$$\widetilde{V_\iota^c} = \sum_{k=1}^{N_S}\overline{D_k}\frac{W_k}{\overline{W}}\frac{\partial \widetilde{X_k}}{\partial x_i} \tag{71}$$

and:

$$\overline{D_k} \sim \frac{\bar{\mu}}{\bar{\rho}S_{ch_k}} \tag{72}$$

S_{ch_k} being the Schmidt number of specie k (cf. next section on AVBP simplified transport for its definition).

The **filtered heat flux q** is expressed as:

$$\overline{q_\iota} = \overline{-\lambda \frac{\partial T}{\partial x} + \sum_{k=1}^{N_S} J_{k,\iota} h_k} \tag{73}$$

It can be approximated as:

$$\overline{q_\iota} \sim \bar{\lambda} \frac{\partial \tilde{T}}{\partial x} + \sum_{k=1}^{N_S} \overline{J_{k,\iota}} \widetilde{h_k} \tag{74}$$

with:

$$\bar{\lambda} \sim \frac{\bar{\mu} \overline{C_p}(\tilde{T})}{Pr} \tag{75}$$

Pr being the Prandtl number (cf. next section on AVBP simplified transport for its definition).

Sub-grid scale fluxes

The application of filtering operations to non-linear relations lead to unclosed terms which describe the effect of filtered scales. Hence, this terms (to which we add the sgs superscript) require modeling to be able to solve them.

The **unresolved sub-grid scale viscous stress tensor $\bar{\tau}_{ij}^{sgs}$**:

$$\bar{\tau}_{ij}^{sgs} = -\bar{\rho}\left(\widetilde{u_\iota u_J} - \tilde{u}_i \tilde{u}_j\right) \tag{76}$$

is modelled by introducing a sub-grid scale turbulent viscosity ν_t to model the sub-grid turbulent stresses (Boussinesq assumption) as follows:

$$\bar{\tau}_{ij}^{sgs} \sim 2\bar{\rho}\nu_t \left(\widetilde{S_{\iota J}} - \frac{1}{3}\delta_{ij}\widetilde{S_{ll}}\right) \tag{77}$$

Various sub-grid scale models (cf. next sub-section) can be used to compute ν_t.

The **unresolved species diffusion flux $\overline{J_{k,\iota}^{sgs}}$**:

$$\overline{J_{k,\iota}^{sgs}} = -\bar{\rho}\left(\widetilde{u_\iota Y_k} - \widetilde{u_\iota}\widetilde{Y_k}\right) \tag{78}$$

is modelled by:

$$\overline{J_{k,\iota}^{sgs}} = -\bar{\rho}\left(\overline{D_k} \frac{W_k}{\bar{W}} \frac{\partial \widetilde{X_k}}{\partial x_i} - \widetilde{Y_k} \widetilde{V_\iota^{c,t}}\right) \tag{79}$$

introducing to the turbulent diffusion viscosity:

$$\widetilde{V_\iota^{c,t}} = \sum_{k=1}^{N_S} \overline{D_k^t} \frac{W_k}{\bar{W}} \frac{\partial \widetilde{X_k}}{\partial x_i} \tag{80}$$

$\overline{D_k^t}$ is the turbulent diffusivity defined as:

$$\overline{D_k^t} = \frac{\bar{\mu}}{\bar{\rho} S_{ch_k^t}} \tag{81}$$

$S_{ch_k^t}$ is the turbulent Schmidt number for species k supposed identical for all species. In CERFACS' AVBP solver, the standard S_{ch}^t value is 0.7.

The **unresolved heat diffusion flux $\boldsymbol{q_i^{sgs}}$** :

$$\overline{q_\iota^{sgs}} = -\bar{\rho}(\widetilde{u_\iota E} - \widetilde{u_\iota}\tilde{E}) \tag{82}$$

is modelled by:

$$\overline{q_\iota^{sgs}} = -\lambda^t \frac{\partial \tilde{T}}{\partial x} + \sum_{k=1}^{N_S} \overline{J_{k,\iota}}\,\widetilde{h_k} \tag{83}$$

with:

$$\lambda^t = \frac{\bar{\mu}\overline{C_p}(\tilde{T})}{Pr^t} \tag{84}$$

Pr^t being the turbulent Prandtl number. It is also supposed constant wuth a value of 0.7.

5.1.3 Turbulent viscosity models

The description of the sub-grid scale viscous stress tensor shown in the previous section is based on the turbulent viscosity ν_t. This approach supposes that the effects of the sub-grid scales on the resolved ones are purely dissipative (no backscatter phenomenon). ν_t can be modelized in different ways via sub-grid scale models. Three of these models (Smagorinsky, WALE and Sigma) are briefly described in this section as they are all proposed in CERFACS' AVBP solver.

Smagorinsky model[164]

$$\nu_t = (C_s\Delta_x)^2\sqrt{2\widetilde{S_{\iota J}}\widetilde{S_{\iota J}}} \tag{85}$$

With Δ_x being the characteristic length of the filter (cube-root of the volume of the considered cell) and C_s a constant defined as $0.1 \leq C_s \leq 0.18$. Historically, it was one of the first model developed for LES. The main designed application were homogeneous isotropic turbulent flows. Hence the model is not well suited to wall-bounded flows which present anisotropic turbulence. Moreover, Smagorinsky model is known to be too dissipative which can be problematic.

WALE model [165]

$$\nu_t = (C_w\Delta_x)^2\frac{\left(s_{ij}^d s_{ij}^d\right)^{3/2}}{\left(\tilde{S}_{ij}\tilde{S}_{ij}\right)^{5/2} + \left(s_{ij}^d s_{ij}^d\right)^{5/4}} \tag{86}$$

with:

$$s_{ij}^d = \frac{1}{2}\left(\tilde{g}_{ij}^2 + \tilde{g}_{ij}^2\right) - \frac{1}{3}\tilde{g}_{kk}^2\delta_{ij} \tag{87}$$

Where C_w=0.4929 is a model constant and $\widetilde{g_{\iota J}}$ the resolved velocity gradient. This model was specifically developed for wall-bounded flows.

Sigma model [166]

$$\nu_t = (C_\sigma\Delta_x)^2\frac{\sigma_3(\sigma_1-\sigma_2)(\sigma_2-\sigma_3)}{\sigma_1^2} \tag{88}$$

With C_σ=1.5 and $\sigma_1 \geq \sigma_2 \geq \sigma_3 \geq 0$ the singular values of the tensor built when resolving the velocity gradients. This model, which is similar to WALE, was developed for resolved boundary layers. Hence it is less efficient for wall-modeled LES.

In this study, WALE is used as it represents a good compromise between accuracy and computational cost [23].

5.1.4 AVBP solver numerical parameters

The LES calculations performed in this work use the AVBP code [167,168] developed by CERFACS. AVBP is a massively-parallel code developed to describe compressible reacting flows on unstructured meshes to facilitate computations on complex geometries. It is based on the cell-vertex discretization method [23,167]. The treatment of the boundary conditions is made with the Navier Stokes Characteristic Boundary Conditions (NSCBC) formalism [169]. This section is dedicated to a simplified description of the numerical parameters and methods in the code that will be later mentioned when describing the application.

Numerical schemes

In order to solve the filtered equations, two different numerical schemes can be used with AVBP. An extensive description of the schemes and their intrinsic properties (dispersion, dissipation, stability etc.) is proposed in [170]. Hence a simplified description can be found below:

- **Lax-Wendroff scheme (LW)** [171]
  LW is a central finite volume centered scheme using an explicit time integration with a single Runge-Kutta step. It is 2nd order in time and space and has a moderate computational cost. The associated dissipation error acts as additional diffusion which increases the robustness of the scheme. Hence it is more efficient to avoid wiggles around stiff gradients for example. Therefore, LW is convenient to stabilize computations.

- **Two-step Taylor Galerkin (TTGC)** [172]
  TTGC is a finite element centered scheme using an explicit two-step integration in time. It is 3rd order in time and space. Specifically developed for LES, TTGC presents very good dispersive and dissipative properties. However, is it less robust than LW and its computational cost is higher.

Artificial viscosity

Since the previously mentioned schemes are all spatially centered they are naturally prompt to create wiggles around strong gradients (even though it is less the case with LW than TTGC). In order to avoid those issues, artificial viscosity (AV) can be used, generally by using a sensor based on a predefined criterion to apply it locally. However, too much AV can impact the behavior of the solution. Hence, this parameter needs to be handled with care. Several types of artificial viscosity can be used with AVBP and are mentioned in [23,162]. As rocket engine conditions lead generally to high pressure (see Introduction), the real gas assumption is generally used when performing representative simulations. In such case the Localized Artificial Diffusivity (LAD) method is interesting as its sensor is based on

density gradients, which can be strong for high pressure applications. The method was already used for rocket engines LES computations by Schmitt [74] and Blanchard [23].

AVBP simplified transport

While 1D flame speed computations performed with CHEMKIN or CANTERA can still be competitive in terms of computational cost with detailed transport models like multicomponent or mixture-averaged [56,158] (the latter being used in the calculations shown in the previous chapters), this is not the case for 3D LES. Hence, to avoid heavy computations relying on the Lennard-Jones potentials, a simplified transport approach is proposed in AVBP.

For the LES calculation presented in this work, a power law is used to compute the flow viscosity μ:

$$\mu = \alpha_1 \left(\frac{T}{T_{ref}} \right)^{\beta} \tag{89}$$

With α_1, β and T_{ref} parameters calibrated from CANTERA computation of a reference case. A Sutherland law can also be used [158].

The simplified transport is based on several non-dimensional numbers.

- **The Schmidt number S_{ch_k}** is the ratio between momentum and the molecular diffusivities :

$$S_{ch_k} = \frac{\mu}{\rho D_{m_k}} \tag{90}$$

  with D_{m_k} the molecular diffusivity of species k, defined as:

$$D_{m_k} = \frac{1 - Y_k}{\sum_{j \neq k} \frac{X_j}{D_{jk}}} \tag{91}$$

  With D_{jk} the binary diffusion coefficient of species j in species k.
  The Schmidt number is supposed constant for each species k.

- **The Prandtl number P_r** is the ratio between momentum and thermal diffusivities:

$$P_r = \frac{\nu}{D_{th}} \tag{92}$$

  Where D_{th} is the thermal diffusivity of the mixture, defined as:

$$D_{th} = \frac{\lambda}{\rho C_p} \tag{93}$$

  The Prandtl number can also be written as:

$$P_r = \frac{\mu C_p}{\lambda} \tag{94}$$

  It is also supposed constant for the mixture.

- **The Lewis Number Le_k** (already introduced in Chapter 3) is the ratio between the thermal and molecular diffusivity but can also be written as a function of the previously defined non-dimensional numbers:

$$Le_k = \frac{D_{th}}{D_{m_k}} = \frac{\lambda_u}{\rho_u C_{p_u} D_{m_k}} = \frac{S_{ch_k}}{Pr} \tag{95}$$

The Lewis number of each species is then supposed constant (ρ_u and C_{p_u} are computed for the mixtures as weighted averages). This is a reasonable approximation as all non-dimensional numbers do not vary much across the flame [64,158]. Hence, it is possible to compute the thermal conductivity λ as:

$$\lambda = \frac{\mu C_{p_u}}{Pr} \tag{96}$$

And the molecular diffusion coefficients D_{m_k} as:

$$D_{m_k} = \frac{\mu}{\rho S_{ch_k}} \tag{97}$$

The S_{ch_k} and Pr values are determined prior to the simulation with CANTERA/ARCANE and optimized for target conditions representative of the CFD calculations (laminar flame speeds at different pressures, temperatures and φ for example).

Equation of state – real gases

For all the 1D computations performed in the previous chapters, the perfect gas assumption was used. This is the default equation of state in AVBP as it is valid for the majority of the applications of LES calculations. It writes:

$$P = \rho r T \tag{98}$$

with r being the specific gas constant expressed as the ratio between the universal gas constant R (8.314 $J.mol^{-1}.K^{-1}$) and the average molar mass of the mixture W:

$$r = \frac{R}{W} \tag{99}$$

However, as mentioned in the Introduction, rocket engine combustion chambers tend to exhibit high pressure conditions (~ 100 bar) where the propellants are injected at low temperatures. The transition between subcritical to supercritical thermodynamic conditions is marked by the critical point defined at temperature T_c and pressure P_c. Above this limit, the hypothesis of perfect gas is not valid anymore as the interaction between molecules is not negligible in those conditions: an equation of state for real gases is required.

The critical conditions are well known for main chemical species such as CH_4 or O_2 (cf. Table 12). As well as for stable intermediary species such as C_2H_2 or C_2H_6. However, when it comes to unstable intermediary species (i.e.., radicals) such as for example CH_3O_2 or CH_2OH, no experimental data is available. Several methods can be used to predict their properties. The Lennard-Jones potentials

theory [173,174] is often used as shown in [83,175]. Other predictive approaches like group-contribution methods developed by Joback et al. [176] can be considered. The sensitivity to the values of critical properties of the minor unstable species was evaluated on premixed 1D AVBP flames at high pressure. The results showed very small impact on the flame structure for variations up to +50% of the reference value.

Species	T_c (K)	P_c (bar)
CH_4	190.6	45.9
O_2	154.6	50.4
CO_2	304.1	73.8
H_2O	647.1	220.6

Table 12: Critical properties of main chemical species

In AVBP, two so-called cubic equations of state can be used: Peng Robinson [177] and Soave-Redlich-Kwong [178]. The second one, noted SRK is particularly suitable for cryogenic flow similar to rocket engine injection conditions and was already used for such applications in previous works [66,74,179]. The pressure is computed as follows:

$$P = \frac{\rho r T}{1 - \rho b_m} - \frac{\rho^2 a_m(T)}{1 + \rho b_m} \tag{100}$$

where $a_m(T)$ and b_m are mixture dependent mass coefficients. The first one represents the attractive forces while the other one describes the repulsive ones. They are computed with the mixture law of Van Der Walls as follows (there is N_s species in the system, i and j being different):

$$a_m(T) = \sum_{i=1}^{N_s} \sum_{j=1}^{N_s} a_{ij}(T) Y_i Y_j \tag{101}$$

$$b_m = \sum_{i=1}^{N_s} b_i Y_i \tag{102}$$

With $a_{ij}(T)$ defined as:

$$a_{ij}(T) = \sqrt{a_{ii}(T) a_{jj}(T)}\,(1 - k_{ij}) \tag{103}$$

k_{ij} is called the binary interaction coefficients. $a_{ii}(T)$ and b_i are coefficients for pure species defined as:

$$a_{ii}(T) = \Phi_{C_i} \Psi(T)^2 \tag{104}$$

$$b_i = 0.08664 \frac{r_i T_{c_i}}{P_{c_i}} \tag{105}$$

P_{c_i} and T_{c_i} being respectively the critical pressure and temperature of species i and r_i the previously defined specific gas constant of species i. The other parameters are:

$$\Phi_{C_i} = \frac{0.42747\left(r_i T_{c_i}\right)^2}{P_{c_i}} \tag{106}$$

$$\Psi(T) = 1 + c_i\left(1 - \sqrt{\frac{T}{T_{c_i}}}\right) \tag{107}$$

$$c_i = 0.48508 + 1.5517\omega_i - 0.15613\omega_i^2 \tag{108}$$

ω_i being the acentric factor.

Knowing the coefficients of the SRK equation, it is possible to compute the fluid density described with a third order polynomial:

$$\rho^3 + a_2\rho^2 + a_1\rho + a_0 = 0 \tag{109}$$

The coefficients being defined as:

$$a_0 = \frac{P}{b_m a_m} \tag{110}$$

$$a_1 = -\frac{\bar{r}T}{b_m a_m} \tag{111}$$

$$a_2 = \frac{-Pb_m^2 - \bar{r}Tb_m + a_m}{b_m a_m} \tag{112}$$

5.2 Application case description: the REST HF-10 configuration

In order to evaluate the performances of the chemical scheme developed during this work, the REST HF-10 test case was chosen for an LES application. It consists in a single coaxial injector element, representative of a rocket engine combustion chamber. REST stands for *Rocket Engine Stability IniTiative*. It is a research group formed by CNES, ONERA, CNRS and DLR investigating on combustion instabilities in rocket engines. However, the test case evaluated here is of course not dynamically excited to trigger this kind of instabilities as the focus of this study is to evaluate the impact of chemistry only.

HF-10 is a numerical benchmark test case whose geometry is strongly inspired by the TUM test bench developed by Haidn et al. [50]. As experimental studies based on dedicated setups with optical access venture just above the supercritical conditions (for example $\sim$ 60 bar for experiments ran at the DLR/TUM facilities [49]), HF-10 is fully representative of rocket engine combustion chambers at full thrust with a $\sim$ 100 bar pressure. Hence, the aim of the calculation is to evaluate the differences induced by the use of the newly defined chemistry compared to already existing results on this realistic configuration. Indeed, several HF-10 computations were performed by the REST project participants

for the same operating conditions. Schmitt and Cuenot [180] from EM2C/CERFACS ran AVBP computations comparing a RAMEC-derived ARC and an infinitely fast chemistry (i.e., relaxation to equilibrium) coupled with a beta-pdf [180]. Nicole et al. [181] from ONERA and Horchler et al. [88] from DLR both performed U-RANS calculations using respectively the CEDRE and TAU codes. The first uses the relaxation to equilibrium model with values coming from the GRI-Mech 3.0 mechanism while the second one uses a flamelet model for which the tables were generated with the Zhukov-Kong mechanism (cf. Chapter 2). Finally, Kaess et al. [182] from ArianeGroup also performed U-RANS calculations, using the ANSYS-CFX code and a one-step mechanism. The global comparison of these calculations is performed in [183].

The aim of this work is to compare, with an AVBP computation, the CH_4/O_2 optimized chemistry developed during this thesis to the reference RAMEC-derived ARC presented in [180] as they are both complex chemistries.

It is important to note that the AVBP code has already been used several times for MethaLOx rocket engine calculations. As mentioned in section 2.3.2, Maestro et al. derived an ARC mechanism from Lu's to perform computation of the TUM test bench at 20 bar (GOx/GH_4) [75]. This complex 3D LES computation featuring a highly strained diffusion flame succeeded to capture the pressure profile inside the combustion chamber as well as the wall heat flux (cf. Figure 63).

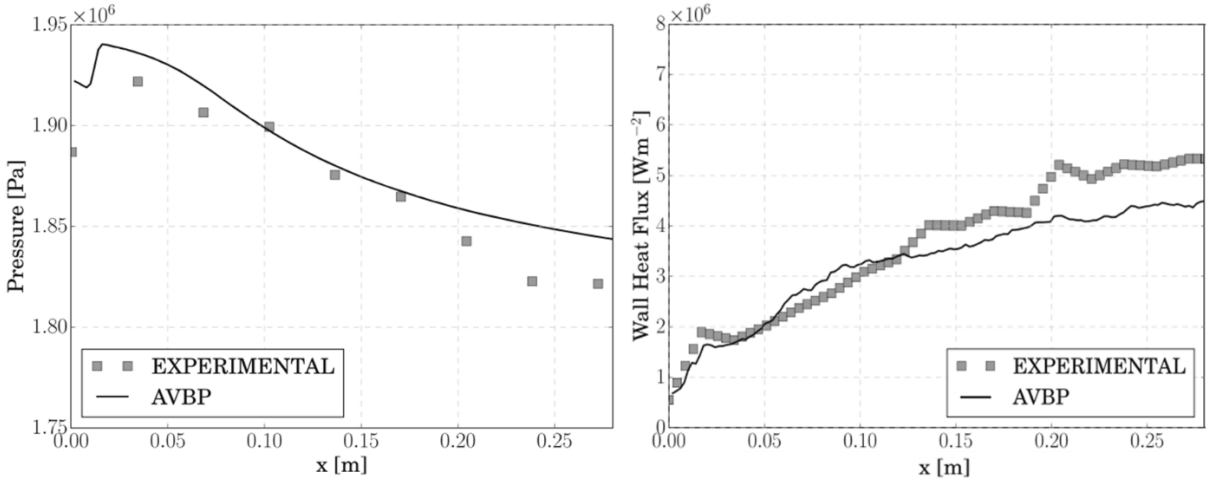

Figure 63: Time averaged axial Pressure and Heat Flux at the walls - figures from [75]

More recently, Blanchard et al. performed calculations on the same test bench geometry (the coaxial injector dimensions slightly vary) also at 20 bar but with liquid oxygen and gaseous methane (LOx/GH_4) and a RAMEC ARC derived chemistry. The AVBP computation was, once again, able to recover the experimental pressure and wall heat losses evolution. Based on these experiences, among others, it was used for the above-mentioned benchmark study of REST [180]. Hence it is also used in this work for the optimized chemistry calculation.

5.2.1 Geometry

The REST HF-10 test case geometry described in this section appears in the previously mentioned literature sources and also in [184]. As mentioned above, this is a CH_4/O_2 coaxial mono-injector configuration with recess. Transcritical oxygen is injected at the center while supercritical methane is injected in the annular outer part. The chamber measures 30 cm long and its section is hexagonal.

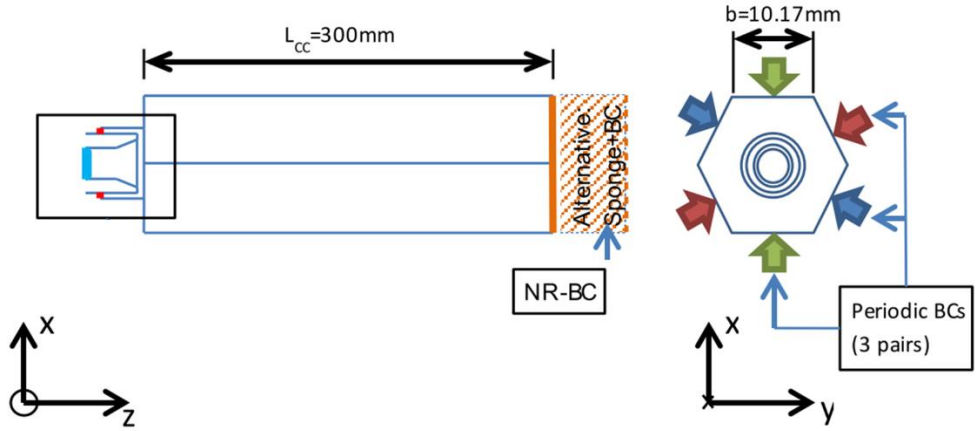

Figure 64: REST HF-10 global geometry from [184]

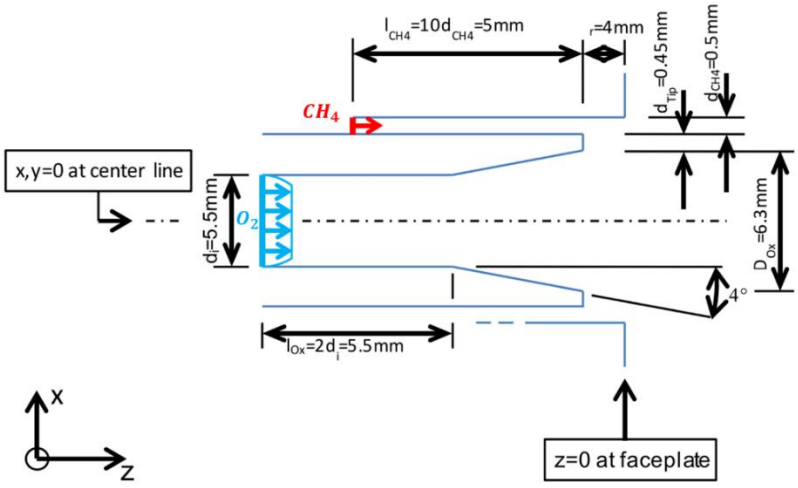

Figure 65: REST HF-10 injector geometry from [184]

5.2.2 Operating conditions

Table 13 below lists the operating conditions of the REST HF-10 test case. The oxidizer to fuel ratio (ROF) yields an equivalence ratio φ=1.18 slightly above stoichiometry to optimize the specific impulse (operating conditions representative of a real rocket engine).

	O_2	CH_4
Injection T (K)	100	231
$\dot{m}$ (kg/s)	0.46	0.136
MR	3.38 – (φ=1.18)	
P_{outlet} (bar)	100	

Table 13: REST HF-10 operating conditions

5.2.3 Boundary conditions and mesh

All the solid walls (i.e.., constituting the injector plate) are considered adiabatic. Wall laws are used to account for the boundary layer formation. As mentioned in the AVBP description, non-reflecting boundary conditions are used for the fuel and oxidizer injection (imposed temperature and mass flow rate with 5% of turbulence) and at the outlet (imposed pressure). The hexagonal walls of the chamber are treated with a periodic axisymmetric condition to simulate the presence of other surrounding injectors, which would be the case in a real rocket engine.

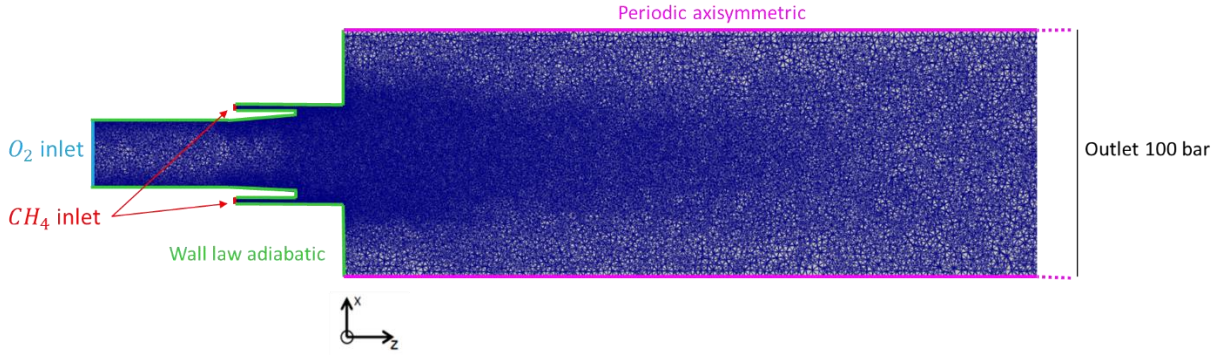

Figure 66: REST HF-10 boundary conditions

The mesh is composed of 11.5 million tetrahedral elements for a total of 2 million nodes. The smallest elements are found near the injector lips and in the recess zone as illustrated on the longitudinal slice of Figure 66. The smaller element size is $14\mu m$ while the largest size at the end of the chamber is $370\mu m$. The mesh is the result of a mesh convergence study made by Schmitt et al. [180]. In order to refine the grid, adaptative mesh refinement (AMR) was applied using criteria such as the Laplacian of velocity and the heat release rate. Hence, the mesh used in this work is the same as the one of [180] (labeled "M1" in that reference).

The convection scheme used for this study is Lax-Wendroff as its dissipative nature helps with chemical stiffness. As mentioned before, WALE is used as sub-grid-scale turbulence model. The Soave-Redlich-Kwong equation of state is used and local filtering is applied with the previously described LAD approach. Because a purely non-premixed flame is expected, no turbulent combustion model is used as explained in Cuenot et al. [185]. Indeed, diffusion flames are naturally thickened by the mesh, so that contrary to premixed flames, no spatial resolution issues arise. Cuenot et al. also demonstrated that even if the sub-grid phenomena that should increase the burning rate are neglected, a relatively coarse mesh (compared within reason to the reaction zone thickness) induces a local over-consumption of the chemical reactants, hence compensating for the loss of information due to filtering and generally leading to a thickening factor close to one. This means that numerical diffusion thickens the flame by the amount it would have been thickened considering flame-turbulence interaction with a sub-grid model. Moreover, the mesh used for the calculation comes from a convergence study on heat release and density gradients performed by Schmitt et al. [180] which guarantees a good resolution in the reactive zone. Finally, recovered global flame structures from IFCM calculations (using a flame-turbulence interaction sub-grid model) and simulations performed with AVBP without such model (with the RAMEC-derived ARC) on the REST HF-10 configuration are very similar [183], giving confidence in the approach used in this study.

5.3 Polimi Opti reduction for REST HF-10 conditions

As presented in the previous chapters the Polimi Opti chemical scheme (described as POLIMI C1-C3 Opti in Figure 61) tailored for CH_4/O_2 combustion at high pressure and temperature was derived. In order to use it for LES computations with AVBP, it is possible to reduce it on target conditions representative of the application case (here REST HF-10). This process, conducted with the ARCANE tool described in the previous chapter, leads to a reduced ARC mechanism. This section details the target cases used for reduction and the validation of the reduced model before using it for a 3D LES simulation.

5.3.1 Reduction targets

Two groups of reduction targets are used: 1D diffusion and premixed flames.The first group of reduction targets is composed of 1D diffusion flames which are identical to the ones used for the derivation of the reference mechanism from [180]. Indeed, as mentioned several times, diffusion flames are characteristic of rocket engine combustion chambers. The targeted pressures (80 and 120 bar) frame the value imposed at the HF-10 outlet (100 bar). The strain a (or the scalar dissipation rate χ for 1D computations in the Z space) is varied from a = 638 to 4700 s^{-1} (corresponding to χ = 100 to 1500 s^{-1}). These values, used by Blanchard for its RAMEC-derived reduction used in [180], were verified for the Polimi Opti mechanism. They correspond to the values extracted from a time-averaged solution of the 3D case, shown on Figure 67. The quantities used to control the error are the integral of the heat release rate and the maximum value of temperature. The complete list of 1D diffusion flame targets is shown on Table 14 below.

$\boldsymbol{\chi\ (s^{-1})}$	$\boldsymbol{P\ (bar)}$
100	80
1500	80
100	120
1500	120

Table 14: 1D diffusion flame target quantities for REST HF-10 test case

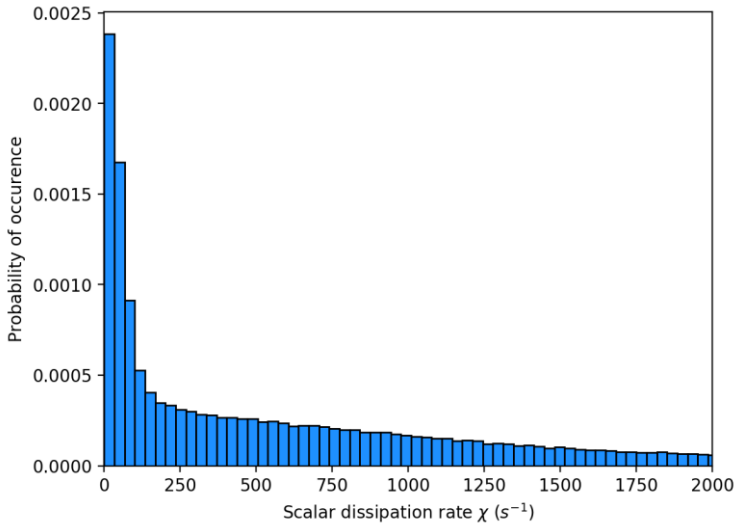

Figure 67: Distribution of scalar dissipation rate in the injection zone of the REST HF-10 test case

As seen in Chapter 2, experimentally obtained laminar premixed flame speeds were used as target points for POLIMI Opti. Indeed, it has been demonstrated that this kind of flame is chemically representative of diffusion flames for CH_4/O_2 mixtures in extreme conditions as the same key pathways and reactions are involved. Hence, various laminar flame speed S_u values extracted from OPTIPRIME datasets and previously used as optimization points are used as reduction targets as well alongside the laminar diffusion flames. As the latter covers the full spectrum of equivalence ratios depending on the observation position, several equivalence ratio conditions for premixed flames are required to correctly describe the full scope of chemical phenomena. For each φ, the experimental values measured at the highest pressure is used. Moreover, using experimental data on which the mechanism was optimized as reduction points guarantees the physical consistency of the mechanism. Table 15 lists all the 1D premixed reduction target conditions.

$\boldsymbol{\varphi}$	$\boldsymbol{P}$ $(\boldsymbol{bar})$	$\boldsymbol{T}$ $(\boldsymbol{K})$
0.5	1.47	454.5
1.0	1.36	412.3
1.5	1.5	419
2.5	14.2	489.6

Table 15: 1D premixed flame target quantities for REST HF-10 test case

5.3.2 Reduced mechanism

Starting from the 30 species and 128 reactions Polimi Opti mechanism, the reduction based on the REST HF-10 targets leads to a 26 species (19 transported, 7 QSS) and 116 reactions mechanism. Table 16 features the transported and QSS species of the Polimi Opti ARC mechanism (on the left column).

	Polimi Opti ARC for REST HF-10	**RAMEC ARC for REST HF-10**
#Reactions	116	88
#Transported species	19	15
#QSS	7	6
Transported species	$H_2\ H\ O_2\ O\ H_2O\ OH\ HO_2\ CO\ CO_2\ CH_4\ CH_3\ CH_3O_2\ CH_3OH\ CH_2OH\ CH_2O\ C_2H_6\ C_2H_4\ C_2H_2\ CH_2CHO$	$H_2\ H\ O\ O_2\ OH\ H_2O\ HO_2\ H_2O_2\ CH_3\ CH_4\ CO\ CO_2\ C_2H_2\ C_2H_4\ C_2H_6$
QSS species	$H_2O_2\ CH_2\ CH_3O\ HCO\ C_2H_3\ C_2H_5\ HCCO$	$HCO\ C_2H_3\ C_2H_5\ CH_2O\ HCCO\ CH_2CO$

Table 16: Composition of the Polimi Opti ARC and RAMEC ARC mechanisms

Ar, He and N_2 were removed as diluents are no longer necessary for pure CH_4/O_2 applications. The other removed species is CH_3O_2H. The rest of the reduction work mainly consisted in analyzing which transported species can be treated with the QSS approximation. This is for example the case for C_2H_5 and C_2H_3 which are intermediary species of the C2 main pathway. The low number of removed species highlights the fact that the Polimi Opti mechanism was already sufficiently reduced on OPTIPRIME

targets for CH_4/O_2 application as only the necessary species with the exception of CH_3O_2H and the diluents remained. It also explains the low level of discrepancies between the Polimi Opti and the ARC mechanisms.

Table 16 compares the transported and QSS species of the Polimi Opti ARC mechanism to the RAMEC-derived ARC of Blanchard used in [180]. The latter is slightly more compact than the Polimi-derived model with 15 transported species, 6 QSS and 88 reactions.

All transported species of the RAMEC-derived ARC mechanism are also found in the Polimi Opti ARC scheme, which in addition includes CH_3O_2, CH_3OH, CH_2OH, CH_2O and CH_2CHO. CH_3O_2 was already identified in 1999 as a key species by Petersen et al. [76] when deriving the RAMEC mechanism. The importance of peroxy species was also notified by Zhukov et al. [85]. However, these species ar not all conserved in the reduction, as shown by the removal of CH_3O_2H by ARCANE.

Other differences lie in the QSS species. H_2O_2 is a QSS species for the Polimi Opti ARC while it is transported in the RAMEC-derived model. HCO, C_2H_3, C_2H_5 and $HCCO$, which are part of the C1 and C2 main pathways, are common QSS species to both mechanisms.

As for the common reactions between the two models, the rate constants are usually defined in a different way, leading to different production rates. Differences in the rate constants lead to a difference in reaction speed for a given temperature. This is for example the case of the optimized $OH + CH_4 = H_2O + CH_3$ reaction where the differences in the Arrhenius parameters lead to changes in the reaction speed behavior at high temperatures. There are also more significant differences in reaction definitions leading to radical behavior changes. For example, $H_2O + O_2 = HO_2 + OH$ is described with a single Arrhenius law for RAMEC while two laws are used for POLIMI Opti, leading to a more complex response to temperature variations. These differences can ultimately have an impact on the species mass fraction fields in a complex 3D LES computation as it will be shown at the end of this chapter (see section 5.5.4).

The complete ARC mechanisms (POLIMI Opti and RAMEC) are detailed in Appendix D.

5.3.3 Reduced mechanism validation

In order to check for the POLIMI Opti ARC validity, the mechanism is first validated against the 1D targets used for reduction by being compared to its POLIMI Opti detailed reference.

Validation on 1D diffusion flames

The observed discrepancies between the reduced and reference mechanisms are listed in Table 17 below. The evaluated quantities are the integral of the heat release rate and the maximum value of temperature as they were used as targets to control the error during reduction. The observed error on these quantities is quite low.

$\chi\ (s^{-1})$	$P\ (bar)$	Error on T_{max}	Error on $\int HR$
100	80	**0.012 %**	**-0.034 %**
1500	80	**0.014 %**	**-0.007 %**
100	120	**0.019 %**	**0.035 %**
1500	120	**0.020 %**	**0.007 %**

Table 17: Errors on 1D diffusion flame target quantities for REST HF-10 test case

Plots of the heat release rate and temperature as functions of the mixture fraction (not shown for brevity) for all targeted conditions confirm the low level of discrepancies obtained after the reduction between the reference mechanism and the ARC. Figure 68 is an example at 120 bar for χ = 1500 s^{-1}.

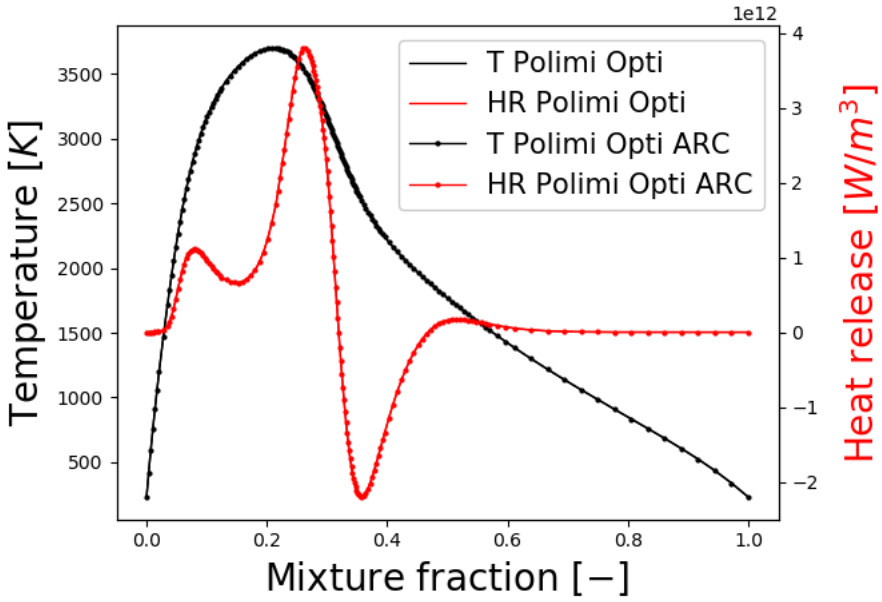

Figure 68: Profile of a 1D highly strained (χ = 1500 s^{-1}) diffusion flame at high pressure (P= 120 bar) showing heat release rate and temperature evolution as a function of the mixture fraction. Comparison between Polimi Opti and the ARC reduced schemes for the REST HF-10 test case

The heat release rate exhibits a classical profile of methane oxycombustion, already described in [23]. There is a main exothermic peak for slightly rich conditions (i.e., Z > 0.2), while a main endothermic peak can be observed for rich conditions ($Z \geq 0.35$). At iso-strain rate, pressure has a direct effect on the heat release rate profile shape. Indeed, an increase in P leads to a slight shift of the main exothermic peak toward leaner conditions while the magnitude of the main endothermic peak increases. This is due to a change in the main reactions contributing to the heat release which is also linked to the shift in the main oxidation pathway described in Chapter 2. On the other hand, at iso-pressure the strain rate directly affects the magnitude of both endothermic and exothermic peaks (which increase with greater values of χ). However, the profile shape (i.e., position and width of the peaks) stays identical.

The species profiles in the Z space shown in Figure 69 for conditions identical to those of Figure 68 confirm that the species evolution as a function of the mixture fraction is correctly recovered by the reduced mechanism. This is the case for all the other conditions listed in Table 14.

Finally, response to strain of the ARC mechanism is verified is verified and shown in Figure 70 for a pressure of 120 bar.

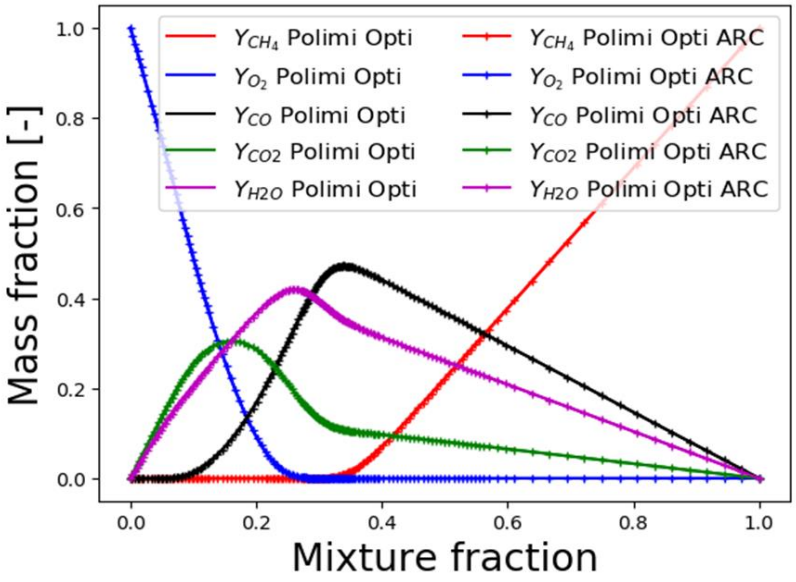

Figure 69: Main species profiles of a 1D highly strained (χ = 1500 s^{-1}) diffusion flame at high pressure (P= 120 bar). Comparison between Polimi Opti and the ARC reduced schemes for the REST HF-10 test case

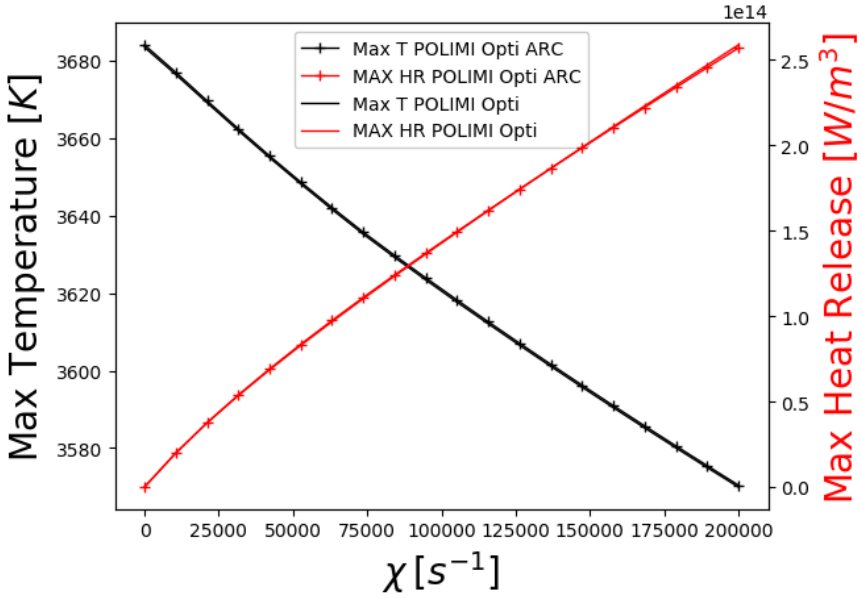

Figure 70: Response to strain of a 1D laminar diffusion flame at 120 bar for the Polimi Opti and Polimi Opti ARC mechanisms

The behavior of the reference Polimi Opti and the derived ARC mechanism was checked for high levels of strain rate (up to χ= 200000 s^{-1}) which are never reached in the REST HF-10 test case. As shown on the figure, the agreement between the two models is very good for the studied range as the relative difference remains below 1% for both the max temperature and heat release rate. The maximum relative difference (0.6 %) is observed for the highest χ. Figure 70 also shows that both mechanisms are far from extinction in the REST HF-10 operating conditions (which can be found on the extreme left part of the graph). Flame quenching appears for even higher χ, highlighting the strong resistance of CH_4/O_2 diffusion flames to strain due to the high reactivity of the mixture.

The behavior of the ARC mechanism was also evaluated at lower pressures, leading to similar conclusions.

Validation on 1D premixed flames

The observed discrepancies between the reduced and reference mechanisms are listed in Table 18. The error was measured for both the max temperature and the laminar flame speed S_u.

φ	$P\ (bar)$	$T\ (K)$	Error on T_{max}	Error on S_u
0.5	1.47	454.5	0.012 %	**0.16%**
1.0	1.36	412.3	0.014 %	**0.44%**
1.5	1.5	419	0.019 %	**0.97%**
2.5	14.2	489.6	0.020 %	**-0.02%**

Table 18: Errors on 1D premixed flame targets for REST HF-10 test case

One can observe that the error is maximum for the φ=1.5 condition. However, it remains below 1% and more importantly below the OPTIPRIME experimental uncertainty of 5%. Hence, these results guarantee that the ARC maintains a good physical behavior.

5.3.4 Compressibility factor

One can remark that the majority of 1D target conditions used for optimization are at pressure greater than P_c for most of the involved species, hence far from the ideal gas assumptions. As the conditions are supercritical, a cubic equation of state should be used for the ARC derivation which is not the case of the calculations made with CANTERA. In order to assess when the ideal gas law can be used or not, the compressibility factor z can be used. When z is close to 1 (in the range 0.95<z<1.05 according to [23]), the ideal gas equation of state is valid. The compressibility factor is defined as follows:

$$z = \frac{P}{\rho r T} \tag{113}$$

Figure 71 shows an instantaneous field from the REST HF-10 calculation conducted with the ARC derived from Polimi Opti. It consists of a slice cut along the longitudinal axis showing the first third of the combustion chamber. On the top part, the heat release rate (HR) field is featured as well as a white isoline representing the stoichiometric mixture fraction for CH_4/O_2 (i.e. Z_{St}=0.2). As illustrated in the heat release rate structure featured on Figure 68, the maximum value of HR is found near Z_{St}, highlighting the position of the flame, i.e., the main reacting zone. The lower part of the figure features the mirror of the upper part but this time the compressibility factor z field is displayed. It can be seen that low values of z, where the real gas equation of states must be used, are mainly found inside the central cryogenic O_2 jet which progressively disintegrates while going through the combustion chamber. The interesting observation is that the Z_{St} iso line, hence the reactive zone, is found outside this region where z is close to 1. This validates the reduction procedure using the ideal gas equation of state. Moreover 2D and 3D DNS calculations performed by Monnier et al. [83] for a premixed turbulent CH_4/O_2 flame at high pressure (56 bar) and stoichiometric conditions showed that the use of real gas thermodynamics leads to small differences with ideal gas modelling, which are almost no perceptible in the 2D case. Additional calculations for methane-oxygen diffusion flames made by Pons et al. [186,187] also showed that the flame structure was identical in both real and ideal gas cases.

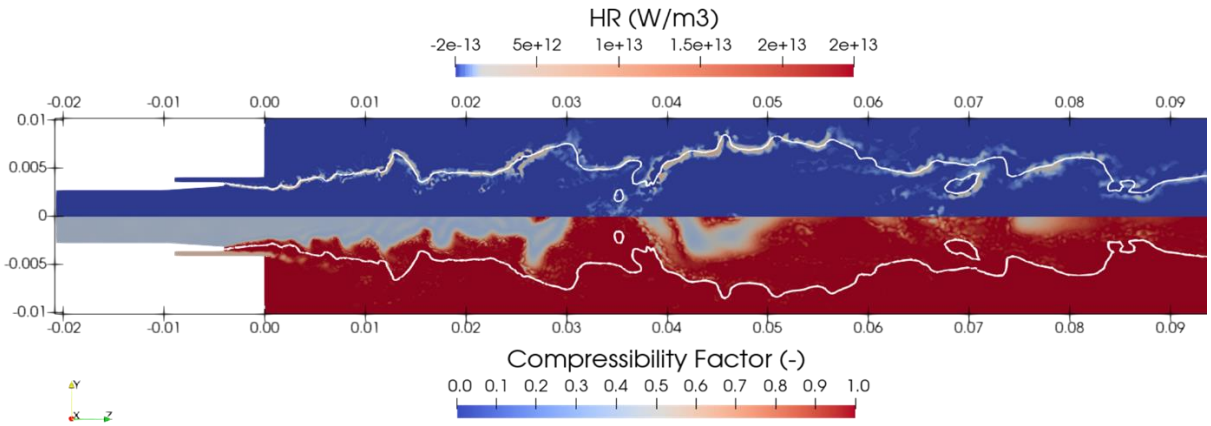

Figure 71: Longitudinal cut of the first third of the REST HF-10 combustion chamber. Mirror fields of the heat release rate (in W/m3) and compressibility factor. The white isoline represents the stoichiometric mixture fraction

5.3.5 1D comparison with the RAMEC ARC mechanism

The differences between the POLIMI Opti and RAMEC ARCs pointed out in section 5.3.2 directly affect the heat release rate as can be seen for a 1D laminar diffusion flame example on Figure 72, for conditions corresponding to one of the reduction targets: high strain (χ=1500s^{-1}) and high pressure (120 bar).

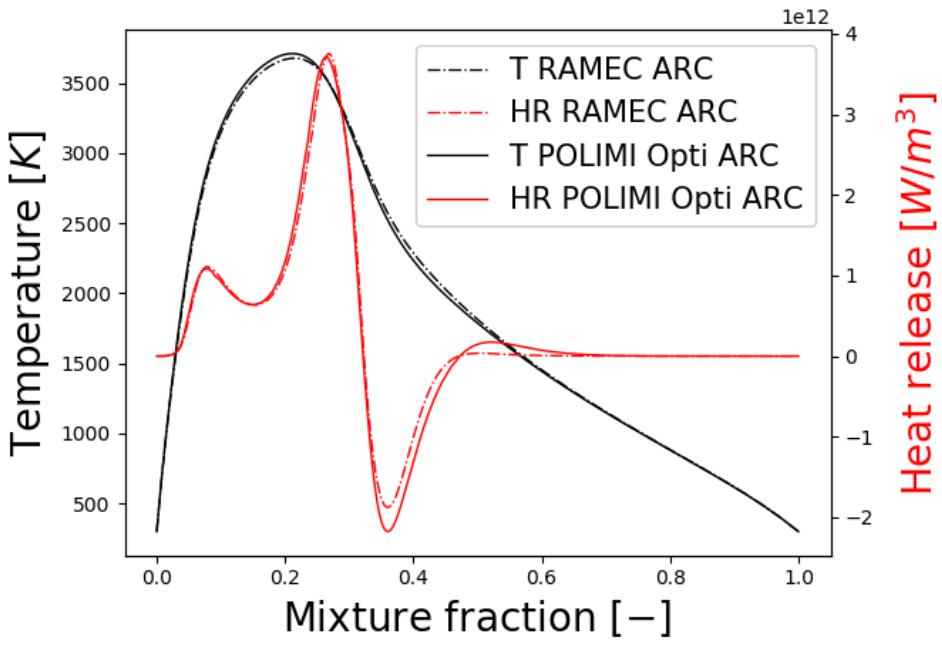

Figure 72: Profiles of a 1D highly strained (χ = 1500 s^{-1}) diffusion flame at high pressure (P= 120 bar) showing heat release rate and temperature evolution as functions of the mixture fraction. Comparison between Polimi Opti ARC and RAMEC-derived ARC

The two mechanisms seem to globally agree for the lean mixture (Z<0.2) despite a slight offset of the main exothermic peak position. Indeed, the latter is located for leaner conditions for the Polimi Opti

ARC. Moreover, the RAMEC ARC seems to slightly underestimate the peak value with a 1.5% relative discrepancy. Far more important discrepancies appear on the rich side, where the RAMEC ARC seems to underestimate the main endothermic peak (relative difference of 16%) as well as the rich minor exothermic peak around Z=0.5. Some light differences can also be seen on the temperature curve. As 3D calculations will feature the interaction between the chemistry and the turbulence of the flow, differences on the flame structure are also expected for the REST HF-10 test case.

5.3.6 Validation on pseudo 1D AVBP calculations

Before running 3D LES computations with the Polimi Opti ARC mechanism, it is important to verify its correct behavior with simplified transport in AVBP. As presented in section 5.1.4, the Prandtl number P_r is supposed constant for the mixture while the Schmidt number S_{ch} is constant per species. These numbers are computed in advance with ARCANE following the equations mentioned in 5.1.4. Their values are computed from the burnt gases properties of a set of 1D flames representative of the LES conditions. The obtained values are then optimized to minimize the error between the detailed and reduced mechanism with simplified transport. This allows to compensate for potential errors generated by the reduction process. S_{ch} and P_r values for the POLIMI Opti ARC mechanism are detailed in Appendix D.

Blanchard et al. already performed 2D laminar diffusion flame computations for chemistry validation in AVBP [66]. However, as seen in Chapter 2, laminar premixed flames (also used as target for reduction on REST HF-10 conditions) are chemically representative of laminar diffusion flames for the studied mixtures. Laminar premixed flames are all the more interesting as an experimental reference is available with the OPTIPRIME database. Finally, 1D premixed flames are easier and less costly to implement than 2D diffusion flames. Hence, three 1D premixed flames are computed for the conditions φ=0.5 to 1.5 of Table 15 which are both optimization and reduction targets. The obtained profiles are compared to reference 1D CANTERA computations in the same conditions, using mixture-averaged and not simplified transport.

Computations are performed on a thin rectangular domain of length L = 2 cm along the horizontal x axis and height h = 2 m along the vertical y axis, with $L \ll h$ as illustrated by Figure 73. The mesh is highly refined in the x direction while it consists of a single element in the y direction. This strategy guarantees that the y dimension as no influence on the flow. Hence, the computation is qualified as "pseudo 1D". Temperature, mixture composition and fresh gas velocity are imposed at the inlet. The latter is chosen equal to S_u values from CANTERA calculations in order to stabilize the flame in the domain. Pressure is imposed at the outlet. The calculation initialization is performed by imposing a temperature profile coming from CANTERA. No LAD is used. The Law-Wendroff convective scheme is chosen because of its cost effectiveness as it is 2.5 more efficient (in terms of iteration/s) than TTGC. Moreover, computations were conducted for both convective schemes at φ=1 showing identical results.

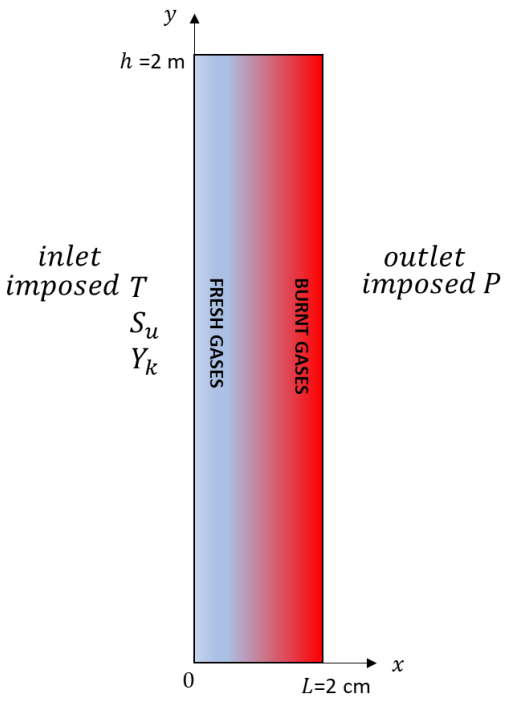

Figure 73: Sketch of the computational domain used for pseudo 1D calculations with AVBP

The mesh size Δx is chosen to be representative of the REST HF-10 3D case, hence the simulation timestep Δt_{CFL} is also representative of the application. Indeed, Δx and Δt_{CFL} are linked by a parameter called CFL through a relation defined as:

$$\Delta t_{CFL} = \Delta x \frac{CFL}{u + u_a} \tag{114}$$

where u is the flow velocity, u_a the acoustic velocity and Δx the size of the smallest element. CFL values are chosen according to the selected convection scheme for numerical stability reasons. For Lax-Wendroff the recommended value is 0.7.

For REST HF-10, and more generally for 3D LES rocket engine calculations with similar parameters, the characteristic order of magnitude of Δt_{CFL} is around 1 to 5 x 10^{-9}s. In order to be representative enough, a regular mesh with Δx = 10 μm was used for every tested equivalence ratio condition. Such values allow a sufficient discretization of the flame thickness δ_f (on average 8 points in the flame front depending on the case). It yields a Δt_{CFL} of the order of magnitude of 2 ns depending on the case. Results are presented for the stoichiometric case.

A mesh convergence study was performed on S_u, confirming the chosen Δx. Pressure, temperature, flow speed, density, heat release rate as well as species mass fraction profiles are monitored. Graphs on Figure 74 show a good overall agreement between the 1D CANTERA profiles and the pseudo 1D AVBP results. Despite the highly refined mesh, there is a 9% discrepancy on S_u, with AVBP slightly underestimating the value. The rest of the u profile is similar for both solvers. Small differences can be seen on the pressure profiles. This is due to the constant pressure assumption in CANTERA, neglecting the small pressure drop through the flame which is observed with AVBP. However, the relative difference is very small (0.2 %), so negligible. The main discrepancies can be observed for the heat release rate HR which maximum value is underestimated by AVBP (8% relative difference), directly related to the above mentioned S_u gap.

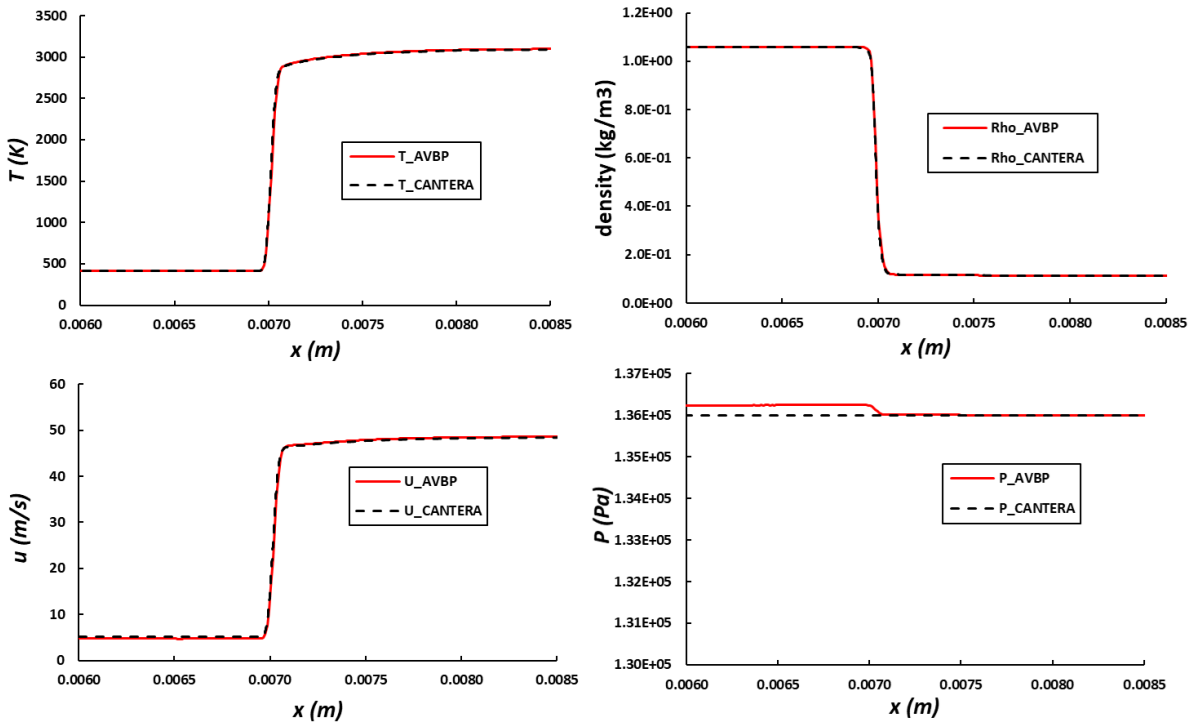

Figure 74: Profiles of T, density, u and P for a 1D premixed CH_4 / O_2 flame at φ=1 and P=1.36 bar (target 2 of Table 15*) computed with CANTERA vs pseudo 1D AVBP calculations with the Polimi Opti ARC mechanism – zoomed on the flame region*

Figure 75 features the HR profile zoomed on the flame. It highlights the level of discretization of the reactive zone with AVBP. As mentioned above, despite having around 9 points in the flame front, the maximum peak value is not fully captured at φ=1. A slight shift on the peak position between CANTERA and AVBP can also be observed but it is negligible.

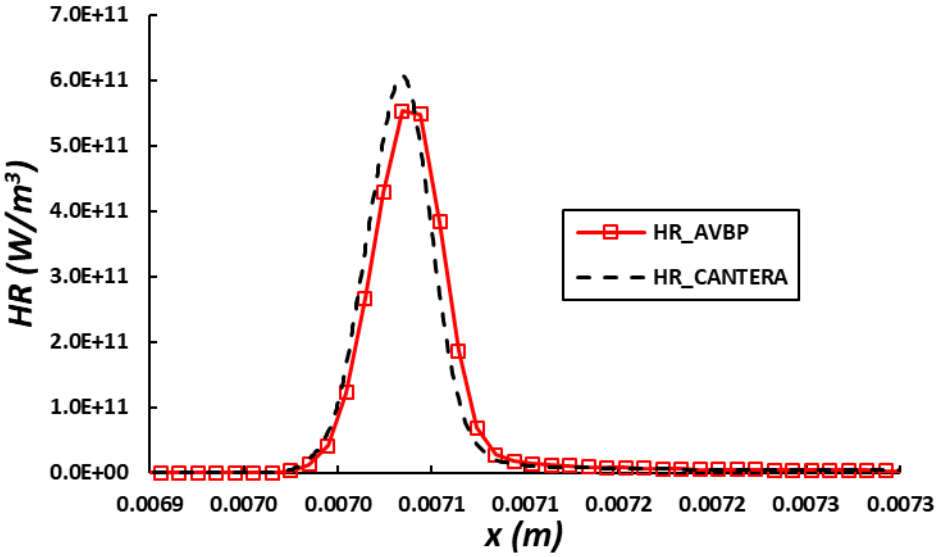

Figure 75: Profiles of heat release rate zoomed on the reactive zone for a 1D premixed CH_4 / O_2 flame at φ=1 and P=1.36 bar (target 2 of Table 15*) computed with CANTERA vs pseudo 1D AVBP calculations with the Polimi Opti ARC mechanism – zoomed on the flame region*

Figure 76 features mass fraction profiles of different species for the same flame. The evolution of the main species such as CH_4, H_2O, CO and CO_2 is well described by AVBP. Some discrepancies can be observed for intermediary species such as CH_3 or for example C_2H_6. Indeed, AVBP tends to slightly overestimate the value of the maximum mass fraction. However, these species are found in small quantities (Y is one and two orders of magnitude below the one of the main species for CH_3 and C_2H_6, respectively). Moreover, some maxima of similar species are well recovered like for example CH_2O (not shown).

To complete the analysis and add information to the S_u and HR discrepancies, profiles of species production rates (i.e., species source terms) are also investigated. Indeed, as seen in Chapter 2, these values have direct repercussions on the heat release rate, as they are directly proportional to it. This time, some discrepancies can be observed for the fuel consumption rate as seen on Figure 77. The minimum value is not well captured by AVBP for CH_4 (10.7% relative difference) while the gap is much smaller for O_2 (3.5%). Other main species such as CO and CO_2, which production rates are shown on Figure 78, show low levels of discrepancies between CANTERA and AVBP. Intermediary species such as CH_3 and OH exhibit interesting profiles: they are produced in the preheating zone (beginning of the reaction zone) before being immediately consumed in the flame, hence featuring a maximum followed by a minimum value.

Both OH peaks are well captured by AVBP while CH_3 exhibits a stiffer evolution. Hence, even if the global profile is well described with AVBP, the peak values are both underestimated. Differences on the production rates may be due to under-resolution despite the high level of refinement of the mesh (Δx being in the micrometer range). Another source of difference is the different calculation of backward rate constants k_j^b in AVBP and CANTERA: both codes use the Gibbs free energy G to compute the equilibrium constant, and hence k_j^b. In CANTERA, thermodynamic NASA polynomials are used to compute G and then the corresponding k_j^b at a given temperature each time it is required. In AVBP, Gibbs free energy is computed beforehand with CANTERA/ARCANE. Then, an Arrhenius law is directly fitted on the k_j^f / K_j ratio (which is equal to k_j^b cf. Chapter 2), using an additional temperature polynomial to perfect the fit if required. Then the chemistry file used by AVBP to compute the production rates directly uses this fitted k_j^b. However, as seen in the graphs previously described, discrepancies remain quite small.

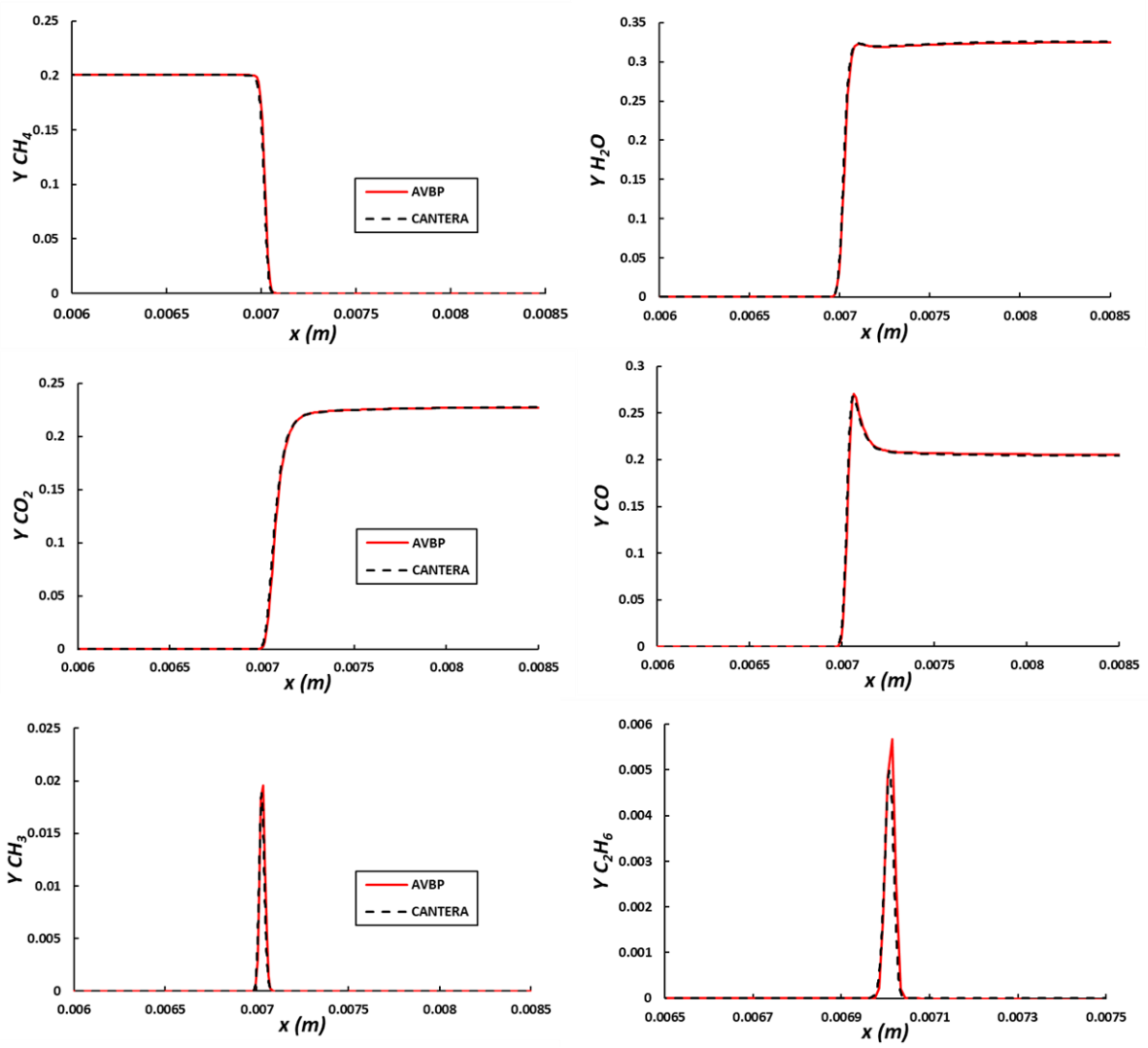

Figure 76: Profiles of mass fractions of various species for a 1D premixed CH_4 / O_2 flame at φ=1 and P=1.36 bar (target 2 of Table 15*) computed with CANTERA vs pseudo 1D AVBP calculations with the Polimi Opti ARC mechanism – zoomed on the flame region*

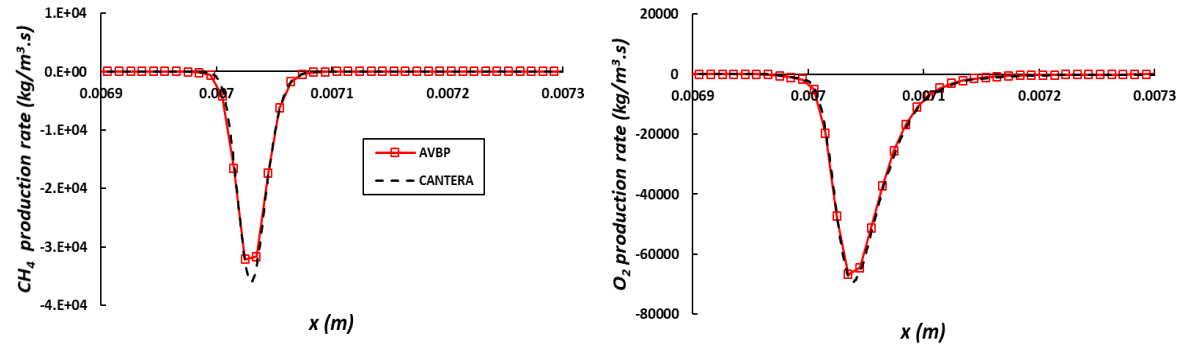

Figure 77: Profiles of production rates for CH_4 and O_2 species for a 1D premixed CH_4 / O_2 flame at φ=1 and P=1.36 bar (target 2 of Table 15*) computed with CANTERA vs pseudo 1D AVBP calculations with the Polimi Opti ARC mechanism – zoomed on the flame region*

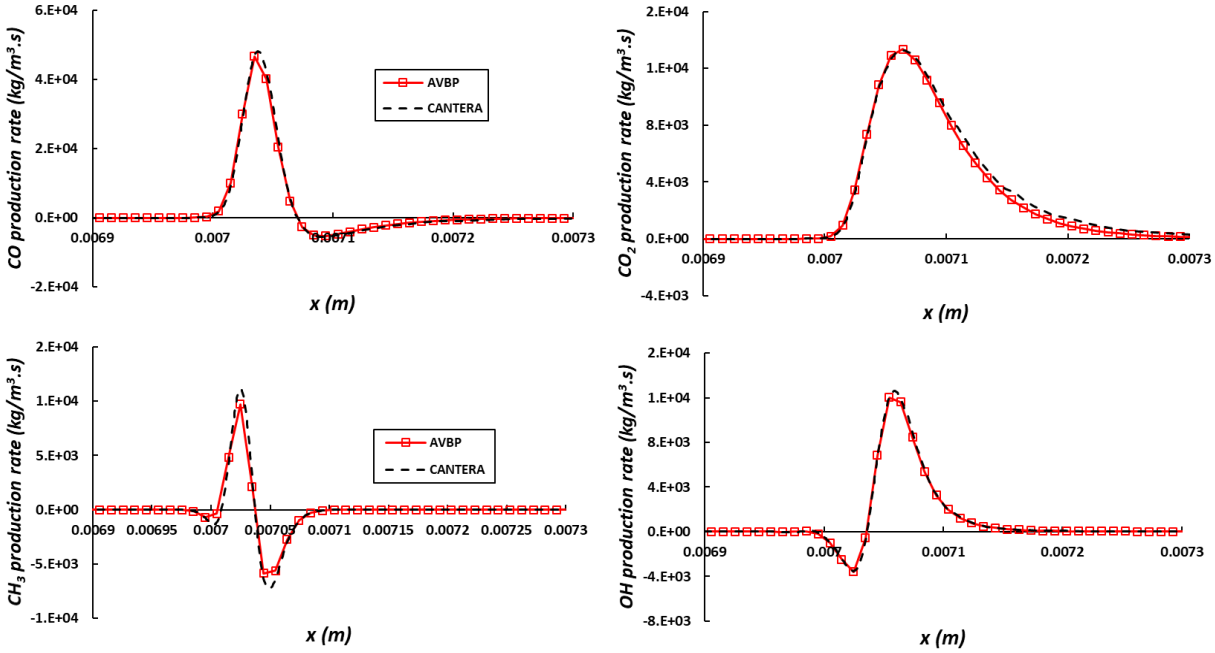

Figure 78: Profiles of production rates for CO, CO_2, CH_3 and OH species for a 1D premixed CH_4 / O_2 flame at φ=1 and P=1.36 bar (target 2 of Table 15*) computed with CANTERA vs pseudo 1D AVBP calculations with the Polimi Opti ARC mechanism – zoomed on the flame region*

The conclusions drawn in this section are identical for the other tested cases (φ=0.5 and 1.5). Hence, the simplified AVBP transport does not seem to affect the chemistry behavior significantly. As the chemistry is also representative of diffusion flames for CH_4/O_2 mixtures, no significant impact of the simplified transport is expected for the 3D REST HF-10 test case.

5.4 The chemical stiffness issue

5.4.1 Chemical timescale

Kinetic mechanisms in given operating conditions are characterized by their chemical timescale τ_c. It is defined as the chemical timescale of the limiting species, hence the one that reacts the fastest in the system. Its numerical definition is the following:

$$\tau_c = min(\tau_{c_k}) = min\left(\frac{[Y_k]}{\dot{\omega}_k}\right) \quad (115)$$

$[Y_k]$ being the concentration of species k and $\dot{\omega}_k$ its production rate. In order to accurately describe the evolution of a chemical system over time, it is crucial that the simulation timestep Δt_{CFL} is smaller than the chemical timescale τ_c. Indeed, if it is not the case, the chemistry is under-resolved in time.

Hence, the temporal evolution of the species mass fractions can be distorted, leading to negative mass fractions. Having really small values of τ_c , meaning a system that evolves in a quasi-instantaneous way is called chemical stiffness. Figure 79 illustrates an example of this situation in a pseudo 1D AVBP calculation for a CH_4/O_2 premixed flame at stoichiometry in the same conditions as in the previous section. The mass fraction profile of C_2H_6 is compared to the 1D CANTERA profile used as a reference. The left graph shows the effect of an under-resolved chemical timescale (i.e., $\Delta t_{CFL} > \tau_c$) leading to oscillations around the equilibrium point, hence wiggles and eventually non-physical slightly negative values of $Y_{C_2H_6}$. On the right graph a well-resolved chemical timescale (i.e., $\Delta t_{CFL} < \tau_c$) shows a correct mass fraction profile (almost no wiggles and a positive Y_k).

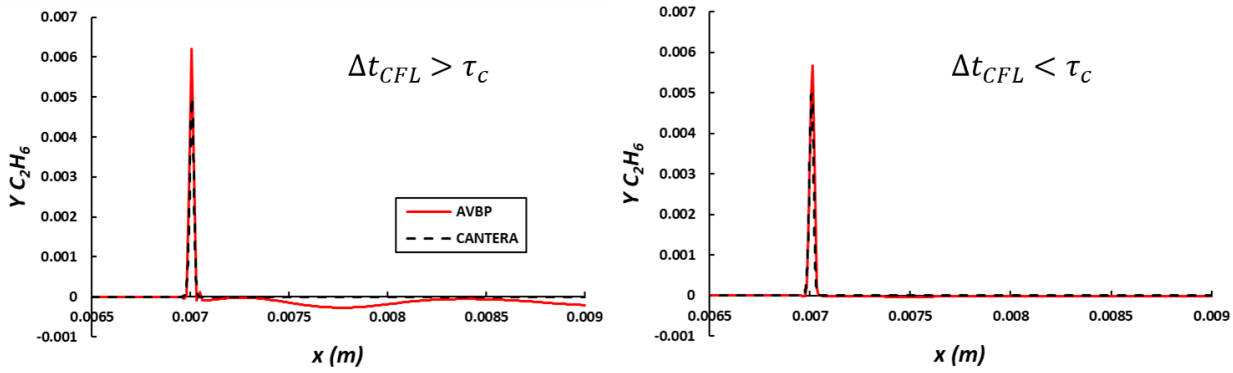

Figure 79: Profiles of C_2H_6 mass fraction species for a 1D premixed CH_4 / O_2 flame at φ=1 and P=1.36 bar (target 2 of Table 15) – the left graph shows an under-resolved chemical timescale while the right graph shows a well-resolved chemical timescale

As mentioned in the previous section, the simulation timestep is directly driven by the mesh. The typical time steps for LES of rocket engines combustion chambers are quite small, of the order of magnitude of 1 to 5 x 10^{-9}s. However, the characteristic chemical timescale τ_c can be even smaller. Indeed, rocket engine conditions are prone to enhance chemical stiffness as described in [23]. Diffusion flames with high value of strain rate lead to high heat release rates, meaning more chemical stiffness with thinner reactive zone, requiring a better spatial discretization. Furthermore, higher pressures lead to higher reaction rates as the temperature increases. Hence, it also leads to more chemical stiffness.

It is possible to estimate the chemical timescales of all the transported species of the mechanism (and eventually τ_c) before performing the 3D LES calculations from 1D representative cases as illustrated on Figure 80. However, it is important to keep in mind that the real 3D value of τ_c can be different from the previous evaluation as the 3D case may deviate from the representative 1D cases, and that chemically stiff zones can be very localized. Indeed, in the REST HF-10 case, it is generally in the flame region at the injector lips where the reactive zone is spatially thinner compared to the rest of the domain.

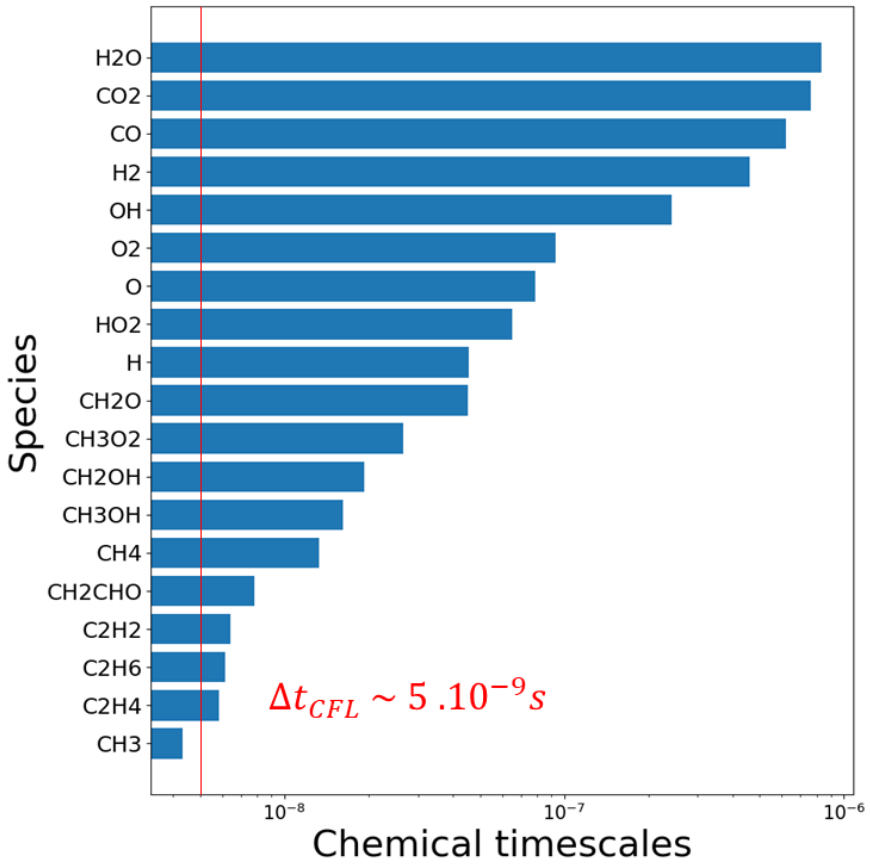

Figure 80: Example of chemical timescales obtained with the Polimi Opti ARC mechanism for a 1D diffusion flame at P=120 bar and χ=1500 s^{-1}computed with CANTERA

In the example of Figure 80, CH_3 has the smallest chemical time scale, hence it imposes τ_c. In this case, it is the only species causing a direct problem since the Δt_{CFL} is low enough. The stiffer species are generally intermediary species, such as C_2H_2 or C_2H_6 in our example. However, it can be enough to trigger species mass fraction issues as methyl is involved in many key reactions already identified in the previous sections. One can also notice that the fuel CH_4 has a quite low chemical time scale compared to other species, which can be problematic when trying to reduce the stiffness. Finally, as mentioned before, it is important to keep in mind that Figure 80 approximates what could be encountered in the 3D case, hence species are potentially even stiffer.

5.4.2 How to deal with chemical stiffness: state of the art

6 The evolution of chemical source terms over time (i.e., the variation over time of the production rates $\dot{\omega}_k$) is described by the following initial value problem (IVP) :

$$\begin{cases} \dfrac{\partial(\rho Y_k)}{\partial t} = \dot{\omega}(\rho Y_k, T) \\ Y_k(0) = Y_k^0 \end{cases} \tag{116}$$

The initial mass fraction of species k noted Y_k^0 is known and the production rate of the same species $\dot{\omega}(\rho Y_k, T)$ is a function of the mass fractions and time. In order for the chemical system to evolve, the

IVP is advanced in time with the known source terms to get the mass fraction of species k at the next timestep $\rho Y_k^{t+\Delta t_{CFL}}$. Once it is obtained, the chemical source term can be updated :

$$\dot{\omega}\ (t + \Delta t_{CFL}) = \dot{\omega}(\rho Y_k^{t+\Delta t_{CFL}}) = \frac{\rho Y_k^{(t+\Delta t_{CFL})} - \rho Y_k^{(t)}}{\Delta t_{CFL}} \tag{117}$$

In AVBP the default resolution method for the IVP is explicit, based on an Euler method. An explicit resolution means that the solution at the instant $t + \Delta t_{CFL}$ (i.e., $\rho Y_k^{(t+\Delta t_{CFL})}$) only depends on the previous instant t:

$$\rho Y_k^{(t+\Delta t_{CFL})} = \rho Y_k^{(t)} + \dot{\omega}(\rho Y_k^{(t)})\Delta t_{CFL} \tag{118}$$

The main disadvantage is that this method is directly time-step dependent. Hence, if the latter is too large (which is typically the case in stiff problems), it can trigger instabilities and eventually lead to numerical divergence [161].

In order to overcome this issue, several approaches have been developed. The simplest one consists in using the quasi steady state approximation (QSSA) [158]. It can be applied on radical species which concentration does not vary much over time (hence are consumed just after being created). Their concentrations can then be computed analytically as function of non-QSS species concentrations. Since the QSS species are not transported anymore, the global stiffness of the chemical system is decreased. As mentioned before, this operation can be done with the ARCANE tool during a reduction process. Depending how much error is tolerated during the reduction, more or less species can be concerned. However, some intermediary species have concentration evolutions that are not fast enough over time to be accounted as QSS (for example C_2H_4 or C_2H_6 in the REST HF-10 case). This is all the more the case with high values of strain rate and pressure. Moreover, as seen in Figure 80, CH_4 is also one of the stiffest species and cannot be treated with the QSSA as it is a reactant. This means that other tactics need to be used to reduce the stiffness of the system.

Another approach is subcycling. It consists in solving the IVP by iterating several times over N_{SC} chemical timesteps for one CFL time step. Hence, it leads to the following chemical timestep definition: $\Delta t_{chem} = \Delta t_{CFL}/N_{SC}$. Subcycling avoids the re-evaluation of the Navier-Stokes equations at each iteration while maintaining a good precision for the chemistry. However, the method directly impacts the efficiency of the calculation (i.e., the number of iterations per second). Moreover, as mentioned before, the chemical stiffness is generally very localized. Hence, there is no use for subcycling the chemistry in the entire domain. To tackle this issue, local subcycling methods based on a dynamic sensor are currently developed. Typically, the Local and Dynamical Sub-Cycling procedure (LDSC) developed by A. Pestre [161] featuring a sensor based on τ_c shows interesting results. However, as the number of subcycles are not distributed in a homogenous way, an efficient partitioning need to be performed to avoid load balancing problems that can penalize the computation efficiency.

Other methods were proposed to deal with stiffness by suggesting different ways to solve the IVP. Blanchard [66][23] developped a method called "exponential chemistry", which consists in expressing the production rate as a linear function based on two coefficients $\rho Y_k . A_k$ and B_k, being respectively the sum of the contributions to destruction and creation of species k of the reactions involving it. Such relation can be solved analytically, leading to an expression of $\rho Y_k^{t+\Delta t_{CFL}}$, allowing to finally compute $\dot{\omega}\ (t)$. The method increases the robustness of the source term resolution by avoiding oscillations around the equlibrium as long as the time step is small enough. It was notably tested on 2D CH_4/O_2

diffusion flames and on rocket engines combustion chambers cases (CONFORTH and REST-HF-10 [23]). However, the main drawback is that it is not mass conservative by construction. Hence, a correction step is necessary (detailed in [66,158]). In order not to impact the performances, it is performed only on the species with the largest concentrations. This can sometimes lead to issues in the prediction of the mass fractions of some combustion products [161].

5.4.3 Implicit solving of the chemical source terms

In order to face the stability problem triggered by small time steps, another form of integration of the chemical source terms can be proposed: the implicit resolution. This time, the solution at the instant $t + \Delta t_{CFL}$ depends simultaneously on t and $t + \Delta t_{CFL}$:

$$\rho Y_k^{(t+\Delta t_{CFL})} = \rho Y_k^{(t)} + \dot{\omega}(\rho Y_k^{(t)}, Y_k^{(t+\Delta t_{CFL})}) \Delta t_{CFL} \tag{119}$$

By definition, implicit resolution is unconditionally stable. Hence, it is especially suitable for the resolution of stiff problems, allowing to solve the IVP with important timesteps and high robustness where for explicit integration small values of Δt_{CFL} would be required in order to converge. However, it comes with an important computational cost at each iteration that can be prohibitive for 3D applications. Indeed, the gain entirely depends on the time step ratio between explicit and implicit integration if the latter allows to increase the CFL for example. However, the implicit method can also be used as a temporary solution during the time necessary to stabilize/evacuate a stiff transient phenomenon (for example when changing the kinetic mechanism during the calculation in order not to start over from ignition) before switching back to an explicit method.

The operating conditions of the REST HF-10 case (highly strained diffusion flame at high pressure) makes the POLIMI Opti chemistry very stiff. Hence, during the evacuation of the transient solution, a high number of subcycles (from 150 up to 300) as well as a low CFL (0.5 to 0.3) are necessary for the computation to run. As the calculation already exhibits very low time steps of the order of magnitude of the nanosecond, the high impact of subcycles on the efficiency makes the computation very costly. Moreover, those parameters do not increase the robustness of the simulation. Hence, implicit integration seems like a reasonable option to treat the stiff transient phases.

5.4.4 CVODE solver coupling with AVBP

As AVBP natively only proposes explicit integration for the chemical source terms, a coupling with an implicit solver was made. CVODE [188,189] is a solver coded in C for stiff and non-stiff ordinary differential equations (ODE) which suits the targeted application. For stiff problems resolution, it contains the BDF (backward Differentiation Formulas) method [189]. CVODE can be parametrized (for example in terms of maximum number of internal steps allowed, number of convergence tests, etc.) in order to be adapted to a specific problem. Hence, in order to test the implicit resolution of the chemical source terms, CVODE was coupled to AVBP during the thesis. Figure 81 shows in a simplified way how it was integrated in the LES code.

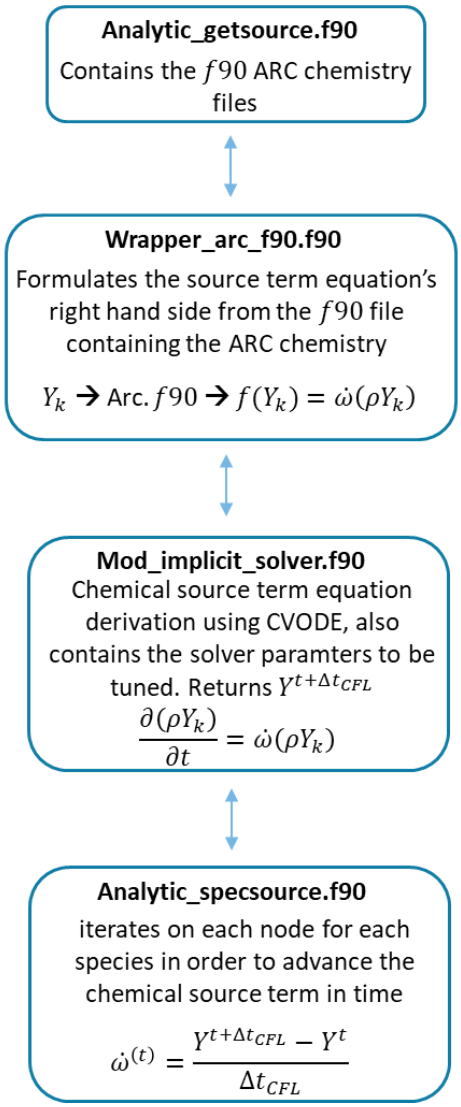

Figure 81: Simplified scheme of CVODE integration in the AVBP code

In AVBP, the ARC mechanisms are stored as separate f90 files containing all the necessary kinetic parameters (forward and backward reaction rates Arrhenius relations, analytical expression of the QSS species concentration, evaluation of the reaction rates etc.). Hence a special function called "Wrapper" is used to formulate the reaction rate of each species k as a function of its mass fraction Y_k. It is then coupled to the "Mod_implicit_solver" function that calls the CVODE solver and controls its parameters. Once $Y_k^{(t+\Delta t_{CFL})}$ is returned, it is used to update the source term of each species thanks to the "Analytic_specsource" function.

5.4.5 1D validation of the CVODE coupling

Once CVODE was coupled to AVBP, a 1D validation on a pseudo 1D AVBP CH_4/O_2 premixed flame at stoichiometry was performed. The conditions are similar to the one of the previous sections (target 2 of Table 15) using the same mesh, representative of the 3D application case. The profiles obtained with the implicit integration with CVODE are then compared to the ones obtained with the classical explicit integration, with the 1D CANTERA calculation as reference. As the 1D case is a premixed flame at low pressure, the chemistry stiffness is not pushed to levels comparable to REST HF-10 case. Hence,

as shown before, no subcycling is required and the CFL number in the explicit case does not need to be decreased. This means that an implicit resolution approach will have no performance advantage on the explicit resolution as the Δt_{CFL} will be identical for both cases (CFL = 0.7 with Lax-Wendroff convective scheme). However, the 1D case allows to verify the good functioning of the CVODE solver and to ensure its correct coupling with AVBP. The implicit and explicit calculations were run for the same amount of time on the same number of cores to be comparable (12 Xeon Gold 6140 on CERFACS's KRAKEN cluster). Results are shown on Table 19.

Solving method	**Explicit**	**Implicit**
# of subcycles	0	0
Δt_{CFL} (s)	2.512E-9	2.512E-9
Average efficiency (ite/s)	503	160
Total simulated time (s)	2.22E-3	0.07E-3

Table 19: performances obtained during the validation of the CVODE solver for a 1D AVBP premixed flame

The table highlights the clear gap in efficiency between the 2 solving methods, leading to a simulated time more than 300 times larger in the explicit case than the implicit. However, the simulated 7 ms of the implicit method featured in Table 19 are enough for the implicit calculation to converge. Results are displayed on Figure 82.

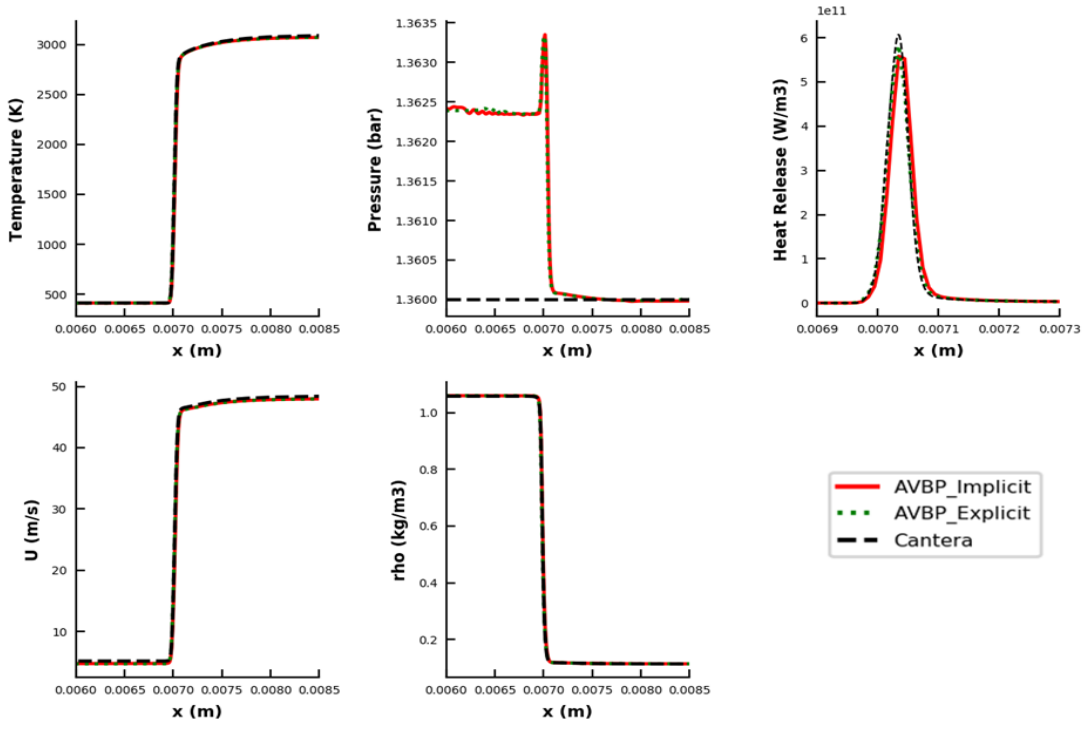

Figure 82: Profiles for a stoichiometric CH_4/O_2 flame (conditions of target 2 of Table 15*) with AVBP explicit and implicit integration of the chemical source terms vs CANTERA with the Polimi Opti ARC mechanism – zoomed on the flame region*

All profiles of temperature, pressure, heat release rate, speed and density match between the explicit and implicit integrations (the pressure difference between AVBP and CANTERA on the fresh gas side was already addressed in a previous section). These observations are identical for species profiles and reaction rates (see examples on Figure 83). Hence, this test validates the coupling of the CVODE solver with AVBP.

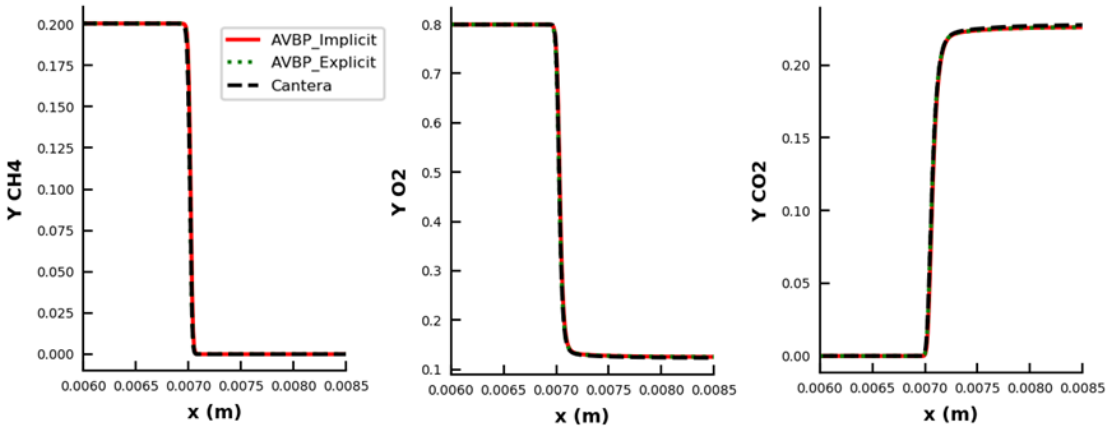

Figure 83: Mass fraction profiles for a stoichiometric CH_4/O_2 flame (conditions of target 2 of Table 15*) for AVBP pseudo 1D calculations for explicit and implicit solving of the chemical source terms vs CANTERA with the Polimi Opti ARC mechanism – zoomed on the flame region*

5.4.6 Implicit integration applied to 3D LES

To assess the performance of implicit chemistry integration in 3D LES, twelve-hours runs were conducted on the REST HF-10 configuration for three different cases as illustrated on Table 20. Each calculation used 15 nodes of CERFACS's KRAKEN cluster, corresponding to 432 Xeon Gold 6140 cores. In order to initialize the calculation, an existing solution of a run performed with the RAMEC ARC was used. The kinetic model was changed and species from POLIMI Opti ARC absent from the solution were added while the non-necessary ones were removed. Then, computations were performed during a full convective time (i.e. 1 ms) in order to evacuate potential transient phenomena. Once this process is completed, the benchmark study can be performed.

The implicit integration with CVODE was compared to 2 explicit integration cases: one with 300 subscycles and the other one with 150, both with a CFL of 0.3. These settings correspond to the working parameters initially used for the REST HF-10 computations with the Polimi Opti ARC mechanism. Indeed, an increase in CFL or a decrease in the number of subcycles in these conditions inevitably led to a crash of the calculation. For each case, the LW convective scheme is employed as it is precise enough, less costly and more robust than TTGC, hence helping when dealing with stiff combustion.

As shown on Table 20, the robustness of the implicit method allows to run a 12h calculation without any subcycle and a CFL of 0.7. Such parameters are out reach with the AVBP-native explicit integration of the chemical source terms for the current REST HF-10 calculation with the Polimi Opti ARC mechanism. Hence, the use of an implicit solver allows to employ larger timesteps while being stable. It is also interesting to note that, as expected with the used parameters, the efficiency is not comparable with the pseudo 1D computations, whether in the case of the explicit or implicit

integration. For example, for the latter the computation is 800 less efficient than in 1D, the ratio being higher for explicit methods. This highlights the high cost of 3D LES computations.

Test case	Explicit 300 SC	Explicit 150 SC	Implicit 0 SC
# of subcycles	300	150	0
CFL	0.3	0.3	0.7
Convective scheme	LW	LW	LW
Δt_{CFL} (s)	3.27E-09	3.28E-09	7.9E-09
Average efficiency (ite/s)	0.19	0.37	0.19
Total # of iterations	8191	15660	7776
Total simulated time (s)	26.64E-06	51.28E-06	45.2E-06

Table 20: performances obtained for implicit calculations of the chemical source terms in 3D AVBP calculations of the REST-HF-10 configuration with the Polimi Opti ARC mechanism. Comparison with 2 different explicit integration cases

Even if the implicit integration has a high computational cost, it is competitive against explicit computation for the REST HF-10 configuration. Indeed, the efficiency reported in Table 20 and Figure 84, show that, despite being as efficient as the explicit 300 SC case at CFL = 0.3 with 0.19 iterations per second, the use of implicit integration allows to compute 88% of the total simulated time reached by the explicit 150 SC case (which is the most efficient of this study) thanks to a higher CFL which leads to a bigger time step. Hence, it is competitive compared to the explicit 300 SC case which cannot reach more than 51.9 % of the 150 SC case total simulated time. This conclusion is highly interesting since the 300 SC case conditions are the one used for the REST HF-10 simulation initial calculations (150 SC being too unstable for long runs). Moreover, apart from larger time steps, the main advantage of the implicit integration remains its robustness. Its unconditional stability is highly appreciable for computations like the REST HF-10 case.

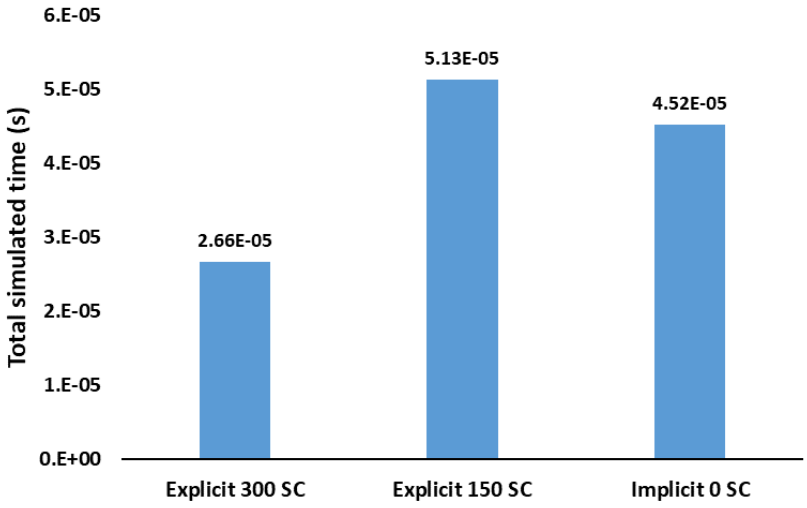

Figure 84: Performances in terms of total simulated time for the implicit solving with CVODE compared to the explicit approach for the REST HF-10 3D AVBP calculation

Hence, the implicit resolution of the chemical source terms is used for the initial phases of the REST HF-10 calculations, allowing to evacuate the stiff transient phenomena due to the change of ARC chemistry (i.e., for at least one convective time, roughly equivalent to 1 ms in the studied case). Once this is passed, the simulation. Returns back to explicit integration with most efficient settings (i.e., a number of subcycles smaller than 150). Moreover, as the coupling of CVODE with AVBP was proved to be functional, efficient and robust for the studied case, it is currently used for other applications such as ignition transient in other configurations.

5.5 REST HF-10 calculation results and analysis

5.5.1 Calculation parameters

Table 21 presents the main calculation parameters used in AVBP for the reference case (using RAMEC ARC used in [190]) and the computations based on the newly developed POLIMI Opti ARC chemistry.

	RAMEC ARC Reference	**POLIMI Opti ARC Full explicit**	**POLIMI Opti ARC Implicit (transient phase)**	**POLIMI Opti ARC Explicit (stable phase)**
LAD threshold	5	2	2 to 3	2
LAD coefficient	1	2	1.5	1.5
Convective scheme	TTGC	LW	LW	LW
CFL	0.7	0.2	0.2	0.3
# of subcycles (SC)	**6**	**300**	**0**	**50**
Efficiency (ite/s)	0.9	0. 19	0.19	1.6
Δt_{LES} (s)	8.48E-09	2.00E-09	2.00E-09	3.23E-09
average τ_c (s)	2.53E-10	2.35E-11	2.35E-11	2.35E-11
min τ_c (s)	6.83E-11	1.57E-11	1.57E-11	1.57E-11

Table 21: REST HF-10 main calculation parameters in AVBP

Three cases have been consecutively run with the POLIMI Opti ARC mechanism. The first one (full explicit) refers to the initial methodology based on explicit integration with subcycling. As mentioned in the previous section, it required a high number of subcycles (SC=300) as well as a low CFL (0.2) to guarantee numerical stability. This is explained by the high stiffness of the chemistry in the extreme conditions of the REST HF-10 test case, as given by the minimum chemical time of 1.57 10^{-11} s to be compared to the CFL timestep of 2. 10^{-9} s. In the reference RAMEC ARC case, one can see that the minimum τ_c encountered during the calculation is only slightly higher, but as it is reached for a small

number of iterations the average chemical time step τ_c (defined as the smallest τ_{c_k} among the species on average during a full run) is only one order of magnitude lower than the CFL time step Δt_{LES}. Hence, the reference calculation requires ony SC=6 subcycles, while the POLIMI Opti ARC requires SC=300 due to an average τ_c that stays low. This extreme stiffness was not detected by the 1D calculations as was displayed in Figure 79. In 3D LES computations phenomena linked to the interaction with turbulence may have a non-negligible impact on τ_c.

In order to overcome this issue and evacuate the transient phenomena due to the change of the chemical scheme during the initialization (cf. section 5.4.6), implicit time integration of the chemical source terms was used in the first times of the simulation (column "Implicit (transient phase)" in Table 21). As mentioned in the previous section, this type of integration allows to avoid subcycling while remaining stable, and therefore to be more efficient compared to the 300 SC case. It is used to compute one convective time scale (which is 1 ms for REST HF-10), before switching back to explicit integration. Because the computation is more stable once the transient phase has been passed, it is possible to decrease the number of SC by a factor 6 (i.e., from the initial 300 to 50). In addition, the CFL number can be increased up to 0.3. Hence the efficiency is far better, and the simulation can be run long enough for time averaging (column “explicit (stable phase)” in Table 21) The simulation is then run for 4 convective times (i.e., 4 ms) as was done for the reference RAMEC ARC case [180].

The difference in efficiency between the RAMEC ARC computation and the POLIMI Opti ARC Explicit one mainly come from the difference in convective scheme (which effect is analyzed in the following section). Indeed, TTGC's cost is roughly 2 times the one of LW. In the REST HF-10 case, this ratio is lowered to 1.7 since the POLIMI Opti ARC Explicit calculation requires 50 SC versus 6 for the RAMEC ARC. Hence, despite using an expensive convective scheme, the lower stiffness of the RAMEC ARC chemistry allows a larger time step, hence a higher computation speed.

Finally, the RAMEC and POLIMI Opti ARC calculations also differ in the Localized Artificial Viscosity (LAD) parameters. The lower the "LAD threshold", the more artificial viscosity is activated at locations of high density gradients. The higher the "LAD coefficient", the more diffusion is applied to the gradients. Overall the POLIMI Opti ARC cases use lower threshold and higher coefficient than the RAMEC ARC case because of higher chemical stiffness. The effect of these parameters (as well as the convective scheme) on the flow and the flame structure are analyzed in the next section.

5.5.2 Convective scheme, LAD activation and flame topology

Impact of the convective scheme:

As mentioned in the previous section, the POLIMI Opti ARC calculations were conducted with the LW scheme because of its robustness, low cost and sufficient precision. However, the lower global stiffness of the RAMEC ARC calculation allowed the use of the higher order TTGC scheme in order to tend to a more accurate solution [180]. Hence, an intermediate check needs to be performed before directly comparing the two calculations in order to assess the impact of the convective scheme for REST HF-10. In order to do so, a RAMEC ARC calculation was performed using the LW scheme. In order to limit the computation costs, the run was 0.5 convective time (i.e. 0.5 ms) long. Checks have shown that this simulation time was enough to reach a steady state (no more significant temporal evolution of the target pressure and mass flow rates) making it possible to compare the RAMEC ARC TTGC and LW computation.

In order to first assess the impact on the flow topology, fields of the velocity magnitude are investigated . Figure 85 represents a longitudinal cut of the REST HF-10 computational domain.

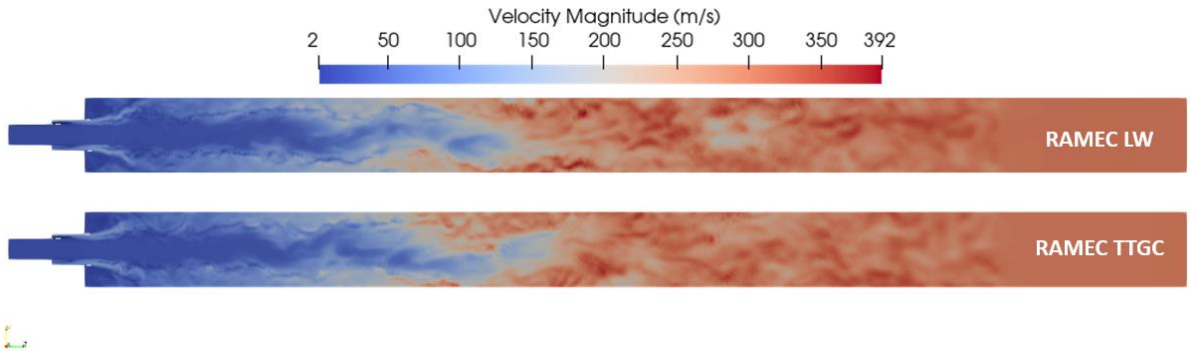

Figure 85: Longitudinal cuts of instantaneous velocity magnitude fields for REST HF-10. RAMEC ARC computation with LW scheme on the top, TTGC on the bottom

Qualitatively speaking, the flow structure seems globally identical with both convective schemes. The numerical values also seem similar, showing an acceleration of the flow in the chamber as the distance from the injector increases.

In order to precisely assess the impact of the convective scheme in the reactive zone, a PDF of the scalar dissipation rates is extracted in an area close the injector where a characteristic diffusion flame can be found. This operation is performed for both LW and TTGC cases, similarly to what was done in section 5.3.1 (same area if extraction) and shown on figure Figure 67. The results for the RAMEC ARC calculations are presented on Figure 86.

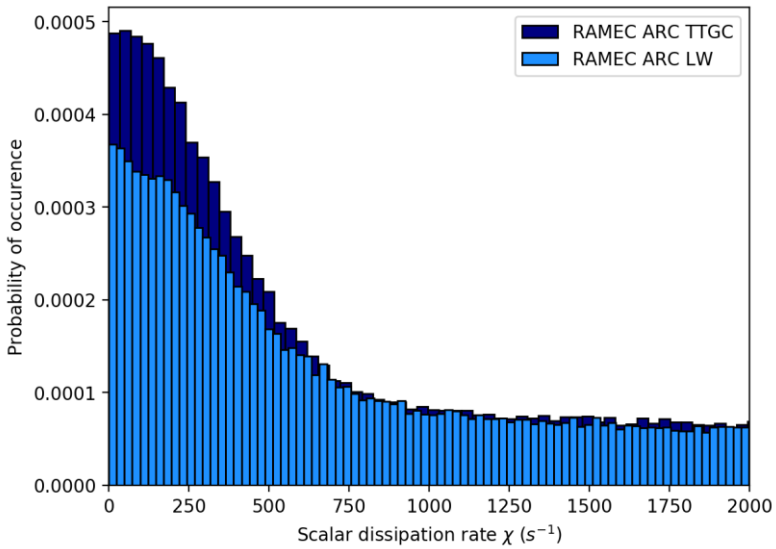

Figure 86: Statistics of scalar dissipation rate in the injection zone of the REST HF-10 test case with RAMEC ARC chemistry for computations with TTGC and LW convective schemes

One can see that the PDF structures are quite similar, the order of magnitude of probability of occurrence for a given χ being identical. Hence the flame structure of the TTGC computation case is well recovered by the LW one. These conclusions support the comparison of the ARCs RAMEC TTGC computation to the POLIMI Opti LW one in the context of REST HF-10. One possible explanation of the

convective scheme not strongly impacting the flame structure with iso-chemistry for the REST HF-10 case could be the very fine mesh in the reactive zone (cf. section 5.2.3).

LAD and flow topology:

In order to investigate the effect of the Localized Artificial Diffusivity activation in the REST HF-10 configuration, Figure 87 displays longitudinal cuts of instantaneous solutions close to the injector It features the "av_threshold" variable field. The latter describing where the LAD is applied. The higher the value, the more intensively artificial diffusivity is applied. Three different calculations are investigated: respectively from top to bottom POLIMI Opti with LW, RAMEC with TTGC and the RAMEC LW test case.

The center image of Figure 87 shows the reference calculation with the RAMEC ARC mechanism and TTGC scheme. One can see that the LAD is activated at a high level in a large area starting in the recess zone (i.e., as soon as CH_4 is injected). These activation zones follow the density changes induced by the flame. The bottom image of the figure shows the same calculation, this time with the LW convective scheme. Interestingly, as LW is more dissipative than TTGC, the LAD is far less applied (thinner and less regular zones). However, it is still present in the recess. The similarities in the application areas suggest once again that the convective scheme does not strongly impact the flame structure at iso-chemistry for REST HF-10. Finally, the top image of Figure 87 shows the POLIMI Opti ARC calculation using LW and the LAD parameters introduced in Table 21. Despite the latter parameters being stricter because of a higher global stiffness, LAD is almost not activated in the injection zone and appears in a more pronounced way downstream the recess in the flame zone. Overall, in the injection zone the "av_threshold" field seems weaker than in the RAMEC-ARC calculation with LW and TTGC. As the only difference between the top and bottom cases is the ARC chemistry, this implies that the RAMEC ARC chemistry could trigger stronger density gradients than the POLIMI Opti.

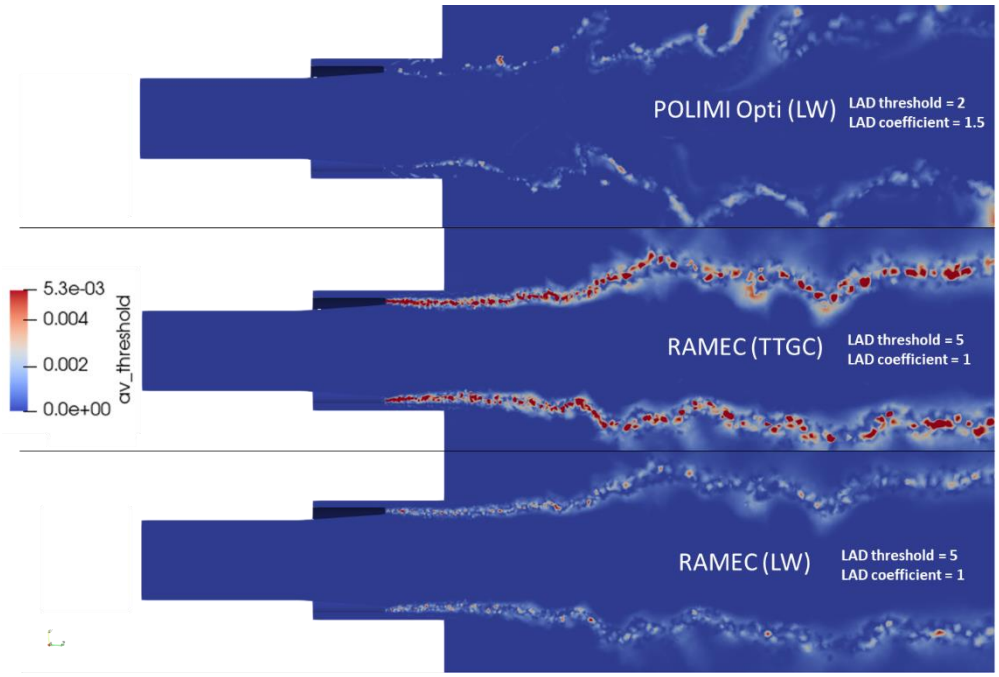

Figure 87: artificial viscosity activation (av_threshold) in the injection zone of the REST HF-10 case for different convection schemes and chemical mechanisms – longitudinal cut of instantaneous fields

This behavior finally affects the flame structure as can be seen on Figure 88. The POLIMI Opti-ARC calculation exhibits a much more turbulent flame than the RAMEC-ARC cases. Indeed, the application of LAD directly at injection tends to laminarize the flow and the flame due to added artificial viscosity.

Flame topology:

In order to visualize the flame structure, longitudinal cuts of instantaneous temperature fields are displayed on Figure 88 for the RAMEC and POLIMI Opti ARC calculations.

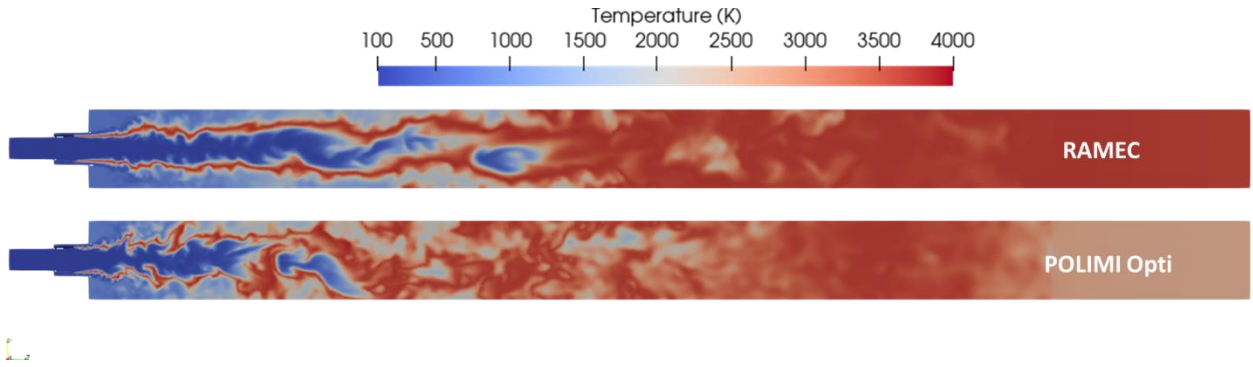

Figure 88: Longitudinal cuts of instantaneous temperature fields for REST HF-10. POLIMI Opti ARC computation on the top, RAMEC ARC on the bottom

If both cases feature a diffusion flame anchored at the injector lips, one can see that the flame is far more flat in the RAMEC ARC case (top) than the POLIMI Opti ARC computation (bottom), where turbulent structures wrinkle the flame front as soon as it leaves the injector zone. This behavior is confirmed by the velocity magnitude fields displayed on Figure 89 which allow to appreciate the flow wrinkles (bottom).

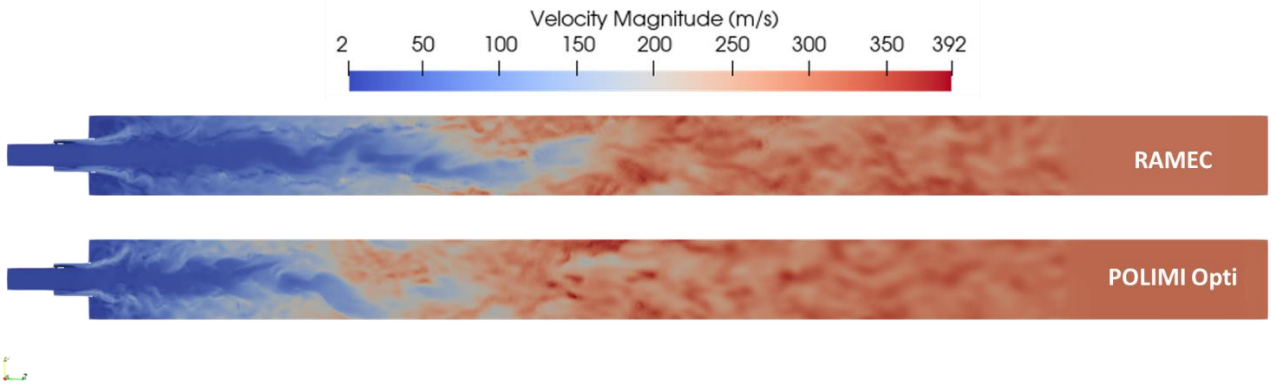

Figure 89: Longitudinal cuts of velocity magnitude fields for REST HF-10. POLIMI Opti ARC computation on the top, RAMEC ARC on the bottom

The difference in flame topology is also visible on the time-averaged fields as seen on Figure 90 which represents the average temperature fields for both chemistries. As mentioned before, all the results were averaged over 4 convective times (i.e., 4 ms).

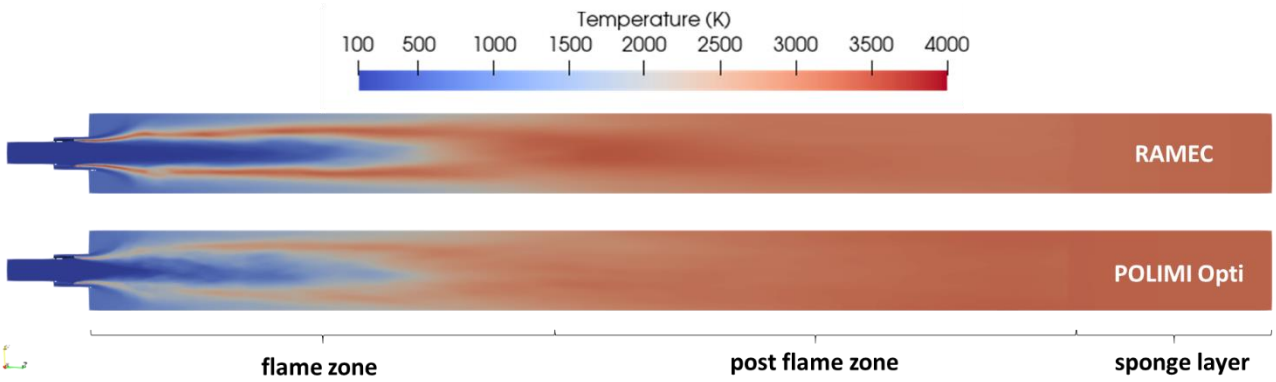

Figure 90: Longitudinal cuts of time-averaged temperature fields for REST HF-10. POLIMI Opti ARC computation on the bottom, RAMEC ARC on the top

The effects of turbulence on the POLIMI Opti ARC case lead to a much more diffused reactive zone than in the RAMEC ARC case. However, it is interesting to notice that the overall flame length (labelled as "flame zone" on the figure) seems quite similar between the two chemistries. In the "post flame zone", the RAMEC ARC chemistry leads to slightly hotter combustion products. This is again a consequence of lower turbulence intensity, as seen on the instantaneous fields of Figure 88, where less mixing between the cold and hot gas occurs and larger pockets of hotter gases appear. Finally, the last 5 cm of the chamber consist in a sponge layer for both cases, as indicated by the case definition recalled on Figure 64.

As diffusion flames are located around stoichiometry line is the location, another way to visualize more clearly the flame zone and assess its length is to plot an isocontour of the stoichiometric mixture fraction (Z_{St}=0.2 for CH_4/O_2 mixtures) as done in Figure 91 focusing on the first third of the combustion chamber. The figure is a longitudinal mirror plot featuring the RAMEC ARC results on the top and the POLIMI Opti ARC on the bottom. One can see that the obtained flame length with POLIMI Opti ARC is slightly shorter than the RAMEC ARC one. However, both remain in close agreement, confirming the conclusions of Figure 90.

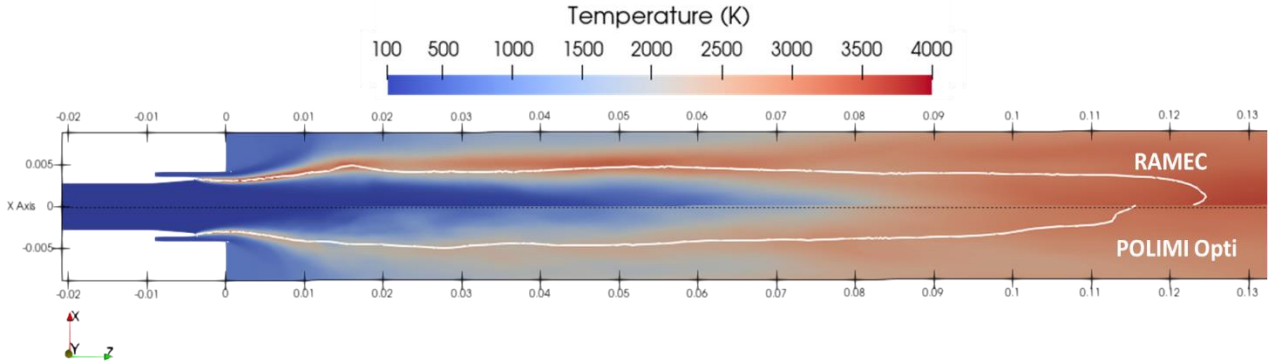

Figure 91: Longitudinal mirror cut of the average temperature field for RAMEC ARC and POLIMI Opti ARC chemistries, first third of the chamber. White line corresponds to stoichiometry.

It also important to keep in mind that a mixture at the stoichiometric line does not necessarily burn in any conditions. Hence a complementary analysis by plotting average mirror fields of the heat release rate as shown on the longitudinal mirror plots of Figure 92 is required.

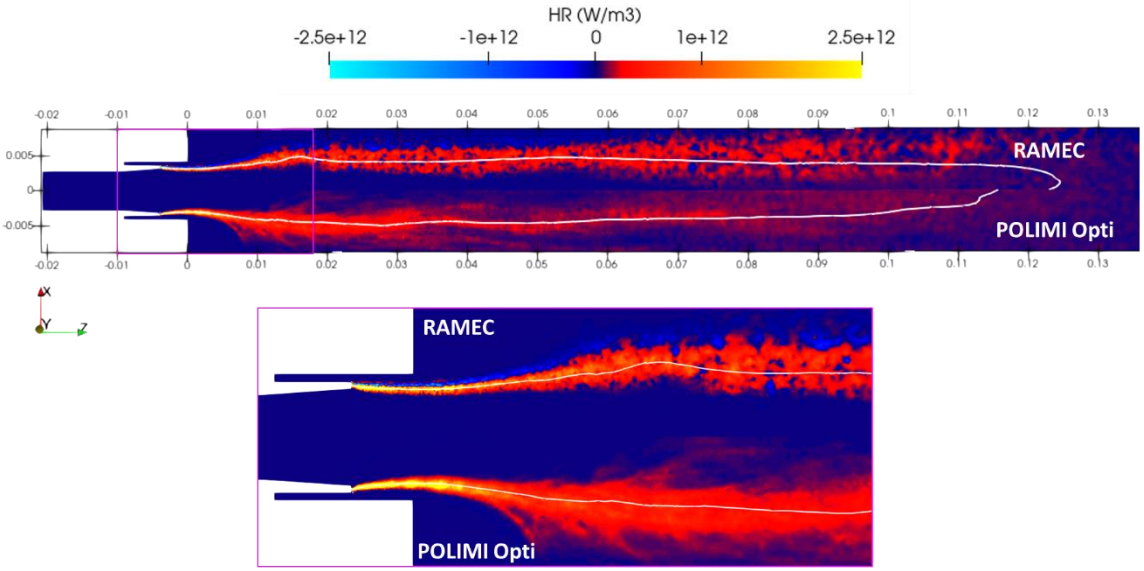

Figure 92: Longitudinal mirror cuts of the average heat release rate fields for RAMEC ARC and POLIMI Opti ARC chemistries, first third of the chamber. White line corresponds to stoichiometry. Bottom : zoom on the injector zone.

One can see that, as expected, the maximum heat release rate perfectly follows the Z_{St} line which is characteristic of a diffusion flame. On the top image, one can also see that the overall field of heat release rate is spottier and slightly thinner in the RAMEC ARC case compared to the POLIMI Opti ARC case, due to both effects of chemistry stiffness and lower turbulence intensity. In addition, the heat release rate intensity strongly decreases after z = 3cm in the POLIMI Opti Arc scheme. In order to understand this difference, the bottom part of Figure 92 features a zoom on the injector region. One can see that the heat release zone is broader for POLIMI Opti ARC on both sides of the Z_{St} line, as a result of the higher turbulence level described at the beginning of the section. This leads to a more intense combustion in this zone, hence a slightly shorter flame.

Another way to visualize the effect of turbulence on the flame structure is to look at the scatter plot extracted form average fields in the same zone as the PDFs of scalar dissipation rates were taken from. Figure 93 represents these scatter plots for the RAMEC and POLIMI Opti ARC calculations. The data is compared to temperature profiles from two reference 1D laminar diffusion flames from Cantera computed with the corresponding chemistry to serve as a reference. These computations were conducted for the minimum and maximum scalar dissipation rates used for the mechanism reduction with ARCANE (respectively χ=100 and 1500 s^{-1} cf. Table 14) in order to cover the extremum cases.

One can see that for both cases, the structure of the 1D laminar diffusion flame is well recovered. However, the RAMEC ARC calculation captures it best, with slight discrepancies on the rich side. POLIMI Opti however, even if following the global temperature profile evolution, displays a much more scattered profile with lower values than the Cantera reference for lean and stoichiometric conditions. This type of shift and scattering is directly induced by turbulence (cf. [180] where it is also observed when comparing ARC and IFCM chemistries – the latter being coupled with a beta-pdf).The same conclusion can be drawn from scatter plots of species mass fraction as shown on Figure 94.

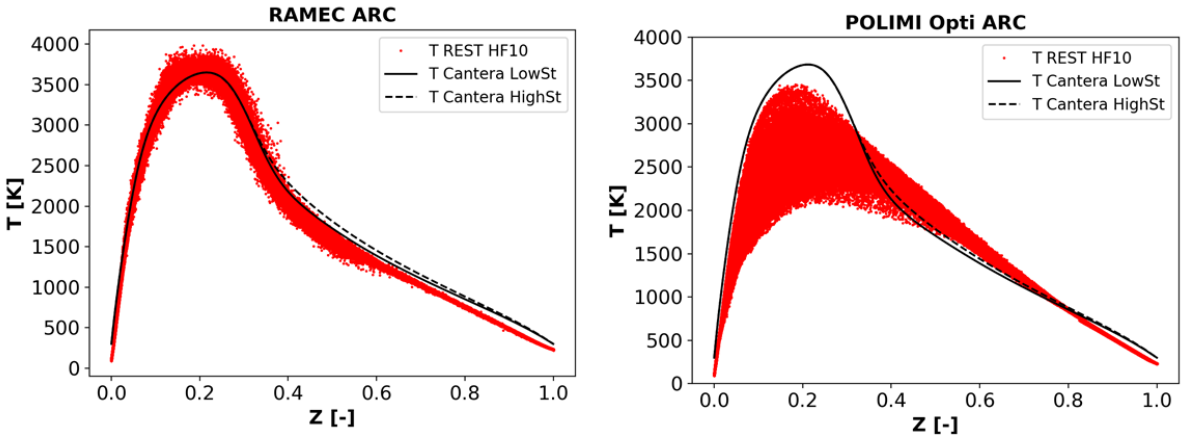

Figure 93: Scatter plots of temperature in the extraction zone close to the injector for RAMEC ARC calculation (left) and POLIMI Opti (right). 1D Cantera temperature profiles for a laminar diffusion flames at 100 bar for min (Low St) and max (High St) target scalar dissipation rates of reduction are superimposed

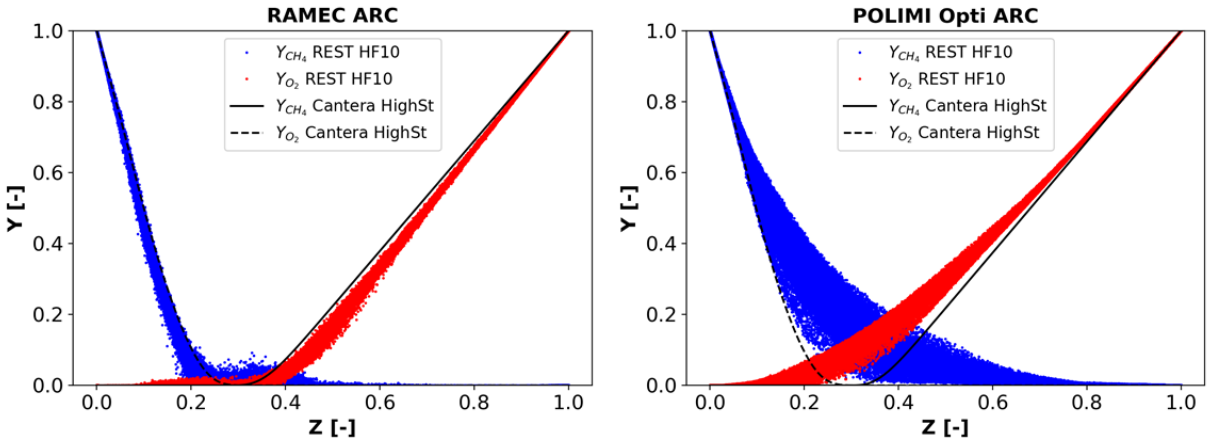

Figure 94: Scatter plots of O_2 and CH_4 mass fractions in the extraction zone close to the injector for RAMEC ARC calculation (left) and POLIMI Opti (right). 1D Cantera profiles for a laminar diffusion flames at 100 bar and χ=1500s^{-1} are superimposed

5.5.3 Averaged longitudinal profiles per cross section

In order to characterize the flow and the flame in the whole combustion chamber, some variables were averaged in transverse slabs of constant thickness (1 mm) and displayed over the z longitudinal axis. Average profiles of temperature and pressure are shown for both chemistries on Figure 95 which also displays the theorical equilibrium values obtained at 100 bar and same global equivalence ratio with CANTERA. As equilibrium calculations do not depend on the chemical kinetics and as almost identical NASA polynomials are used, the theoretical equilibrium state is the same for both chemistries.

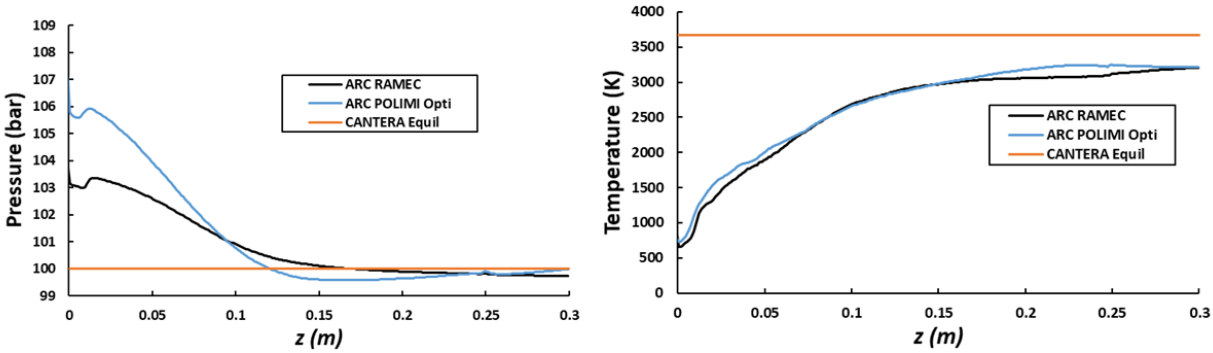

Figure 95: Longitudinal cross section averages of pressure and temperature for RAMEC ARC and POLIMI Opti ARC calculations. Theoretical equilibrium values are also indicated for reference. Flame zone ends around z=0.12 m.

All profile shapes match the ones of [180], and the target output pressure of 100 bar is well reached for both cases. While the temperature profiles are almost identical for both chemistries, the pressure differs in the flame zone (which ends at around z=0.12 m), with a P higher by 3 bars for the POLIMI Opti ARC case. This difference is the direct consequence of the more intense combustion with the POLIMI Opti ARC due to more turbulence. Another interesting results is that on average equilibrium is not reached in any case, the exit temperature being around 500 K lower than the theoretical temperature.

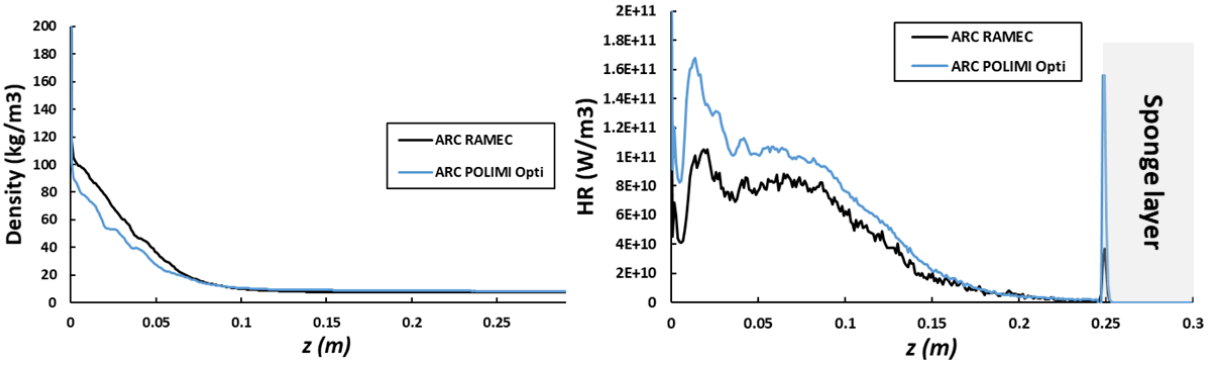

Figure 96: Longitudinal cross section averages of and heat release rate for RAMEC ARC and POLIMI Opti ARC calculations. Flame zone ends around z=0.12 m.

Figure 96 displays the average profiles of density and heat release rate HR. As for the pressure and temperature profiles, the main discrepancies between both chemistries are found in the flame zone, with a density slightly more important for RAMEC ARC than for POLIMI Opti ARC. This is directly linked to the pressure difference. As mentioned before, because of the more turbulent flame, POLIMI Opti ARC exhibits a higher heat release rate than RAMEC ARC. However, the HR shows almost identical shapes for both calculations in the flame and post flame zones (the latter begins at around z=0.12 m). The higher values are logically seen in the flame zone, and then HR progressively decreases while getting further away from the injector. The last peak at z=0.25 cm is non-physical as it corresponds to the start of the sponge layer.

5.5.4 Analysis of chemical species average fields and profiles

In order to provide an in-depth understanding of the chemical phenomena at stake for both calculations and their impact on the global results, the average fields and profiles of the chemical species mass fractions are now studied.

Post-flame O_2 mass fraction

To begin with, the fuel (CH_4) and oxidizer (O_2) average mass fraction fields are investigated as shown on Figure 97.

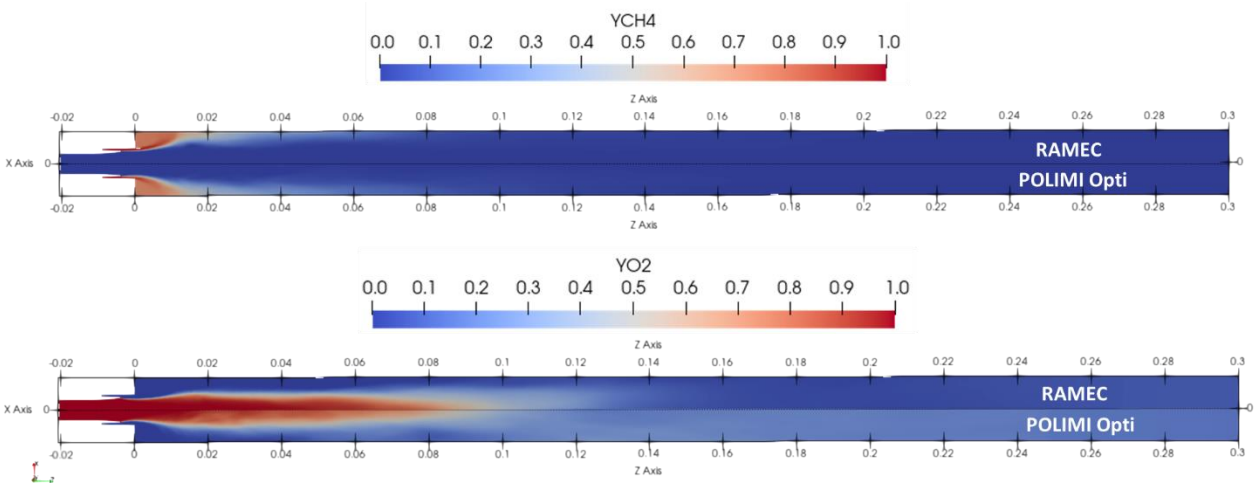

Figure 97: Longitudinal mirror cuts for both chemistries of the average fields of species mass fractions (CH_4 on the top, O_2 on the bottom)

One can see that the CH_4 average fields are very close for both chemistries, showing fast consumption of the fuel as soon as the flame starts. These similarities between the two mechanisms are also visible on the longitudinal cross section averages presented on Figure 98. The high concentration zone finishes a bit earlier for POLIMI Opti ARC case, which is consistent with the previously made analyses. As for O_2, one can see on the average fields that the high concentration core has the same shape for both cases. However, it is a bit shorter for POLIMI Opti ARC, once again highlighting the more efficient combustion of the latter. Perhaps the most interesting fact of Figure 97 is that O_2 is still present in a non-negligible amount in the post-flame zone of POLIMI Opti ARC whereas it is close to zero in the case of RAMEC ARC. The longitudinal cross section averages of Figure 98 allow to appreciate the full extent of the differences between the mechanisms. Indeed, there more than a factor 2 on the O_2 mass fraction in the post-flame zone.

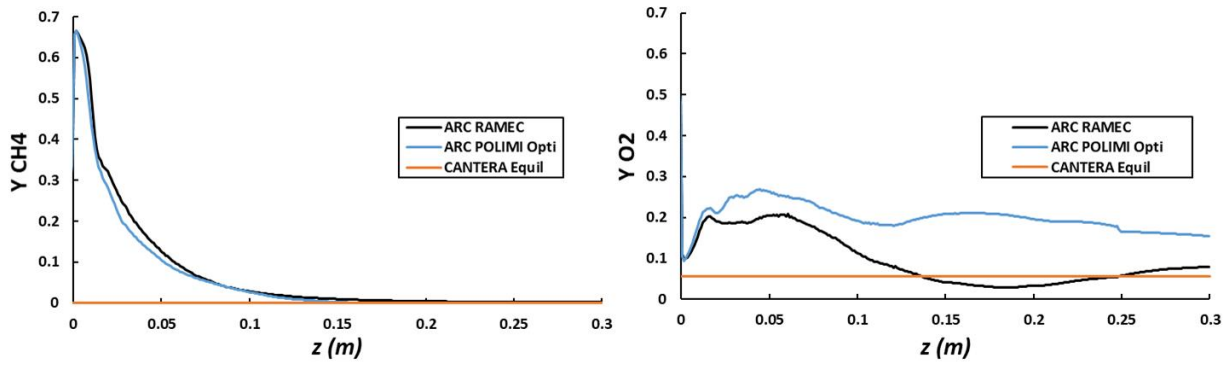

Figure 98: Longitudinal cross section averages of CH_4 and O_2 for both chemistries. Theoretical equilibrium values are reported for reference. Flame zone ends around z=0.12 m.

In order to explain this phenomenon, an investigation of the kinetics at stake is required. When analyzing the reaction rates in the post-flame zone for both models, one reaction is particularly preeminent: $H + O_2(+M) = HO_2(+M)$. Figure 99 displays its evolution as a function of the inverse of temperature for RAMEC and POLIMI Opti, highlighting striking differences.

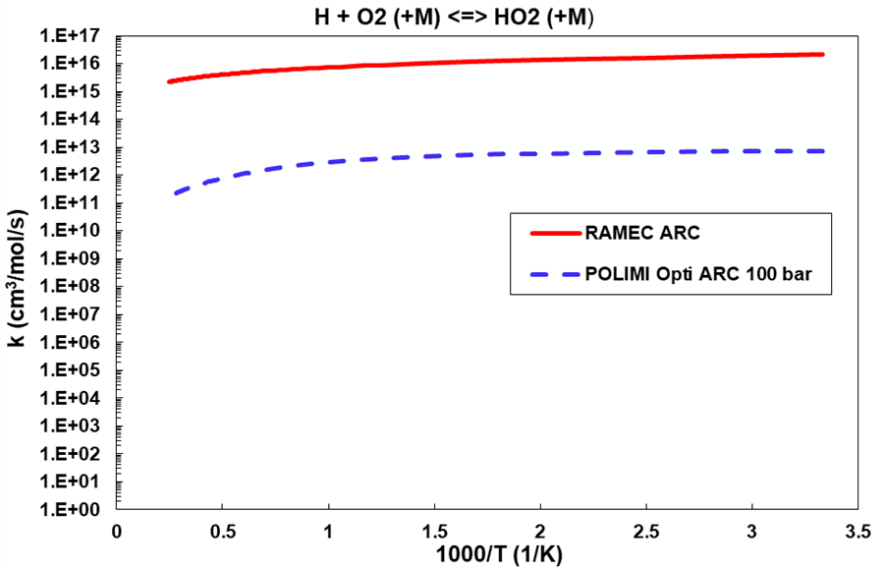

Figure 99: Rate constant of HO_2 formation over 1000/T for the POLIMI Opti ARC and RAMEC ARC

The first main difference lies in the fact that the reaction rate of HO_2 formation does not include any pressure dependency in the RAMEC ARC mechanism while this is the case for POLIMI Opti ARC (and natively for POLIMI C1-C3). Hence, the latter is shown at a pressure of 100 bar, which is the value found in the chamber in the post-flame zone. Moreover, one can see that the RAMEC ARC rate constant is far more important than the POLIMI Opti one (with on average respectively $\sim 10^{16}$ against $\sim 10^{12}$ $cm^3/mol/s$). This means that the O_2 consumption is much faster with RAMEC ARC than POLIMI Opti ARC which explains the mass fraction differences observed in the post-flame zone. The third and last interesting point regarding this reaction is that its rate constant was optimized with OPTISMOKE ++ leading to slightly lower values than the reference, but consistent with the recent literature evaluations [191]. Moreover, another reaction stands out in the post-flame region when performing the reaction rates analysis. Its behavior is illustrated on Figure 100.

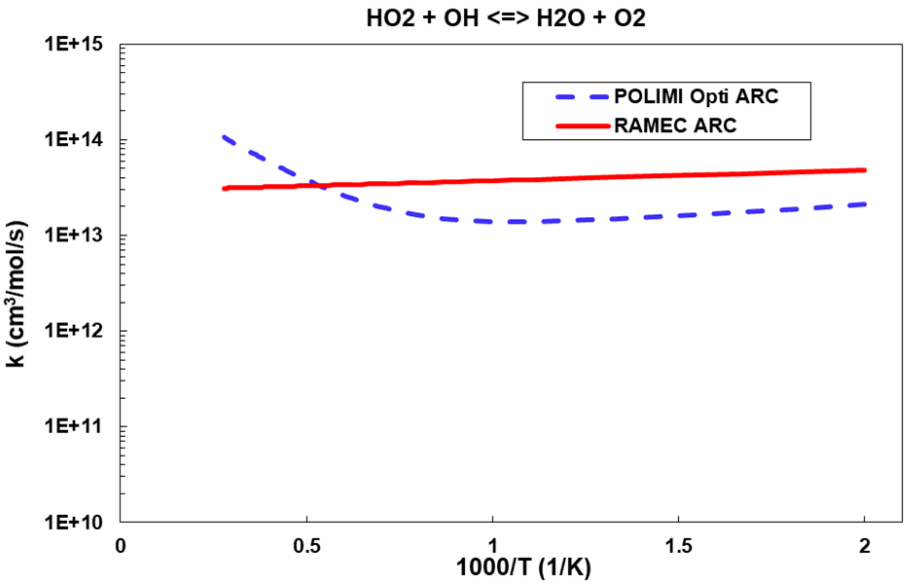

Figure 100: Rate constant of $HO_2 + OH = H_2O + O_2$ reaction over 1000/T for the POLIMI Opti ARC and RAMEC ARC

When looking at $HO_2 + OH = H_2O + O_2$ it appears that for high temperature (hence the conditions of interest for REST HF-10) the reaction is much faster (meaning higher value of k) for POLIMI Opti than RAMEC ARC. This shows that O_2 production is hence faster for POLIMI Opti, leading to a more important mass fraction in the post-flame zone.

Post-flame H_2O mass fraction

Another interesting phenomenon in this zone arise when looking at the H_2O mass fraction. The average fields shown on Figure 101 show that there is more water in the post-flame region for the RAMEC ARC calculation than for the POLIMI Opti one.

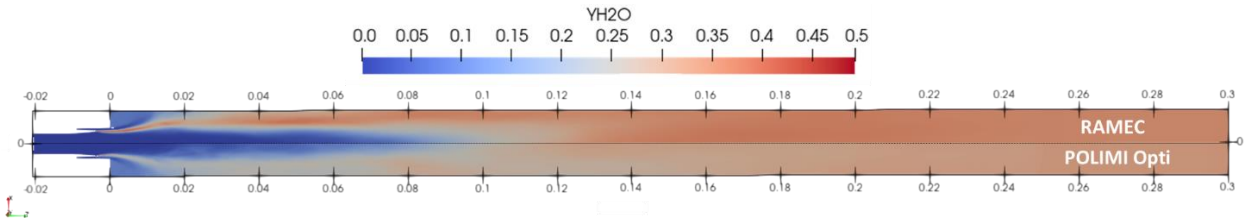

Figure 101: Longitudinal mirror cuts for both chemistries of the average fields of species mass fraction of H_2O

This observation is confirmed by the longitudinal cross section average shown on Figure 102. The difference in mass fractions is not as significant as the one in O_2 but the graph still shows a substantial gap between the mechanisms on the whole chamber length.

Analyzing the reaction rates allow to point out $H_2O + O_2 = HO_2 + OH$ for which the rate constant is illustrated as a function of the inverse of temperature on Figure 103. The latter shows that H_2O reaction with O_2 is faster for POLIMI Opti ARC at high temperature. The consumption of H_2O with this mechanism is all the more boosted that the concentration of O_2 is high on the post-flame region as shown above. This reaction also tends to produce large amount of OH and HO_2 in the post-flame zone, faster than RAMEC ARC. This observation is confirmed by the mass fraction longitudinal cross section averages of Figure 102 and the average fields of Figure 104.

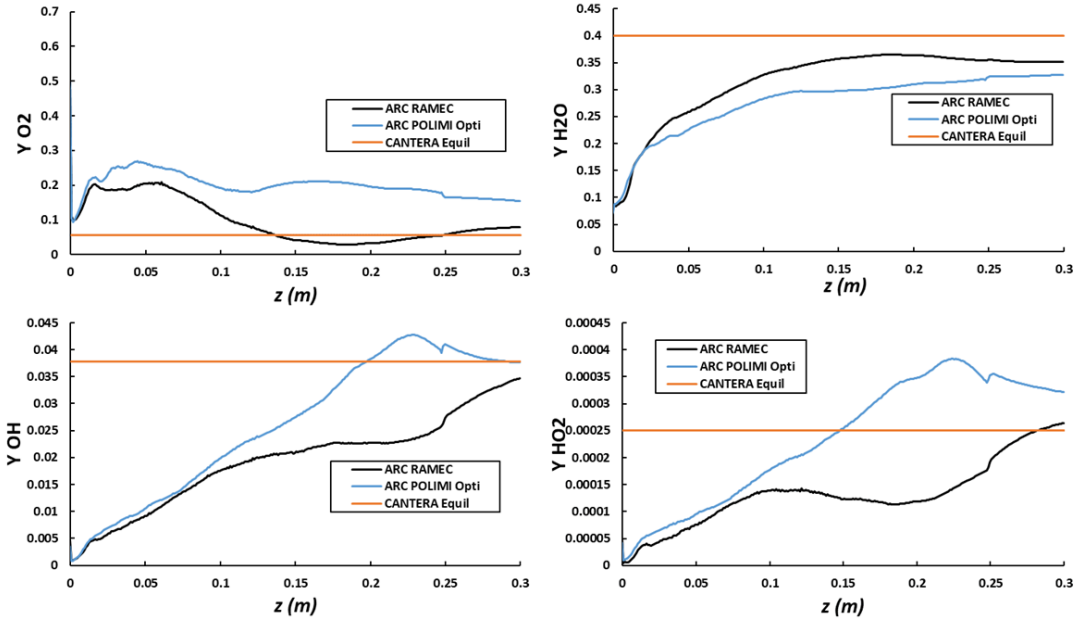

Figure 102: Longitudinal cross section averages of O_2, H_2O, OH and HO_2 for both chemistries. Theoretical equilibrium values are reported for reference. Flame zone ends around z=0.12 m.

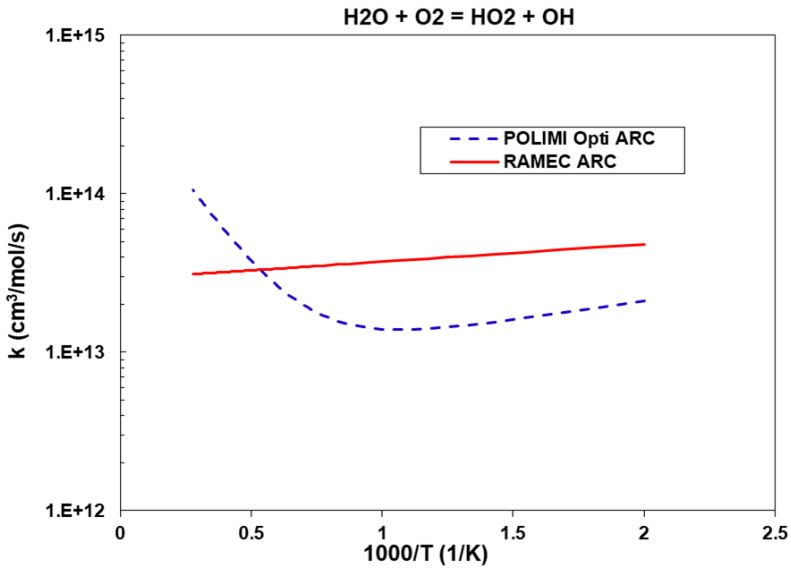

Figure 103: Rate constant of a H_2O reaction with O_2 over 1000/T for the POLIMI Opt ARCi and RAMEC ARC

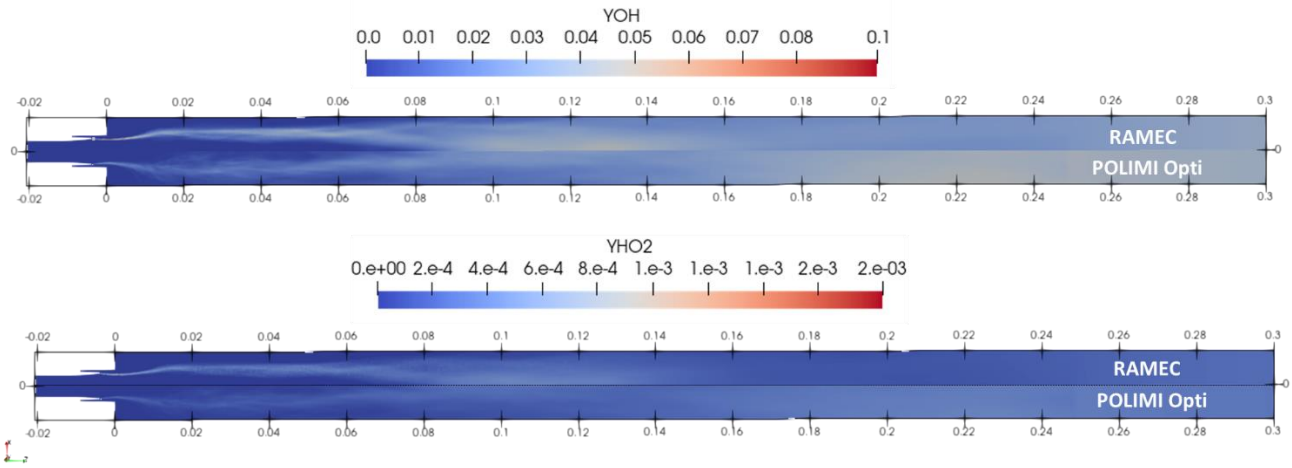

Figure 104: Longitudinal mirror cuts for both chemistries of the average fields of species mass fractions (OH on the top, HO_2 on the bottom)

$CO - CO_2$ equilibrium

CO and CO_2 are interesting to be investigated as the equilibrium between those species is key to recover a correct final temperature [23]. The average fields featured on Figure 105 and longitudinal cross section averages of Figure 106 help analyze the differences.

For the POLIMI Opti ARC case, CO peaks appear before CO_2 which seems consistent with the formation of the final combustion products. Indeed, a strong decrease in CO quantity can be spotted in the post-flame zone both on the average cuts and the longitudinal cross section averages. One can also suppose that the excess of O_2 and OH in the same region boosts the CO_2 production. The CO-CO_2 equilibrium is perceived in a different way for the RAMEC ARC case.

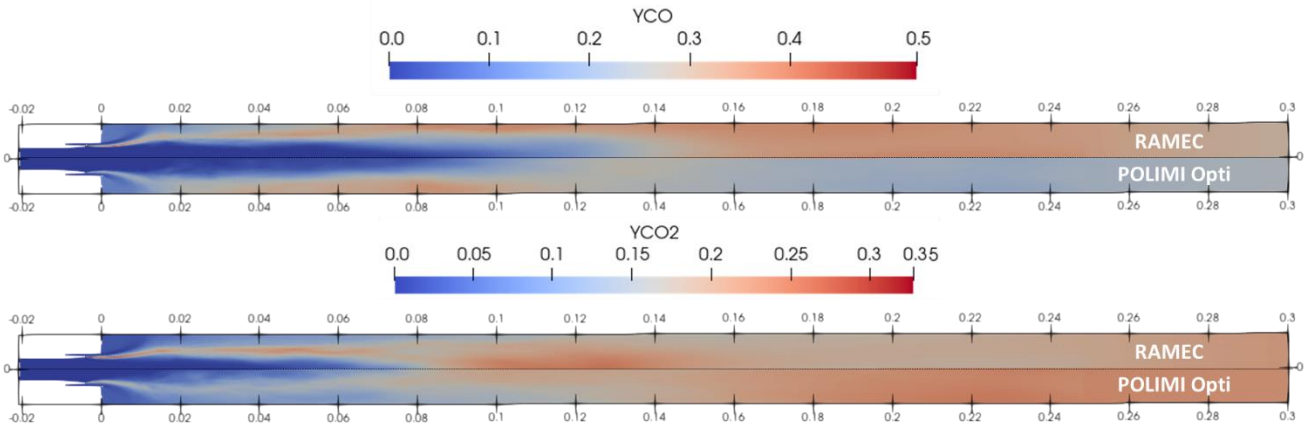

Figure 105: Longitudinal mirror cuts for both chemistries of the average fields of species mass fractions (CO on the top, CO_2 on the bottom)

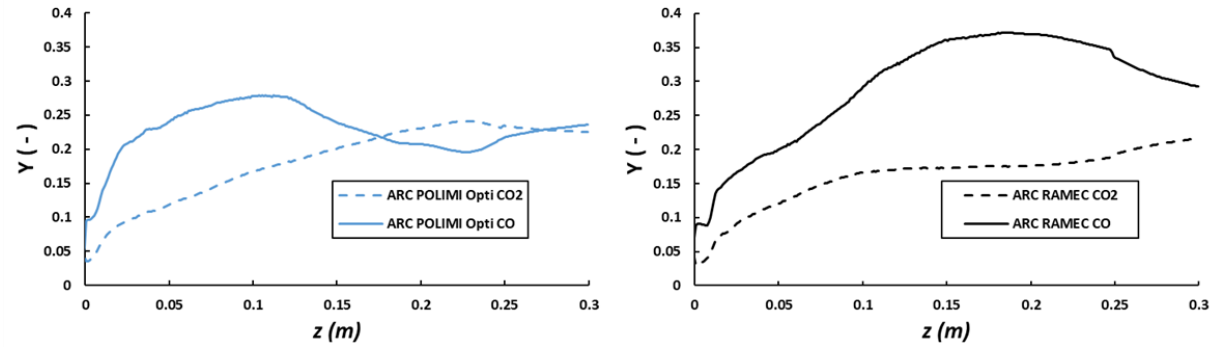

Figure 106: Longitudinal cross section averages of CO and CO_2 for the POLIMI Opti ARC (left) and RAMEC ARC (right). Flame zone ends around z=0.12 m.

Indeed, one can see on the average fields a local high concentration of CO_2 in the near-post flame zone where the hot gases are present, but it remains quite weak compared to the amount of CO that peaks after, at the end of the chamber. Moreover, when looking at the longitudinal cross section averages of Figure 106, this local CO_2 maximum is not really visible, suggesting that it has no impact on the 3D field. One can also observe that the overall amount of CO is way above the one of CO_2 with up to a factor 2 for RAMEC ARC whereas the mass fraction levels are comparable (or at least close to each other) for POLIMI Opti ARC. This suggests that large amounts of CO did not convert yet into CO_2 in the RAMEC ARC calculation. Indeed, one of the explanation is that the necessary species to boost this conversion (O_2, OH, HO_2) are no present in sufficient quantities. This could mean that RAMEC ARC chemistry is possibly further away from global equilibrium than the POLIMI Opti ARC for the CO-CO_2 equilibrium. The difference between the two mechanisms in CO_2 mass fraction can be appreciated on Figure 107. Complementary analyses of the reaction rates allow to confirm the above-mentioned hypotheses by highlighting key reactions.

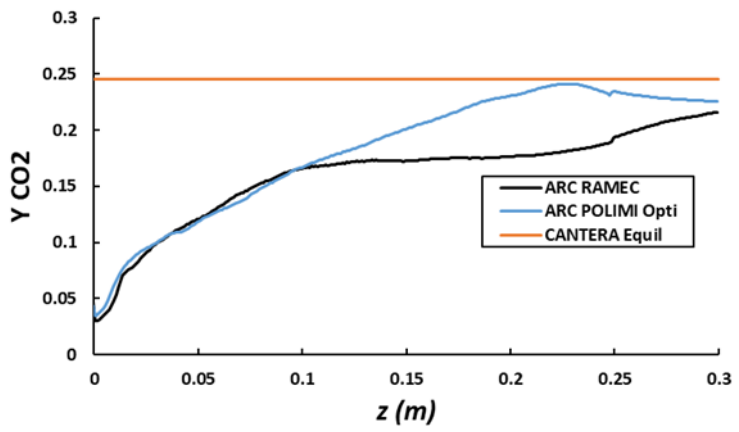

Figure 107: Longitudinal cross section average of CO_2 for both chemistries and theoretical equilibrium. Flame zone ends around z=0.12 m.

The $CO + OH = CO_2 + H$ reaction was already identified as a key exothermic reaction for the optimization process. Its rate constant is higher for POLIMI Opti ARC than for RAMEC ARC especially for temperatures of the order of magnitude of the ones encountered in the post flame zone (cf. Figure 108), leading to a faster CO - CO_2 conversion. Moreover, in this case the high concentration of OH further increases the reaction speed. Hence, this explains the lower CO concentration for POLIMI Opti ARC compared to RAMEC ARC for which it is not fast consumed. Moreover, $HCO + OH = CO + H_2O$ (with a reaction rate independent of temperature as shown on Figure 109) is faster for RAMEC ARC, which emphasizes the larger amount of CO and H_2O as well as the low OH levels in the post flame zone compared to POLIMI Opti ARC.

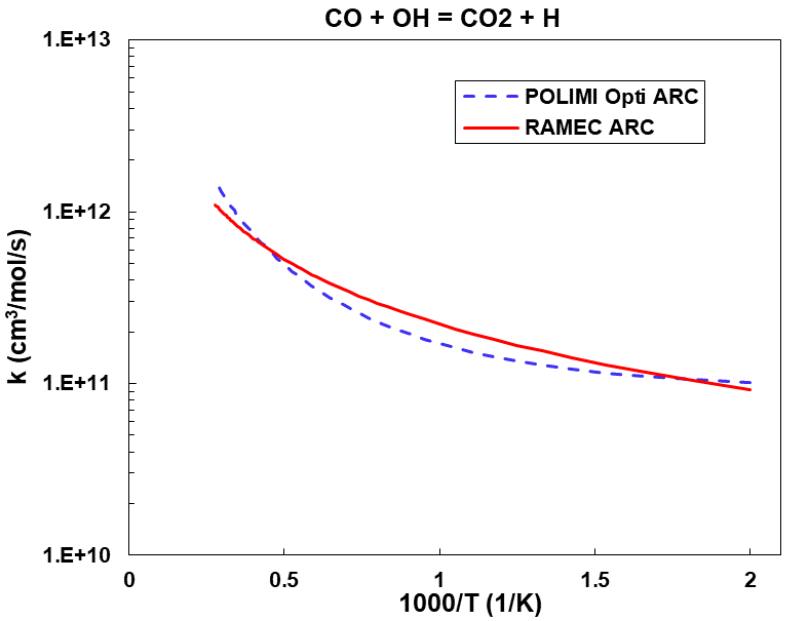

Figure 108: Rate constant of a CO_2 formation reaction over 1000/T for the POLIMI Opti ARC and RAMEC ARC

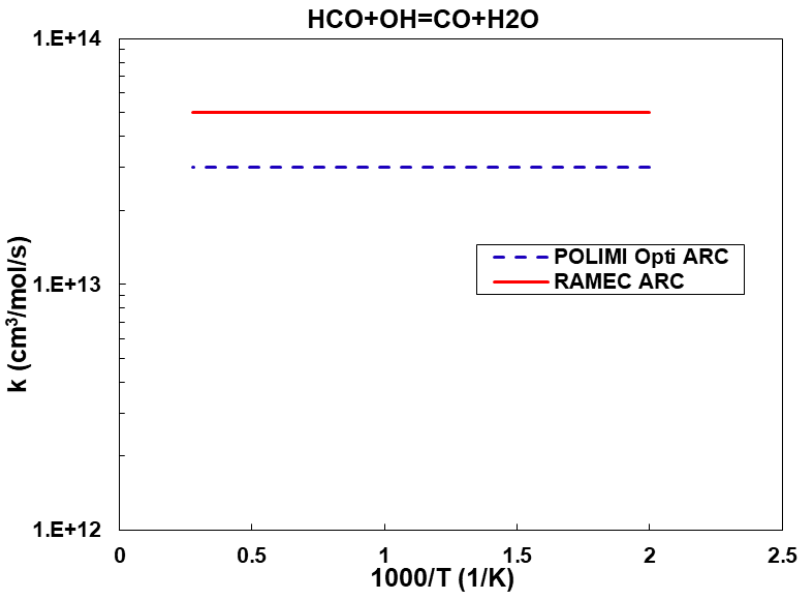

Figure 109: Rate constant of a CO formation reaction over 1000/T for the POLIMI Opti ARC and RAMEC ARC

5.5.5 Power budget and equilibrium

Another way to assess how REST HF-10 computations compares to the theoretical equilibrium is to perform a global analysis of the chamber power. First, the maximum theoretical power released by the flame (assuming a complete combustion in adiabatic conditions) can be quantified. A first estimate of this theoretical power P_{theo} can be computed thanks to the following relation:

$$P_{theo} = \dot{m}_{CH_4} LHV_{CH_4} / \varphi \tag{120}$$

Where $\dot{m_{CH_4}}$ is the methane mass flow rate (in $kg\ s^{-1}$) which is supposed completely burnt and LHV_{CH_4} the lower heating value of the fuel. With LHV_{CH_4} = 50 $MJ\ kg^{-1}$ and the $\dot{m_{CH_4}}$ and φ values taken from the REST HF-10 operating conditions listed in Table 13, one can deduce that:

$$P_{theo} = 5.76\ \text{MW} \tag{121}$$

A more precise estimate can be performed by evaluating $P_{theo_{Cant}}$, the product of the total mass flow rate of reactants $\dot{m_{tot}}$ and the sensible enthalpy of the burnt gases composition obtained with a constant enthalpy and pressure equilibrium calculation. This equilibrium calculation is performed with CANTERA and the initial conditions are also the ones found in Table 13. As already mentioned, theoretical equilibrium state is the same for both RAMEC and POLIMI Opti ARC chemistries. T_i is the initial temperature and T_{eq} the equilibrium one. Sensible enthalpy is obtained by integrating the evolution of Cp_{eq} over the temperature between T_i and T_f. It yields:

$$P_{theo_{Cant}} = \dot{m}_{tot} \int_{T_i}^{T_{eq}} Cp_{eq}(T) dT = 4.19\ \text{MW} \tag{122}$$

In order to gain accuracy, the enthalpy of reaction $\Delta_r H^0$ can be added. It is a negative term since the transformation is exothermic and yields:

$$P_{theo_{Cant}} = \dot{m}_{tot}\left(\int_{T_i}^{T_{eq}} Cp_{eq}(T)dT + \Delta_r H^0\right) = 4.16\ \text{MW} \quad (123)$$

In order to compare $P_{theo_{Cant}}$ to the power emitted by the flames of the AVBP calculations performed with POLIMI Opti and RAMEC ARC, their respective heat release rates $\dot{\omega}_T$ (defined in Chapter 2) are integrated on the chamber volume. Moreover, an interesting way to visualize the power evolution inside the domain is to compute a cumulative integral by first integrating $\dot{\omega}_T$ on a chamber cross section and then sum each surface integral values along the z longitudinal axis as proposed in [23]. Hence, this method allows to appreciate the evolution of emitted power as the distance from the injector increases. The expression of the cumulative power $P_{cumul_{AVBP}}$ is the following:

$$P_{cumul_{AVBP}} = \int_{z_o}^{z_{end}} \int_{S} \dot{\omega}_T \, \mathrm{dS} \; dz' \quad (124)$$

The starting position of the integration z_0 is at the injector lips and the final one just before the sponge layer (z_{end}=0.24 m). $P_{cumul_{AVBP}}$ for RAMEC and POLIMI Opti ARC calculations as well as the theoretical equilibrium power $P_{theo_{Cant}}$ are displayed on Figure 110 .

One can see a fast evolution of $P_{cumul_{AVBP}}$ for both chemistries in the flame region (i.e. up to about z=0.12m). Then the growths rate of the power drastically decreases, almost reaching a plateau for both models. The results also shows that $P_{cumul_{POLIMI\ opti\ ARC}}$ is always greater than $P_{cumul_{RAMEC\ ARC}}$. This is consistent with the previous analyses since the POLIMI Opti calculation yields a more turbulent, hence more energetic flame.

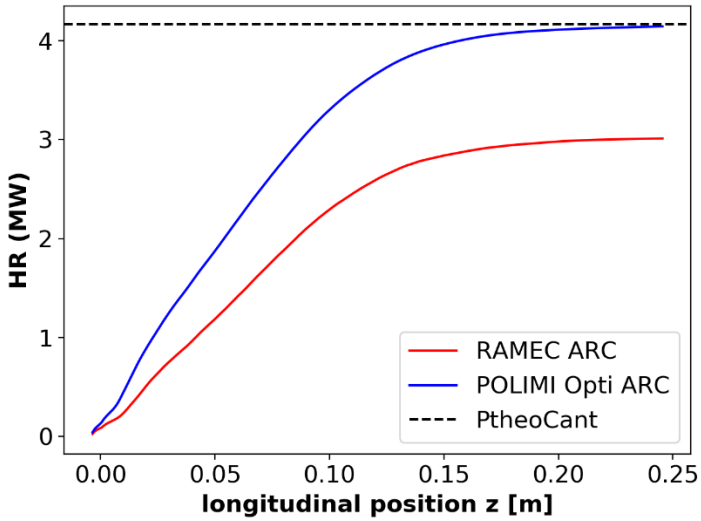

Figure 110: Axial power evolution for the REST HF-10 combustion chamber compared to theoretical equilibrium power

Finally, $P_{cumul_{POLIMI\ opti\ ARC}}$ seems to asymptotically tend toward $P_{theo_{Cant}}$ without ever reaching it. In fact, as seen in the previous sections, neither POLIMI Opti or RAMEC ARCs seem to reach the theoretical equilibrium at the exit of the REST HF-10 configuration. Indeed, theoretical equilibrium supposes a complete combustion between CH_4 and O_2, and the REST HF-10 test case features recirculation zones at the injector exit (see Figure 97). Hence, pockets of unburnt methane stagnate in

those areas. The entirety of the trapped amounts of fuel does not have time to fully react in the flame during the 4 ms averaging time, hence giving a temperature lower than the one from the equilibrium calculation. Figure 110 indeed illustrates that both chemistries seem to tend toward their own respective equilibrium.

This can also be shown by taking the average burnt gas composition at the exit of the combustion chamber (for example at z_{end}) for both POLIMI Opti and RAMEC ARCs. Performing equilibrium calculations for those conditions show that the system will no longer significantly evolve and will quickly stabilize toward a temperature (smaller than theoretical T_{eq}) and composition close to the one of the chamber exit. 0D CANTERA computations show that this stabilization is 10^4 faster than the convective time τ_{conv} (cf. Figure 111).

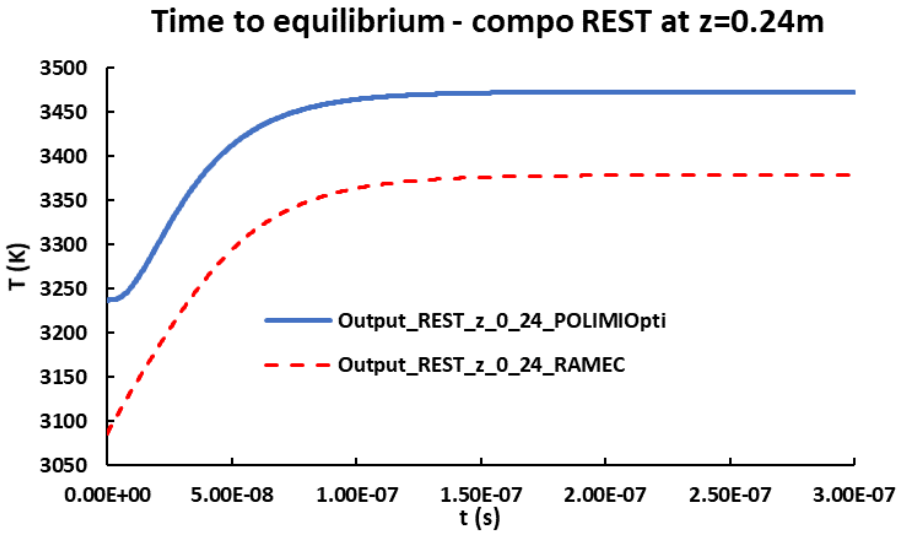

Figure 111: CANTERA 0D computation with burnt gas composition at z=0.24m for both chemistries

Conclusion on REST HF-10

This section shows the value of a detailed and optimized chemistry for MethaLOx rocket engine LES simulations. Despite being slightly bigger than the reference RAMEC (19 transported species versus 15), POLIMI Opti ARC allows to capture interesting phenomena that were not visible with RAMEC ARC or other chemistries used in the literature on this test case [183].

First, the flame stabilization position and length is quite comparable for both chemistries, both case exhibiting a diffusion flame anchored at the injector lips. However, some differences are visible in the heat release rate structure with a broader reaction zone for POLIMI Opti ARC calculation which ends a bit before the one of RAMEC ARC. This is due to the first difference between the two flames structures which is turbulence. Indeed, it is highly suspected that chemistry effects with POLIMI Opti ARC trigger smoother density gradients than RAMEC ARC in the recess zone, hence leading to less LAD activation. Consequently, a much more turbulent flame structure is recovered with the POLIMI Opti calculation, producing a more efficient combustion, hence a broader heat release rate structure than the RAMEC ARC case.

Another difference pointed out by the POLIMI Opti calculation is the post-flame structure. The optimized chemistry exhibits much more O_2 than the RAMEC ARC in this region (up to a factor 2), and

less H_2O. The observation are based on the observation of average field mass fractions and cross section averages. Analyses of the reaction rates in this zone coupled with plots of rate constant versus the temperature allow to point out the reasons of these differences. In the case of O_2 one key reaction in particular (which behavior was optimized for POLIMI Opti ARC and confirmed with recent results from the literature) illustrates why RAMEC consumes the oxygen faster. POLIMI Opti leading to less H_2O in the post-flame region can also be mostly explained by its reaction with oxygen, leading to the creation of OH and HO_2. Enhanced by already important concentrations of O_2, the H_2O consumption reaction is faster in the case of POLIMI Opti ARC at high temperature. The last major difference between the two mechanisms lies in the CO-CO_2 equilibrium perception. POLIMI Opti ARC exhibits consistent fields and longitudinal average values of those species, leading to an amount of CO_2 close to equilibrium while RAMEC exhibits important quantities of non-converted CO. A phenomenon that can also be explained with the analyses of rate constants of key reactions.

In summary, the optimized POLIMI Opti chemistry allows to recover a correct global flame structure and length while pointing out phenomena previously not well or not at all captured in the post-flame region that can eventually and significantly affect the structure of the flow and the species distribution.

General conclusion and perspectives

This thesis work has allowed to bring a new look to the kinetics of methane oxycombustion in extreme pressure and temperature conditions.

The building of a CH_4/O_2 flame speed database in never reached before conditions was realized thanks to the OPTIPRIME combustion chamber developed at CNRS ICARE using the isochoric method [112]. The development of a new end-of-adiabaticity criterion for isochoric flame speed measurements [122] helped to extract the most extreme points from the experimental campaign. Data was acquired for a broad range of pressure, temperature and equivalence ratios allowing to enlarge the literature resources on the subject, until now mainly limited to the atmospheric pressure.

The obtain database was then compared to different chemical schemes. The model used for the benchmark comparison where both models initially developed for methane oxycombustion (for example the reference RAMEC mechanism) or recent details mechanisms from the literature such as FFCM1 [95] or POLIMI C1-C3 [134]. This global analysis allowed to demonstrate that all these mechanisms tend to underestimate the flame speed for lean, stoichiometric and slightly rich mixtures (with a maximum discrepancy at stoichiometry) while overestimating it for rich mixtures [132]. Recent isobaric flame speed measurements made by Turner et al. from Texas A&M university confirmed the OPTIPRIME data base results as well as their behavior compared to the kinetic mechanism [192].

As POLIMI C1-C3 was identified as the best performing mechanism on the tested equivalence ratios range, it was used as the starting point of an optimization process. Key reactions for correct oxycombustion description for the range of acquired data and even higher pressure were identified through sensitivity analysis. The objective of the optimization process being to tune the Arrhenius parameters and third body efficiencies of those reactions in order for the mechanism to match the experimental data while remaining in the physical known boundaries of these parameters. In order to do so, the OPTISMOKE++ [136] tool developed and validated by ULB and POLIMI [154] was used. To complete the experimental database, low dilution ignition delay times from the literature initially used as targets to derive the RAMEC mechanism [76,78] were added to the flame speed traces. This process allowed to obtain a POLIMI Opti mechanism, tailored to describe methane oxycombustion in extreme conditions.

The last step of this work consisted in applying the obtained model to 3D LES computations representative of rocket engine conditions. In order to do so, the widely studied supercritical REST HF-10 mono-injector configuration [183,184] was used. As results of computations performed with a reduced RAMEC ARC mechanism were available, they were used as a reference for comparison. POLIMI Opti was reduced on targets representative of the REST HF-10 case without losing its accuracy thanks to the ARCANE tool [65] in order to obtain a compact ARC mechanism. As the detailed optimized chemistry is much stiffer than RAMEC for 3D applications, it was decided to couple the CVODE implicit solver [188] to AVBP. Implicit resolution of the chemical source terms helped to stabilize the calculation which was later on continued with an explicit resolution. An analysis of the REST HF-10 calculation

results with POLIMI Opti with the help of average fields confirms that the stabilization position of the flame already identified in the literature was well recovered. However, in-depth investigation of longitudinal average values and rate constants of both RAMEC and POLIMI Opti mechanism show major differences in the post-flame structure. Indeed, the optimized kinetic model allows to capture interesting phenomena that were not visible with the RAMEC reference calculation. This involves a more turbulent flame, far more O_2 and less H_2O in the post-flame area for POLIMI Opti and a different perception of the CO-CO_2 equilibrium. These differences, as shown in the corresponding chapter, mainly come from the definition of rate constants of key reactions, some of which were modified during the optimization process. In conclusion, as they affect various parameters, considering those phenomena would strongly benefit to an accurate description of combustion in a MethaLox engine. Thus, in order to further improve the model's performances in the post-flame zone, acquisition of additional experimental data in these conditions would be very appreciable. For example, composition measurements of burnt gases from ONERA's MASCOTTE test bench firings in gas generator conditions.

Moreover, the process developed during this research work can be applied to other fuels and/or industrial applications. This work allowed to develop tools and link already existing ones to identify the need, build an experimental database, perform a chemical scheme benchmark study, identify key reactions, and optimize the mechanism in order to reduce it for high fidelity LES calculations.

Efforts in obtaining kinetic models for CH_4/O_2 combustion are also still underway around the world, with for example the recent work of Liberatori et al. [193] developing a method to tune a skeletal mechanism derived from Zhukov's to match ignition delay times using the CSP method to identify sensitive reactions faster.

Many improvements are also still possible for the models and processes developed in this thesis. In order for example to boost the efficiency of the implicit resolution of the chemical source terms in LES calculations, prototype dynamic methods were tested. The use of a sensor based on the chemical time step hence restricts the use of implicit integration to stiff zones only, allowing to gain substantial computational time. However, despite showing very encouraging results on 1D simulations, work is still needed on the definition of the sensor and the load balancing for an efficient use on 3D calculations. Moreover, even if relatively compact and efficient, ARC chemistries still have a non-negligible computational cost leading to time and money consuming calculations. They are perfectly suited for the academic environment but less for the industry. Note however that with the increase in computational power, these models become more and more affordable by various actors. Several attempts to develop global mechanisms capable of giving results representative enough of the detailed ones were attempted for CH_4/O_2 combustion. For example, the GLOMECH approach gave promising results [23,72]. In order to capitalize from this experience, a more improved an partially automated approach using experimental targets and tools such as OPTISMOKE ++ could be considered. Moreover, in order to better predict and understand the stiffness of complex chemical mechanisms in 3D turbulence-affected environments, some dedicated stability studies should be performed in order to point out and treat the triggering mechanisms.

In summary, the description of methane oxycombustion in rocket engines remains more than ever a topical issue of major importance as part of the current massive effort to develop reusable launch vehicles around the world.

Appendices

Appendix A – Reaction contributions to the heat release

1- 1D diffusion flame – 100 bar, χ=1000 s^{-1}

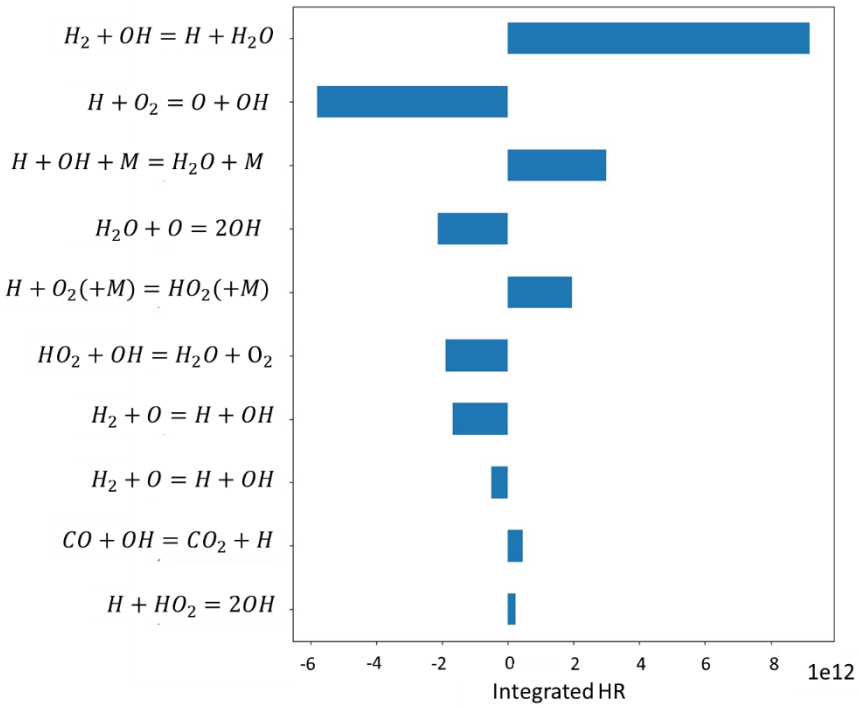

2- 1D premixed flames – 100 bar

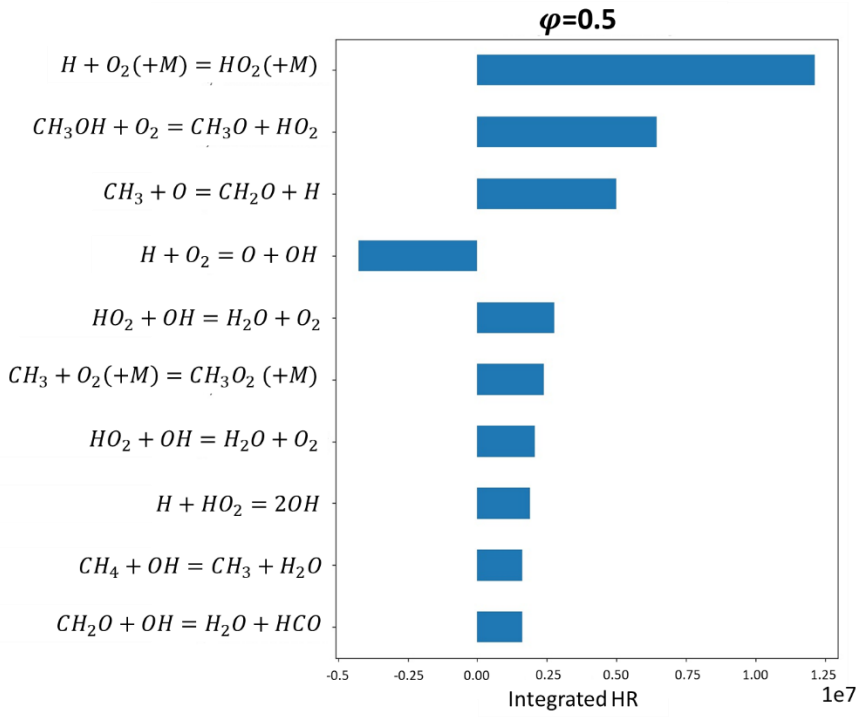

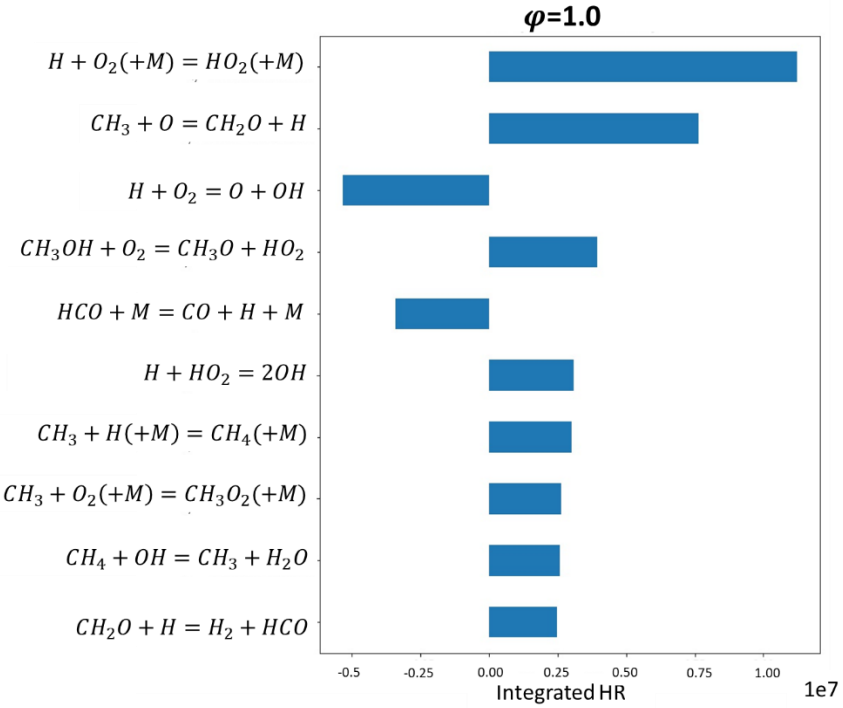

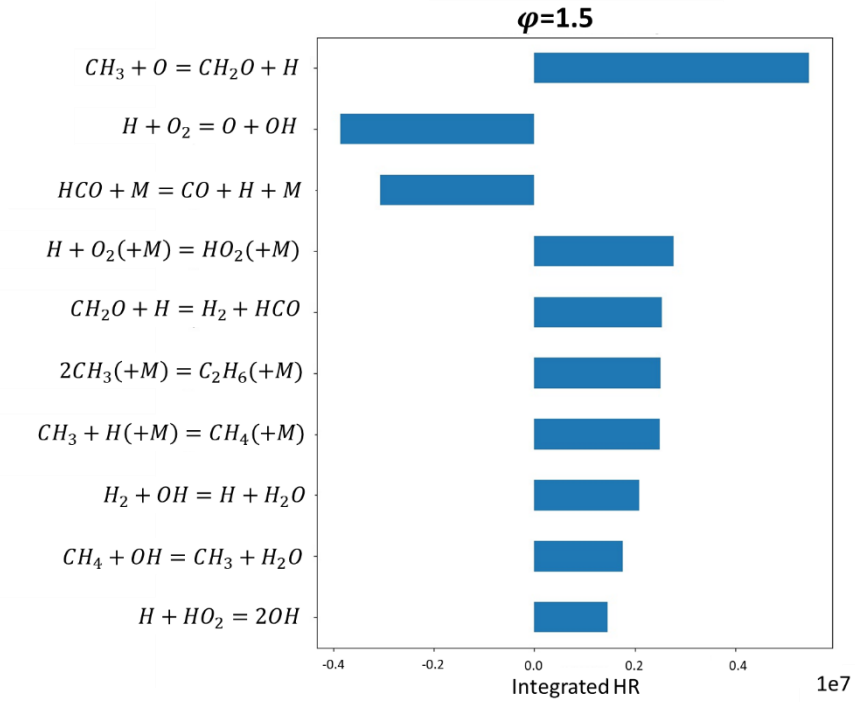
φ=1.5
$CH_3 + O = CH_2O + H$
$H + O_2 = O + OH$
$HCO + M = CO + H + M$
$H + O_2(+M) = HO_2(+M)$
$CH_2O + H = H_2 + HCO$
$2CH_3(+M) = C_2H_6(+M)$
$CH_3 + H(+M) = CH_4(+M)$
$H_2 + OH = H + H_2O$
$CH_4 + OH = CH_3 + H_2O$
$H + HO_2 = 2OH$
-0.4
-0.2
0.0
0.2
0.4
Integrated HR
1e7

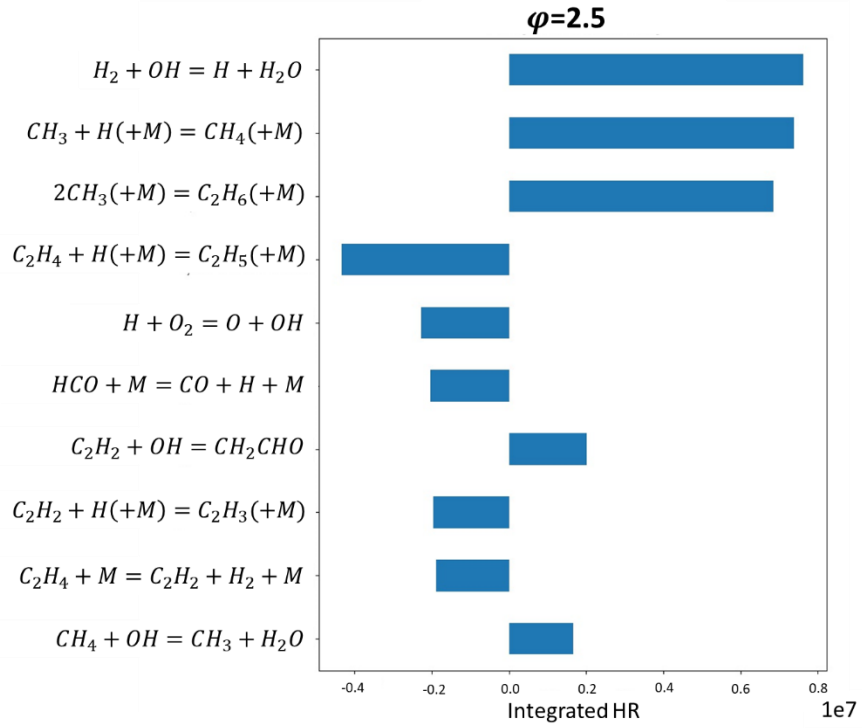
φ=2.5
$H_2 + OH = H + H_2O$
$CH_3 + H(+M) = CH_4(+M)$
$2CH_3(+M) = C_2H_6(+M)$
$C_2H_4 + H(+M) = C_2H_5(+M)$
$H + O_2 = O + OH$
$HCO + M = CO + H + M$
$C_2H_2 + OH = CH_2CHO$
$C_2H_2 + H(+M) = C_2H_3(+M)$
$C_2H_4 + M = C_2H_2 + H_2 + M$
$CH_4 + OH = CH_3 + H_2O$
-0.4
-0.2
0.0
0.2
0.4
0.6
0.8
Integrated HR
1e7

Appendix B – Supplementary data of the OPTIPRIME CH_4/O_2 campaign

1- Raw data treatment example

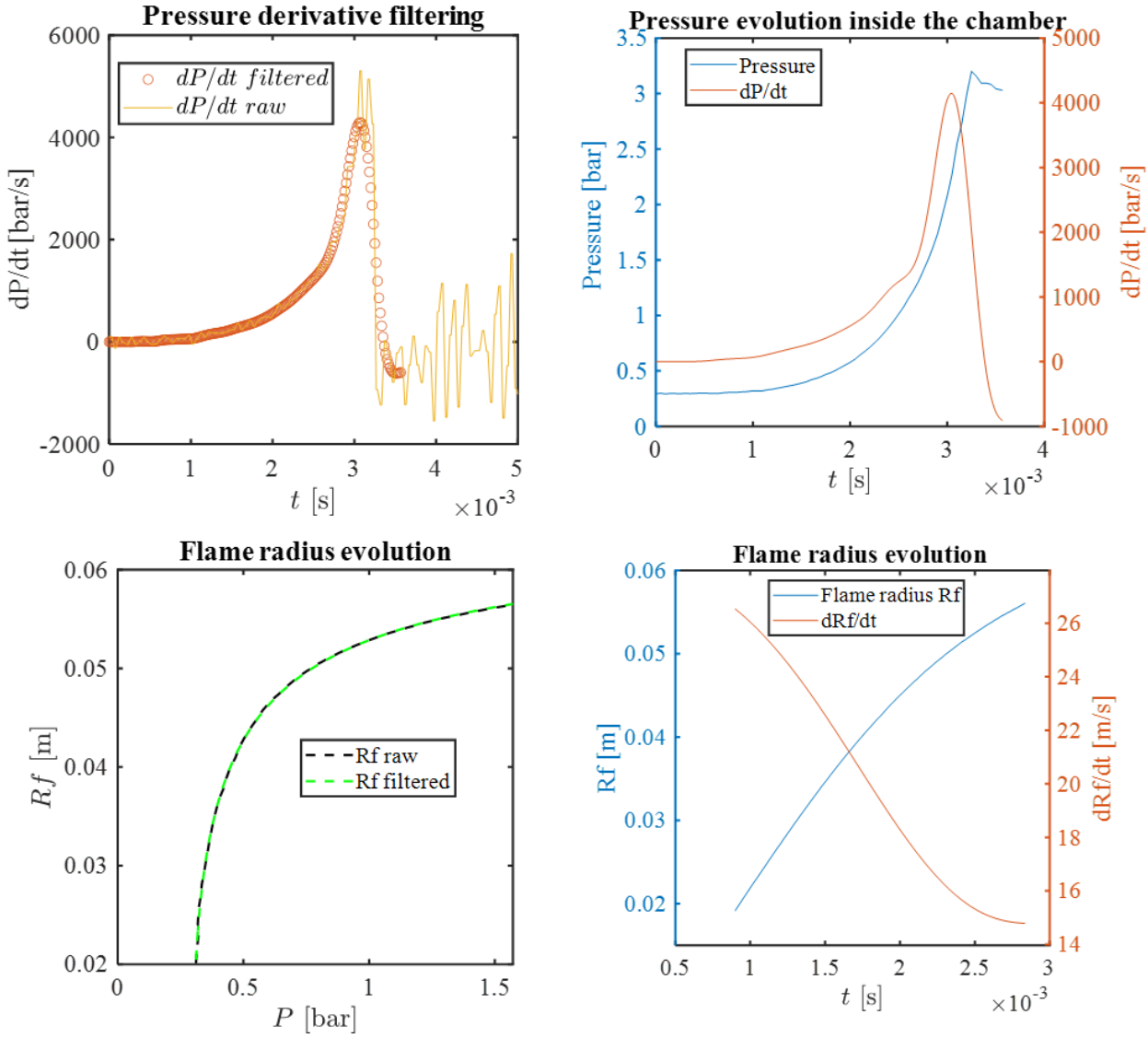

Figure 112: Raw pressure and radius data treatment for a stoichiometric CH4/O2 firing with OPTIPRIME

2- Flame images examples

Shots taken with a Phantom V2512 camera

CH_4/O_2 firing at φ=0.5

Sample rate: 60 000 fps
Exposure: 16 μs
Resolution: 1024x256

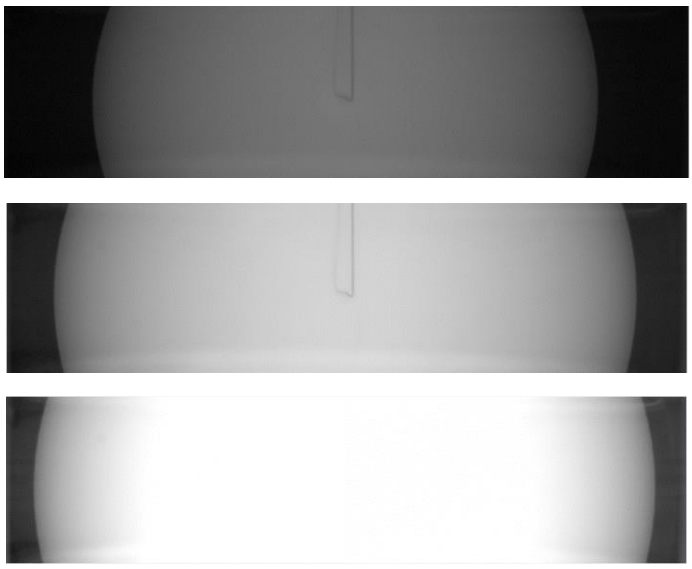

CH_4/O_2 firing at φ=1.0

Sample rate: 110 000 fps
Exposure: 6 μs
Resolution: 1024x208

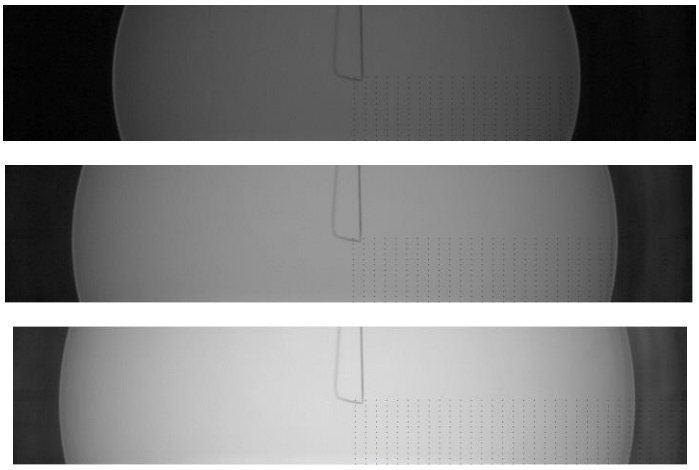

CH4/O2 firing at φ=2.5

Sample rate: 10 000 fps
Exposure: 10 μs
Resolution: 1024x768

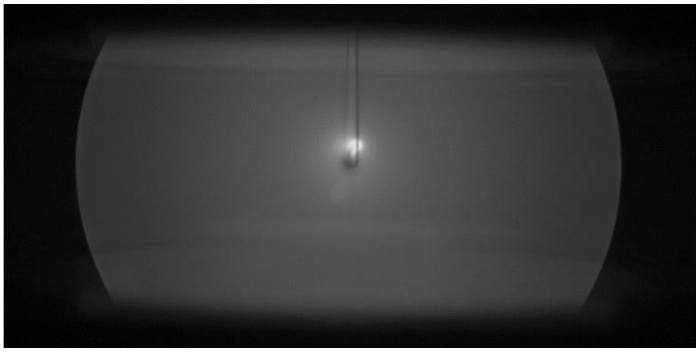

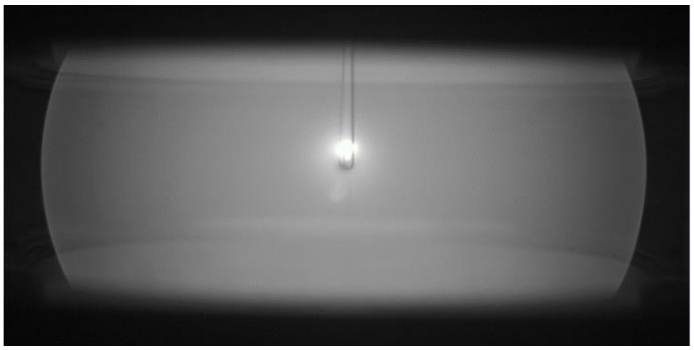

3- CH_4/O_2 OPTIPRIME campaign results - $S_u = f(P,T)$ vs mechanisms

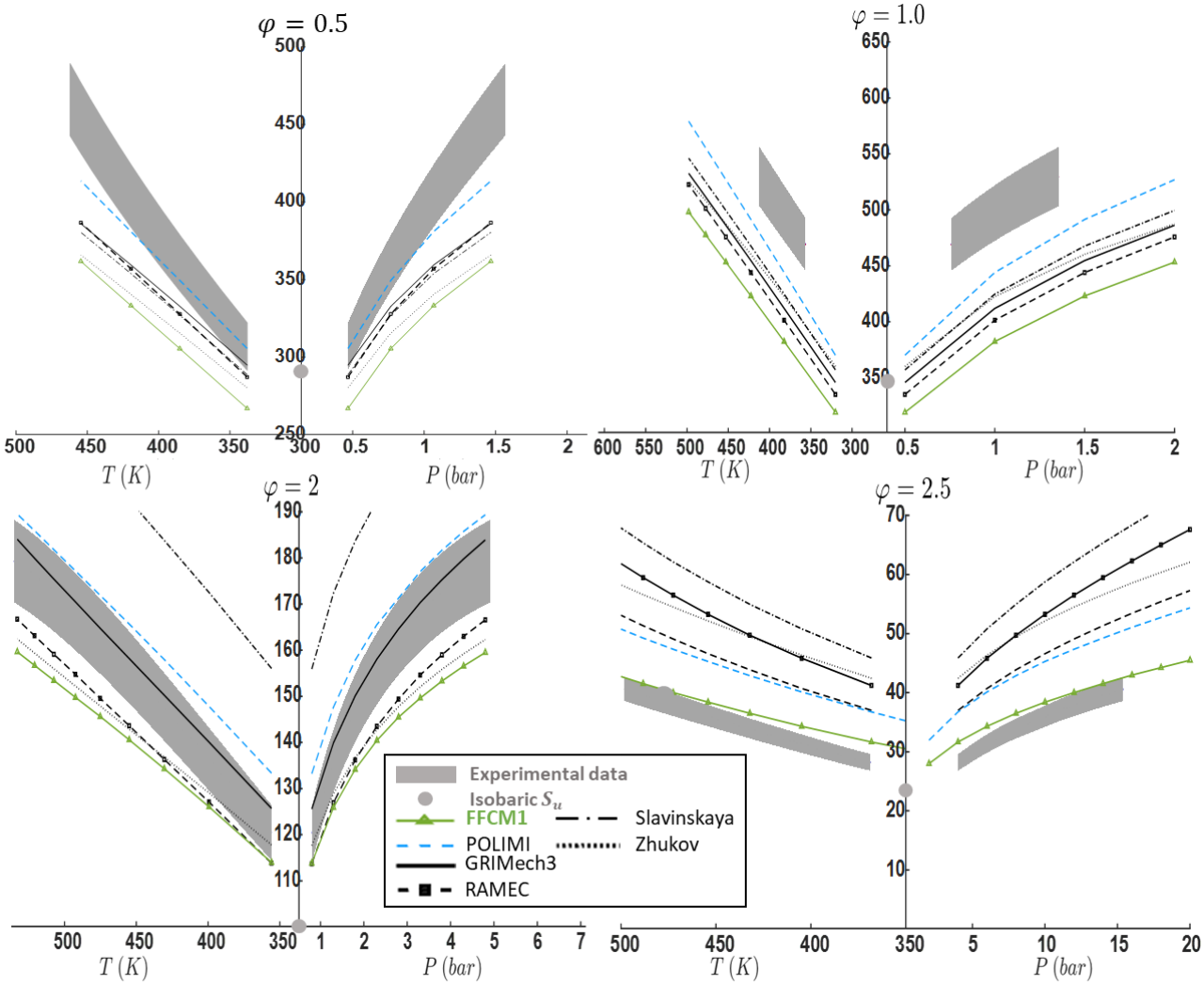

Figure 113: Flame speed S_u [cm.s −1] for CH_4 / O_2 mixtures at various equivalence ratios φ (thickened traces) as a function of T and P compared to several kinetic mechanisms (lines). Single symbols are for experimental isobaric flame speeds.

4- CH_4/O_2 OPTIPRIME campaign results - P, T, S_u experimental traces

φ =0.5 - P_0=0.3 bar		
P	T_u	S_u
0.30	300	0
0.47	337.94	306.81
0.57	355.81	326.56
0.67	371.36	344.33
0.77	385.17	360.67
0.87	397.61	375.9
0.97	408.95	390.29
1.07	419.39	403.99
1.17	429.06	417.14
1.27	438.09	429.85
1.37	446.55	442.19
1.47	454.53	454.23
1.57	462.07	466.01

φ =1 - P_0=0.3 bar		
P	T_u	S_u
0.3	303.71	0
0.57	358.22	474.36
0.67	373.28	487.64
0.77	386.61	500.07
0.87	398.58	511.95
0.97	409.46	523.45
1.07	419.45	534.71
1.17	428.69	545.83
1.27	437.29	556.87
1.37	445.34	567.89
1.47	452.9	578.95
1.57	460.05	590.07

φ =1 - P_0=0.4 bar		
P	T_u	S_u
0.40	301.95	0
0.76	356.24	468.86
0.86	367.67	481.19
0.96	378.06	492.43
1.06	387.6	502.78
1.16	396.43	512.37
1.26	404.65	521.34
1.36	412.34	529.75

φ =1.5 - P_0=0.4 bar		
P	T_u	S_u
0.4	299.15	0
0.81	357.61	339.07
0.91	368.11	349.24
1.01	377.69	358.53
1.11	386.52	367.1
1.21	394.7	375.03
1.31	402.33	382.43
1.41	409.49	389.35
1.51	416.23	395.85
1.61	422.6	401.97
1.71	428.64	407.76

φ =1.5 - P_0=0.5 bar		
P	T_u	S_u
0.5	297.5	0
0.98	352.83	316.74
1.08	361.5	325.38
1.18	369.52	333.45
1.28	377	341.04
1.38	384.01	348.21
1.48	390.61	355.02
1.58	396.84	361.5
1.68	402.75	367.68
1.78	408.38	373.61
1.88	413.74	379.3
1.98	418.86	384.77
2.08	423.77	390.05
2.18	428.48	395.14
2.28	433.02	400.07
2.38	437.38	404.85
2.48	441.59	409.48

φ =1.75 - P_0=0.4 bar		
P	T_u	S_u
0.40	300.86	0
0.84	362.49	228.72
0.94	372.6	232.98
1.04	381.85	236.88
1.14	390.38	240.47
1.24	398.3	243.82
1.34	405.7	246.94
1.44	412.65	249.87
1.54	419.2	252.64
1.64	425.39	255.26
1.74	431.27	257.75
1.84	436.87	260.13
1.94	442.2	262.4
2.04	447.31	264.57
2.14	452.21	266.66
2.24	456.91	268.66
2.34	461.43	270.59
2.44	465.78	272.46
2.54	469.99	274.26
2.64	474.05	276
2.74	477.98	277.69
2.84	481.78	279.33
2.94	485.47	280.92
3.04	489.06	282.47
3.14	492.54	283.97
3.24	495.92	285.44
3.34	499.21	286.86
3.44	502.42	288.26
3.54	505.55	289.61

φ =1.75 - P_0=0.5 bar		
P	T_u	S_u
0.5	299.17	0
1.04	359.83	215.68
1.14	368.02	219.47
1.24	375.62	222.99
1.34	382.73	226.29
1.44	389.42	229.4
1.54	395.72	232.33
1.64	401.68	235.12
1.74	407.35	237.77
1.84	412.74	240.3
1.94	417.9	242.72
2.04	422.83	245.04
2.14	427.55	247.27
2.24	432.09	249.42
2.34	436.47	251.49
2.44	440.68	253.5
2.54	444.75	255.43
2.64	448.68	257.31
2.74	452.48	259.13
2.84	456.17	260.89
2.94	459.74	262.61
3.04	463.21	264.28
3.14	466.59	265.91
3.24	469.87	267.49
3.34	473.06	269.03
3.44	476.17	270.54
3.54	479.2	272.02
3.64	482.16	273.46
3.74	485.05	274.86
3.84	487.87	276.24
3.94	490.63	277.59
4.04	493.33	278.91
4.14	495.97	280.21

φ =2 - P_0=0.4 bar		
P	T_u	S_u
0.4	298.25	0
0.81	355.8	120.28
0.91	366.05	124.02
1.01	375.39	127.45
1.11	383.99	130.6
1.21	391.95	133.53
1.31	399.38	136.25
1.41	406.34	138.79
1.51	412.89	141.18
1.61	419.08	143.43
1.71	424.95	145.54
1.81	430.53	147.55
1.91	435.85	149.44
2.01	440.93	151.24
2.11	445.8	152.95
2.21	450.47	154.57
2.31	454.96	156.12
2.41	459.29	157.6
2.51	463.46	159
2.61	467.49	160.34
2.71	471.38	161.63
2.81	475.15	162.85
2.91	478.81	164.02
3.01	482.35	165.14
3.11	485.79	166.22
3.21	489.14	167.24
3.31	492.4	168.22
3.41	495.57	169.16
3.51	498.65	170.06
3.61	501.67	170.93
3.71	504.6	171.75
3.81	507.47	172.54
3.91	510.28	173.29
4.01	513.02	174.02
4.11	515.7	174.71
4.21	518.32	175.37
4.31	520.89	176
4.41	523.4	176.6
4.51	525.87	177.18
4.61	528.29	177.73
4.71	530.66	178.25
4.81	532.98	178.75
4.91	535.26	179.23

φ =2 - P_0=0.5 bar		
P	T_u	S_u
0.5	298.22	0
1.04	358.53	122.54
1.14	366.6	126.07
1.24	374.1	129.2
1.34	381.11	131.99
1.44	387.69	134.47
1.54	393.9	136.69
1.64	399.78	138.69
1.74	405.36	140.5
1.84	410.68	142.13
1.94	415.75	143.62
2.04	420.61	144.97
2.14	425.26	146.21
2.24	429.73	147.36
2.34	434.03	148.41
2.44	438.18	149.39
2.54	442.18	150.31
2.64	446.05	151.17
2.74	449.79	151.97
2.84	453.42	152.73
2.94	456.94	153.45
3.04	460.35	154.14
3.14	463.67	154.79
3.24	466.89	155.42
3.34	470.03	156.03
3.44	473.09	156.61
3.54	476.07	157.18
3.64	478.98	157.73
3.74	481.82	158.26
3.84	484.6	158.78
3.94	487.31	159.3
4.04	489.96	159.8
4.14	492.55	160.29
4.24	495.09	160.77
4.34	497.57	161.25
4.44	500.01	161.72
4.54	502.4	162.18
4.64	504.74	162.64
4.74	507.04	163.09
4.84	509.29	163.54
4.94	511.51	163.99
5.04	513.68	164.43

φ =2.5 - P_0=2 bar					
P	T_u	S_u	P	T_u	S_u
2	310.62	0	6.43	411.36	31.969
4.02	368.54	28.195	6.51	412.42	32.067
4.06	369.31	28.254	6.58	413.47	32.165
4.09	370.09	28.315	6.65	414.54	32.265
4.13	370.88	28.377	6.73	415.61	32.365
4.17	371.67	28.44	6.81	416.69	32.466
4.20	372.46	28.504	6.88	417.77	32.568
4.24	373.26	28.569	6.96	418.86	32.67
4.28	374.07	28.636	7.04	419.96	32.773
4.32	374.89	28.703	7.13	421.07	32.878
4.36	375.71	28.772	7.21	422.18	32.982
4.40	376.53	28.841	7.29	423.3	33.088
4.44	377.36	28.911	7.38	424.42	33.194
4.48	378.2	28.982	7.47	425.56	33.302
4.53	379.04	29.054	7.56	426.69	33.41
4.57	379.89	29.127	7.65	427.84	33.519
4.61	380.75	29.201	7.74	428.99	33.629
4.66	381.61	29.276	7.83	430.15	33.739
4.70	382.48	29.352	11.10	464.56	37.116
4.75	383.35	29.428	11.25	465.91	37.252
4.80	384.23	29.505	11.40	467.27	37.389
4.84	385.12	29.584	11.55	468.63	37.527
4.89	386.01	29.662	11.71	469.99	37.665
4.94	386.91	29.742	11.87	471.36	37.804
4.99	387.82	29.823	12.03	472.73	37.944
5.04	388.73	29.904	12.19	474.11	38.085
5.09	389.65	29.986	12.36	475.49	38.226
5.14	390.58	30.069	12.52	476.87	38.368
5.19	391.51	30.152	12.70	478.26	38.511
5.25	392.44	30.236	12.87	479.65	38.654
5.30	393.38	30.321	13.05	481.05	38.799
5.36	394.33	30.407	13.22	482.45	38.944
5.41	395.29	30.493	13.41	483.87	39.091
5.47	396.25	30.58	13.59	485.28	39.238
5.53	397.21	30.668	13.78	486.71	39.387
5.59	398.18	30.756	13.97	488.15	39.537
5.65	399.16	30.845	14.17	489.58	39.687
5.71	400.15	30.935	14.37	491.03	39.839
5.77	401.13	31.025	14.57	492.48	39.992
5.83	402.13	31.117	14.78	493.94	40.145
5.89	403.13	31.209	14.98	495.39	40.299
5.96	404.14	31.301	15.19	496.85	40.453
6.02	405.15	31.395	15.41	498.3	40.608
6.09	406.17	31.489			
6.16	407.21	31.584			
6.22	408.24	31.679			
6.29	409.27	31.775			
6.36	410.31	31.871			

φ =2.5 - P_0=3 bar		
P	T_u	S_u
3	306.28	0
6.03	363.58	26.287
6.08	364.31	26.345
6.13	365.05	26.404
6.18	365.79	26.463
6.24	366.54	26.523
6.29	367.29	26.583
6.34	368.05	26.644
6.40	368.82	26.705
6.46	369.59	26.767
6.51	370.36	26.829
6.57	371.14	26.892
6.63	371.93	26.955
6.69	372.71	27.018
6.75	373.51	27.082
6.81	374.32	27.147
6.87	375.12	27.213
6.94	375.94	27.278
7.00	376.76	27.345
7.06	377.58	27.411
7.13	378.41	27.479
7.20	379.25	27.547
7.27	380.09	27.615
7.33	380.94	27.684
7.40	381.79	27.753
7.47	382.65	27.823
7.55	383.51	27.894
7.62	384.38	27.965
7.69	385.26	28.036
7.77	386.14	28.109
7.85	387.03	28.182
7.92	387.92	28.255
8.00	388.81	28.328
8.08	389.72	28.403
8.16	390.63	28.478
8.24	391.55	28.553
8.33	392.47	28.629
8.41	393.4	28.706
8.50	394.33	28.783
8.59	395.26	28.86
8.67	396.2	28.939
8.76	397.16	29.017
8.86	398.11	29.097
8.95	399.06	29.176
9.04	400.03	29.257
9.14	401	29.338
9.23	401.98	29.419
9.33	402.96	29.501

P	T_u	S_u
9.43	403.95	29.584
9.53	404.95	29.668
9.63	405.94	29.752
9.74	406.95	29.837
9.85	407.97	29.922
9.95	408.99	30.009
10.06	410.01	30.095
10.17	411.05	30.182
10.29	412.09	30.27
10.40	413.13	30.359
10.52	414.18	30.448
10.63	415.23	30.537
10.75	416.29	30.628
10.88	417.36	30.719
11.00	418.43	30.81
11.12	419.5	30.902
11.25	420.59	30.995
11.38	421.68	31.089
11.51	422.78	31.184
15.13	449.4	33.516
15.32	450.66	33.628
15.52	451.93	33.742
15.72	453.2	33.856
15.92	454.47	33.97
16.12	455.74	34.085
16.33	457.02	34.2
16.54	458.3	34.316
16.76	459.59	34.433
16.97	460.88	34.55
17.19	462.17	34.667
17.41	463.46	34.784
17.63	464.74	34.901
17.86	466.01	35.017
18.08	467.27	35.132

5- $\boldsymbol{CH_4/O_2}$ OPTIPRIME diluted targets at stoichiometry campaign results - $\boldsymbol{S_u = f(P,T)}$ vs mechanisms

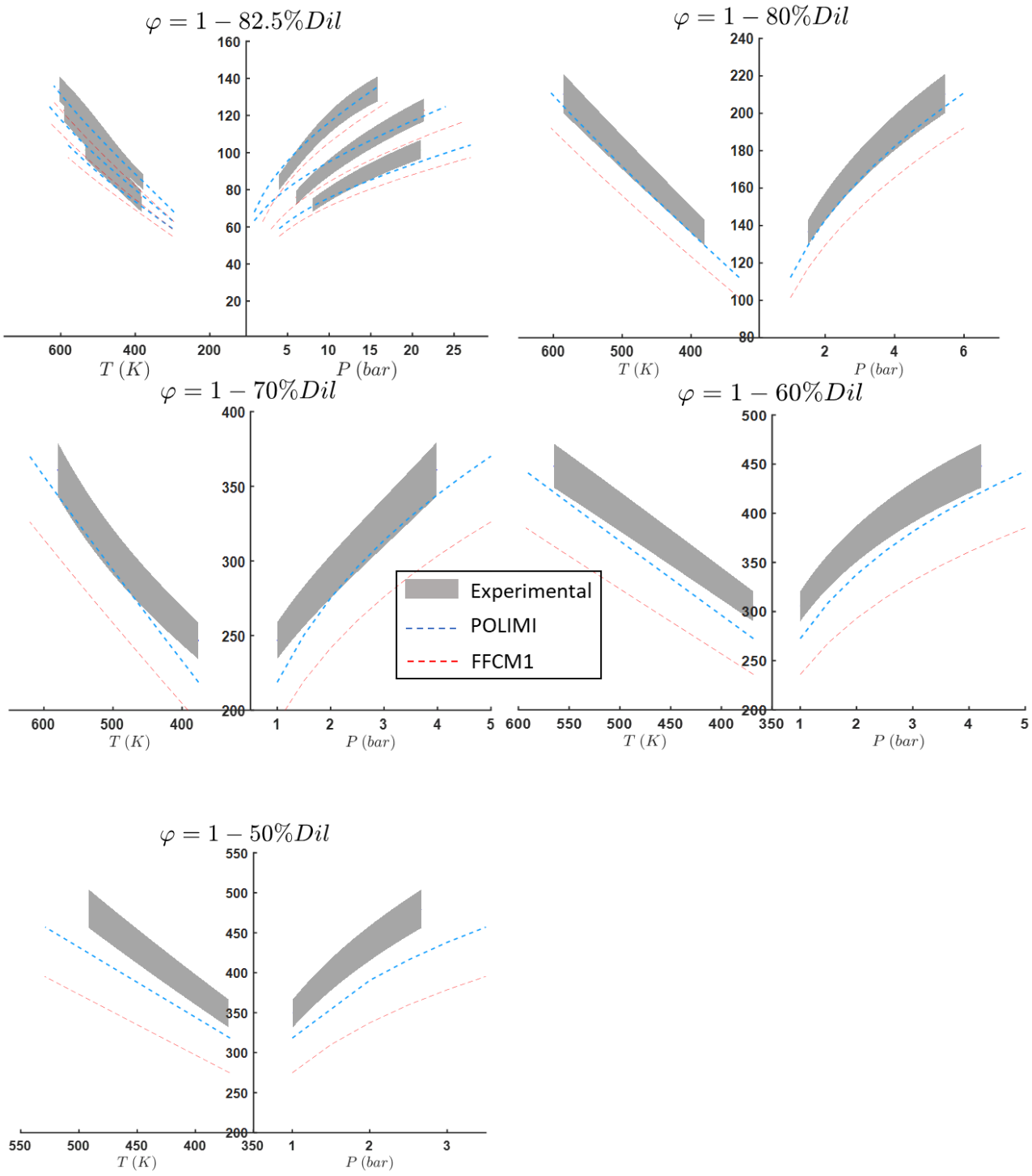

6- CH_4/O_2 OPTIPRIME diluted targets at stoichiometry - P, T, S_u experimental traces

φ =1 - 82.5%Dil - P_0=2 bar

P	T_u	S_u
2.00	295.99	0
4.01	378.43	84.166
4.03	379.25	84.311
4.06	380.15	84.469
4.09	381.15	84.648
4.13	382.24	84.843
4.16	383.22	85.02
4.18	384.1	85.181
4.21	384.98	85.341
4.24	385.91	85.514
4.27	386.98	85.711
4.31	388.12	85.924
4.34	389.11	86.111
4.37	390.02	86.282
4.40	390.94	86.458
4.44	392.06	86.673
4.48	393.26	86.905
4.51	394.31	87.109
4.54	395.24	87.29
4.57	396.13	87.464
4.60	397.13	87.663
4.64	398.34	87.903
4.68	399.5	88.134
4.72	400.52	88.341
4.75	401.49	88.536
4.79	402.59	88.76
4.83	403.76	89
4.87	405.05	89.264
4.91	406.28	89.52
4.95	407.36	89.744
4.98	408.21	89.922
5.03	409.63	90.222
5.07	410.68	90.443
5.10	411.56	90.63
5.13	412.49	90.829
5.18	413.66	91.08
5.22	414.76	91.316
5.26	416.04	91.593
5.30	417.2	91.845
5.34	418.25	92.076
5.39	419.54	92.358
5.44	420.87	92.653
5.49	422.12	92.93
5.54	423.41	93.216
5.59	424.72	93.51
5.63	425.94	93.784
5.68	427.19	94.066
5.72	428.3	94.317
5.77	429.5	94.59
5.82	430.84	94.896
5.87	432.19	95.206
5.92	433.32	95.466
5.97	434.59	95.759
6.02	435.86	96.052
6.07	437.07	96.334
6.12	438.24	96.607
6.17	439.59	96.923
6.23	441	97.252
6.28	442.34	97.57
6.34	443.64	97.877
6.39	445	98.197
6.46	446.47	98.547
6.51	447.78	98.859
6.56	449.03	99.156
6.62	450.31	99.465
6.68	451.74	99.807
6.74	453.18	100.15
6.80	454.53	100.48
6.86	455.83	100.79
6.92	457.17	101.12
6.98	458.71	101.49
7.05	460.19	101.85
7.11	461.5	102.17
7.17	462.88	102.5
7.24	464.37	102.87
7.31	465.88	103.23
7.37	467.29	103.58
7.43	468.61	103.9
7.50	470.15	104.28
7.59	471.89	104.71
7.67	473.55	105.12
7.72	474.73	105.4
7.80	476.39	105.81
7.88	477.95	106.19
7.94	479.2	106.5
7.99	480.31	106.77
8.08	482.09	107.21
8.15	483.64	107.59
8.23	485.13	107.96
8.30	486.65	108.33
8.39	488.28	108.73
8.46	489.82	109.11
8.54	491.33	109.48
8.62	492.9	109.86
8.70	494.51	110.26
8.78	496.06	110.64
8.87	497.61	111.02
8.96	499.32	111.43
9.04	500.97	111.83
9.13	502.51	112.21
9.21	504.03	112.58
9.30	505.81	113.01
9.40	507.5	113.42
9.49	509.14	113.81
9.58	510.77	114.2
9.67	512.43	114.6
9.76	514.11	115.01
9.86	515.85	115.42
9.95	517.5	115.81
10.04	519.08	116.19
10.14	520.71	116.57
10.25	522.59	117.02
10.35	524.32	117.43
10.45	526.06	117.83
10.55	527.82	118.24
10.66	529.59	118.66
10.76	531.31	119.05
10.87	533.1	119.47
10.98	534.89	119.88
11.09	536.66	120.28
11.20	538.51	120.71
11.32	540.33	121.12
11.43	542.07	121.51
11.54	543.84	121.91
11.65	545.69	122.32
11.77	547.5	122.73
11.89	549.38	123.14
12.02	551.29	123.57
12.14	553.12	123.97
12.25	554.93	124.36
12.38	556.83	124.78
12.50	558.67	125.17
12.64	560.65	125.6
12.77	562.65	126.03
12.91	564.6	126.44
13.03	566.35	126.81
13.18	568.51	127.26
13.30	570.29	127.63
13.42	571.96	127.98
13.55	573.82	128.36
13.71	576.03	128.82
13.82	577.62	129.14
13.98	579.8	129.58
14.15	582.15	130.05
14.31	584.31	130.49
14.44	586.04	130.83
14.59	588.13	131.24
14.74	590.15	131.64
14.90	592.19	132.03
15.05	594.2	132.42
15.20	596.08	132.78
15.36	598.25	133.2
15.51	600.14	133.56
15.65	601.86	133.88
15.79	603.69	134.22

φ =1 - 82.5%Dil - P_0=3 bar

P	T_u	S_u	P	T_u	S_u	P	T_u	S_u
3	300	0	9.00	441.15	88.228	14.47	518.57	105.83
6.02	383.67	75.614	9.07	442.25	88.474	14.59	520.05	106.17
6.06	384.53	75.8	9.14	443.4	88.731	14.72	521.65	106.54
6.10	385.3	75.968	9.21	444.59	88.994	14.85	523.21	106.9
6.14	386.17	76.155	9.28	445.78	89.261	14.98	524.72	107.26
6.18	387.08	76.354	9.35	446.97	89.527	15.12	526.32	107.63
6.22	387.99	76.55	9.44	448.3	89.824	15.26	527.96	108.01
6.26	388.78	76.721	9.51	449.54	90.101	15.40	529.58	108.39
6.31	389.89	76.962	9.59	450.76	90.373	15.53	531.12	108.75
6.35	390.9	77.181	9.66	451.98	90.648	15.67	532.72	109.12
6.39	391.73	77.361	9.74	453.23	90.927	15.81	534.32	109.5
6.43	392.53	77.535	9.82	454.47	91.206	15.95	535.92	109.87
6.48	393.67	77.782	9.90	455.77	91.497	16.09	537.54	110.25
6.52	394.39	77.939	9.98	457.02	91.778	16.25	539.23	110.64
6.55	395.09	78.093	10.06	458.22	92.047	16.39	540.8	111.01
6.60	396.03	78.297	10.14	459.47	92.327	16.53	542.43	111.4
6.65	397.09	78.528	10.22	460.79	92.623	16.69	544.1	111.79
6.68	397.83	78.688	10.31	462.11	92.922	16.84	545.78	112.18
6.73	398.88	78.917	10.39	463.43	93.218	16.99	547.37	112.56
6.79	399.95	79.149	10.48	464.72	93.51	17.15	549.09	112.96
6.83	400.88	79.353	10.56	466.01	93.801	17.31	550.83	113.38
6.88	401.8	79.554	10.65	467.38	94.11	17.47	552.5	113.77
6.94	403.11	79.84	10.74	468.71	94.411	17.62	554.11	114.15
6.97	403.64	79.955	10.83	470.07	94.717	17.78	555.82	114.55
7.00	404.36	80.114	10.93	471.41	95.021	17.96	557.6	114.98
7.05	405.39	80.339	11.01	472.62	95.294	18.11	559.24	115.37
7.11	406.46	80.573	11.09	473.89	95.582	18.28	560.92	115.76
7.13	406.93	80.675	11.19	475.22	95.883	18.45	562.69	116.18
7.21	408.57	81.033	11.28	476.56	96.188	18.63	564.53	116.62
7.29	410.09	81.367	11.37	477.9	96.491	18.80	566.21	117.02
7.35	411.21	81.613	11.46	479.21	96.79	18.97	567.88	117.42
7.39	412.05	81.796	11.56	480.54	97.091	19.14	569.63	117.83
7.45	413.15	82.037	11.66	481.99	97.422	19.33	571.46	118.27
7.51	414.26	82.281	11.76	483.34	97.729	19.51	573.27	118.7
7.57	415.5	82.553	11.85	484.63	98.021	19.68	574.94	119.1
7.63	416.62	82.799	11.96	486.2	98.379	19.87	576.72	119.53
7.69	417.64	83.024	12.08	487.81	98.747	20.06	578.55	119.97
7.75	418.84	83.289	12.18	489.18	99.06	20.25	580.41	120.41
7.79	419.64	83.466	12.28	490.54	99.372	20.44	582.17	120.83
7.83	420.36	83.623	12.38	491.98	99.7	20.63	583.95	121.26
7.89	421.42	83.858	12.49	493.41	100.03	20.82	585.77	121.7
7.96	422.73	84.146	12.60	494.93	100.38	21.02	587.61	122.14
8.01	423.61	84.341	12.71	496.38	100.71	21.22	589.48	122.59
8.08	425.03	84.654	12.82	497.77	101.03	21.42	591.3	123.03
8.17	426.62	85.006	12.93	499.2	101.36			
8.24	427.75	85.255	13.05	500.83	101.73			
8.28	428.49	85.419	13.17	502.37	102.08			
8.34	429.62	85.668	13.28	503.73	102.4			
8.40	430.68	85.902	13.40	505.31	102.76			
8.45	431.52	86.089	13.53	506.94	103.14			
8.51	432.66	86.342	13.61	507.98	103.37			
8.59	434.11	86.664	13.69	508.97	103.6			
8.67	435.41	86.952	13.82	510.62	103.98			
8.73	436.4	87.172	13.94	512.16	104.34			
8.79	437.5	87.417	14.05	513.55	104.66			
8.86	438.68	87.679	14.20	515.29	105.07			
8.93	439.91	87.952	14.35	517.11	105.49			

φ =1 - 82.5%Dil - P_0=4 bar

P	T_u	S_u	P	T_u	S_u	P	T_u	S_u
4	300.03	0	11.78	438.32	82.424	18.50	511.34	97.117
8.01	383.4	71.644	11.87	439.44	82.645	18.66	512.82	97.419
8.07	384.31	71.821	11.95	440.53	82.863	18.81	514.26	97.713
8.11	385.09	71.973	12.04	441.62	83.079	18.96	515.66	97.999
8.17	385.95	72.139	12.13	442.78	83.309	19.12	517.08	98.292
8.22	386.92	72.328	12.22	443.92	83.536	19.29	518.66	98.614
8.28	387.85	72.51	12.31	445.06	83.761	19.45	520.08	98.905
8.33	388.63	72.66	12.41	446.19	83.986	19.61	521.55	99.206
8.38	389.45	72.821	12.50	447.32	84.212	19.78	523.07	99.518
8.43	390.31	72.988	12.59	448.45	84.437	19.95	524.59	99.83
8.49	391.19	73.16	12.68	449.61	84.668	20.11	525.97	100.11
8.54	392.09	73.335	12.78	450.78	84.901	20.29	527.53	100.43
8.60	392.93	73.499	12.88	451.95	85.134	20.46	529.08	100.75
8.65	393.8	73.669	12.97	453.12	85.367	20.64	530.6	101.07
8.71	394.7	73.845	13.07	454.29	85.601	20.81	532.11	101.38
8.77	395.61	74.022	13.17	455.48	85.838	21.00	533.72	101.71
8.82	396.47	74.19	13.27	456.65	86.072			
8.87	397.29	74.35	13.37	457.82	86.305			
8.93	398.23	74.535	13.47	459.01	86.544			
8.99	399.14	74.712	13.58	460.26	86.794			
9.05	399.97	74.873	13.68	461.45	87.032			
9.10	400.77	75.03	13.79	462.65	87.272			
9.16	401.76	75.224	13.89	463.88	87.518			
9.22	402.69	75.406	14.00	465.07	87.756			
9.29	403.65	75.593	14.10	466.25	87.992			
9.35	404.66	75.791	14.21	467.48	88.239			
9.42	405.64	75.984	14.32	468.7	88.485			
9.48	406.55	76.161	14.43	469.93	88.731			
9.54	407.47	76.342	14.54	471.2	88.986			
9.61	408.42	76.529	14.66	472.51	89.25			
9.67	409.41	76.722	14.78	473.81	89.51			
9.74	410.45	76.926	14.90	475.08	89.767			
9.81	411.43	77.119	15.01	476.34	90.021			
9.88	412.36	77.302	15.13	477.6	90.273			
9.94	413.36	77.497	15.25	478.84	90.524			
10.02	414.42	77.706	15.37	480.19	90.796			
10.09	415.44	77.906	15.50	481.52	91.063			
10.16	416.39	78.094	15.61	482.76	91.315			
10.23	417.44	78.3	15.73	484.01	91.567			
10.30	418.41	78.492	15.86	485.35	91.838			
10.36	419.3	78.666	15.99	486.67	92.104			
10.43	420.22	78.848	16.12	488	92.374			
10.51	421.35	79.07	16.25	489.34	92.644			
10.58	422.34	79.264	16.37	490.61	92.901			
10.65	423.33	79.459	16.51	492.03	93.189			
10.73	424.36	79.662	16.64	493.36	93.459			
10.81	425.44	79.875	16.78	494.71	93.732			
10.88	426.46	80.076	16.91	496.08	94.01			
10.96	427.51	80.285	17.05	497.42	94.282			
11.04	428.57	80.495	17.18	498.72	94.547			
11.12	429.6	80.698	17.33	500.18	94.844			
11.20	430.67	80.909	17.47	501.57	95.126			
11.28	431.82	81.137	17.61	502.86	95.388			
11.36	432.89	81.349	17.75	504.3	95.681			
11.44	433.95	81.559	17.91	505.77	95.98			
11.53	435.04	81.774	18.05	507.14	96.26			
11.61	436.14	81.992	18.20	508.55	96.546			
11.69	437.2	82.203	18.35	510	96.843			

φ =1 - 80.0%Dil - P_0=0.75 bar					
P	T_u	S_u	P	T_u	S_u
0.75	298.46	0	2.76	467.19	167.12
1.51	380.83	136.4	2.79	468.98	167.77
1.53	382.34	136.93	2.82	470.7	168.39
1.55	383.73	137.41	2.85	472.49	169.03
1.56	384.82	137.8	2.88	474.33	169.7
1.57	385.91	138.18	2.92	476.23	170.38
1.58	387.04	138.58	2.95	478.21	171.1
1.60	388.31	139.03	2.99	480.18	171.81
1.62	389.61	139.49	3.03	482.12	172.51
1.63	390.94	139.96	3.07	484.18	173.26
1.65	392.42	140.48	3.11	486.25	174.01
1.67	393.71	140.93	3.14	488.25	174.74
1.68	394.88	141.35	3.18	490.12	175.41
1.69	396.11	141.78	3.22	491.98	176.09
1.71	397.5	142.27	3.26	494.22	176.9
1.73	399.05	142.82	3.30	496.31	177.66
1.75	400.37	143.29	3.34	498.27	178.38
1.76	401.61	143.73	3.38	500.13	179.05
1.78	402.75	144.13	3.42	502.15	179.79
1.80	404.33	144.69	3.47	504.33	180.58
1.82	405.93	145.25	3.51	506.38	181.33
1.84	407.41	145.78	3.55	508.47	182.09
1.86	408.55	146.18	3.60	510.62	182.88
1.87	409.68	146.58	3.64	512.71	183.64
1.89	411.21	147.12	3.69	514.81	184.41
1.91	412.78	147.68	3.73	516.95	185.19
1.93	414.33	148.23	3.78	519.17	186.01
1.95	415.73	148.73	3.83	521.4	186.82
1.97	417.17	149.24	3.88	523.51	187.6
1.99	418.65	149.76	3.93	525.72	188.41
2.01	420.22	150.32	3.98	527.98	189.24
2.04	421.77	150.87	4.03	530.18	190.05
2.06	423.3	151.42	4.08	532.34	190.84
2.08	424.79	151.95	4.13	534.45	191.62
2.10	426.32	152.49	4.19	536.88	192.52
2.13	427.96	153.07	4.24	539.32	193.42
2.15	429.31	153.56	4.30	541.77	194.32
2.17	430.7	154.05	4.36	543.96	195.13
2.19	432.36	154.64	4.41	546.17	195.95
2.22	434.26	155.32	4.47	548.5	196.81
2.25	436.15	156	4.53	550.89	197.7
2.27	437.52	156.48	4.59	553.26	198.57
2.29	439.06	157.03	4.65	555.51	199.41
2.32	440.71	157.62	4.71	557.94	200.31
2.35	442.44	158.24	4.77	560.42	201.23
2.37	444.04	158.81	4.84	562.88	202.15
2.39	445.49	159.33	4.90	565.27	203.04
2.42	447.31	159.98	4.96	567.63	203.92
2.45	449.15	160.64	5.03	570.13	204.85
2.48	450.98	161.3	5.10	572.68	205.8
2.51	452.68	161.91	5.17	575.25	206.76
2.54	454.4	162.53	5.24	577.79	207.71
2.57	456.27	163.2	5.31	580.31	208.65
2.60	458.15	163.87	5.38	582.81	209.59
2.63	459.99	164.53	5.46	585.39	210.56
2.66	461.69	165.14			
2.69	463.47	165.79			
2.72	465.31	166.45			

φ =1 - 70.0%Dil - P_0=0.5 bar

P	T_u	S_u
0.5	299.34	0
1.00	376.25	246.43
1.02	378.33	247.31
1.04	380.58	248.26
1.06	383.03	249.31
1.08	385.35	250.3
1.10	387.62	251.27
1.12	389.81	252.21
1.14	392.19	253.23
1.16	394.62	254.29
1.18	397.14	255.38
1.21	399.84	256.56
1.23	402.55	257.74
1.26	405	258.82
1.28	407.46	259.91
1.31	409.91	260.99
1.33	412.37	262.09
1.36	414.9	263.23
1.38	417.48	264.39
1.41	420.27	265.65
1.44	423.01	266.9
1.47	425.69	268.13
1.50	428.56	269.45
1.53	431.51	270.82
1.57	434.61	272.27
1.60	437.54	273.65
1.63	440.37	275
1.67	443.17	276.33
1.71	446.38	277.88
1.75	449.75	279.52
1.79	452.98	281.1
1.83	456.17	282.68
1.87	459.31	284.25
1.91	462.8	286.01
1.96	466.28	287.79
2.01	469.78	289.59
2.05	473.16	291.35
2.10	476.5	293.11
2.15	479.83	294.89
2.20	483.46	296.85
2.25	487.03	298.8
2.30	490.29	300.6
2.35	493.78	302.55
2.41	497.44	304.62
2.47	501.56	307
2.54	505.49	309.29
2.60	509.28	311.54
2.66	512.93	313.74
2.72	516.54	315.95
2.78	520.11	318.16
2.86	524.3	320.81
2.93	528.47	323.49
3.01	532.6	326.19
3.08	536.77	328.96
3.16	540.94	331.79
3.25	545.16	334.72
3.32	549.14	337.53
3.41	553.18	340.43
3.50	557.83	343.84
3.59	562.28	347.19
3.69	566.61	350.51
3.78	570.95	353.92
3.88	575.46	357.55
3.99	580.1	361.36

φ =1 - 60.0%Dil - P_0=0.5 bar

P	T_u	S_u
0.5	296.2	0
1.00	368.83	305.45
1.02	370.19	306.45
1.03	371.55	307.46
1.04	372.9	308.45
1.05	374.35	309.52
1.07	375.89	310.66
1.08	377.41	311.78
1.10	378.96	312.92
1.11	380.54	314.09
1.13	382.1	315.24
1.14	383.61	316.35
1.15	385.01	317.39
1.17	386.41	318.42
1.18	387.85	319.48
1.20	389.49	320.69
1.21	391.11	321.88
1.23	392.73	323.08
1.25	394.46	324.36
1.27	396.18	325.62
1.28	397.88	326.88
1.30	399.54	328.1
1.32	401.18	329.31
1.34	402.81	330.51
1.36	404.52	331.77
1.37	406.21	333.02
1.39	407.9	334.26
1.41	409.61	335.52
1.43	411.31	336.77
1.45	413	338.02
1.47	414.86	339.39
1.50	416.78	340.8
1.52	418.68	342.2
1.54	420.67	343.66
1.57	422.71	345.17
1.59	424.73	346.66
1.62	426.64	348.05
1.64	428.43	349.37
1.66	430.2	350.68
1.68	432.02	352.02
1.71	433.93	353.42
1.73	435.81	354.8
1.76	437.78	356.25
1.79	439.96	357.85
1.82	442.12	359.44
1.85	444.26	361.01
1.88	446.41	362.59
1.91	448.53	364.15
1.94	450.62	365.68
1.97	452.67	367.19
2.00	454.7	368.67
2.03	456.7	370.14
2.06	458.95	371.8
2.10	461.19	373.43
2.13	463.38	375.04
2.17	465.76	376.79
2.20	468.13	378.52
2.24	470.47	380.23
2.28	472.69	381.86
2.31	474.87	383.45
2.35	477.03	385.03
2.39	479.35	386.72
2.43	481.72	388.46
2.47	484.06	390.16
2.51	486.39	391.86
2.55	488.71	393.55
2.59	491	395.22
2.63	493.32	396.91
2.68	495.67	398.62
2.72	497.98	400.3
2.77	500.54	402.16
2.82	503.46	404.28
2.88	506.34	406.37
2.93	509.04	408.33
2.98	511.4	410.04
3.03	513.72	411.72
3.07	516.06	413.4
3.12	518.47	415.14
3.17	520.85	416.86
3.22	523.29	418.62
3.29	526.51	420.94
3.36	529.68	423.22
3.43	532.79	425.45
3.49	535.37	427.3
3.55	537.91	429.12
3.61	540.42	430.92
3.66	542.83	432.63
3.72	545.2	434.33
3.78	547.55	436
3.85	550.46	438.06
3.92	553.47	440.2
4.00	556.43	442.3
4.07	559.37	444.37
4.15	562.26	446.41
4.22	565.11	448.42

φ =1 - 50.0%Dil - P_0=0.5 bar

P	T_u	S_u
0.5	300.76	0
1.01	371.52	349.18
1.02	372.7	350.4
1.03	373.94	351.69
1.04	375.18	352.98
1.05	376.4	354.25
1.07	377.67	355.57
1.08	379.03	356.99
1.09	380.38	358.39
1.11	381.71	359.79
1.12	383.07	361.21
1.13	384.53	362.73
1.15	385.98	364.25
1.16	387.42	365.76
1.18	388.84	367.26
1.19	390.36	368.85
1.21	391.85	370.42
1.22	393.32	371.98
1.24	394.79	373.53
1.25	396.1	374.91
1.27	397.41	376.29
1.28	398.7	377.66
1.30	399.97	379.01
1.31	401.42	380.54
1.33	402.89	382.11
1.35	404.35	383.65
1.36	405.79	385.19
1.38	407.35	386.86
1.40	408.96	388.57
1.42	410.55	390.27
1.44	412.12	391.95
1.46	413.72	393.67
1.48	415.34	395.4
1.50	416.94	397.12
1.51	418.52	398.82
1.54	420.15	400.57
1.56	421.87	402.43
1.58	423.57	404.26
1.60	425.25	406.09
1.62	426.93	407.9
1.65	428.61	409.73
1.67	430.28	411.54
1.69	431.92	413.33
1.71	433.56	415.11
1.74	435.24	416.94
1.76	436.89	418.75
1.78	438.53	420.54
1.80	440.15	422.32
1.83	442.06	424.41
1.86	443.97	426.52
1.89	445.86	428.6
1.92	447.73	430.66
1.95	449.79	432.94
1.98	451.89	435.26
2.01	453.97	437.56
2.04	456.02	439.84
2.07	457.91	441.95
2.10	459.7	443.94
2.13	461.47	445.91
2.16	463.22	447.87
2.19	464.99	449.85
2.22	466.78	451.87
2.25	468.56	453.86
2.28	470.32	455.84
2.31	472.18	457.94
2.35	474.32	460.35
2.39	476.43	462.74
2.43	478.52	465.11
2.46	480.6	467.47
2.50	482.81	469.98
2.54	484.98	472.46
2.59	487.13	474.92
2.63	489.25	477.34
2.67	491.34	479.73

φ =1 - 0.0%Dil - P_0=0.3 bar

P	T_u	S_u
0.3	303.71	0
0.57	358.22	474.36
0.67	373.28	487.64
0.77	386.61	500.07
0.87	398.58	511.95
0.97	409.46	523.45
1.07	419.45	534.71
1.17	428.69	545.83
1.27	437.29	556.87
1.37	445.34	567.89
1.47	452.9	578.95
1.57	460.05	590.07

Appendix C – Optimization results

1- Genetic algorithm trials

Parameter	Value
Max iterations	10 000
Max function evaluations	80 000
Convergence tolerance	1e-8
Solution Target	1e-6
Seed	1000
Mutation Rate	0.5
Crossover Rate	0.9
Replacement Type	chc=50
Population Size	100

Figure 114: Parameters used for the Genetic Algorithm optimization trials - the parameters indicated here are the one that gave the best results of the objective function

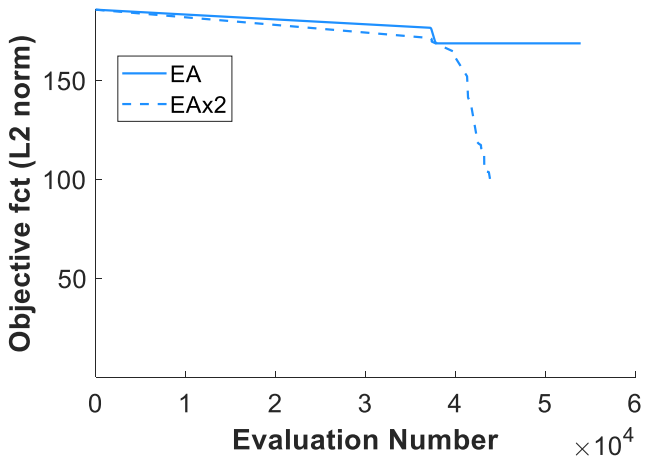

Figure 115: Evolution of the objective function with the Genetic Algorithm method (EAx2 represent the configuration for which all uncertainties were doubled)

2- Complete results of the optimization process with the DIRECT method

A. Laminar flame speed results

Optimization targets

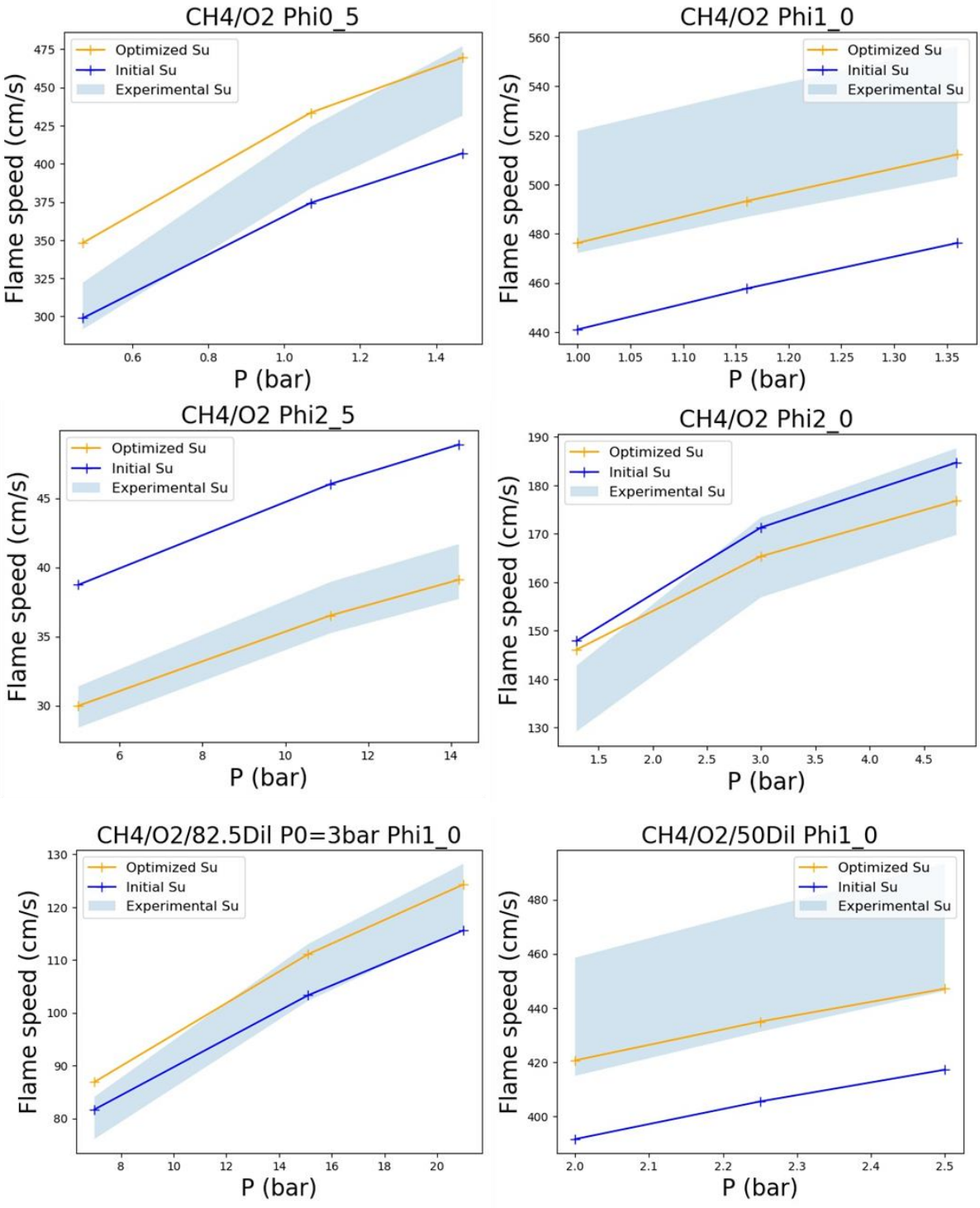

Control targets

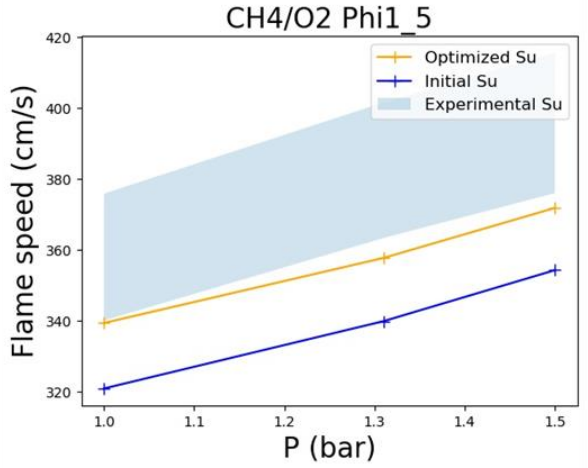

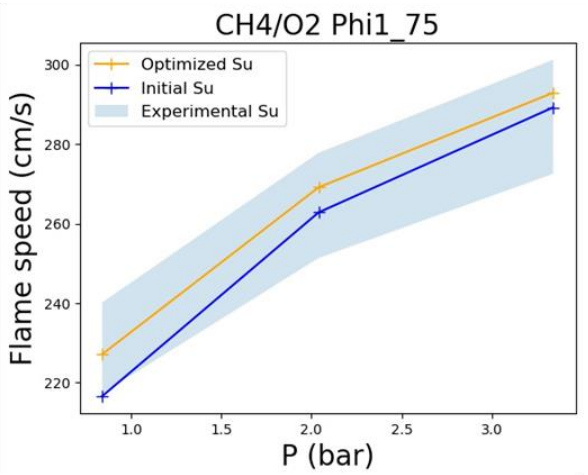

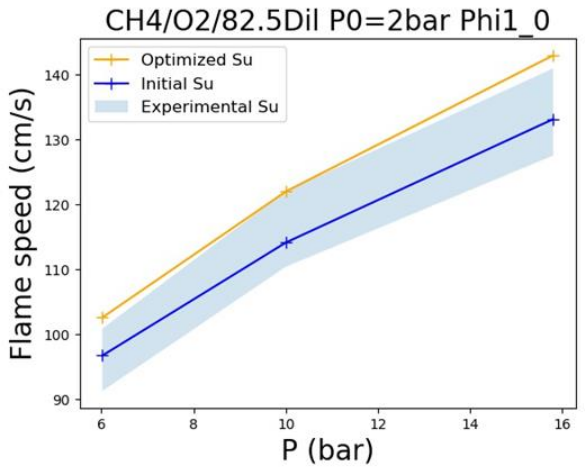

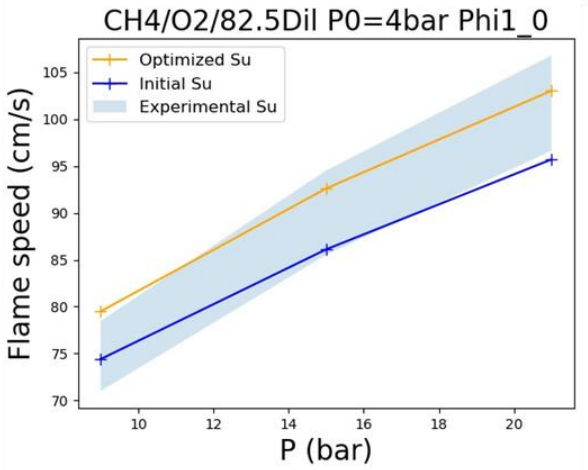

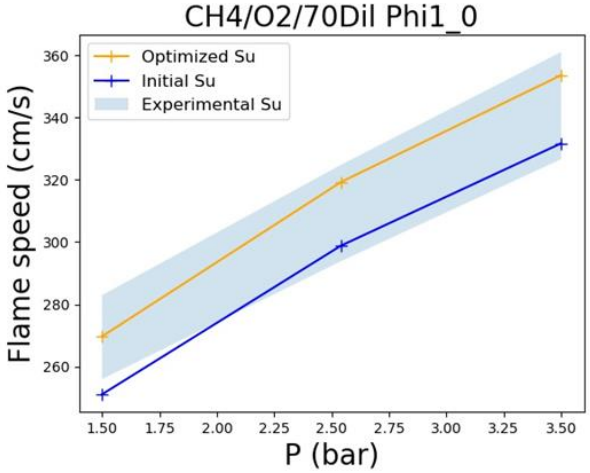

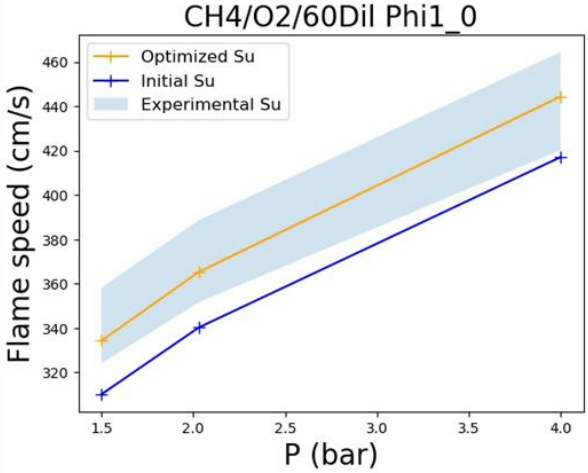

B. Ignition delay times results

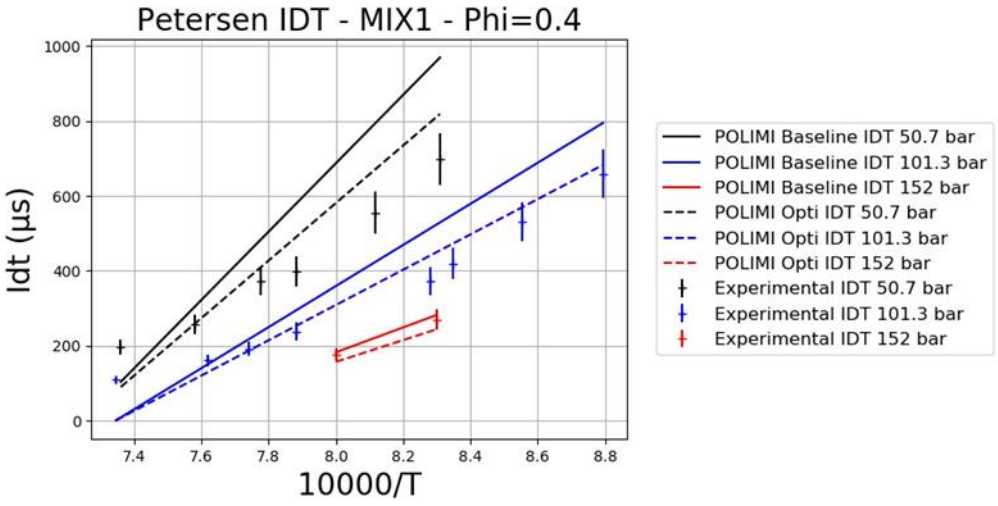

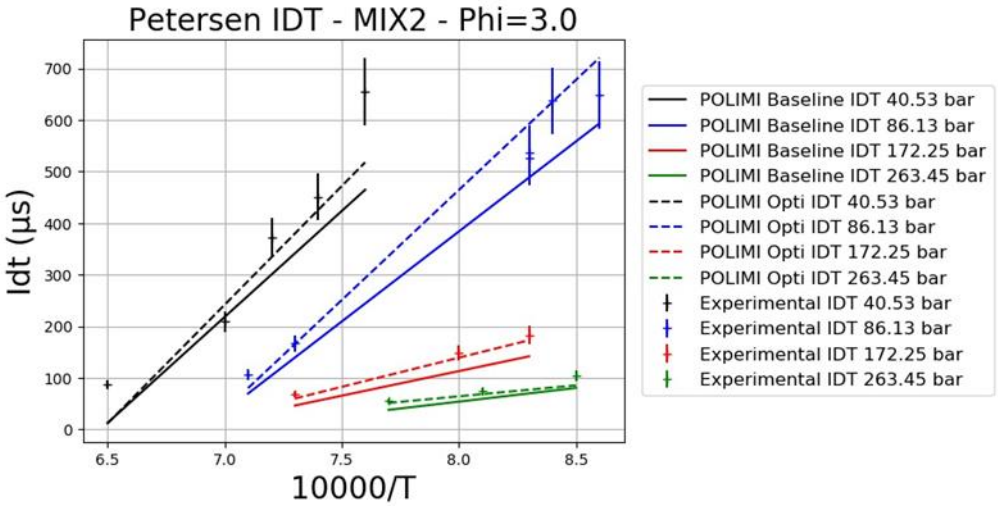

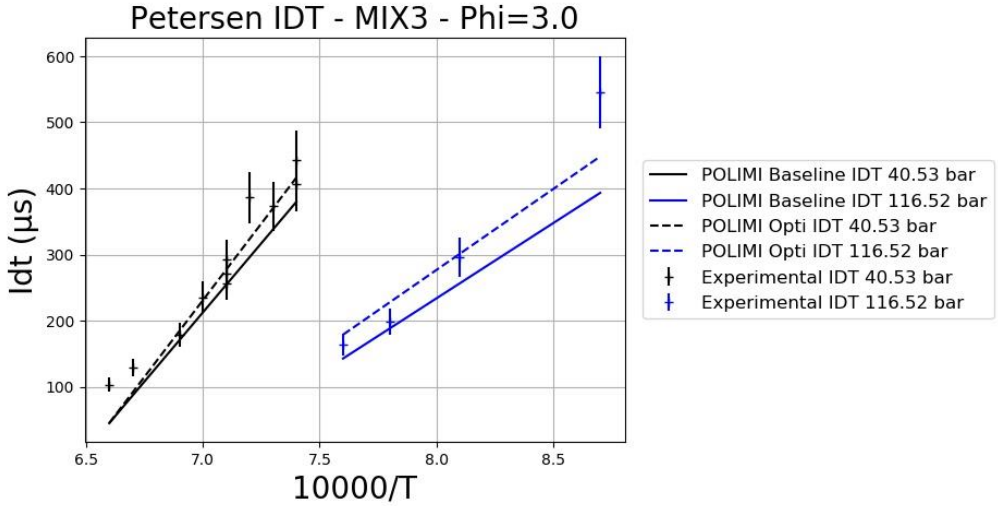

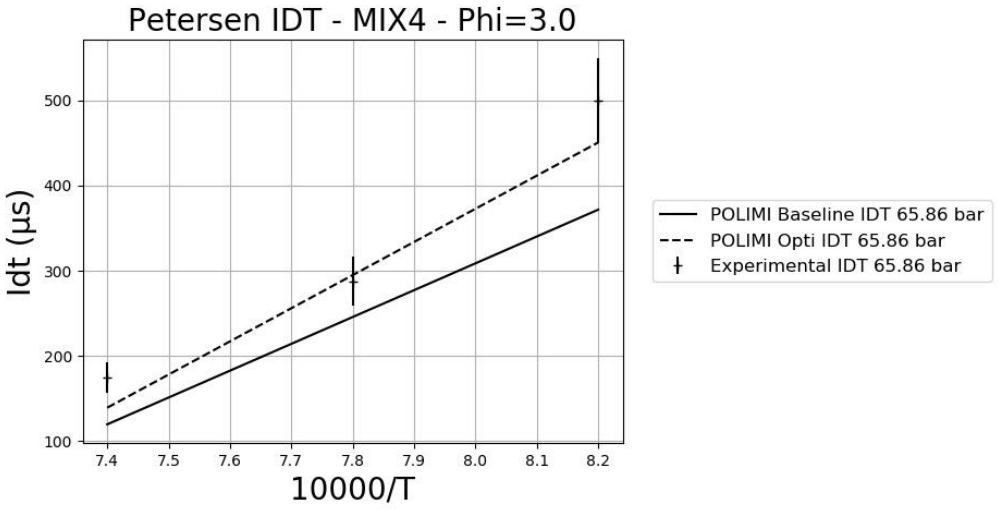
Petersen IDT - MIX4 - Phi=3.0
Idt (µs)
10000/T
POLIMI Baseline IDT 65.86 bar
POLIMI Opti IDT 65.86 bar
Experimental IDT 65.86 bar

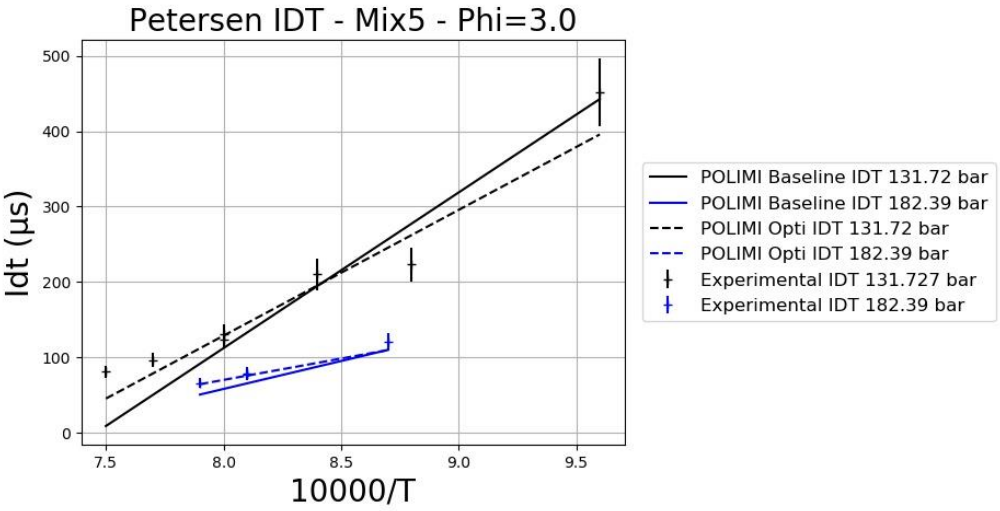
Petersen IDT - Mix5 - Phi=3.0
Idt (µs)
10000/T
POLIMI Baseline IDT 131.72 bar
POLIMI Baseline IDT 182.39 bar
POLIMI Opti IDT 131.72 bar
POLIMI Opti IDT 182.39 bar
Experimental IDT 131.727 bar
Experimental IDT 182.39 bar

Appendix D – ARC Reduced mechanisms

1-POLIMI Opti ARC

#Reactions	116
#Transported species	19
#QSS	7
Transported species	$H_2\ H\ O_2\ O\ H_2O\ OH\ HO_2\ CO\ CO_2\ CH_4\ CH_3\ CH_3O_2\ CH_3OH\ CH_2OH\ CH_2O\ C_2H_6\ C_2H_4\ C_2H_2\ CH_2CHO$
QSS species	$H_2O_2\ CH_2\ CH_3O\ HCO\ C_2H_3\ C_2H_5\ HCCO$

- **The computed Prandtl number** for the mixture is $\boldsymbol{P_r}$ **= 0.635**
- **The computed Schmidt numbers** for the transported species are the following:

Species	$\boldsymbol{S_{ch}}$
$\boldsymbol{H_2}$	0.236
$\boldsymbol{H}$	0.142
$\boldsymbol{O_2}$	0.838
$\boldsymbol{O}$	0.541
$\boldsymbol{H_2O}$	0.574
$\boldsymbol{OH}$	0.548
$\boldsymbol{HO_2}$	0.836
$\boldsymbol{CO}$	0.852
$\boldsymbol{CO_2}$	1.113
$\boldsymbol{CH_4}$	0.777
$\boldsymbol{CH_3}$	0.776
$\boldsymbol{CH_3O_2}$	1.061
$\boldsymbol{CH_3OH}$	0.986
$\boldsymbol{CH_2OH}$	0.991
$\boldsymbol{CH_2O}$	0.965
$\boldsymbol{C_2H_6}$	1.131
$\boldsymbol{C_2H_4}$	0.869
$\boldsymbol{C_2H_2}$	0.922
$\boldsymbol{CH_2CHO}$	1.145

No.	Reaction	A (variable unit)	b (-)	Ea (cal/mol)
1	2 O + M ⟷ O2 + M CH4:2.00E+00 CO:1.75E+00 CO2:3.60E+00 H2:2.40E+00 H2O:1.54E+01	1.200000E+11	-1.000000E+00	0.000000E+00
2	H + O + M ⟷ OH + M CH4:2.00E+00 CO:1.50E+00 CO2:2.00E+00 H2:2.00E+00 H2O:6.00E+00	5.000000E+11	-1.000000E+00	0.000000E+00
3	H2 + O ⟷ H + OH	5.000000E+01	2.670000E+00	2.631736E+07
4	HO2 + O ⟷ O2 + OH	2.000000E+10	0.000000E+00	0.000000E+00
5	H2O2 + O ⟷ HO2 + OH	9.630000E+03	2.000000E+00	1.673600E+07
6	CH3 + O ⟷ CH2O + H	8.430000E+10	0.000000E+00	0.000000E+00
7	CH4 + O ⟷ CH3 + OH	1.020000E+06	1.500000E+00	3.598240E+07
8	CO + O + M ⟷ CO2 + M CH4:2.00E+00 CO:1.50E+00 CO2:3.50E+00 H2:2.00E+00 H2O:6.00E+00 O2:6.00E+00	6.020000E+08	0.000000E+00	1.255200E+07
9	HCO + O ⟷ CO + OH	3.000000E+10	0.000000E+00	0.000000E+00
10	HCO + O ⟷ CO2 + H	3.000000E+10	0.000000E+00	0.000000E+00
11	CH2O + O ⟷ HCO + OH	3.900000E+10	0.000000E+00	1.481136E+07
12	C2H2 + O ⟷ H + HCCO	1.020000E+04	2.000000E+00	7.949600E+06
13	C2H3 + O ⟷ CH2CO + H	3.000000E+10	0.000000E+00	0.000000E+00
14	C2H4 + O ⟷ CH3 + HCO	1.920000E+04	1.830000E+00	9.204800E+05
15	C2H5 + O ⟷ CH2O + CH3	1.320000E+11	0.000000E+00	0.000000E+00
16	C2H6 + O ⟷ C2H5 + OH	8.980000E+04	1.920000E+00	2.380696E+07
17	HCCO + O ⟷ 2 CO + H	1.000000E+11	0.000000E+00	0.000000E+00
18	CH2CO + O ⟷ HCCO + OH	1.000000E+10	0.000000E+00	3.347200E+07
19	CO + O2 ⟷ CO2 + O	2.500000E+09	0.000000E+00	1.999952E+08
20	CH2O + O2 ⟷ HCO + HO2	1.000000E+11	0.000000E+00	1.673600E+08
21	H + O2 + M ⟷ HO2 + M CO:7.50E-01 CO2:1.50E+00 H2O:0.00E+00 O2:0.00E+00	2.800000E+12	-8.600000E-01	0.000000E+00
22	H + 2 O2 ⟷ HO2 + O2	3.000000E+14	-1.720000E+00	0.000000E+00
23	H + H2O + O2 ⟷ H2O + HO2	9.380000E+12	-7.600000E-01	0.000000E+00
24	H + O2 ⟷ O + OH	8.300000E+10	0.000000E+00	6.030399E+07
25	2 H + M ⟷ H2 + M CH4:2.00E+00 CO2:0.00E+00 H2:0.00E+00 H2O:0.00E+00	1.000000E+12	-1.000000E+00	0.000000E+00
26	2 H + H2 ⟷ 2 H2	9.000000E+10	-6.000000E-01	0.000000E+00
27	2 H + H2O ⟷ H2 + H2O	6.000000E+13	-1.250000E+00	0.000000E+00
28	CO2 + 2 H ⟷ CO2 + H2	5.500000E+14	-2.000000E+00	0.000000E+00
29	H + OH + M ⟷ H2O + M CH4:2.00E+00 H2:7.30E-01 H2O:3.65E+00	2.200000E+16	-2.000000E+00	0.000000E+00
30	H + HO2 ⟷ H2O + O	3.970000E+09	0.000000E+00	2.807464E+06
31	H + HO2 ⟷ H2 + O2	2.800000E+10	0.000000E+00	4.468512E+06
32	H + HO2 ⟷ 2 OH	1.340000E+11	0.000000E+00	2.656840E+06
33	H + H2O2 ⟷ H2 + HO2	1.210000E+04	2.000000E+00	2.175680E+07
34	H + H2O2 ⟷ H2O + OH	1.000000E+10	0.000000E+00	1.506240E+07
35	CH3 + H (+M) ⟷ CH4 (+M) 7.83E-01 7.40E+01 2.94E+03 6.96E+03 CH4:2.0E+00 CO:1.5E+00 CO2:2.0E+00 H2:2.0E+00 H2O:6.0E+00	2.477000E+27 1.270000E+13	-4.760000E+00 -6.300000E-01	1.020896E+07 1.602472E+06
36	CH4 + H ⟷ CH3 + H2	6.600000E+05	1.620000E+00	4.535456E+07
37	H + HCO (+M) ⟷ CH2O (+M)	1.350000E+18	-2.570000E+00	5.962200E+06

No.	Reaction	A	b	Ea
	7.82E-01 2.71E+02 2.76E+03 6.57E+03 CH4:2.0E+00 CO:1.5E+00 CO2:2.0E+00 H2:2.0E+00 H2O:6.0E+00	1.090000E+09	4.800000E-01	-1.087840E+06
38	H + HCO ⟷ CO + H2	7.340000E+10	0.000000E+00	0.000000E+00
39	CH2O + H ⟷ H2 + HCO	2.300000E+07	1.050000E+00	1.370260E+07
40	C2H2 + H (+M) ⟷ C2H3 (+M)	3.800000E+34	-7.270000E+00	3.020848E+07
	7.51E-01 9.85E+01 1.30E+03 4.17E+03 C2H6:3.0E+00 CH4:2.0E+00 CO:1.5E+00 CO2:2.0E+00 H2:2.0E+00 H2O:6.0E+00	5.600000E+09	0.000000E+00	1.004160E+07
41	C2H3 + H (+M) ⟷ C2H4 (+M)	1.400000E+24	-3.860000E+00	1.389088E+07
	7.82E-01 2.07E+02 2.66E+03 6.10E+03 C2H6:3.0E+00 CH4:2.0E+00 CO:1.5E+00 CO2:2.0E+00 H2:2.0E+00 H2O:6.0E+00	6.080000E+09	2.700000E-01	1.171520E+06
42	C2H3 + H ⟷ C2H2 + H2	3.000000E+10	0.000000E+00	0.000000E+00
43	C2H4 + H (+M) ⟷ C2H5 (+M)	1.200000E+36	-7.620000E+00	2.916248E+07
	9.75E-01 2.10E+02 9.84E+02 4.37E+03 CH4:2.0E+00 CO:1.5E+00 CO2:2.0E+00 H2:2.0E+00 H2O:6.0E+00	1.080000E+09	4.540000E-01	7.614880E+06
44	C2H4 + H ⟷ C2H3 + H2	1.325000E+03	2.530000E+00	5.121216E+07
45	C2H5 + H (+M) ⟷ C2H6 (+M) 8.42E-01 1.25E+02 2.22E+03 6.88E+03 CO2:2.0E+00 H2:2.0E+00 H2O:6.0E+00 CO2:2.0E+00 H2:2.0E+00 H2O:6.0E+00	1.990000E+35 5.210000E+14	-7.080000E+00 -9.900000E-01	2.797004E+07 6.610720E+06
46	C2H5 + H ⟷ C2H4 + H2	2.000000E+09	0.000000E+00	0.000000E+00
47	C2H6 + H ⟷ C2H5 + H2	1.150000E+05	1.900000E+00	3.150552E+07
48	CH2CO + H ⟷ H2 + HCCO	5.000000E+10	0.000000E+00	3.347200E+07
49	CH2CO + H ⟷ CH3 + CO	1.130000E+10	0.000000E+00	1.434275E+07
50	CO + H2 (+M) ⟷ CH2O (+M) 9.32E-01 1.97E+02 1.54E+03 1.03E+04 CH4:2.0E+00 CO:1.5E+00 CO2:2.0E+00 H2:2.0E+00 H2O:6.0E+00	5.070000E+21 4.300000E+04	-3.420000E+00 1.500000E+00	3.529204E+08 3.330464E+08
51	H2 + OH ⟷ H + H2O	2.160000E+05	1.510000E+00	1.435112E+07
52	2 OH (+M) ⟷ H2O2 (+M)	2.300000E+12	-9.000000E-01	-7.112800E+06
	7.35E-01 9.40E+01 1.76E+03 5.18E+03 CH4:2.0E+00 CO:1.5E+00 CO2:2.0E+00 H2:2.0E+00 H2O:6.0E+00	7.400000E+10	-3.700000E-01	0.000000E+00
53	2 OH ⟷ H2O + O	3.570000E+01	2.400000E+00	-8.828240E+06
54	HO2 + OH ⟷ H2O + O2	2.900000E+10	0.000000E+00	-2.092000E+06
55	H2O2 + OH ⟷ H2O + HO2	1.750000E+09	0.000000E+00	1.338880E+06
56	H2O2 + OH ⟷ H2O + HO2	5.800000E+11	0.000000E+00	3.999904E+07
57	CH4 + OH ⟷ CH3 + H2O	1.000000E+05	1.600000E+00	1.305408E+07
58	CO + OH ⟷ CO2 + H	4.760000E+04	1.228000E+00	2.928800E+05
59	HCO + OH ⟷ CO + H2O	5.000000E+10	0.000000E+00	0.000000E+00
60	CH2O + OH ⟷ H2O + HCO	3.430000E+06	1.180000E+00	-1.870248E+06
61	C2H2 + OH ⟷ CH2CO + H	2.180000E-07	4.500000E+00	-4.184000E+06
62	C2H2 + OH ⟷ CH3 + CO	4.830000E-07	4.000000E+00	-8.368000E+06
63	C2H3 + OH ⟷ C2H2 + H2O	5.000000E+09	0.000000E+00	0.000000E+00
64	C2H4 + OH ⟷ C2H3 + H2O	3.600000E+03	2.000000E+00	1.046000E+07
65	C2H6 + OH ⟷ C2H5 + H2O	3.540000E+03	2.120000E+00	3.640080E+06
66	CH2CO + OH ⟷ H2O + HCCO	7.500000E+09	0.000000E+00	8.368000E+06
67	2 HO2 ⟷ H2O2 + O2	1.300000E+08	0.000000E+00	-6.819920E+06
68	2 HO2 ⟷ H2O2 + O2	4.200000E+11	0.000000E+00	5.020800E+07
69	CH3 + HO2 ⟷ CH4 + O2	1.000000E+09	0.000000E+00	0.000000E+00

No.	Reaction	A	b	Ea
70	CO + HO2 ⟷ CO2 + OH	1.500000E+11	0.000000E+00	9.874240E+07
71	CH2O + HO2 ⟷ H2O2 + HCO	1.000000E+09	0.000000E+00	3.347200E+07
72	CH3 + O2 ⟷ CH2O + OH	3.600000E+07	0.000000E+00	3.740496E+07
73	CH3 + OH ⟷ CH2O + H2	8.000000E+09	0.000000E+00	0.000000E+00
74	CH3 + H2O2 ⟷ CH4 + HO2	2.450000E+01	2.470000E+00	2.167312E+07
75	2 CH3 (+M) ⟷ C2H6 (+M)	1.770000E+44	-9.670000E+00	2.602448E+07
	5.32E-01 1.51E+02 1.04E+03 4.97E+03	2.120000E+13	-9.700000E-01	2.594080E+06
	C2H6:3.0E+00 CH4:2.0E+00 CO:1.5E+00			
	CO2:2.0E+00 H2:2.0E+00 H2O:6.0E+00			
76	2 CH3 ⟷ C2H5 + H	4.990000E+09	1.000000E-01	4.435040E+07
77	CH3 + HCO ⟷ CH4 + CO	2.648000E+10	0.000000E+00	0.000000E+00
78	CH2O + CH3 ⟷ CH4 + HCO	3.320000E+00	2.810000E+00	2.451824E+07
79	C2H4 + CH3 ⟷ C2H3 + CH4	2.270000E+02	2.000000E+00	3.849280E+07
80	C2H6 + CH3 ⟷ C2H5 + CH4	6.140000E+03	1.740000E+00	4.372280E+07
81	H2O + HCO ⟷ CO + H + H2O	2.244000E+15	-1.000000E+00	7.112800E+07
82	HCO + M ⟷ CO + H + M	1.870000E+14	-1.000000E+00	7.112800E+07
	CH4:2.00E+00 CO:1.50E+00 CO2:2.00E+00			
	H2:2.00E+00 H2O:0.00E+00			
83	HCO + O2 ⟷ CO + HO2	7.600000E+09	0.000000E+00	1.673600E+06
84	C2H3 + O2 ⟷ CH2O + HCO	3.980000E+09	0.000000E+00	-1.004160E+06
85	C2H4 (+M) ⟷ C2H2 + H2 (+M)	7.000000E+47	-9.310000E+00	4.178142E+08
	7.35E-01 1.80E+02 1.04E+03 5.42E+03	8.000000E+12	4.400000E-01	3.714137E+08
	CH4:2.0E+00 CO:1.5E+00 CO2:2.0E+00			
	H2:2.0E+00 H2O:6.0E+00			
86	C2H5 + O2 ⟷ C2H4 + HO2	8.400000E+08	0.000000E+00	1.621300E+07
87	HCCO + O2 ⟷ 2 CO + OH	1.600000E+09	0.000000E+00	3.573136E+06
88	2 HCCO ⟷ C2H2 + 2 CO	1.000000E+10	0.000000E+00	0.000000E+00

For fall-off reactions, the k_0 is given first, then the k_∞. Troe parameters for the fall-off function (respectively A, T_3, T_1 and T_2) are given below the reaction. The third body efficiencies are also given.

2-RAMEC ARC

	RAMEC ARC for REST HF-10
#Reactions	88
#Transported species	15
#QSS	6
Transported species	$H_2\ H\ O\ O_2\ OH\ H_2O\ HO_2\ H_2O_2\ CH_3$ $CH_4\ CO\ CO_2\ C_2H_2\ C_2H_4\ C_2H_6$
QSS species	$HCO\ C_2H_3\ C_2H_5\ CH_2O\ HCCO\ CH_2CO$

- **The computed Prandtl number** for the mixture is $\boldsymbol{P_r}$ **= 0.582**
- **The computed Schmidt numbers** for the transported species are the following:

Species	$\boldsymbol{S_{ch}}$
H_2	0.233
H	0.154
O	0.557
O_2	0.847
OH	0.567
H_2O	0.620
HO_2	0.852
H_2O_2	0.857
CH_3	0.799
CH_4	0.800
CO	0.908
CO_2	1.106
C_2H_2	1.030
C_2H_4	1.035
C_2H_6	1.141

- **Complete RAMEC ARC mechanism:**

For fall-off reactions, the k_0 is given first, then the k_∞. Troe parameters for the fall-off function (respectively A, T_3, T_1 and T_2) are given below the reaction. The third body efficiencies are also given.

No.	Reaction	A (variable unit)	b (-)	Ea(cal/mol)
1	2 O + M ⟷ O2 + M CH4:2.00E+00 CO:1.75E+00 CO2:3.60E+00 H2:2.40E+00 H2O:1.54E+01	1.200000E+11	-1.000000E+00	0.000000E+00
2	H + O + M ⟷ OH + M CH4:2.00E+00 CO:1.50E+00 CO2:2.00E+00 H2:2.00E+00 H2O:6.00E+00	5.000000E+11	-1.000000E+00	0.000000E+00
3	H2 + O ⟷ H + OH	5.000000E+01	2.670000E+00	2.631736E+07
4	HO2 + O ⟷ O2 + OH	2.000000E+10	0.000000E+00	0.000000E+00
5	H2O2 + O ⟷ HO2 + OH	9.630000E+03	2.000000E+00	1.673600E+07
6	CH3 + O ⟷ CH2O + H	8.430000E+10	0.000000E+00	0.000000E+00
7	CH4 + O ⟷ CH3 + OH	1.020000E+06	1.500000E+00	3.598240E+07
8	CO + O + M ⟷ CO2 + M CH4:2.00E+00 CO:1.50E+00 CO2:3.50E+00 H2:2.00E+00 H2O:6.00E+00 O2:6.00E+00	6.020000E+08	0.000000E+00	1.255200E+07
9	HCO + O ⟷ CO + OH	3.000000E+10	0.000000E+00	0.000000E+00
10	HCO + O ⟷ CO2 + H	3.000000E+10	0.000000E+00	0.000000E+00
11	CH2O + O ⟷ HCO + OH	3.900000E+10	0.000000E+00	1.481136E+07
12	C2H2 + O ⟷ H + HCCO	1.020000E+04	2.000000E+00	7.949600E+06
13	C2H3 + O ⟷ CH2CO + H	3.000000E+10	0.000000E+00	0.000000E+00
14	C2H4 + O ⟷ CH3 + HCO	1.920000E+04	1.830000E+00	9.204800E+05
15	C2H5 + O ⟷ CH2O + CH3	1.320000E+11	0.000000E+00	0.000000E+00
16	C2H6 + O ⟷ C2H5 + OH	8.980000E+04	1.920000E+00	2.380696E+07
17	HCCO + O ⟷ 2 CO + H	1.000000E+11	0.000000E+00	0.000000E+00
18	CH2CO + O ⟷ HCCO + OH	1.000000E+10	0.000000E+00	3.347200E+07
19	CO + O2 ⟷ CO2 + O	2.500000E+09	0.000000E+00	1.999952E+08
20	CH2O + O2 ⟷ HCO + HO2	1.000000E+11	0.000000E+00	1.673600E+08
21	H + O2 + M ⟷ HO2 + M CO:7.50E-01 CO2:1.50E+00 H2O:0.00E+00 O2:0.00E+00	2.800000E+12	-8.600000E-01	0.000000E+00
22	H + 2 O2 ⟷ HO2 + O2	3.000000E+14	-1.720000E+00	0.000000E+00
23	H + H2O + O2 ⟷ H2O + HO2	9.380000E+12	-7.600000E-01	0.000000E+00
24	H + O2 ⟷ O + OH	8.300000E+10	0.000000E+00	6.030399E+07
25	2 H + M ⟷ H2 + M CH4:2.00E+00 CO2:0.00E+00 H2:0.00E+00 H2O:0.00E+00	1.000000E+12	-1.000000E+00	0.000000E+00
26	2 H + H2 ⟷ 2 H2	9.000000E+10	-6.000000E-01	0.000000E+00
27	2 H + H2O ⟷ H2 + H2O	6.000000E+13	-1.250000E+00	0.000000E+00
28	CO2 + 2 H ⟷ CO2 + H2	5.500000E+14	-2.000000E+00	0.000000E+00
29	H + OH + M ⟷ H2O + M CH4:2.00E+00 H2:7.30E-01 H2O:3.65E+00	2.200000E+16	-2.000000E+00	0.000000E+00
30	H + HO2 ⟷ H2O + O	3.970000E+09	0.000000E+00	2.807464E+06
31	H + HO2 ⟷ H2 + O2	2.800000E+10	0.000000E+00	4.468512E+06
32	H + HO2 ⟷ 2 OH	1.340000E+11	0.000000E+00	2.656840E+06
33	H + H2O2 ⟷ H2 + HO2	1.210000E+04	2.000000E+00	2.175680E+07
34	H + H2O2 ⟷ H2O + OH	1.000000E+10	0.000000E+00	1.506240E+07
35	CH3 + H (+M) ⟷ CH4 (+M) 7.83E-01 7.40E+01 2.94E+03 6.96E+03 CH4:2.0E+00 CO:1.5E+00 CO2:2.0E+00 H2:2.0E+00 H2O:6.0E+00	2.477000E+27 1.270000E+13	-4.760000E+00 -6.300000E-01	1.020896E+07 1.602472E+06
36	CH4 + H ⟷ CH3 + H2	6.600000E+05	1.620000E+00	4.535456E+07
37	H + HCO (+M) ⟷ CH2O (+M) 7.82E-01 2.71E+02 2.76E+03 6.57E+03 CH4:2.0E+00 CO:1.5E+00 CO2:2.0E+00 H2:2.0E+00 H2O:6.0E+00	1.350000E+18 1.090000E+09	-2.570000E+00 4.800000E-01	5.962200E+06 -1.087840E+06
38	H + HCO ⟷ CO + H2	7.340000E+10	0.000000E+00	0.000000E+00

39	CH2O + H ⟷ H2 + HCO	2.300000E+07	1.050000E+00	1.370260E+07
40	C2H2 + H (+M) ⟷ C2H3 (+M)	3.800000E+34	-7.270000E+00	3.020848E+07
	7.51E-01 9.85E+01 1.30E+03 4.17E+03	5.600000E+09	0.000000E+00	1.004160E+07
	C2H6:3.0E+00 CH4:2.0E+00 CO:1.5E+00			
	CO2:2.0E+00 H2:2.0E+00 H2O:6.0E+00			
41	C2H3 + H (+M) ⟷ C2H4 (+M)	1.400000E+24	-3.860000E+00	1.389088E+07
	7.82E-01 2.07E+02 2.66E+03 6.10E+03	6.080000E+09	2.700000E-01	1.171520E+06
	C2H6:3.0E+00 CH4:2.0E+00 CO:1.5E+00			
	CO2:2.0E+00 H2:2.0E+00 H2O:6.0E+00			
42	C2H3 + H ⟷ C2H2 + H2	3.000000E+10	0.000000E+00	0.000000E+00
43	C2H4 + H (+M) ⟷ C2H5 (+M)	1.200000E+36	-7.620000E+00	2.916248E+07
	9.75E-01 2.10E+02 9.84E+02 4.37E+03	1.080000E+09	4.540000E-01	7.614880E+06
	CH4:2.0E+00 CO:1.5E+00 CO2:2.0E+00			
	H2:2.0E+00 H2O:6.0E+00			
44	C2H4 + H ⟷ C2H3 + H2	1.325000E+03	2.530000E+00	5.121216E+07
45	C2H5 + H (+M) ⟷ C2H6 (+M) 8.42E-	1.990000E+35	-7.080000E+00	2.797004E+07
	01 1.25E+02 2.22E+03 6.88E+03	5.210000E+14	-9.900000E-01	6.610720E+06
	CO2:2.0E+00 H2:2.0E+00 H2O:6.0E+00			
	CO2:2.0E+00 H2:2.0E+00 H2O:6.0E+00			
46	C2H5 + H ⟷ C2H4 + H2	2.000000E+09	0.000000E+00	0.000000E+00
47	C2H6 + H ⟷ C2H5 + H2	1.150000E+05	1.900000E+00	3.150552E+07
48	CH2CO + H ⟷ H2 + HCCO	5.000000E+10	0.000000E+00	3.347200E+07
49	CH2CO + H ⟷ CH3 + CO	1.130000E+10	0.000000E+00	1.434275E+07
50	CO + H2 (+M) ⟷ CH2O (+M) 9.32E-	5.070000E+21	-3.420000E+00	3.529204E+08
	01 1.97E+02 1.54E+03 1.03E+04	4.300000E+04	1.500000E+00	3.330464E+08
	CH4:2.0E+00 CO:1.5E+00 CO2:2.0E+00			
	H2:2.0E+00 H2O:6.0E+00			
51	H2 + OH ⟷ H + H2O	2.160000E+05	1.510000E+00	1.435112E+07
52	2 OH (+M) ⟷ H2O2 (+M)	2.300000E+12	-9.000000E-01	-7.112800E+06
	7.35E-01 9.40E+01 1.76E+03 5.18E+03	7.400000E+10	-3.700000E-01	0.000000E+00
	CH4:2.0E+00 CO:1.5E+00 CO2:2.0E+00			
	H2:2.0E+00 H2O:6.0E+00			
53	2 OH ⟷ H2O + O	3.570000E+01	2.400000E+00	-8.828240E+06
54	HO2 + OH ⟷ H2O + O2	2.900000E+10	0.000000E+00	-2.092000E+06
55	H2O2 + OH ⟷ H2O + HO2	1.750000E+09	0.000000E+00	1.338880E+06
56	H2O2 + OH ⟷ H2O + HO2	5.800000E+11	0.000000E+00	3.999904E+07
57	CH4 + OH ⟷ CH3 + H2O	1.000000E+05	1.600000E+00	1.305408E+07
58	CO + OH ⟷ CO2 + H	4.760000E+04	1.228000E+00	2.928800E+05
59	HCO + OH ⟷ CO + H2O	5.000000E+10	0.000000E+00	0.000000E+00
60	CH2O + OH ⟷ H2O + HCO	3.430000E+06	1.180000E+00	-1.870248E+06
61	C2H2 + OH ⟷ CH2CO + H	2.180000E-07	4.500000E+00	-4.184000E+06
62	C2H2 + OH ⟷ CH3 + CO	4.830000E-07	4.000000E+00	-8.368000E+06
63	C2H3 + OH ⟷ C2H2 + H2O	5.000000E+09	0.000000E+00	0.000000E+00
64	C2H4 + OH ⟷ C2H3 + H2O	3.600000E+03	2.000000E+00	1.046000E+07
65	C2H6 + OH ⟷ C2H5 + H2O	3.540000E+03	2.120000E+00	3.640080E+06
66	CH2CO + OH ⟷ H2O + HCCO	7.500000E+09	0.000000E+00	8.368000E+06
67	2 HO2 ⟷ H2O2 + O2	1.300000E+08	0.000000E+00	-6.819920E+06
68	2 HO2 ⟷ H2O2 + O2	4.200000E+11	0.000000E+00	5.020800E+07
69	CH3 + HO2 ⟷ CH4 + O2	1.000000E+09	0.000000E+00	0.000000E+00
70	CO + HO2 ⟷ CO2 + OH	1.500000E+11	0.000000E+00	9.874240E+07
71	CH2O + HO2 ⟷ H2O2 + HCO	1.000000E+09	0.000000E+00	3.347200E+07
72	CH3 + O2 ⟷ CH2O + OH	3.600000E+07	0.000000E+00	3.740496E+07
73	CH3 + OH ⟷ CH2O + H2	8.000000E+09	0.000000E+00	0.000000E+00
74	CH3 + H2O2 ⟷ CH4 + HO2	2.450000E+01	2.470000E+00	2.167312E+07
75	2 CH3 (+M) ⟷ C2H6 (+M)	1.770000E+44	-9.670000E+00	2.602448E+07
	5.32E-01 1.51E+02 1.04E+03 4.97E+03	2.120000E+13	-9.700000E-01	2.594080E+06
	C2H6:3.0E+00 CH4:2.0E+00 CO:1.5E+00			

	CO2:2.0E+00 H2:2.0E+00 H2O:6.0E+00			
76	2 CH3 ⟷ C2H5 + H	4.990000E+09	1.000000E-01	4.435040E+07
77	CH3 + HCO ⟷ CH4 + CO	2.648000E+10	0.000000E+00	0.000000E+00
78	CH2O + CH3 ⟷ CH4 + HCO	3.320000E+00	2.810000E+00	2.451824E+07
79	C2H4 + CH3 ⟷ C2H3 + CH4	2.270000E+02	2.000000E+00	3.849280E+07
80	C2H6 + CH3 ⟷ C2H5 + CH4	6.140000E+03	1.740000E+00	4.372280E+07
81	H2O + HCO ⟷ CO + H + H2O	2.244000E+15	-1.000000E+00	7.112800E+07
82	HCO + M ⟷ CO + H + M	1.870000E+14	-1.000000E+00	7.112800E+07
	CH4:2.00E+00 CO:1.50E+00 CO2:2.00E+00			
	H2:2.00E+00 H2O:0.00E+00			
83	HCO + O2 ⟷ CO + HO2	7.600000E+09	0.000000E+00	1.673600E+06
84	C2H3 + O2 ⟷ CH2O + HCO	3.980000E+09	0.000000E+00	-1.004160E+06
85	C2H4 (+M) ⟷ C2H2 + H2 (+M)	7.000000E+47	-9.310000E+00	4.178142E+08
	7.35E-01 1.80E+02 1.04E+03 5.42E+03	8.000000E+12	4.400000E-01	3.714137E+08
	CH4:2.0E+00 CO:1.5E+00 CO2:2.0E+00			
	H2:2.0E+00 H2O:6.0E+00			
86	C2H5 + O2 ⟷ C2H4 + HO2	8.400000E+08	0.000000E+00	1.621300E+07
87	HCCO + O2 ⟷ 2 CO + OH	1.600000E+09	0.000000E+00	3.573136E+06
88	2 HCCO ⟷ C2H2 + 2 CO	1.000000E+10	0.000000E+00	0.000000E+00

Appendix E – Averaged longitudinal profiles per cross section of the REST HF-10 test case

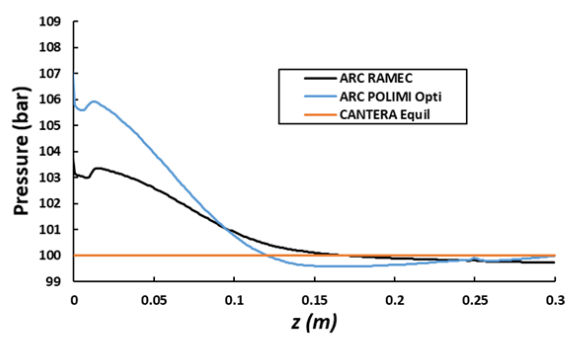

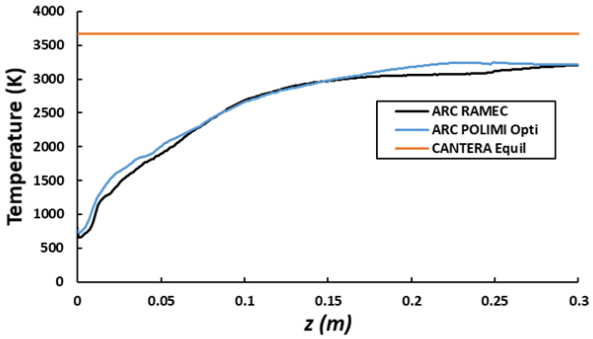

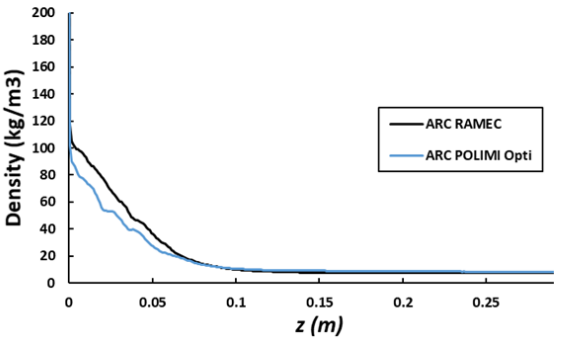

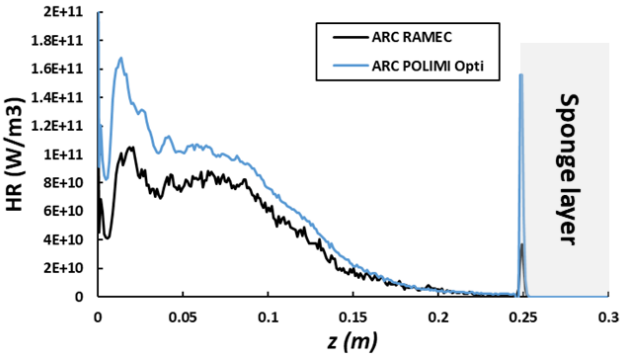

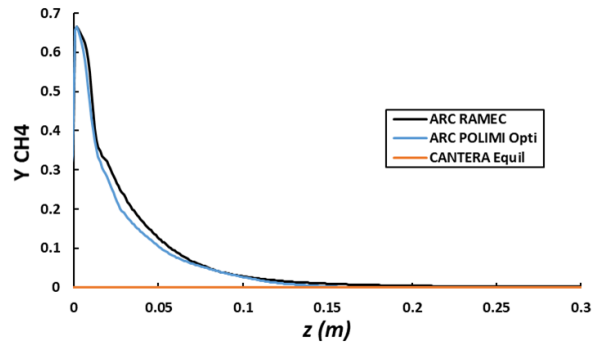

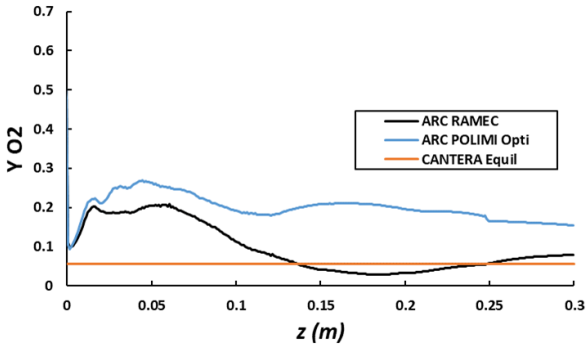

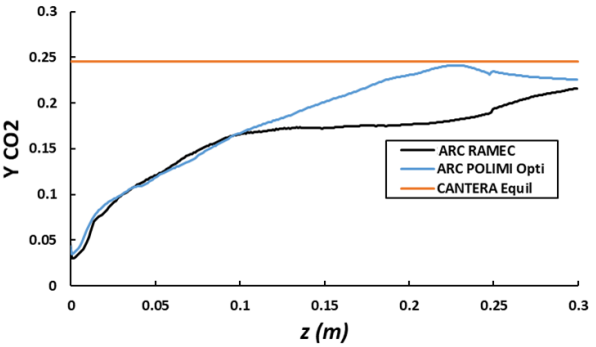

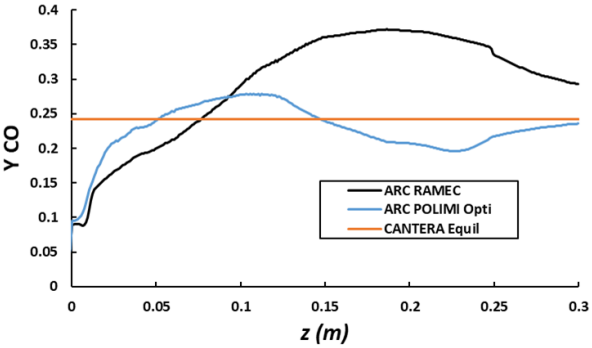

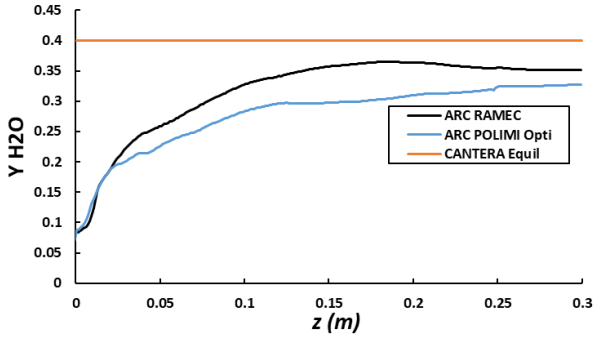
Y H2O
z (m)
ARC RAMEC
ARC POLIMI Opti
CANTERA Equil

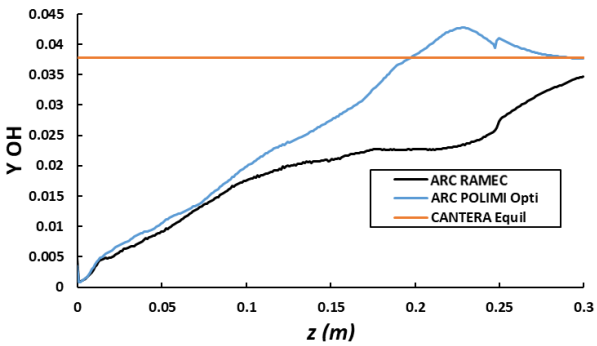
Y OH
z (m)
ARC RAMEC
ARC POLIMI Opti
CANTERA Equil

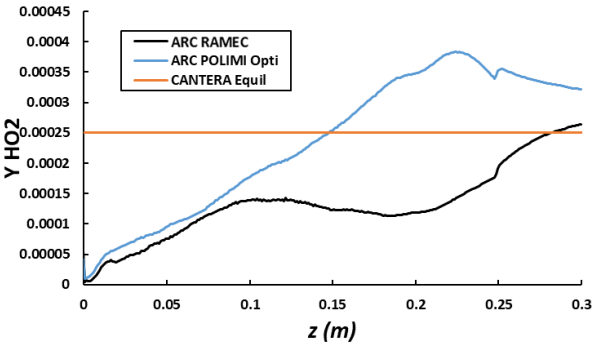
Y HO2
z (m)
ARC RAMEC
ARC POLIMI Opti
CANTERA Equil

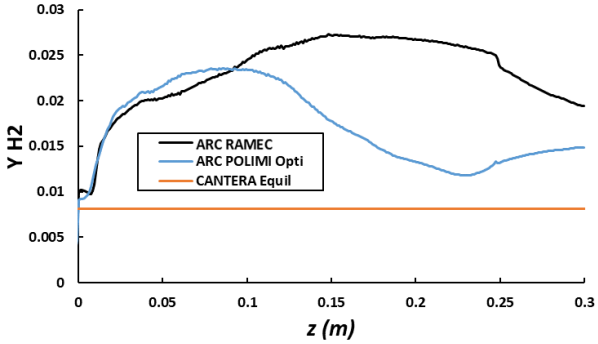
Y H2
z (m)
ARC RAMEC
ARC POLIMI Opti
CANTERA Equil

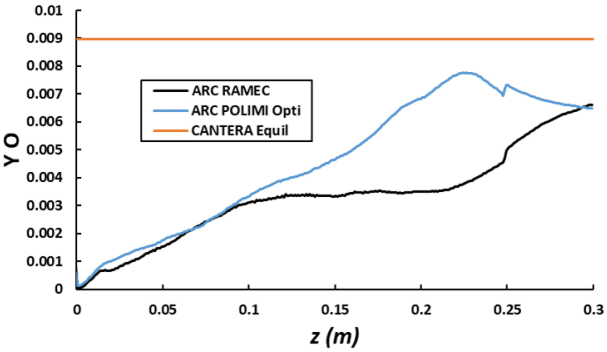
Y O
z (m)
ARC RAMEC
ARC POLIMI Opti
CANTERA Equil

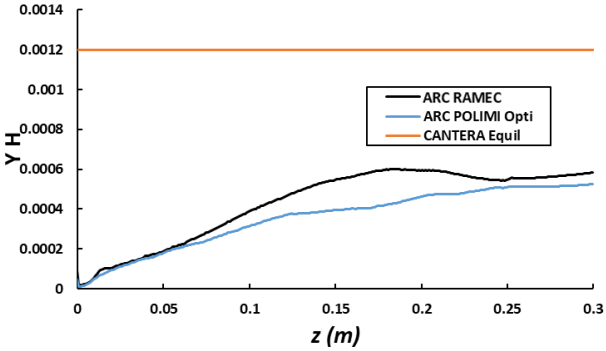
Y H
z (m)
ARC RAMEC
ARC POLIMI Opti
CANTERA Equil

References

[1] UNOOSA (United Nations Office for Outer Space Affairs), Online Index of Objects Launched into Outer Space - https://www.unoosa.org/oosa/osoindex/search-ng.jspx, (n.d.).

[2] D. ZAJACKOWSKI, N. MAUBERT, L'émergence et le développement du New Space aux États-Unis - Note thématique du Bureau du CNES et Service Spatial de l'Ambassade de France à Washington D.C., n.d.

[3] NASA COTS program page - https://www.nasa.gov/commercial-orbital-transportation-services-cots, (n.d.).

[4] What are SmallSats ? Nasa web page - https://www.nasa.gov/content/what-are-smallsats-and-cubesats, (n.d.).

[5] ICEYE company website - https://www.iceye.com/contact, (n.d.).

[6] MarCO mission webpage, JPL website - https://www.jpl.nasa.gov/missions/mars-cube-one-marco, (n.d.).

[7] Starlink website - https://www.starlink.com/technology, n.d.

[8] Andrew Parsonson's European Launch Vehicles - https://europeanspaceflight.com/download/european-launch-vehicles/, (n.d.).

[9] H.W. Jones, The Recent Large Reduction in Space Launch Cost, 48th Int. Conf. Environ. Syst. (2018) 81.

[10] J. Wilken, S. Stappert, M. Sippel, Parametric Cost Estimation in the Preliminary Design Phase of Reusable Launch Vehicles, Sp. Cost Eng. Conf. (2021) 1–13.

[11] O. Gogdet, J. Mansouri, J. Breteau, A.P. De Mirand, Launch Vehicles System Studies in the " Future Launchers Preparatory Programme ": the Reusability Option for Ariane Evolutions ., in: EUCASS, 2019: pp. 1–16.

[12] Falcon 9 vehicle description - SpaceX website - https://www.spacex.com/vehicles/falcon-9/, (n.d.).

[13] Starship vehicle description - SpaceX website - https://www.spacex.com/vehicles/starship/, (n.d.).

[14] M. Illig, S. Ishimoto, E. Dumont, CALLISTO , a demonstrator for reusable launchers, in: EUCASS 2022 Conf., n.d.

[15] J. Vila, J. Hassin, Technology acceleration process for the THEMIS low cost and reusable prototype, in: EUCASS 2019 Conf., n.d.

[16] H. Gilibert, European Launchers : preparing the future . Launch service prices disrupted, in: EUCASS 2022 Conf., n.d.

[17] A. Patureau De Mirand, J.-M. Bahu, E. Louaas, Ariane Next, a vision for a reusable cost efficient European rocket, in: EUCASS 2019 Conf., n.d.: pp. 1–9.

[18] MaiaSpace Website - https://maia-space.com/, (n.d.).

[19] L.T. De Luca, T. Shimada, V.P. Sinditskii, M. Calabro, Chemical Rocket Propulsion: A Comprehensive Survey of Energetic Materials, Springer Aerospace Technology, 2017.

[20] Hybrid Propulsion for Space - Company webpage - https://hypr-space.com/, (n.d.).

[21] G.P. Sutton, Rocket Propulsion Elements - 9th edition, John Wiley, 2016.

[22] V. Yang, M. Hbiballah, J. Hulka, M. Popp, Liquid Rocket Thrust Chambers: Aspects of Modeling, Analysis, and Design, 2004.

[23] S. Blanchard, Multi-physics Large-Eddy Simulation of methane oxy-combustion in Liquid Rocket Engines, Institut National Polytechnique de Toulouse, 2021.

[24] J.C. Oefelein, Y. Vigor, Comprehensive review of liquid-propellant combustion instabilities in f-

1 engines, J. Propuls. Power. 9 (1993) 657–677.
[25] C. Laurent, Présentée et soutenue par : Low-Order Modeling and High-Fidelity Simulations for the Prediction of Combustion Instabilities in Liquid Rocket Engines and Gas Turbines Rapporteurs : Membre(s) du jury, Institut National Polytechnique de Toulouse, 2020.
[26] NASA CEA - Glenn Research Center webpage - https://www1.grc.nasa.gov/research-and-engineering/ceaweb/, (n.d.).
[27] B.J. McBride, Computer Program for Calculation of Complex Chemical Equilibrium Compositions and Applications II. Users Manual and Program Description, 1996.
[28] O.J. Haidn, Advanced rocket engines, NATO R&T Organ. Educ. Notes RTO-EN-AVT-150. (2008).
[29] A. Kong, Reduced Kinetic Mechanism of Methane Oxidation for Rocket Applications Reduced Kinetic Mechanism of Methane Oxidation for Rocket Applications (Master's Thesis), 2015.
[30] G. Hagemann, LOX / Methane The Future is Green, Present. Académie l'Air l'Espace, Paris. (2015).
[31] M. Kurela, P. Noir, Space grade Biomethane production for Themis reusable stage demonstrator Vega Evolution Themis Demonstrator, (n.d.) 1–14.
[32] R.M. Zubrin, A.C. Muscatello, M. Berggren, Integrated Mars In Situ Propellant Production System, J. Aerosp. Eng. 26 (2013) 43–56.
[33] D.Z. Oehler, G. Etiope, Methane seepage on mars: where to look and why, Astrobiology. 17 (2017) 1233–1264.
[34] T. Neill, D. Judd, E. Veith, D. Rousar, Practical uses of liquid methane in rocket engine applications, Acta Astronaut. 65 (2009) 696–705.
[35] T. Kato, D. Terakado, H. Nanri, T. Morito, I. Masuda, H. Asakawa, H. Sakaguchi, Y. Ishikawa, T. Inoue, S. Ishihara, M. Sasaki, Subscale Firing Test for Regenerative Cooling LOX/Methane Rocket Engine, 7th Eur. Conf. Aeronaut. Sp. Sci. (2017) 2–5.
[36] P.H. Joo, M.R.J. Charest, C.P.T. Groth, Ö.L. Gülder, Comparison of structures of laminar methane-oxygen and methane-air diffusion flames from atmospheric to 60atm, Combust. Flame. 160 (2013) 1990–1998.
[37] Launch Vehicles - Relativity Space Website - https://www.relativityspace.com/rockets, (n.d.).
[38] Landspace official website - https://www.landspace.com/, (n.d.).
[39] A. Beil, Chinese Zhuque-2 fails during first methalox orbital launch attempt - https://www.nasaspaceflight.com/2022/12/zhuque2-debut/, NasaSpaceflight.Com. (n.d.).
[40] P. Bellomi, M. Rudnykh, S. Carapellese, D. Liuzzi, G. Caggiano, L. Arione, A.A. Gurtovoy, S.D. Lobov, V.S. Rachuk, E. D'Aversa, A. De Lillis, R.C. Pellegrini, Development of LM10-MIRA liquid oxygen – liquid natural gas expander cycle demonstrator engine, 11 (2019) 447–466.
[41] P. Simontacchi, E. Edeline, R. Blasi, S. Sagnier, N. Ravier, A. Espinosa-Ramos, J. Breteau, Prometheus: Precursor of new low-cost rocket engine family, Proc. Int. Astronaut. Congr. IAC. 2018-Octob (2018) 1–12.
[42] J.H. Morehart, A Survey of LNG-fueled Rocket Engine Development Activity – Non-U.S., AIAA Propuls. Energy Forum, 2021. (2021) 1–10.
[43] G. Ordonneau, L. Vingert, P. Grenard, N. Fdida, A Rocket Engine under a Magnifying Glass, Aerospacelab J. (2016) 1–13.
[44] M. Habiballah, M. Orain, F. Grisch, L. Vingert, P. Gicquel, Experimental studies of high-pressure cryogenic flames on the mascotte facility, Combust. Sci. Technol. 178 (2006) 101–128.
[45] M. Théron, M.M. Benito, B. Vieille, L. Vingert, N. Fdida, Y. Mauriot, R. Blouquin, C. Seitan, Experimental and numerical investigation of LOX / Methane Cryogenic Combustion at low mixture ratio, Eucass 2019. (2019) 1–15.
[46] L. Vingert, N. Fdida, Y. Mauriot, Experimental Investigations of Liquid Oxygen / Methane Combustion at Very Low Mixture Ratio at the Mascotte Test Facility, Ists. (2019) 1–7.

[47] V. Lechner, C. Betrancourt, P. Scouflaire, L. Vingert, S. Ducruix, Dynamic characterization of wall temperature in LOX/CH 4 rocket engine operating conditions using phosphor thermometry , Proc. Combust. Inst. 000 (2022) 1–9.

[48] P. Grenard, N. Fdida, L. Vingert, L.H. Dorey, L. Selle, J. Pichillou, Experimental investigation of heat transfer in a subscale liquid rocket engine at high mixture ratio, J. Propuls. Power. 35 (2019).

[49] J. Lux, O. Haidn, Effect of recess in high-pressure liquid oxygen/methane coaxial injection and combustion, J. Propuls. Power. 25 (2009) 24–32.

[50] O.J.H. S. Silvestri, M. P. Celano, G. Schlieben, C. Kirchberger, Characterization of a Gox-Gch4 Single Element Combustion Chamber, Sp. Propuls. 2014. 1 (2014).

[51] C.B. Von Sethe, S. Soller, O.J. Haidn, Experimental investigation of a single element LOX / GCH4 heat-sink combustion chamber, Eucass 2019. (2019) 1–11.

[52] W. Armbruster, J. Hardi, M. Oschwald, Impact of shear-coaxial injector hydrodynamics on high-frequency combustion instabilities in a representative cryogenic rocket engine, Int. J. Spray Combust. Dyn. 14 (2022) 118–130.

[53] P.G. Robert J. Kee, Michael E. Coltrin, Chemically Reacting Flow: Theory and Practice, Wiley, 2005.

[54] B.J. McBride, M.J. Zehe, S. Gordon, NASA Glenn coefficients for calculating thermodynamic properties of individual species: National Aeronautics and Space Administration, 2002.

[55] F. Lindemann, DISCUSSION ON TNE RADIATION THEORY OF CUEMICAL ACTION". Professor, Trans. Faraday Soc. 17 (1922).

[56] Reaction Design, ANSYS Chemkin Theory Manual 17.0 (15151), 2015.

[57] R.G. Gilbert, J. Troe, Theory of Thermal Unimolecular Reactions in the Fall-off Range. I. Strong Collision Rate Constants, Berichte Der Bunsengesellschaft Für Phys. Chemie. 87 (1983) 161–169.

[58] https://cantera.org/science/kinetics.html -Pressure-Dependent Arrhenius Rate Expressions, (n.d.).

[59] G. Renoux, Étude expérimentale de l'interaction goutte/flamme : propagation d'une flamme dans un aérosol en microgravité et passage d'une goutte à travers un front de flamme, Université d'Orléans, 2020.

[60] G.H. MARKSTEIN, Experimental and Theoretical Studies of Flame-Front Stability, J. Aeronaut. Sci. 18 (1951) 199–209.

[61] P. Clavin, Dynamic behavior of premixed flame fronts in laminar and turbulent flows, Prog. Energy Combust. Sci. 11 (1985) 1–59.

[62] A.P. Kelley, C.K. Law, Nonlinear effects in the extraction of laminar flame speeds from expanding spherical flames, Combust. Flame. 156 (2009) 1844–1851.

[63] F. Halter, T. Tahtouh, C. Mounaïm-Rousselle, Nonlinear effects of stretch on the flame front propagation, Combust. Flame. 157 (2010) 1825–1832.

[64] T. Poinsot, D. Veynante, Theoretical and Numerical Combustion, (2012).

[65] ARCANE - Q. Cazeres, P. Pepiot https://chemistry.cerfacs.fr/en/arcane/, (n.d.).

[66] S. Blanchard, Q. Cazères, B. Cuenot, Chemical modeling for methane oxy-combustion in Liquid Rocket Engines, Acta Astronaut. 190 (2022) 98–111.

[67] R.W. Bilger, The structure of turbulent nonpremixed flames, Symp. Combust. 22 (1989) 475–488.

[68] L. Esclapez, Numerical study of ignition and inter-sector flame propagation in gas turbine., Institut National Polytechnique de Toulouse, 2015.

[69] B. Cuenot, Etude asymptotique et numérique de la structure des flammes de diffusion laminaires et turbulentes, Institut National Polytechnique de Toulouse, 1995.

[70] W.P. Jones, R.P. Lindstedt, Global reaction schemes for hydrocarbon combustion, Combust. Flame. 73 (1988) 233–249.

[71] B.G. Franzelli, Impact of the chemical description on direct numerical simulations and large eddy simulations of turbulent combustion in industrial aero-engines, 2011.

[72] J. Strauss, Development of Global Chemical Reaction Scheme for Methane and Oxygen in Rocket Applications to be Used in Large-Eddy Simulation, (2020).

[73] J. Zips, C. Traxinger, P. Breda, M. Pfitzner, Assessment of presumed/transported probability density function methods for rocket combustion simulations, J. Propuls. Power. 35 (2019) 747–764.

[74] T. Schmitt, Large-Eddy Simulations of the Mascotte Test Cases Operating at Supercritical Pressure, Flow, Turbul. Combust. 105 (2020) 159–189.

[75] D. Maestro, B. Cuenot, L. Selle, Large Eddy Simulation of Combustion and Heat Transfer in a Single Element GCH4/GOx Rocket Combustor, Flow, Turbul. Combust. 103 (2019) 699–730.

[76] E.L. Petersen, D.F. Davidson, R.K. Hanson, Kinetics modeling of shock-induced ignition in low-dilution CH4/O2 mixtures at high pressures and intermediate temperatures, Combust. Flame. 117 (1999) 272–290.

[77] A. Hertzberg, A.P. Bruckner, D.W. Bogdanoff, Ram accelerator: A new chemical method for accelerating projectiles to ultrahigh velocities, AIAA J. 26 (1988) 195–203.

[78] E.L. Petersen, D.F. Davidson, R.K. Hanson, Ignition delay times of ram accelerator mixtures, 32nd Jt. Propuls. Conf. Exhib. 15 (1996).

[79] V.V.L. Gregory P. Smith, David M. Golden, Michael Frenklach, Nigel W. Moriarty, Boris Eiteneer, Mikhail Goldenberg, C. Thomas Bowman, Ronald K. Hanson, Soonho Song, William C. Gardiner, GRI-MECH 3.0, (n.d.).

[80] E.L. Petersen, R.K. Hanson, Reduced kinetics mechanisms for ram accelerator combustion, J. Propuls. Power. 15 (1999) 591–600.

[81] P. Natale, G. Saccone, F. Battista, Cfd Kinetic Scheme Validation for Liquid Rocket Engine Fuelled By, (2019) 8.

[82] F. Battista, D. Ricci, P. Natale, D. Cardillo, M. Fragiacomo, G. Propellant, Hyprob-New : Recent Developments of the Lox / Lch4, Sp. Propuls. 2020+1. (2021) 1–10.

[83] F. Monnier, G. Ribert, Simulation of high-pressure methane-oxygen combustion with a new reduced chemical mechanism, Combust. Flame. 235 (2022) 111735.

[84] N. Jaouen, L. Vervisch, P. Domingo, G. Ribert, Automatic reduction and optimisation of chemistry for turbulent combustion modelling: Impact of the canonical problem, Combust. Flame. 175 (2017) 60–79.

[85] V.P. Zhukov, A.F. Kong, A compact reaction mechanism of methane oxidation at high pressures, Prog. React. Kinet. Mech. 43 (2018) 62–78.

[86] V.P. Zhukov, Kinetic model of alkane oxidation at high pressure from methane to n-heptane, Combust. Theory Model. 13 (2009) 427–442.

[87] V.P. Zhukov, V.A. Sechenov, A.Y. Starikovskii, Autoignition of a lean propane-air mixture at high pressures, Kinet. Catal. 46 (2005) 319–327.

[88] T. Horchler, S. Fechter, REST HF-10 Test Case : Numerical Simulation of a Single Coaxial LOX-CH4 Injector with Forced Mass Flow Oscillations Using the DLR TAU-Code, (2022).

[89] N.A. Slavinskaya, A. Meddi, J.H. Starcke, O.J. Haidn, Methane skeletal mechanism for space propulsion applications, 52nd AIAA/SAE/ASEE Jt. Propuls. Conf. 2016. (2016).

[90] N.A. Slavinskaya, U. Riedel, S.B. Dworkin, M.J. Thomson, Detailed numerical modeling of PAH formation and growth in non-premixed ethylene and ethane flames, Combust. Flame. 159 (2012) 979–995.

[91] G. Rozenchan, D.L. Zhu, C.K. Law, S.D. Tse, Outward propagation, burning velocities, and

chemical effects of methane flames up to 60 ATM, Proc. Combust. Inst. 29 (2002) 1461–1470.

[92] N.A. Slavinskaya, O.J. Haidn, Kinetic mechanism for low pressure oxygen / methane ignition and combustion, 49th AIAA Aerosp. Sci. Meet. Incl. New Horizons Forum Aerosp. Expo. (2011) 1–13.

[93] G. Saccone, P. Breda, P. Natale, F. Battista, G. Saccone, P. Breda, P. Natale, F. Battista, G. Saccone, P. Breda, P. Natale, Reduced kinetic mechanism for methane / oxygen rocket engine applications : a reliable and numerically efficient methodology applications : a reliable and numerically efficient methodology, (2023).

[94] T. Lu, C.K. Law, A criterion based on computational singular perturbation for the identification of quasi steady state species: A reduced mechanism for methane oxidation with NO chemistry, Combust. Flame. 154 (2008) 761–774.

[95] G.P. Smith, Y. Tao, and H. Wang, Foundational Fuel Chemistry Model Version 1.0 (FFCM-1), http://nanoenergy.stanford.edu/ffcm1, 2016., (n.d.).

[96] G. Bagheri, E. Ranzi, M. Pelucchi, A. Parente, A. Frassoldati, T. Faravelli, Comprehensive kinetic study of combustion technologies for low environmental impact: MILD and OXY-fuel combustion of methane, Combust. Flame. 212 (2020) 142–155.

[97] F. Winter, S. Silvestri, M.P. Celano, G. Schlieben, O.J. Haidn, High-speed and Emission Imaging of a Coaxial Single Element GOX / GCH 4 Rocket Combustion Chamber, Eucass. (2017) 1–10.

[98] F. Halter, G. Dayma, Laminar flame speed determination at high pressure and temperature conditions for kinetic schemes assessment, in: Proc. Combust. Inst., 2020.

[99] Y. Wang, A. Movaghar, Z. Wang, Z. Liu, W. Sun, F.N. Egolfopoulos, Z. Chen, Laminar flame speeds of methane/air mixtures at engine conditions: Performance of different kinetic models and power-law correlations, Combust. Flame. 218 (2020) 101–108.

[100] F.N. Egolfopoulos, N. Hansen, Y. Ju, K. Kohse-Höinghaus, C.K. Law, F. Qi, Advances and challenges in laminar flame experiments and implications for combustion chemistry, Prog. Energy Combust. Sci. 43 (2014) 36–67.

[101] A. Omari, L. Tartakovsky, Measurement of the laminar burning velocityusing the confined and unconfined spherical flame methods - A comparative analysis, Combust. Flame. 168 (2016) 127–137.

[102] J. Jayachandran, R. Zhao, F.N. Egolfopoulos, Determination of laminar flame speeds using stagnation and spherically expanding flames: Molecular transport and radiation effects, Combust. Flame. 161 (2014) 2305–2316.

[103] D.R. Dowdy, D.B. Smith, S.C. Taylor, A. Williams, The use of expanding spherical flames to determine burning velocities and stretch effects in hydrogen/air mixtures, Symp. Combust. 23 (1991) 325–332.

[104] K. Kumar, C.J. Sung, Laminar flame speeds and extinction limits of preheated n-decane/O2/N2 and n-dodecane/O2/N2 mixtures, Combust. Flame. 151 (2007) 209–224.

[105] A. Movaghar, R. Lawson, F.N. Egolfopoulos, Confined spherically expanding flame method for measuring laminar flame speeds: Revisiting the assumptions and application to C1C4 hydrocarbon flames, Combust. Flame. 212 (2020) 79–92.

[106] A.N. Mazas, D.A. Lacoste, T. Schuller, Experimental and numerical investigation on the laminar flame speed of CH4/O2 mixtures diluted with CO2 and H 2O, Proc. ASME Turbo Expo. 2 (2010) 411–421.

[107] A. Mazas, Etude des flammes prémélangées enrichies en oxygène : analyse des effets de dilution par la vapeur d ' eau et le dioxyde de carbone, Ecole Centrale des Arts et Manufactures, 2010.

[108] B. Lewis, G. Von Elbe, Bernard Lewis and Guenther von Elbe - Combustion, Flames and Explosions of Gases-Academic Press (1987), 1987.

[109] J. Oh, D. Noh, Laminar burning velocity of oxy-methane flames in atmospheric condition,

Energy. 45 (2012) 669–675.
[110] R.M. Fristrom, C. Grunfelder, S. Favin, Methane-oxygen flame structure. I. Characteristic profiles in a low-pressure, laminar, lean, premixed methane-oxygen flame, J. Phys. Chem. 64 (1960) 1386–1392.
[111] B. Lewis, G. Von Elbe, Determination of the speed of flames and the temperature distribution in a spherical bomb from time-pressure explosion records, J. Chem. Phys. 2 (1934) 283–290.
[112] F. Halter, Z. Chen, G. Dayma, C. Bariki, Y. Wang, P. Dagaut, C. Chauveau, Development of an optically accessible apparatus to characterize the evolution of spherically expanding flames under constant volume conditions, Combust. Flame. 212 (2020) 165–176.
[113] F. Fiock, F. Marvin, R. Caldwell, FLAME SPEEDS AND ENERGY CONSIDERATIONS FOR EXPLOSIONS IN A SPHERICAL BOMB, (n.d.).
[114] M. Faghih, Z. Chen, The constant-volume propagating spherical flame method for laminar flame speed measurement, Sci. Bull. 61 (2016) 1296–1310.
[115] F. Halter, G. Dayma, Z. Serinyel, P. Dagaut, C. Chauveau, Laminar flame speed determination at high pressure and temperature conditions for kinetic schemes assessment, Proc. Combust. Inst. 38 (2021) 2449–2457.
[116] R. Addabbo, J.K. Bechtold, M. Matalon, Wrinkling of spherically expanding flames, Proc. Combust. Inst. 29 (2002) 1527–1535.
[117] Y.B. Zeldovich, The Theory of Combustion and Detonation, Publ. Academy of Sciences, USSR, 1944.
[118] G. Darrieus, Propagation d'un front de flamme, in: Congrès de Mécanique Appliquée, 1945.
[119] L. Landau, On the theory of slow combustion, in: Acta Physicochim. USSR, 1944.
[120] Z. Chen, M.P. Burke, Y. Ju, Effects of compression and stretch on the determination of laminar flame speeds using propagating spherical flames, Combust. Theory Model. 13 (2009) 343–364.
[121] C. Xiouris, T. Ye, J. Jayachandran, F.N. Egolfopoulos, Laminar flame speeds under engine-relevant conditions: Uncertainty quantification and minimization in spherically expanding flame experiments, Combust. Flame. 163 (2016) 270–283.
[122] A. Mouze-Mornettas, H. Keck, Y. Wang, Z. Chen, G. Dayma, C. Chauveau, F. Halter, Effect of wall heat transfer on the dynamics of premixed spherical expanding flames, Therm. Sci. Eng. Prog. 29 (2022) 101227.
[123] Z. Chen, M.P. Burke, Y. Ju, Effects of Lewis number and ignition energy on the determination of laminar flame speed using propagating spherical flames, Proc. Combust. Inst. 32 I (2009) 1253–1260.
[124] P. Dai, Z. Chen, Supersonic reaction front propagation initiated by a hot spot in n-heptane/air mixture with multistage ignition, Combust. Flame. 162 (2015) 4183–4193.
[125] L. Pizzuti, C.A. Martins, L.R. Dos Santos, D.R.S. Guerra, Laminar Burning Velocity of Methane/Air Mixtures and Flame Propagation Speed Close to the Chamber Wall, Energy Procedia. 120 (2017) 126–133.
[126] M.M. Elia M., Laminar burning velocity of methane-air-diluent mixtures, J. Eng. Gas Turbines Power. 123 (2001) 190–196.
[127] R.J. Kee, F.M. Rupley, J.A. Miller, Chemkin-Ii: a Fortran Chemical Kinetics Package for the Analysis of Gas-Phase Chemical Kinetics, J. Chem. Inf. Model. 53 (1989) 1689–1699.
[128] R.J. Kee, sss A FORTRAN COMPUTER CODE PACKAGE FOR THE EVALUATION OF GAS-PHASE,MULTICOMPONENT TRANSPORT PROPERTIES, J. Chem. Inf. Model. 53 (2013) 1689–1699.
[129] Z. Chen, On the accuracy of laminar flame speeds measured from outwardly propagating spherical flames: Methane/air at normal temperature and pressure, Combust. Flame. 162 (2015) 2442–2453.

[130] R.R. Burrell, J.L. Pagliaro, G.T. Linteris, Effects of stretch and thermal radiation on difluoromethane/air burning velocity measurements in constant volume spherically expanding flames, Proc. Combust. Inst. 37 (2019) 4231–4238.

[131] Razus, Burning Velocity of Propane−Air Mixtures from Pressure−TimeRecords during Explosions in a Closed Spherical Vessel.pdf, (n.d.).

[132] A. Mouze-mornettas, M.M. Benito, G. Dayma, C. Chauveau, B. Cuenot, F. Halter, Laminar flame speed evaluation for CH 4 / O 2 mixtures at high pressure and temperature for rocket engine applications, Proc. Combust. Inst. 000 (2022) 1–8.

[133] B. Galmiche, Caractérisation expérimentale des flammes laminaires et turbulentes en expansion, Université d'Orléans, 2014.

[134] G. Bagheri, E. Ranzi, M. Pelucchi, A. Parente, A. Frassoldati, T. Faravelli, Comprehensive kinetic study of combustion technologies for low environmental impact: MILD and OXY-fuel combustion of methane, Combust. Flame. 212 (2020) 142–155.

[135] ANSYS CHEMKIN 20.0, ANSYS Reaction Design: San Diego, (2020).

[136] M. Fürst, A. Bertolino, A. Cuoci, T. Faravelli, A. Frassoldati, A. Parente, OptiSMOKE++: A toolbox for optimization of chemical kinetic mechanisms, Comput. Phys. Commun. 264 (2021) 107940.

[137] E. Hu, X. Li, X. Meng, Y. Chen, Y. Cheng, Y. Xie, Z. Huang, Laminar flame speeds and ignition delay times of methane-air mixtures at elevated temperatures and pressures, Fuel. 158 (2015) 1–10.

[138] Y. Wu, V. Modica, B. Rossow, F. Grisch, Effects of pressure and preheating temperature on the laminar flame speed of methane/air and acetone/air mixtures, Fuel. 185 (2016) 577–588.

[139] A. Mouze-Mornettas, G. Dayma, F. Halter, M. Martin Benito, Modelling and reduction of LOx-Methane chemical kinetics for rocket engine application, in: Proc. EUCASS Conf., 2022: pp. 1–10.

[140] A. Bertolino, OPTISMOKE++ crash course, 2021.

[141] D.L. Baulch, M.J. Pilling, C.J. Cobos, R.A. Cox, P. Frank, G. Hayman, T. Just, J.A. Kerr, T. Murrells, J. Troe, R.W. Walker, J. Warnatz, Evaluated Kinetic Data for Combustion Modeling. Supplement I, J. Phys. Chem. Ref. Data. 23 (1994) 847–848.

[142] D.L. Baulch, C.T. Bowman, C.J. Cobos, R.A. Cox, T. Just, J.A. Kerr, M.J. Pilling, D. Stocker, J. Troe, W. Tsang, R.W. Walker, J. Warnatz, Evaluated kinetic data for combustion modeling: Supplement II, J. Phys. Chem. Ref. Data. 34 (2005) 757–1397.

[143] M. Frenklach, H. Wang, M.J. Rabinowitz, Optimization and analysis of large chemical kinetic mechanisms using the solution mapping method-combustion of methane, Prog. Energy Combust. Sci. 18 (1992) 47–73.

[144] D.A. Sheen, H. Wang, The method of uncertainty quantification and minimization using polynomial chaos expansions, Combust. Flame. 158 (2011) 2358–2374.

[145] H.J.C. T. Turányi, T. Nagy, I. Gy. Zsély, M. Cserháti, T. Varga, B. T. Szabó, I. Sedyó, P. T. Kiss, A. Zempléni, Determination of rate parameters based on both direct and indirect measurements, Int. J. Chem. Kinet. 44 (2012) 284–302.

[146] T. Varga, T. Nagy, C. Olm, I.G. Zsély, R. Pálvölgyi, Valkó, G. Vincze, M. Cserháti, H.J. Curran, T. Turányi, Optimization of a hydrogen combustion mechanism using both direct and indirect measurements, Proc. Combust. Inst. 35 (2015) 589–596.

[147] L. Elliott, D.B. Ingham, A.G. Kyne, N.S. Mera, M. Pourkashanian, C.W. Wilson, Genetic algorithms for optimisation of chemical kinetics reaction mechanisms, Prog. Energy Combust. Sci. 30 (2004) 297–328.

[148] JH Holland, Adaptation in natural and artificial systems: an introductory analysis with applications to biology, control, and artificial intelligence, The University of Michigan, 1975.

[149] W. Polifke, W. Geng, K. Döbbeling, Optimization of rate coefficients for simplified reaction mechanisms with genetic algorithms, Combust. Flame. 113 (1998) 119–134.

[150] L. Elliott, D.B. Ingham, A.G. Kyne, N.S. Mera, M. Pourkashanian, C.W. Wilson, Reaction Mechanism Reduction and Optimization Using Genetic Algorithms, Ind. Eng. Chem. Res. (2005) 658–667.

[151] E. El Rassy, A. Delaroque, P. Sambou, H.K. Chakravarty, A. Matynia, On the Potential of the Particle Swarm Algorithm for the Optimization of Detailed Kinetic Mechanisms. Comparison with the Genetic Algorithm, J. Phys. Chem. A. 125 (2021) 5180–5189.

[152] Matynia, Brookesia documentation, (2020).

[153] M. Fürst, Uncertainty Quantification and Optimization of kinetic mechanisms for non-conventional combustion regimes: Turning uncertainties into possibilities, 2020.

[154] A. Bertolino, M.B. Fürst, A. Stagni, A. Frassoldati, M. Pelucchi, C. Cavallotti, T. Faravelli, A. Parente, An evolutionary, data-driven approach for mechanism optimization: theory and application to ammonia combustion, Combust. Flame, under Rev. 229 (2021) 111366.

[155] B.M. Adams, W.J. Bohnhoff, K.R. Dalbey, M.S. Ebeida, J.P. Eddy, M.S. Eldred, R.W. Hooper, P.D. Hough, K.T. Hu, J.D. Jakeman, M. Khalil, K.A. Maupin, J.A. Monschke, E.M. Ridgway, A.A. Rushdi, D. Thomas, J.A. Stephens, L.P. Swiler, J.G. Winokur, Dakota, A Multilevel Parallel Object-Oriented Framework for Design Optimization, Parameter Estimation, Uncertainty Quantification, and Sensitivity Analysis: Version 6.15 User's Manual, (2021).

[156] https://dakota.sandia.gov/sites/default/files/docs/6.0/html-ref/method-coliny_direct.html, (n.d.).

[157] A. Cuoci, A. Frassoldati, T. Faravelli, E. Ranzi, OpenSMOKE++: An object-oriented framework for the numerical modeling of reactive systems with detailed kinetic mechanisms, Comput. Phys. Commun. 192 (2015) 237–264.

[158] Q. Cazères, Analysis and reduction of chemical kinetics for combustion applications, Université de Toulouse, 2021.

[159] P. Pepiot-Desjardins, H. Pitsch, An efficient error-propagation-based reduction method for large chemical kinetic mechanisms, Combust. Flame. 154 (2008) 67–81.

[160] F. Monnier, G. Ribert, Numerical simulations of supercritical CH4/O2 flame propagation in inhomogeneous mixtures following ignition, Proc. Combust. Inst. 000 (2022) 1–9.

[161] A. Pestre, Numerical simulations of aeronautical engine ignitions under realistic high altitude conditions Epaminondas, Institut National Polytechnique de Toulouse, 2023.

[162] T. Jaravel, Prediction of pollutants in gas turbines using Large Eddy Simulation, Institut National Polytechnique de Toulouse, 2016.

[163] R.B.B. Joseph O. Hirschfelder, Charles F. Curtiss, The Molecular Theory of Gases and Liquids, Wiley, 1964.

[164] J. Smagorinsky, General circulation experiments with the primitive equations, Science (80-.). (1963).

[165] F. Nicoud, F. Ducros, Subgrid-scale stress modelling based on the square of the velocity, Flow Meas. Instrum. 62 (1999) 183–200.

[166] F. Nicoud, H.B. Toda, O. Cabrit, S. Bose, J. Lee, Using singular values to build a subgrid-scale model for large eddy simulations, Phys. Fluids. 23 (2011) 0–12.

[167] T. Schönfeld, M. Rudgyard, Steady and unsteady flow simulations using the hybrid flow solver AVBP, AIAA J. 37 (1999) 1378–1385.

[168] N. Gourdain, L. Gicquel, G. Staffelbach, O. Vermorel, F. Duchaine, J.F. Boussuge, T. Poinsot, High performance parallel computing of flows in complex geometries: II. Applications, Comput. Sci. Discov. 2 (2009).

[169] G. Daviller, G. Oztarlik, T. Poinsot, A generalized non-reflecting inlet boundary condition for steady and forced compressible flows with injection of vortical and acoustic waves, Comput. Fluids. 190 (2019) 503–513.

[170] N. Lamarque, Schémas numériques et conditions limites pour la simulation aux grandes échelles de la combustion diphasique dans les foyers d'hélicoptère, Institut National Polytechnique de Toulouse, 2007.

[171] P. Lax, B. Wendroff, Systems of Conservation Laws, Commun. Pure Appl. Math. 13 (1960) 217–237.

[172] O. Colin, M. Rudgyard, Development of High-Order Taylor-Galerkin Schemes for LES, J. Comput. Phys. 162 (2000) 338–371.

[173] A.Z. Panagiotopoulos, Direct Determination of Fluid Phase Equilibria by Simulation in the Gibbs Ensemble : A Review EQUILIBRIA BY SIMULATION IN THE GIBBS, Mol. Simul. (2006) 1–23.

[174] N.K. Koutras, V.I. Harismiadis, D.P. Tassios, Equation of state for the Lennard-Jones fluid, Fluid Phase Equilibria,. 77 (1992) 13–38.

[175] W.A. Cañas-Marín, U.E. Guerrero-Aconcha, J.D. Ortiz-Arango, Comparison of different cubic equations of state and combination rules for predicting residual chemical potential of binary and ternary Lennard-Jones mixtures: Solid-supercritical fluid phase equilibria, Fluid Phase Equilib. 234 (2005) 42–50.

[176] K.G. Joback, R.C. Reid, Estimation of Pure-Component Properties from Group-Contributions, Chem. Eng. Commun. 57 (1987) 233–243.

[177] D.Y. Peng, D.B. Robinson, A New Two-Constant Equation of State, Ind. Eng. Chem. Fundam. 15 (1976) 59–64.

[178] G. Soave, Equilibrium constants from a modified Redlich-Kwong equation of state, Chem. Eng. Sci. 27 (1972) 1197–1203.

[179] M. Ghanbari, M. Ahmadi, A. Lashanizadegan, A comparison between Peng-Robinson and Soave-Redlich-Kwong cubic equations of state from modification perspective, Cryogenics (Guildf). 84 (2017) 13–19.

[180] T. Schmitt, D. Marchal, S. Ducruix, B. Cuenot, REST HF-10 test case : Large-Eddy Simulations using the AVBP solver, (2022) 1–15.

[181] A. Nicole, L. Dorey, REST HF10 test case : Simulation of combustion instabilities induced by flow rate modulations with diffuse interface modelling, (2022).

[182] R. Kaess, S. Köglmeier, R. Behr, O. Knab, REST HF-10 test case : URANS Simulations of Excited Methane Flames under Real Gas Conditions, (n.d.) 1–9.

[183] T. Schmitt, REST HF-10 test case : Synthesis of the Contributions for the Simulation of Excited Methane Flames under Real Gas Conditions, (n.d.) 1–15.

[184] R. Kaess, REST Testcase HF-10 - Test Case Description (ArianeGroup internal report), 2018.

[185] B. Cuenot, F. Shum-Kivan, S. Blanchard, The thickened flame approach for non-premixed combustion: Principles and implications for turbulent combustion modeling, Combust. Flame. (2021) 111702.

[186] L. Pons, N. Darabiha, S. Candel, Pressure effects on nonpremixed strained flames, Combust. Flame. 152 (2008) 218–229.

[187] L. Pons, N. Darabiha, S. Candel, T. Schmitt, B. Cuenot, The structure of multidimensional strained flames under transcritical conditions, Comptes Rendus - Mec. 337 (2009) 517–527.

[188] S.D. Cohen, A.C. Hindmarsh, CVODE, a stiff/nonstiff ODE solver in C, Comput. Phys. 10 (1996) 138–143.

[189] CVODE documentation - https://sundials.readthedocs.io/en/latest/cvode/index.html, (n.d.).

[190] T. Schmitt, D. Marchal, S. Ducruix, B. Cuenot, REST HF-10 test case : Large-Eddy Simulations using the AVBP solver, Proc. 9TH Eur. Conf. Aeronaut. Sp. Sci. (EUCASS. (2022) 1–15.

[191] X. Yang, W. Liang, T. Tan, C.K. Law, Reevaluation of the reaction rate of H + O2 (+M) = HO2 (+M) at elevated pressures, Combust. Flame. 217 (2020) 103–112.

[192] M.A. Turner, E.L. Petersen, Measurement and Kinetics Prediction of Undiluted Methane-

Oxygen Laminar Flame Speeds, AIAA SciTech 2023 Forum. (2023).
[193] J. Liberatori, C. Palmese, R.M. Galassi, M. Valorani, P.P. Ciottoli, CSP-Driven Optimization of a 16-Species Skeletal Mechanism for Methane Ignition at High Pressure, AIAA SciTech 2023 Forum. (2023) 1–14.
[194] M. Furst, A.F. A. Bertolino, A. Cuoci, T. Faravelli, A. Parente, OptiSMOKE ++ User Manual, (2021).

Résumé en français du manuscrit de thèse

Modélisation et réduction de la cinétique chimique LOx-Méthane pour des applications moteur-fusée

Thèse présentée par :

Antoine Mouze-Mornettas

pour obtenir le grade de : **Docteur de l'Université d'Orléans**

Discipline/ Spécialité : Energétique

Table des matières

Nomenclature 15

Introduction 18

Methalox Liquid Rocket Engines, context and objectives 18

1.1 Past and present context of the space industry 18

1.2 Reusable space launchers 21

1.3 A brief introduction to liquid rocket engines (LRE) 22

1.3.1 General principle and architecture 23

1.3.2 LRE performances 25

1.4 MethaLox liquid rocket engines 27

1.4.1 Advantages of MethaLOx LREs 27

1.4.2 Current MethaLox LREs under development 29

1.5 Means of research and development for LREs 31

1.6 Thesis motivations 31

Chapter 2 33

Fundamentals and global strategy 33

2.1 Fundamentals of chemical kinetics 33

2.1.1 Definitions 33

2.1.2 Third body and pressure dependent reactions 35

2.2 Fundamentals of flame structures 36

2.2.1 Laminar Premixed flames 36

2.2.2 Laminar Diffusion flames 37

2.2.3 Turbulent Diffusion flames 39

2.3 Chemical schemes for methane oxycombustion 40

2.3.1 Chemical schemes and CFD 40

2.3.2 State of the art of chemical schemes for methane oxycombustion 42

2.4 Global strategy 45

2.4.1 Pathway analysis 46

2.4.2 Contribution of reactions to the heat release 48

2.4.3 Organization of the manuscript 48

Chapter 3 50
Measuring $CH4/O2$ flame speeds at high pressure and temperature 50
3.1 State of the art of Su experimental determination, isochoric method advantages and limits 50
3.1.1 State of the art of Su determination for methane in extreme conditions 50
3.1.2 The isochoric method 52
3.2 The OPTIPRIME experimental setup 53
3.2.2 Flame stability limits, Lewis number and pressure effect 56
3.2.3 Su determination limits 58
3.3 High-pressure limit for Su extraction in SEF-CONV experiments: definition of a new criterion (extract from the paper published in *Thermal Science and Engineering Progress)* .. 59
3.4 Global overview of Su evaluation with OPTIPRIME, method to compare with kinetic schemes 71
3.4.1 Global overview of Su evaluation with OPTIPRIME 71
3.4.2 Building the numerical Su to be compared with the experimental data 71
3.5 Building the $CH4/O2$ Su database at high pressure and temperature (Paper published in *Proceedings of the Combustion Institute*) 72
3.6 Complementary diluted targets at stoichiometry 82
3.6.1 Global strategy: dilution effect parametric study 82
3.6.2 Diluted targets at stoichiometry: experimental results 84
3.7 Conclusion 85
Chapter 4 86
Kinetic mechanism optimization on experimental targets 86
4.1 Experimental vs numerical results: initial situation 86
4.2 Kinetic mechanisms optimization methods 87
4.2.1 Surrogate models 88
4.2.2 Genetic Algorithms 89
4.2.3 DIRECT algorithm 91
4.3 The OPTISMOKE++ optimization code 91
4.3.1 Reaction rate uncertainty propagation 92
4.3.2 Third-body efficiency optimization 92

4.3.3 Pressure dependent reactions optimization 93
4.3.4 Code structure and workflow 93
4.4 Optimization strategy 95
4.4.1 Flame speed targets 95
4.4.2 Ignition delay time targets 96
4.4.3 Target reactions selection 97
4.4.4 POLIMI C1-C3 reduction 99
4.5 Optimization results 101
4.5.1 Flame speed results 104
4.5.2 Ignition delay time results 106
Chapter 5 111
Application – the REST HF-10 case 111
5.1 Large Eddy Simulation (LES) 112
5.1.1 CFD and turbulence modelling 112
5.1.2 Filtered governing equations in LES 114
5.1.3 Turbulent viscosity models 118
5.1.4 AVBP solver numerical parameters 119
5.2 Application case description: the REST HF-10 configuration 123
5.2.1 Geometry 124
5.2.2 Operating conditions 125
5.2.3 Boundary conditions and mesh 126
5.3 Polimi Opti reduction for REST HF-10 conditions 127
5.3.1 Reduction targets 127
5.3.2 Reduced mechanism 128
5.3.3 Reduced mechanism validation 129
5.3.4 Compressibility factor 132
5.3.5 1D comparison with the RAMEC ARC mechanism 133
5.3.6 Validation on pseudo 1D AVBP calculations 134
5.4 The chemical stiffness issue 139
5.4.1 Chemical timescale 139
5.4.2 How to deal with chemical stiffness: state of the art 141

5.4.3 Implicit solving of the chemical source terms 143
5.4.4 CVODE solver coupling with AVBP 143
5.4.5 1D validation of the CVODE coupling 144
5.4.6 Implicit integration applied to 3D LES 146
5.5 REST HF-10 calculation results and analysis 148
5.5.1 Calculation parameters 148
5.5.2 Convective scheme, LAD activation and flame topology 149
5.5.3 Averaged longitudinal profiles per cross section 155
5.5.4 Analysis of chemical species average fields and profiles 156
5.5.5 Power budget and equilibrium 163
General conclusion and perspectives 167
Appendices 169
Appendix A – Reaction contributions to the heat release 169
1- 1D diffusion flame – 100 bar, χ=1000 $s-1$ 169
2- 1D premixed flames – 100 bar 170
Appendix B – Supplementary data of the OPTIPRIME $\boldsymbol{CH4/O2}$ campaign 172
1- Raw data treatment example 172
2- Flame images examples 173
3- $\boldsymbol{CH4/O2}$ OPTIPRIME campaign results - $\boldsymbol{Su = f(P,T)}$ vs mechanisms 175
4- $\boldsymbol{CH4/O2}$ OPTIPRIME campaign results - $\boldsymbol{P, T, Su}$ experimental traces 176
5- $\boldsymbol{CH4/O2}$ OPTIPRIME diluted targets at stoichiometry campaign results - $\boldsymbol{Su = f(P,T)}$ vs mechanisms 180
6- $\boldsymbol{CH4/O2}$ OPTIPRIME diluted targets at stoichiometry - $\boldsymbol{P, T, Su}$ experimental traces 181
Appendix C – Optimization results 187
1- Genetic algorithm trials 187
2- Complete results of the optimization process with the DIRECT method 188
A. Laminar flame speed results 188
B. Ignition delay times results 190
Appendix D – ARC Reduced mechanisms 192
Appendix E – Averaged longitudinal profiles per cross section of the REST HF-10 test case 200
1. Introduction et objectifs 218

2. Mesures expérimentales de vitesses de flamme laminaires pour des mélanges $\boldsymbol{CH4/O2}$ à haute pression et température 219
3. Optimisation du schéma cinétique POLIMI C1-C3 sur les données expérimentales OPTIPRIME 222
4. Application du modèle sur un calcul LES 3D (REST HF-10) 225
5. Conclusion 228
Sources bibliographiques 230

1. Introduction et objectifs

Depuis la mise en orbite du premier satellite artificiel en 1957 et la course à la Lune qui s'en est suivie, de nouveaux acteurs sont progressivement entrés dans le domaine de l'industrie spatiale. A partir du début des années 2000, les structures privées ont pris une importance croissante aux côtés des programmes étatiques en étant de moins en moins considérées comme des exécutants mais plutôt comme des acteurs à part entière. Ces nouveaux acteurs, portés par le développement des nouvelles technologies (miniaturisation de l'électronique, révolution numérique, fabrication additive, etc.) s'inscrivent dans des logiques de production de masse et de réalisation de profit. Des modes de fonctionnement jusque-là étranger aux programmes spatiaux étatique. Ce mouvement appelé *New Space* a vu naître des acteurs non négligeables (*SpaceX* ou *RocketLab* aux US par exemple) et continue actuellement sur sa lancée dans le développement de lanceurs, constellation de satellites ou applications dérivées.

Le marché de l'accès à l'espace étant ainsi de plus en plus compétitif, les lanceurs réutilisables sont considérés comme une technologie clé pour réduire de manière significative le coût de l'accès à l'orbite. Le seul lanceur réutilisable en service actuellement est le *Falcon 9* de *SpaceX*, mais de nombreux autres projets sont en développement. Une façon de réduire les coûts d'opération tout en gardant de bonnes performances pour le lanceur serait de se tourner vers un carburant jusque-là jamais utilisé dans le cadre de la propulsion spatiale : le méthane (CH_4). En effet, le méthane possède une densité importante permettant d'embarquer plus de carburant à volume donné que l'hydrogène (carburant utilisé par l'étage central d'*Ariane 5* par exemple). Sa température de stockage à l'état liquide est proche de celle de l'oxygène (utilisé comme comburant dans les moteurs fusée) permettant ainsi la construction de réservoirs similaires pour les 2 ergols, entrainant ainsi une diminution des coûts. Par ailleurs le méthane produit moins de suies que les carburants dérivés du kérosène (type RP-1) également utilisés pour des applications spatiales, ce qui est un avantage dans l'optique de réutiliser les moteurs plusieurs fois. En effet, les suies peuvent endommager certaines parties du moteur en générant de fortes contraintes thermiques par rayonnement. Pour terminer, en termes de performances (notamment en termes d'impulsion spécifique Isp), le méthane se situe à mi-chemin entre le RP-1 et l'hydrogène. Ainsi, CH_4 se trouve être le meilleur compromis entre performances et coût pour un lanceur réutilisable.

Le contexte actuel et notamment le projet de développement du moteur-fusée européen MethaLOx PROMETHEUS [41], fait du développement de modèles cinétiques de l'oxycombustion du méthane à haute pression un sujet prioritaire. La réalisation de simulations haute-fidélité à l'aide de ce modèle permettrait en effet d'accélérer le développement du moteur en limitant le nombre d'essais réels qui sont eux, coûteux. Le principal défi réside dans la compréhension des phénomènes cinétiques en jeu lors de l'oxydation du méthane en condition moteur-fusée. En effet, les conditions de fonctionnement sont extrêmes en termes de température (du fluide cryogénique dans l'injecteur à une flamme turbulente dans la chambre) et de pression (jusqu'à 100 bars ou plus) hors de portée de la plupart des bancs de mesures expérimentaux à l'exception de rares dispositifs expérimentaux dédiés, à la mise en œuvre coûteuse ne donnant que peu d'information sur les phénomènes fondamentaux. La mise au point récente de la chambre de combustion isochore OPTIPRIME [112] développée au laboratoire ICARE (CNRS d'Orléans) permet justement la mesure de vitesse de flamme laminaire en conditions extrême. L'objectif de ce travail de thèse est dans un premier temps de développer une base de données expérimentale de vitesses de flamme en mélange CH_4/O_2 en conditions jamais atteintes auparavant pour ces mélanges (haute pression et température pour un large spectre de richesse φ).

Différents modèles cinétiques existants (aussi appelés mécanismes) provenant de la littérature sont ensuite comparés à la base de données. Le mécanisme présentant le moins d'écart avec les résultats expérimentaux est ensuite sélectionné pour passer par une phase d'optimisation sur les données OPTIPRIME à l'aide d'un code dédié. Une fois obtenu un modèle capable de décrire l'oxycombustion du méthane en conditions moteur-fusée, on peut ensuite l'utiliser dans une simulation haute-fidélité LES 3D afin de comparer son comportement avec celui de modèles déjà existants (la plupart développés sur un faible nombre de données expérimentales). Pour cela une étape de réduction du schéma est nécessaire au préalable afin de réduire le coût de calcul. La réduction est effectuée à l'aide du code ARCANE [65] et le calcul LES avec le code AVBP [167], tous deux développés au CERFACS.

2. Mesures expérimentales de vitesses de flamme laminaires pour des mélanges $\boldsymbol{CH_4/O_2}$ à haute pression et température

Les deux principaux modes de combustion existants sont le prémélange et la diffusion. Dans le premier cas, le combustible et le comburant sont mélangés avant l'allumage. Dans le second, le combustible et l'oxydant sont injectés séparément et la flamme se développe à l'interface stœchiométrique entre les deux flux. Ces deux modes de combustion peuvent être laminaires ou turbulents. Dans le cadre de l'application moteur-fusée, les flammes de diffusion constituent le mode prédominant. Il faut noter qu'il est très difficile de retirer expérimentalement des informations de telles flammes en conditions représentatives d'un moteur fusée. D'une part à cause des pressions extrêmes difficiles à reproduire en laboratoire sur la durée mais également à cause des valeurs de contrainte (*strain*) très élevées. Cependant, des analyses de chemins réactionnels et de contribution au dégagement de chaleur (noté HR) ont été réalisées à l'aide de calculs 1D CANTERA de flammes de prémélange et de diffusion en condition moteur-fusée. Elles montrent que les voies réactionnelles principales ainsi que les réactions contribuant le plus au HR sont identiques pour les deux modes de combustion. Ainsi, les vitesses des flammes laminaires prémélangées peuvent être utilisées comme cibles de référence expérimentales pour un mécanisme cinétique qui sera a posteriori appliqué aux flammes de diffusion CH_4/O_2. Concernant ce type de flammes, les conditions extrêmes découlant de la combustion dans l'oxygène pur limitent grandement le nombre de données expérimentales disponibles dans la littérature. Ainsi, les seules mesures qui ont été effectuées se trouvent à pression atmosphérique.

L'une des solutions utilisées pour monter en pression et surmonter les limites actuelles des dispositifs expérimentaux consiste à étudier l'expansion de la flamme dans des conditions isochores. Cette méthode, initialement proposée par Lewis et Von Elbe [111], est appelée ici SEF-CONV (pour *Spherical Expanding Flame at Constant Volume*). L'idée générale est d'enregistrer l'évolution de la pression au cours du temps à l'intérieur de la chambre de combustion afin de calculer la vitesse de flamme laminaire S_u. La conversion des réactifs en produits chauds à travers le front de flamme entraîne une augmentation rapide de la pression et une augmentation correspondante de la température des gaz imbrûlés et brûlés. La technique du volume constant lie ainsi l'évolution instantanée de la vitesse de la flamme à l'historique de la pression. En d'autres termes, en un seul tir, les vitesses de flamme peuvent être obtenues pour une gamme de pressions et de températures plus élevées [101,105,112].

Afin de calculer la vitesse de la flamme en connaissant l'évolution de la pression en fonction du temps à l'intérieur de la chambre, plusieurs hypothèses doivent être faites :

- La pression P est spatialement uniforme dans la chambre
- Les gaz brûlés et imbrûlés sont considérés comme des gaz parfaits
- Il n'y a pas de réactions chimiques dans les gaz frais
- La flamme est parfaitement sphérique avec un front de flamme infiniment fin
- Le gaz imbrûlé est comprimé de manière isentropique

Sur la base de ces hypothèses, l'expression suivante de la vitesse de la flamme laminaire par rapport au mélange imbrûlé S_u peut-être dérivée [113] :

$$S_u = \frac{dR_f}{dt} - \frac{R_0^3 - R_F^3}{3\gamma_u R_f^2 P}\frac{dP}{dt} \tag{125}$$

Elle est définie comme la différence entre la vitesse de la flamme dans le référentiel du laboratoire et la vitesse d'expansion des gaz frais. R_f et R_0 étant respectivement le rayon de la flamme et de la chambre intérieure, et γ_u le rapport de capacité thermique des gaz imbrûlés. Cette relation suppose la connaissance de l'évolution simultanée de R_f et de P. Avec OPTIPRIME, le premier est accessible via une caméra haute vitesse et un accès optique (une caractéristique unique pour une chambre de combustion isochore rendue possible via une couronne de quartz sur 360°) et le second via des capteurs de pression rapides (cf. *Figure 116*). Le banc expérimental et la méthode de mesure sont détaillés dans [112,115].

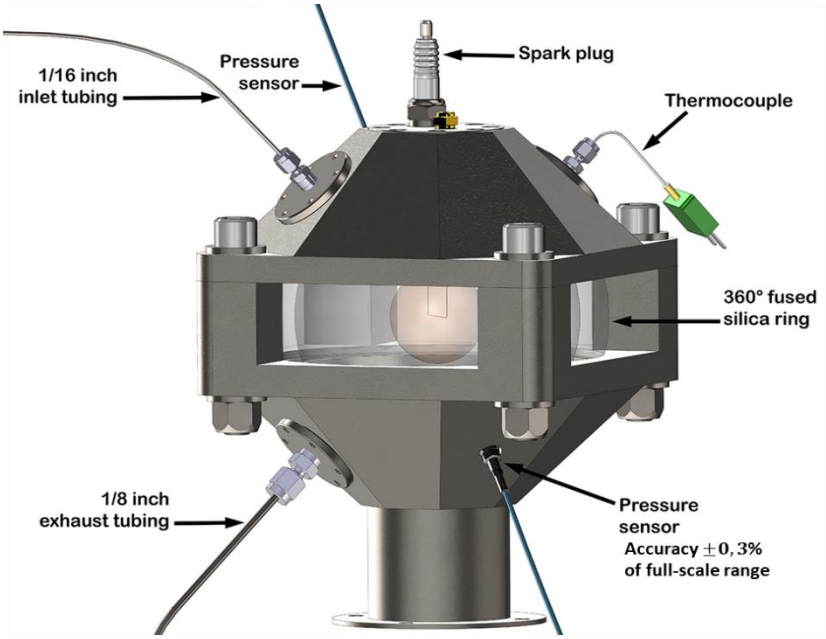

Figure 116: Chambre de combustion isochore OPTIPRIME

Cependant, l'une des principales difficultés des expériences SEF-CONV est d'identifier précisément les limites du domaine de pression compatible avec les hypothèses émises pour calculer S_u. En effet, au début de la propagation, la flamme est affectée par des effets d'étirement (ce qu'on appelle la limite basse-pression) alors qu'à la fin, les pertes de chaleur à la paroi affectent l'hypothèse de compression isentropique des gaz frais (limite de haute-pression). Le fait d'être en dehors de ces limites signifie donc que les principales hypothèses permettant de dériver la relation S_u ne sont plus valides. La compréhension de ces phénomènes est donc cruciale pour une bonne détermination de la vitesse de flamme. La *Figure 117* représente l'évolution simultanée de R_f et P au cours du temps. La zone de sécurité pour l'extraction de S_u est indiquée comme "zone de conditions isochoriques". Elle montre

que la pression maximale mesurée atteinte lors d'un tir est plus importante que la pression finale exploitée.

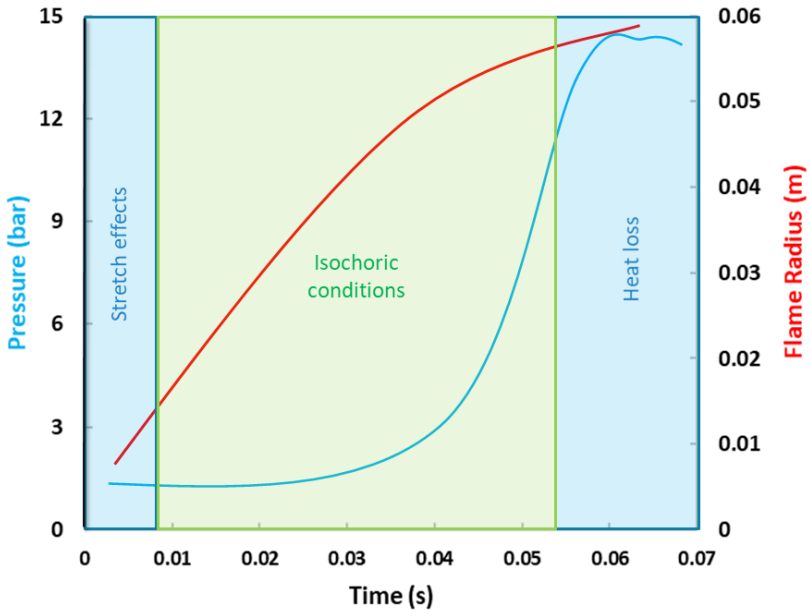

Figure 117: Limites de le zone de détermination de S_u

La limite haute-pression n'est pas évidente à définir [101,112,130,131]. Ainsi, une étude a été spécialement réalisée pour ce travail de thèse dans le but de définir le critère le plus précis et versatile possible. Les conclusions de ce travail ont été publiées dans *Thermal Science and Engineering Progress* [122]. Le critère (basé sur l'évolution de l'épaisseur de préchauffage de la flamme δ_{PH} et la recherche de son minimum) est d'abord présenté, puis validé sur des simulations DNS réalisées par Chen et al. avec le code *A-SURF* [120,124]. Enfin, ses performances sont comparées à d'autres critères de la littérature, prouvant son efficacité.

La construction d'une base de données expérimentale de S_u en mélange CH_4/O_2 à haute pression, température et large gamme de φ est ensuite réalisée. La réalisation des mesures et leurs analyses sont détaillées dans un article publié dans *Proceedings of the Combustion Institute* [132]. Après avoir détaillé les défis posés par la mesure de S_u en conditions d'oxycombustion à haute pression (notamment des variations quasi instantanées nécessitant l'adaptation des protocoles de mesure et de post-traitement), l'article étudie d'abord les effets d'étirement initiaux affectant les flammes. En effet, les valeurs d'étirement rencontrées sont jusqu'à dix fois plus importantes que les mélanges CH_4/air, et le critère de limite basse-pression utilisée classiquement (2 fois la pression initiale P_0) doit donc être réévalué. Une fois la base de données construite pour un large spectre de richesses φ et de conditions (*P,T*), les résultats expérimentaux sont comparés à un panel de mécanismes cinétiques présélectionnés. La sélection de modèles évalués inclue des schémas cinétiques initialement pensés pour décrire l'oxycombustion (comme le RAMEC [76], basé sur des délais d'auto-allumage dilués uniquement) ou des mécanismes plus généralistes et plus récents (comme *FFCM1* [95] ou POLIMI C1-C3 [134] par exemple). Les résultats de cette étude sont présentés sur la *Figure 118*. On remarque d'emblée qu'aucun des mécanismes testés ne capture correctement le S_u expérimental pour les conditions testées. La tendance générale des modèles semble être de sous-estimer S_u proche stoichiométrie puis de le surestimer pour les mélanges riches. Après analyse, il s'avère que le modèle présentant le moins d'écarts est le POLIMI C1-C3. Les différences de comportement s'expliquent en partie par la nature des cibles expérimentales ayant servi à l'ajustement des schémas et à la façon dont

ils décrivent les réactions clés. POLIMI C1-C3 est ensuite analysé par le biais d'une étude de sensibilité sur les constantes de vitesse de réaction k pour les conditions testées. L'objectif est d'identifier les réactions sensibles clés à ajuster au cours d'un processus d'optimisation pour correspondre à l'ensemble de la base de données expérimentale. Enfin, une corrélation $S_u = f(P, T, \varphi)$ ajustée sur la base de données OPTIPRIME et les sources bibliographiques existantes est proposée.

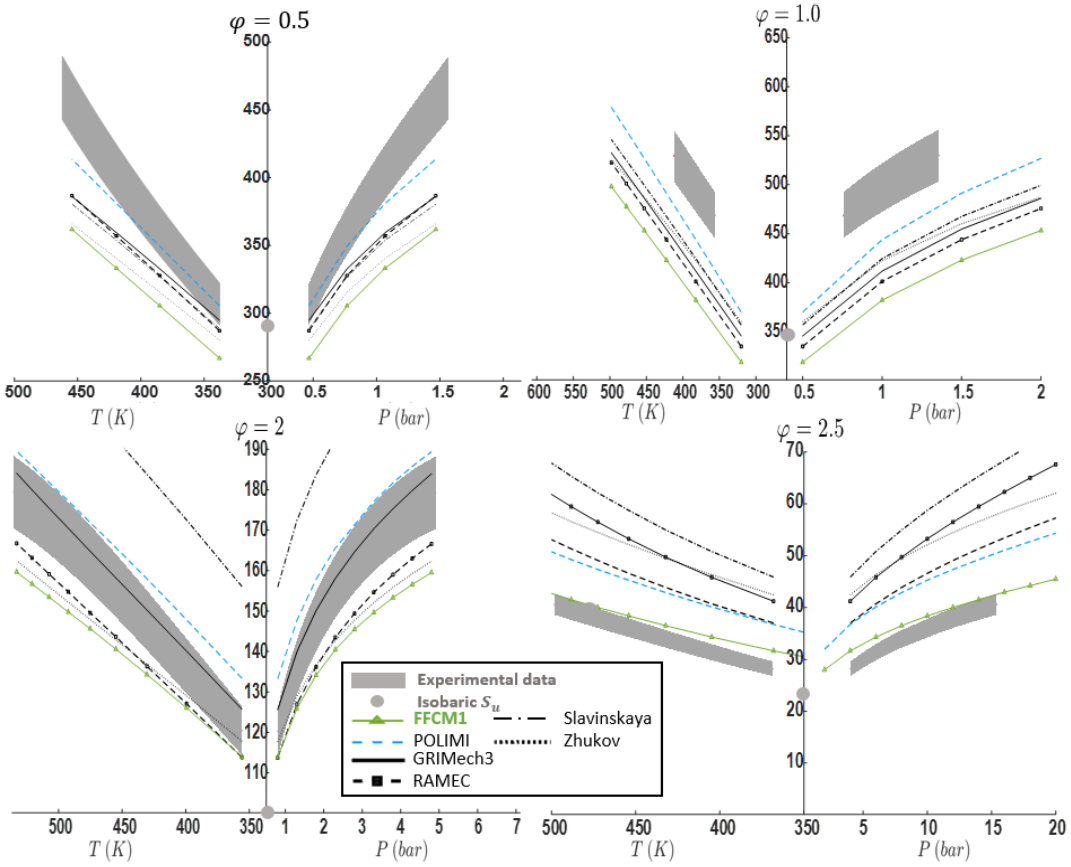

Figure 118: Flame speed S_u $[cm.s^{-1}]$ for CH_4/O_2 mixtures at various equivalence ratios φ (thickened traces) as a function of T and P compared to several kinetic mechanisms (lines). Single symbols are for experimental isobaric flame speeds.

Pour les conditions proches de la stoichiométrie, la P_0 des tirs a été choisie sub-atmosphérique afin de minimiser les valeurs de pression et vitesses en fin de propagation pouvant être prohibitives pour OPTIPRIME. Par ailleurs, les mêmes conditions mènent rapidement à des instabilités thermo-diffusives en fin de propagation [61,116] notamment à φ=1 limitant ainsi la pression maximale atteinte. Afin de palier à ce problème et d'obtenir des données à plus haute pression, des mesures complémentaires ont été réalisées à la stoichiométrie pour des mélanges oxydants dilués à l'aide d'Hélium. Ce dernier modifie la diffusivité thermique en l'augmentant, ce qui a pour conséquence d'avoir un effet stabilisant sur le front de flamme. Ainsi ces mesures permettent de monter jusque 20 bars (dans le cas de 82.5% de diluant en volume) pour des températures cependant plus basses que ce qu'on atteindrai avec de l'O_2 pur. Néanmoins les réactions clés mises en jeu sont les mêmes que pour les conditions d'oxycombustion (vérifié par analyse de sensibilité), soulignant l'intérêt de ces mesures.

3. Optimisation du schéma cinétique POLIMI C1-C3 sur les données expérimentales OPTIPRIME

Comme mentionné dans la section précédente, le mécanisme POLIMI C1-C3 a été identifié comme présentant le moins d'écart relatif avec les expériences de mesures de S_u pour l'ensemble du set de conditions étudiées. Il a donc été choisi comme point de départ du processus d'optimisation.

Les données de S_u complémentaires en mélange dilué à φ=1 et haute pression sont également utilisées car ces réactions ont été reconnues comme représentatives des conditions non diluées. Les cibles sont séparées en deux groupes : cibles d'optimisation et cibles de contrôle. Le premier groupe comprend les conditions expérimentales correspondant aux mélanges CH_4/O_2 à φ=0.5-1.0-2.0-2.5 et aux mélanges dilués à la stœchiométrie (82.5 et 50 % de diluant dans le mélange oxydant), ce qui permet de couvrir une large gamme de conditions. L'autre groupe est utilisé pour évaluer la qualité du processus d'optimisation a posteriori.

De plus, afin de compléter la base de données expérimentale servant de support à l'optimisation du modèle, des délais d'auto allumage (notés IDT) provenant de la littérature ont été ajoutés. Ces derniers, provenant de l'étude de Petersen et al. [76,78], présentent les conditions à haute pression les moins diluées de la littérature (aucune mesure d'IDT n'ayant été effectuée en conditions CH_4/O_2 pur). L'ensemble de la procédure d'optimisation a été résumé dans une publication de la conférence *EUCASS 2022* [139] et est présenté succinctement dans cette section.

L'idée est de minimiser l'écart relatif entre les points expérimentaux et numériques (quantifié par une *fonction objectif*). Pour cela on vient modifier les paramètres de la loi d'Arrhenius (cf. variables en rouge ci-dessous) des réactions clés identifiées au préalable à l'aide d'analyses de sensibilité sur la vitesse de flamme pour les conditions investiguées. La procédure d'optimisation peut être axée sur A, b, Ea séparément ou simultanément. Un paramètre optimisé est aussi appelé *paramètre actif*.

$$k = \boldsymbol{A}T^{\boldsymbol{b}}e^{-\frac{\boldsymbol{Ea}}{RT}} \tag{126}$$

Pour que le processus d'optimisation reste valable physiquement, l'incertitude sur les paramètres actifs doit être prise en compte lorsqu'elle existe. Par exemple, Baulch et al. [141,142] ont inventorié les valeurs d'incertitude des constantes de vitesse k pour un large panel de réactions pour des gammes de températures données. Comme pour les paramètres b et Ea, la littérature est peu abondante l'incertitude sur k est généralement propagée aux autres variables [154]. En général, la stratégie consiste à cibler les réactions qui maximisent le produit de leur sensibilité par l'incertitude sur leurs paramètres d'Arrhenius pour la gamme des cibles expérimentales.

Lorsque le nombre de cibles expérimentales et de réactions à ajuster dans le mécanisme étudié sont assez faibles, une optimisation manuelle des paramètres d'Arrhenius peut être envisagée. Cependant, dès que le nombre de cibles augmente (via multiplication des conditions de richesse, pression et température) il en va de même pour le nombre de réactions clés à ajuster. Un algorithme est donc nécessaire pour mener à bien ce processus. En effet, dans le cas de cette étude, les analyses de sensibilité ont permis d'identifier 30 réactions clés à ajuster pour couvrir l'intégralité des conditions testées. Ceci mène à un total de 96 paramètres actifs en comptant les efficacités de 3^{e} corps.

Comme il offre la possibilité d'utiliser différents algorithmes d'optimisation et d'ajuster simultanément les trois paramètres d'Arrhenius ainsi que les efficacités de troisième corps sur une large gamme de cibles expérimentales (profils d'espèces en PSR, délais d'allumage et vitesses de flamme laminaire), le code OPTISMOKE++ V1 [136] a été choisi pour l'optimisation du mécanisme POLIMI C1-C3 sur la base des données OPTIPRIME CH_4/O_2 et d'IDT de la littérature. La structure du code et des exemples d'application sont détaillés dans la littérature [154,194]. Après plusieurs essais comparatifs, l'algorithme d'optimisation DIRECT [136,156] est sélectionné.

Par ailleurs, comme la fonction objectif devra être évaluée à chaque itération, l'utilisation de la totalité des points constituant les traces de S_u conduirait à une augmentation importante du coût de calcul. En effet, POLIMI C1-C3 est un mécanisme de grande taille et la convergence en vitesse de flamme peut prendre du temps. Afin d'éviter ce problème tout en respectant les évolutions des traces, seuls trois points par conditions testées seront utilisés. Un à la pression et à la température initiale (dit "point bas"), un aux conditions P,T finales ("point haut") ainsi qu'un point intermédiaire entre les deux. En comptant les IDT, le nombre total de points expérimentaux (ou contraintes d'optimisation) est de 54.

Pour accélérer encore plus le processus d'optimisation, le schéma cinétique est également réduit à l'aide de l'outil ARCANE [65] développé au CERFACS. Les cibles de réductions sont choisies identiques aux cibles d'optimisation, ainsi le schéma réduit a le même comportement que le modèle détaillé sur ces points (à une erreur négligeable près). On passe ainsi d'un schéma à 114 espèces et 1999 réactions à un schéma réduit composé de 30 espèces et 128 réactions au coût de calcul beaucoup plus abordable.

Les résultats obtenus sont illustrés sur la *Figure 119* représentant l'écart relatif moyen pour chaque trace de vitesse pour les cibles d'optimisation et de contrôle. La *Figure 120* représente quant à elle les résultats pour les délais d'auto-allumage. Le détail des résultats est présenté dans [139].

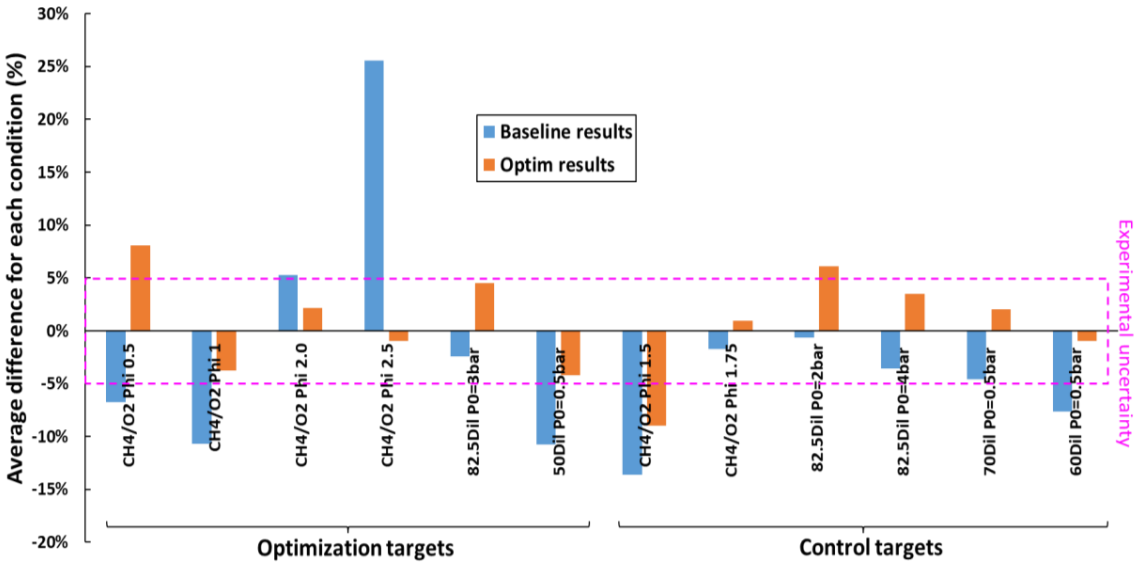

Figure 119: Résultats du processus d'optimisation pour les vitesses de flamme

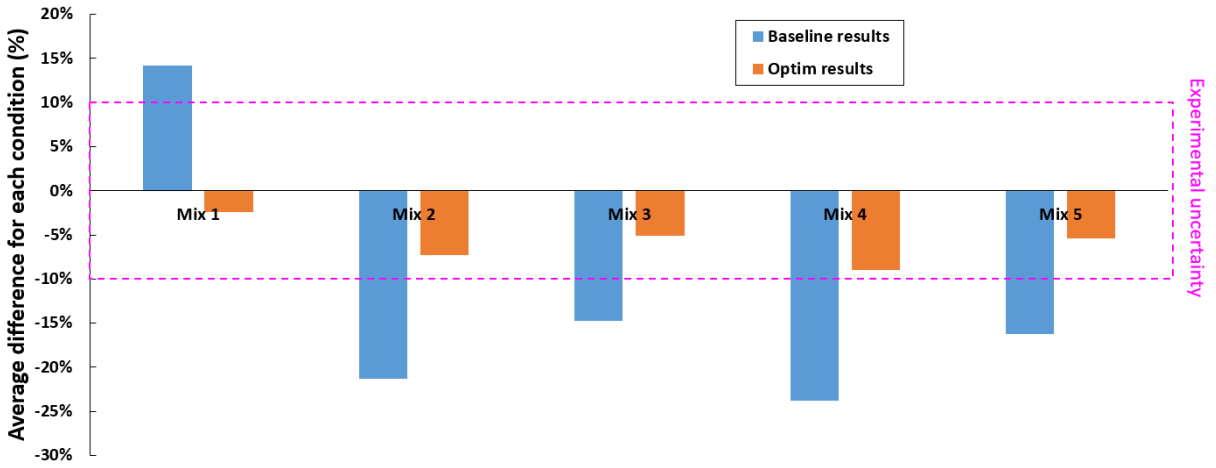

Figure 120: Résultats du processus d'optimisation pour les délais d'auto allumage

La majorité des écarts moyens ont été réduits à l'intérieur de la zone d'incertitude expérimentale de ±5%. Certaines conditions restent supérieures à cet écart, comme CH_4/O_2 à φ=0.5 (cible d'optimisation), CH_4/O_2 à φ =1.5 et le cas à 82.5% de diluant à la stœchiométrie (toutes deux cibles de contrôle). Cependant, ces écarts moyens restent acceptables. Enfin, la condition en mélange pauvre est la seule cible d'optimisation en dehors de la plage d'incertitude expérimentale alors que le comportement des autres a été grandement amélioré (en particulier les conditions riches CH_4/O_2 à φ=2.5). Les conditions pauvres sont particulièrement difficiles à optimiser pour les mélanges non dilués car elles ne présentent pas beaucoup de réactions clés de sensibilité négative spécifiques. On remarquera cependant que le comportement des cibles de contrôle n'a pas été trop affecté par le processus d'optimisation, ce qui souligne la qualité du processus mis en œuvre.

Finalement, le processus global décrit dans cette section mène à un mécanisme composé de 30 espèces et 128 réactions, dérivé de POLIMI C1-C3 et entièrement optimisé sur des cibles de vitesse de flamme CH_4/O_2 à haute pression et température provenant de la base de données OPTIPRIME ainsi que des délais d'allumage provenant de la littérature. Ce mécanisme (dénommé POLIMI Opti) peut être maintenant utilisé pour des calculs 0 ou 1D avec des solveurs de type CANTERA ou CHEMKIN. Il est également possible de l'utiliser pour des calculs CFD 3D en condition moteurs-fusée via une autre étape de réduction préalable sur des cibles représentatives du cas étudié. Cet aspect est développé dans la section suivante.

4. Application du modèle sur un calcul LES 3D (REST HF-10)

Afin d'évaluer les performances et le comportement du schéma cinétique développé au cours de ce travail de thèse dans le cadre d'une simulation CFD LES 3D avec le code de calcul CERFACS AVBP, le cas de calcul REST HF-10 est choisi. Il s'agit d'une géométrie présentant un injecteur coaxial unique, représentatif d'une chambre de combustion de moteur-fusée. Cette configuration de référence possède une géométrie fortement inspirée du banc d'essai TUM développé par Haidn et al [50]. Alors que les études expérimentales basées sur des installations dédiées avec accès optique s'aventurent juste au-dessus des conditions supercritiques (par exemple ~ 60 bar pour les expériences menées dans les installations DLR/TUM [49]), HF-10 est réellement représentatif des chambres de combustion des

moteur-fusée en régime de pleine poussée avec une pression de 100 bar et une richesse proche de la stoichiométrie.

Le but final du calcul est d'évaluer les différences induites par l'utilisation de la chimie optimisée nouvellement définie par rapport aux résultats déjà existants sur cette configuration réaliste. En effet, plusieurs calculs ont été effectués sur la configuration REST HF-10 pour des conditions de fonctionnement identiques [183]. Ces publications détaillent la géométrie du cas de calcul, ses conditions opératoires ainsi que les conditions aux limites utilisées. Le résultat nous intéressant particulièrement provient d'un calcul qui a été mené avec une chimie ARC dérivée du RAMEC [190]. Les chimies ARC (pour *Analytical Reduced Chemistry*) sont des chimies réduites obtenues à l'aide d'ARCANE permettant de traiter les espèces rapides à l'aide de l'approximation des régimes quasi stationnaires (QSSA). Ces espèces ne seront ainsi plus transportées, retirant du coût de calcul et de la raideur temporelle au système.

Afin d'être adapté au calcul REST HF-10 et d'obtenir un ARC, le schéma cinétique POLIMI Opti a été réduit avec ARCANE sur des cibles représentative, à savoir des flammes de diffusion hautement étirées et à haute pression caractéristiques des moteur-fusée. Après vérification de la validité de la réduction, ce processus permet d'obtenir un schéma ARC POLIMI Opti de 19 espèces transportées, 116 réactions et 7 QSS. Le schéma ARC RAMEC utilisé comme point de comparaison est quant à lui constitué de 15 espèces transportées, 88 réactions et 6 QSS. Le comportement de l'ARC POLIMI Opti sous AVBP est évalué au préalable à l'aide de calculs pseudo 1D.

Il faut par ailleurs savoir que les conditions de calcul LES 3D d'oxycombustion à haute pression et haute valeur d'étirement affectent directement les temps caractéristiques des espèces chimiques [23] en les réduisant drastiquement. Le pas temps chimique τ_c étant calculé comme le minimum de tous les temps chimiques, on se retrouve fréquemment dans des situations où ce dernier est inférieur au pas de temps de la simulation Δt_{CFL} qui est lui directement tributaire des conditions d'écoulement et du maillage. Cette situation de sous-résolution temporelle, appelée raideur chimique, peut entrainer des erreurs non négligeables dans la prédiction des fractions massiques allant jusqu'au crash du calcul [161]. De plus, un certain nombre d'espèces ayant un temps chimique très faible sont impossibles à mettre en QSS (par exemple le fuel lui-même ou des espèces proches comme CH_3), il faut donc trouver d'autres moyen de diminuer la raideur temporelle. Le sous-cyclage (calcul de plusieurs τ_c pour un Δt_{CFL}) a été utilisé pour le calcul REST mené avec la chimie ARC POLIMI Opti. Cependant, le nombre important de sous-cycles à effectuer pour obtenir un calcul stable est assez prohibitif en termes de coût. Ainsi, l'intégration des termes sources chimiques de manière implicite (par opposition à la méthode explicite jusque-là utilisée avec AVBP) a été implémentée au cours de ce travail de thèse. Pour ce faire, le solveur implicite d'équations différentielles CVODE [188,189] a été couplé à AVBP. Après plusieurs étapes de validation sur des cas de calcul 1D intermédiaires, l'utilisation de l'intégration implicite permet de régler le problème de raideur temporelle causé principalement par la solution transitoire contenant l'ancienne chimie RAMEC à évacuer du domaine de calcul lors de l'initialisation.

Afin palier à tout problème de raideur (i-e sous-résolution) spatiale et de compenser les défauts des schémas numériques employés, de la viscosité numérique est employée. Dans le cas spécifique de la simulation REST à haute pression où l'hypothèse des gaz réels est employée, l'utilisation d'une viscosité artificielle basée sur les gradients de densité (LAD – *Localized Artificial Diffusivity* [74]) est toute indiquée [23].

Afin de garantir un fonctionnement correct du calcul, les paramètres de tolérance imposés pour le LAD doivent être plus stricts dans le cas du calcul ARC POLIMI Opti que dans celui de l'ARC RAMEC. Cependant, malgré un seuil de déclenchement plus bas dans le premier cas, on observe une absence de d'application du LAD dans la zone de recess (là où la flamme est a priori la plus fine et la raideur spatiale potentiellement plus importante) dans le cas de calcul ARC POLIMI Opti contrairement au

calcul ARC RAMEC. Cette différence n'est a priori pas due au schéma numérique convectif employé. En effet, le calcul de référence ARC RAMEC emploie le schéma TTGC [23] tandis que le cas ARC POLIMI Opti emploie un schéma de type LW [23], plus diffusif et donc plus accommodant vis-à-vis de la raideur spatiale. Pour prouver l'indépendance vis-à-vis du schéma numérique, un calcul simulant 0.5 temps convectifs utilisant la chimie ARC RAMEC a été effectué avec le schéma LW. Malgré une activation moindre du LAD par rapport au calcul TTGC dû à une plus grande diffusivité, on observe toujours un déclenchement dans la zone de recess dans ce cas de figure. Reste donc la cinétique chimique pour induire cette différence (en affectant notamment les gradients de température et densité). Les effets décris ci-dessus ont un impact direct sur la topologie de l'écoulement, entrainant une "rigidification" de la flamme dans le cas de la chimie ARC RAMEC et une flamme beaucoup plus turbulente dans le cas ARC POLIMI Opti. Ce comportement ainsi que les phénomènes décris précédemment sont visibles sur la *Figure 121* illustrant les zones d'activation du LAD.

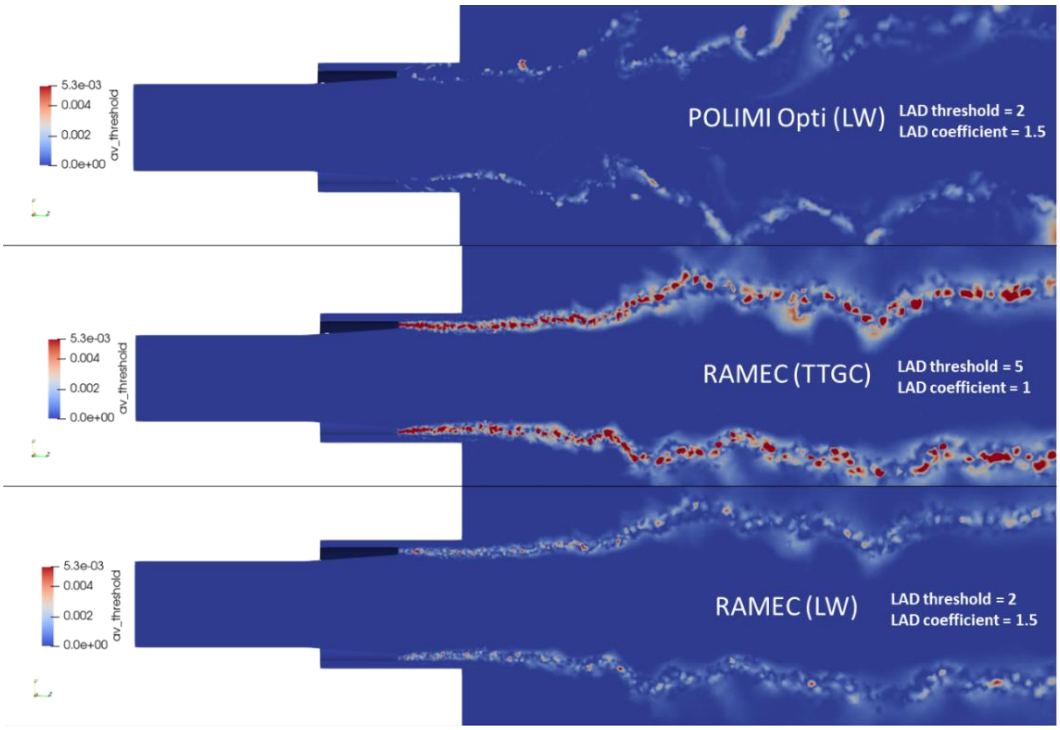

Figure 121: Zones d'activation de la viscosité artificielle (av_threshold) pour la zone d'injection du calcul REST HF-10 pour différents paramètres numériques - coupe longitudinale des solutions instantanées

La différence de topologie se visualise sur les champs moyens de température et de dégagement de chaleur. Ce dernier étant globalement plus important chez POLIMI Opti dû aux effets de turbulence plus élevés. Cependant, même si de légères différences peuvent être observées, la longueur de la flamme est tout à fait comparable pour les deux chimies.

L'analyse des champs moyens de fraction massiques et des moyennes par sections perpendiculaires à l'axe longitudinal tend également à prouver que l'oxydation du carburant est potentiellement plus complexe pour la chimie optimisée que pour la chimie de référence RAMEC. En effet, OH et HO_2 se trouvent présents en quantités plus faibles chez POLIMI Opti indiquant qu'ils sont probablement plus rapidement consommés par des réactions impliquant CH_4. Cette observation est confirmée par l'analyse des constantes de vitesse des réactions concernées à haute température (plus importantes chez POLIMI Opti). Ces phénomènes conduisent à un surplus important d'oxygène dans la zone post-flamme par rapport au calcul RAMEC. Cette poche d'O_2 est également due à la dissociation de l'eau, un phénomène qui est beaucoup plus discret chez RAMEC. La dissociation plus importante de H_2O chez POLIMI Opti est également confirmée par l'analyse des constantes de vitesse pour des conditions

équivalentes à celles de la zone post-flamme. La troisième différence majeure entre les 2 mécanismes réside dans la description de l'équilibre CO- CO_2. POLIMI Opti présente des champs cohérents et des valeurs moyennes longitudinales de ces espèces, conduisant à une quantité de CO_2 proche de l'équilibre alors que RAMEC présente des quantités importantes de CO non consommé. Ce comportement, qui peut être aussi illustré par des études $k = f(T)$, indique que même si les deux mécanismes n'ont pas atteint l'équilibre à la fin de la chambre de combustion REST HF-10, POLIMI Opti en est peut-être plus proche.

En résumé, la chimie optimisée de POLIMI Opti permet de mettre en évidence des phénomènes qui n'avaient été que partiellement ou pas du tout pris en compte auparavant. Ceci affectent de manière significative la topologie de l'écoulement et la distribution des espèces. Ces phénomènes peuvent maintenant être pris en compte pour une conception plus précise des chambres de combustion des moteurs-fusées MethaLox.

5. Conclusion

Ce travail de thèse a permis d'apporter un nouveau regard sur la cinétique de l'oxycombustion du méthane dans des conditions extrêmes de pression et de température.

La constitution d'une base de données de vitesses de flamme CH_4/O_2 dans des conditions jamais atteintes auparavant a été réalisée grâce à la chambre de combustion OPTIPRIME développée au laboratoire CNRS ICARE en utilisant la méthode isochore. Le développement d'un nouveau critère de fin d'adiabaticité pour les mesures de vitesse de flammes en conditions isochores a permis d'extraire les points les plus extrêmes (en termes de P et T) de la campagne expérimentale. Les données ont été acquises pour une large gamme de pression, de température et richesses, permettant ainsi d'élargir les ressources bibliographiques sur le sujet, jusqu'à présent principalement limitées à la pression atmosphérique.

La base de données obtenue a ensuite été comparée à différents schémas cinétiques, anciens et récents, dont certains initialement développés pour décrire l'oxycombustion du méthane. Cette analyse globale a permis de démontrer que tous ces mécanismes ont tendance à sous-estimer la vitesse de flamme S_u pour les mélanges pauvres, stœchiométriques et légèrement riches (avec un écart maximal à la stœchiométrie) et à la surestimer pour les mélanges riches [132]. Des mesures isobares récentes effectuées par Turner et al. de l'université Texas A&M ont confirmé le comportement des résultats d'OPTIPRIME [192].

POLIMI C1-C3 a été utilisé comme point de départ d'un processus d'optimisation. Il a en effet été identifié comme le mécanisme le plus performant dans la gamme de conditions explorées. Des analyses de sensibilité préalables ont permis d'identifier les réactions clés de l'oxycombustion pour les conditions testées et même pour des pressions plus élevées. Le code OPTISMOKE++ a été ensuite utilisé pour paramétrer les variables d'Arrhenius de ces réactions afin de réduire l'écart relatif avec les données expérimentales. Les traces de S_u OPTIPRIME ainsi que des délais d'auto-inflammation à faible dilution provenant de la littérature ont été utilisés pour constituer la base de données de référence. Ce processus a finalement permis l'obtention d'un mécanisme POLIMI Opti, adapté pour décrire l'oxycombustion du méthane dans des conditions extrêmes.

La dernière étape de ce travail a consisté à appliquer le modèle obtenu à des calculs LES 3D représentatifs des conditions de fonctionnement moteur-fusée. Pour ce faire, la configuration mono-injecteur en régime supercritique REST HF-10 déjà largement étudiée a été utilisée. Les résultats des

calculs effectués avec un mécanisme réduit RAMEC ARC étant disponibles, ils ont été utilisés comme référence pour la comparaison. POLIMI Opti a été également réduit au préalable sur des cibles représentatives du cas 3D à l'aide de l'outil ARCANE, menant ainsi à un mécanisme ARC compact. Par ailleurs, afin de régler les problèmes de raideur temporelle, il a été décidé de coupler le solveur implicite CVODE à AVBP. La résolution implicite des termes sources chimiques a permis de stabiliser le calcul, qui a ensuite été poursuivi avec une résolution explicite classique. L'analyse des résultats obtenus confirme que le schéma cinétique optimisé permet de capturer des phénomènes spécifiques qui n'étaient pas, ou peu, visibles avec le calcul de référence RAMEC. A savoir une flamme plus turbulente, un phénomène d'oxydation du combustible plus complexe comprenant diverses espèces, une dissociation de l'eau plus importante et une perception différente de l'équilibre CO-CO_2. En conclusion, la prise en compte de ces phénomènes, non capturés avec RAMEC, bénéficierait grandement à une description précise d'un moteur MethaLox.

Par ailleurs, le processus mis en place au cours de ce travail de recherche peut être appliqué à d'autres carburants et/ou applications industrielles. Ce travail a permis de développer des outils et de mettre au point un processus pour identifier les besoins, construire une base de données expérimentale, réaliser une étude comparative des schémas chimiques, identifier les réactions clés et optimiser un mécanisme afin de le réduire pour finalement l'appliquer à des calculs LES haute-fidélité.

De nombreuses améliorations sont encore possibles pour les modèles et les processus développés dans cette thèse. Afin, par exemple, d'augmenter l'efficacité de la résolution implicite des termes sources chimiques, des méthodes dynamiques ont été testées. L'utilisation d'un senseur basé sur le pas de temps chimique limiterai l'utilisation de l'intégration implicite aux seules zones raides, permettant ainsi de gagner un temps de calcul substantiel. Cependant, malgré des résultats très encourageants sur des simulations 1D, des travaux sont encore nécessaires sur la définition exacte du senseur et la répartition de la charge pour une utilisation efficace sur des calculs 3D. En outre, même si elles sont relativement compactes et efficaces, les chimies ARC ont encore un coût de calcul non négligeable. Elles restent parfaitement adaptées à l'environnement académique mais moins à l'industrie. Notons toutefois qu'avec l'augmentation de la puissance de calcul, ces modèles deviennent de plus en plus abordables pour les différents acteurs. Par ailleurs, plusieurs tentatives de développement de mécanismes globaux capables de donner des résultats suffisamment représentatifs des mécanismes détaillés ont été tentées pour la combustion de CH_4/O_2. Par exemple, l'approche GLOMECH [23,72] a donné des résultats prometteurs . Afin de capitaliser sur cette expérience, une approche améliorée, utilisant des cibles expérimentales et des outils tels que OPTISMOKE ++ pourrait être envisagée. De plus, afin de mieux prédire et comprendre la raideur des chimies complexes dans des environnements 3D affectés par la turbulence, des études de stabilité spécifiques devraient être réalisées afin de mettre en évidence et de traiter les mécanismes de déclenchement d'instabilités.

En résumé, la description de l'oxycombustion du méthane dans les moteurs de fusée reste plus que jamais un sujet d'actualité d'une importance majeure dans le cadre de l'effort massif actuel pour développer des véhicules de lancement réutilisables dans le monde entier.

Sources bibliographiques

[1] UNOOSA (United Nations Office for Outer Space Affairs), Online Index of Objects Launched into Outer Space - https://www.unoosa.org/oosa/osoindex/search-ng.jspx, (n.d.).

[2] D. ZAJACKOWSKI, N. MAUBERT, L'émergence et le développement du New Space aux États-Unis - Note thématique du Bureau du CNES et Service Spatial de l'Ambassade de France à Washington D.C., n.d.

[3] NASA COTS program page - https://www.nasa.gov/commercial-orbital-transportation-services-cots, (n.d.).

[4] What are SmallSats ? Nasa web page - https://www.nasa.gov/content/what-are-smallsats-and-cubesats, (n.d.).

[5] ICEYE company website - https://www.iceye.com/contact, (n.d.).

[6] MarCO mission webpage, JPL website - https://www.jpl.nasa.gov/missions/mars-cube-one-marco, (n.d.).

[7] Starlink website - https://www.starlink.com/technology, n.d.

[8] Andrew Parsonson's European Launch Vehicles - https://europeanspaceflight.com/download/european-launch-vehicles/, (n.d.).

[9] H.W. Jones, The Recent Large Reduction in Space Launch Cost, 48th Int. Conf. Environ. Syst. (2018) 81.

[10] J. Wilken, S. Stappert, M. Sippel, Parametric Cost Estimation in the Preliminary Design Phase of Reusable Launch Vehicles, Sp. Cost Eng. Conf. (2021) 1–13.

[11] O. Gogdet, J. Mansouri, J. Breteau, A.P. De Mirand, Launch Vehicles System Studies in the " Future Launchers Preparatory Programme ": the Reusability Option for Ariane Evolutions ., in: EUCASS, 2019: pp. 1–16.

[12] Falcon 9 vehicle description - SpaceX website - https://www.spacex.com/vehicles/falcon-9/, (n.d.).

[13] Starship vehicle description - SpaceX website - https://www.spacex.com/vehicles/starship/, (n.d.).

[14] M. Illig, S. Ishimoto, E. Dumont, CALLISTO , a demonstrator for reusable launchers, in: EUCASS 2022 Conf., n.d.

[15] J. Vila, J. Hassin, Technology acceleration process for the THEMIS low cost and reusable prototype, in: EUCASS 2019 Conf., n.d.

[16] H. Gilibert, European Launchers : preparing the future . Launch service prices disrupted, in: EUCASS 2022 Conf., n.d.

[17] A. Patureau De Mirand, J.-M. Bahu, E. Louaas, Ariane Next, a vision for a reusable cost efficient European rocket, in: EUCASS 2019 Conf., n.d.: pp. 1–9.

[18] MaiaSpace Website - https://maia-space.com/, (n.d.).

[19] L.T. De Luca, T. Shimada, V.P. Sinditskii, M. Calabro, Chemical Rocket Propulsion: A Comprehensive Survey of Energetic Materials, Springer Aerospace Technology, 2017.

[20] Hybrid Propulsion for Space - Company webpage - https://hypr-space.com/, (n.d.).

[21] G.P. Sutton, Rocket Propulsion Elements - 9th edition, John Wiley, 2016.

[22] V. Yang, M. Hbiballah, J. Hulka, M. Popp, Liquid Rocket Thrust Chambers: Aspects of Modeling, Analysis, and Design, 2004.

[23] S. Blanchard, Multi-physics Large-Eddy Simulation of methane oxy-combustion in Liquid Rocket Engines, Institut National Polytechnique de Toulouse, 2021.

[24] J.C. Oefelein, Y. Vigor, Comprehensive review of liquid-propellant combustion instabilities in f-1 engines, J. Propuls. Power. 9 (1993) 657–677.

[25] C. Laurent, Présentée et soutenue par : Low-Order Modeling and High-Fidelity Simulations for the Prediction of Combustion Instabilities in Liquid Rocket Engines and Gas Turbines Rapporteurs : Membre(s) du jury, Institut National Polytechnique de Toulouse, 2020.

[26] NASA CEA - Glenn Research Center webpage - https://www1.grc.nasa.gov/research-and-engineering/ceaweb/, (n.d.).

[27] B.J. McBride, Computer Program for Calculation of Complex Chemical Equilibrium Compositions and Applications II. Users Manual and Program Description, 1996.

[28] O.J. Haidn, Advanced rocket engines, NATO R&T Organ. Educ. Notes RTO-EN-AVT-150. (2008).

[29] A. Kong, Reduced Kinetic Mechanism of Methane Oxidation for Rocket Applications Reduced Kinetic Mechanism of Methane Oxidation for Rocket Applications (Master's Thesis), 2015.

[30] G. Hagemann, LOX / Methane The Future is Green, Present. Académie l'Air l'Espace, Paris. (2015).

[31] M. Kurela, P. Noir, Space grade Biomethane production for Themis reusable stage demonstrator Vega Evolution Themis Demonstrator, (n.d.) 1–14.

[32] R.M. Zubrin, A.C. Muscatello, M. Berggren, Integrated Mars In Situ Propellant Production System, J. Aerosp. Eng. 26 (2013) 43–56.

[33] D.Z. Oehler, G. Etiope, Methane seepage on mars: where to look and why, Astrobiology. 17 (2017) 1233–1264.

[34] T. Neill, D. Judd, E. Veith, D. Rousar, Practical uses of liquid methane in rocket engine applications, Acta Astronaut. 65 (2009) 696–705.

[35] T. Kato, D. Terakado, H. Nanri, T. Morito, I. Masuda, H. Asakawa, H. Sakaguchi, Y. Ishikawa, T. Inoue, S. Ishihara, M. Sasaki, Subscale Firing Test for Regenerative Cooling LOX/Methane Rocket Engine, 7th Eur. Conf. Aeronaut. Sp. Sci. (2017) 2–5.

[36] P.H. Joo, M.R.J. Charest, C.P.T. Groth, Ö.L. Gülder, Comparison of structures of laminar methane-oxygen and methane-air diffusion flames from atmospheric to 60atm, Combust. Flame. 160 (2013) 1990–1998.

[37] Launch Vehicles - Relativity Space Website - https://www.relativityspace.com/rockets, (n.d.).

[38] Landspace official website - https://www.landspace.com/, (n.d.).

[39] A. Beil, Chinese Zhuque-2 fails during first methalox orbital launch attempt - https://www.nasaspaceflight.com/2022/12/zhuque2-debut/, NasaSpaceflight.Com. (n.d.).

[40] P. Bellomi, M. Rudnykh, S. Carapellese, D. Liuzzi, G. Caggiano, L. Arione, A.A. Gurtovoy, S.D.

Lobov, V.S. Rachuk, E. D'Aversa, A. De Lillis, R.C. Pellegrini, Development of LM10-MIRA liquid oxygen – liquid natural gas expander cycle demonstrator engine, 11 (2019) 447–466.

[41] P. Simontacchi, E. Edeline, R. Blasi, S. Sagnier, N. Ravier, A. Espinosa-Ramos, J. Breteau, Prometheus: Precursor of new low-cost rocket engine family, Proc. Int. Astronaut. Congr. IAC. 2018-Octob (2018) 1–12.

[42] J.H. Morehart, A Survey of LNG-fueled Rocket Engine Development Activity – Non-U.S., AIAA Propuls. Energy Forum, 2021. (2021) 1–10.

[43] G. Ordonneau, L. Vingert, P. Grenard, N. Fdida, A Rocket Engine under a Magnifying Glass, Aerospacelab J. (2016) 1–13.

[44] M. Habiballah, M. Orain, F. Grisch, L. Vingert, P. Gicquel, Experimental studies of high-pressure cryogenic flames on the mascotte facility, Combust. Sci. Technol. 178 (2006) 101–128.

[45] M. Théron, M.M. Benito, B. Vieille, L. Vingert, N. Fdida, Y. Mauriot, R. Blouquin, C. Seitan, Experimental and numerical investigation of LOX / Methane Cryogenic Combustion at low mixture ratio, Eucass 2019. (2019) 1–15.

[46] L. Vingert, N. Fdida, Y. Mauriot, Experimental Investigations of Liquid Oxygen / Methane Combustion at Very Low Mixture Ratio at the Mascotte Test Facility, Ists. (2019) 1–7.

[47] V. Lechner, C. Betrancourt, P. Scouflaire, L. Vingert, S. Ducruix, Dynamic characterization of wall temperature in LOX/CH 4 rocket engine operating conditions using phosphor thermometry , Proc. Combust. Inst. 000 (2022) 1–9.

[48] P. Grenard, N. Fdida, L. Vingert, L.H. Dorey, L. Selle, J. Pichillou, Experimental investigation of heat transfer in a subscale liquid rocket engine at high mixture ratio, J. Propuls. Power. 35 (2019).

[49] J. Lux, O. Haidn, Effect of recess in high-pressure liquid oxygen/methane coaxial injection and combustion, J. Propuls. Power. 25 (2009) 24–32.

[50] O.J.H. S. Silvestri, M. P. Celano, G. Schlieben, C. Kirchberger, Characterization of a Gox-Gch4 Single Element Combustion Chamber, Sp. Propuls. 2014. 1 (2014).

[51] C.B. Von Sethe, S. Soller, O.J. Haidn, Experimental investigation of a single element LOX / GCH4 heat-sink combustion chamber, Eucass 2019. (2019) 1–11.

[52] W. Armbruster, J. Hardi, M. Oschwald, Impact of shear-coaxial injector hydrodynamics on high-frequency combustion instabilities in a representative cryogenic rocket engine, Int. J. Spray Combust. Dyn. 14 (2022) 118–130.

[53] P.G. Robert J. Kee, Michael E. Coltrin, Chemically Reacting Flow: Theory and Practice, Wiley, 2005.

[54] B.J. McBride, M.J. Zehe, S. Gordon, NASA Glenn coefficients for calculating thermodynamic properties of individual species: National Aeronautics and Space Administration, 2002.

[55] F. Lindemann, DISCUSSION ON TNE RADIATION THEORY OF CUEMICAL ACTION". Professor, Trans. Faraday Soc. 17 (1922).

[56] Reaction Design, ANSYS Chemkin Theory Manual 17.0 (15151), 2015.

[57] R.G. Gilbert, J. Troe, Theory of Thermal Unimolecular Reactions in the Fall-off Range. I. Strong Collision Rate Constants, Berichte Der Bunsengesellschaft Für Phys. Chemie. 87 (1983) 161–169.

[58] https://cantera.org/science/kinetics.html -Pressure-Dependent Arrhenius Rate Expressions, (n.d.).

[59] G. Renoux, Étude expérimentale de l'interaction goutte/flamme : propagation d'une flamme dans un aérosol en microgravité et passage d'une goutte à travers un front de flamme, Université d'Orléans, 2020.

[60] G.H. MARKSTEIN, Experimental and Theoretical Studies of Flame-Front Stability, J. Aeronaut. Sci. 18 (1951) 199–209.

[61] P. Clavin, Dynamic behavior of premixed flame fronts in laminar and turbulent flows, Prog. Energy Combust. Sci. 11 (1985) 1–59.

[62] A.P. Kelley, C.K. Law, Nonlinear effects in the extraction of laminar flame speeds from expanding spherical flames, Combust. Flame. 156 (2009) 1844–1851.

[63] F. Halter, T. Tahtouh, C. Mounaïm-Rousselle, Nonlinear effects of stretch on the flame front propagation, Combust. Flame. 157 (2010) 1825–1832.

[64] T. Poinsot, D. Veynante, Theoretical and Numerical Combustion, (2012).

[65] ARCANE - Q. Cazeres, P. Pepiot https://chemistry.cerfacs.fr/en/arcane/, (n.d.).

[66] S. Blanchard, Q. Cazères, B. Cuenot, Chemical modeling for methane oxy-combustion in Liquid Rocket Engines, Acta Astronaut. 190 (2022) 98–111.

[67] R.W. Bilger, The structure of turbulent nonpremixed flames, Symp. Combust. 22 (1989) 475–488.

[68] L. Esclapez, Numerical study of ignition and inter-sector flame propagation in gas turbine., Institut National Polytechnique de Toulouse, 2015.

[69] B. Cuenot, Etude asymptotique et numérique de la structure des flammes de diffusion laminaires et turbulentes, Institut National Polytechnique de Toulouse, 1995.

[70] W.P. Jones, R.P. Lindstedt, Global reaction schemes for hydrocarbon combustion, Combust. Flame. 73 (1988) 233–249.

[71] B.G. Franzelli, Impact of the chemical description on direct numerical simulations and large eddy simulations of turbulent combustion in industrial aero-engines, 2011.

[72] J. Strauss, Development of Global Chemical Reaction Scheme for Methane and Oxygen in Rocket Applications to be Used in Large-Eddy Simulation, (2020).

[73] J. Zips, C. Traxinger, P. Breda, M. Pfitzner, Assessment of presumed/transported probability density function methods for rocket combustion simulations, J. Propuls. Power. 35 (2019) 747–764.

[74] T. Schmitt, Large-Eddy Simulations of the Mascotte Test Cases Operating at Supercritical Pressure, Flow, Turbul. Combust. 105 (2020) 159–189.

[75] D. Maestro, B. Cuenot, L. Selle, Large Eddy Simulation of Combustion and Heat Transfer in a Single Element GCH4/GOx Rocket Combustor, Flow, Turbul. Combust. 103 (2019) 699–730.

[76] E.L. Petersen, D.F. Davidson, R.K. Hanson, Kinetics modeling of shock-induced ignition in low-dilution CH4/O2 mixtures at high pressures and intermediate temperatures, Combust. Flame. 117 (1999) 272–290.

[77] A. Hertzberg, A.P. Bruckner, D.W. Bogdanoff, Ram accelerator: A new chemical method for

accelerating projectiles to ultrahigh velocities, AIAA J. 26 (1988) 195–203.

[78] E.L. Petersen, D.F. Davidson, R.K. Hanson, Ignition delay times of ram accelerator mixtures, 32nd Jt. Propuls. Conf. Exhib. 15 (1996).

[79] V.V.L. Gregory P. Smith, David M. Golden, Michael Frenklach, Nigel W. Moriarty, Boris Eiteneer, Mikhail Goldenberg, C. Thomas Bowman, Ronald K. Hanson, Soonho Song, William C. Gardiner, GRI-MECH 3.0, (n.d.).

[80] E.L. Petersen, R.K. Hanson, Reduced kinetics mechanisms for ram accelerator combustion, J. Propuls. Power. 15 (1999) 591–600.

[81] P. Natale, G. Saccone, F. Battista, Cfd Kinetic Scheme Validation for Liquid Rocket Engine Fuelled By, (2019) 8.

[82] F. Battista, D. Ricci, P. Natale, D. Cardillo, M. Fragiacomo, G. Propellant, Hyprob-New : Recent Developments of the Lox / Lch4, Sp. Propuls. 2020+1. (2021) 1–10.

[83] F. Monnier, G. Ribert, Simulation of high-pressure methane-oxygen combustion with a new reduced chemical mechanism, Combust. Flame. 235 (2022) 111735.

[84] N. Jaouen, L. Vervisch, P. Domingo, G. Ribert, Automatic reduction and optimisation of chemistry for turbulent combustion modelling: Impact of the canonical problem, Combust. Flame. 175 (2017) 60–79.

[85] V.P. Zhukov, A.F. Kong, A compact reaction mechanism of methane oxidation at high pressures, Prog. React. Kinet. Mech. 43 (2018) 62–78.

[86] V.P. Zhukov, Kinetic model of alkane oxidation at high pressure from methane to n-heptane, Combust. Theory Model. 13 (2009) 427–442.

[87] V.P. Zhukov, V.A. Sechenov, A.Y. Starikovskii, Autoignition of a lean propane-air mixture at high pressures, Kinet. Catal. 46 (2005) 319–327.

[88] T. Horchler, S. Fechter, REST HF-10 Test Case : Numerical Simulation of a Single Coaxial LOX-CH4 Injector with Forced Mass Flow Oscillations Using the DLR TAU-Code, (2022).

[89] N.A. Slavinskaya, A. Meddi, J.H. Starcke, O.J. Haidn, Methane skeletal mechanism for space propulsion applications, 52nd AIAA/SAE/ASEE Jt. Propuls. Conf. 2016. (2016).

[90] N.A. Slavinskaya, U. Riedel, S.B. Dworkin, M.J. Thomson, Detailed numerical modeling of PAH formation and growth in non-premixed ethylene and ethane flames, Combust. Flame. 159 (2012) 979–995.

[91] G. Rozenchan, D.L. Zhu, C.K. Law, S.D. Tse, Outward propagation, burning velocities, and chemical effects of methane flames up to 60 ATM, Proc. Combust. Inst. 29 (2002) 1461–1470.

[92] N.A. Slavinskaya, O.J. Haidn, Kinetic mechanism for low pressure oxygen / methane ignition and combustion, 49th AIAA Aerosp. Sci. Meet. Incl. New Horizons Forum Aerosp. Expo. (2011) 1–13.

[93] G. Saccone, P. Breda, P. Natale, F. Battista, G. Saccone, P. Breda, P. Natale, F. Battista, G. Saccone, P. Breda, P. Natale, Reduced kinetic mechanism for methane / oxygen rocket engine applications : a reliable and numerically efficient methodology applications : a reliable and numerically efficient methodology, (2023).

[94] T. Lu, C.K. Law, A criterion based on computational singular perturbation for the identification of quasi steady state species: A reduced mechanism for methane oxidation with NO chemistry,

Combust. Flame. 154 (2008) 761–774.

[95] G.P. Smith, Y. Tao, and H. Wang, Foundational Fuel Chemistry Model Version 1.0 (FFCM-1), http://nanoenergy.stanford.edu/ffcm1, 2016., (n.d.).

[96] G. Bagheri, E. Ranzi, M. Pelucchi, A. Parente, A. Frassoldati, T. Faravelli, Comprehensive kinetic study of combustion technologies for low environmental impact: MILD and OXY-fuel combustion of methane, Combust. Flame. 212 (2020) 142–155.

[97] F. Winter, S. Silvestri, M.P. Celano, G. Schlieben, O.J. Haidn, High-speed and Emission Imaging of a Coaxial Single Element GOX / GCH 4 Rocket Combustion Chamber, Eucass. (2017) 1–10.

[98] F. Halter, G. Dayma, Laminar flame speed determination at high pressure and temperature conditions for kinetic schemes assessment, in: Proc. Combust. Inst., 2020.

[99] Y. Wang, A. Movaghar, Z. Wang, Z. Liu, W. Sun, F.N. Egolfopoulos, Z. Chen, Laminar flame speeds of methane/air mixtures at engine conditions: Performance of different kinetic models and power-law correlations, Combust. Flame. 218 (2020) 101–108.

[100] F.N. Egolfopoulos, N. Hansen, Y. Ju, K. Kohse-Höinghaus, C.K. Law, F. Qi, Advances and challenges in laminar flame experiments and implications for combustion chemistry, Prog. Energy Combust. Sci. 43 (2014) 36–67.

[101] A. Omari, L. Tartakovsky, Measurement of the laminar burning velocityusing the confined and unconfined spherical flame methods - A comparative analysis, Combust. Flame. 168 (2016) 127–137.

[102] J. Jayachandran, R. Zhao, F.N. Egolfopoulos, Determination of laminar flame speeds using stagnation and spherically expanding flames: Molecular transport and radiation effects, Combust. Flame. 161 (2014) 2305–2316.

[103] D.R. Dowdy, D.B. Smith, S.C. Taylor, A. Williams, The use of expanding spherical flames to determine burning velocities and stretch effects in hydrogen/air mixtures, Symp. Combust. 23 (1991) 325–332.

[104] K. Kumar, C.J. Sung, Laminar flame speeds and extinction limits of preheated n-decane/O2/N2 and n-dodecane/O2/N2 mixtures, Combust. Flame. 151 (2007) 209–224.

[105] A. Movaghar, R. Lawson, F.N. Egolfopoulos, Confined spherically expanding flame method for measuring laminar flame speeds: Revisiting the assumptions and application to C1C4 hydrocarbon flames, Combust. Flame. 212 (2020) 79–92.

[106] A.N. Mazas, D.A. Lacoste, T. Schuller, Experimental and numerical investigation on the laminar flame speed of CH4/O2 mixtures diluted with CO2 and H 2O, Proc. ASME Turbo Expo. 2 (2010) 411–421.

[107] A. Mazas, Etude des flammes prémélangées enrichies en oxygène : analyse des effets de dilution par la vapeur d ’ eau et le dioxyde de carbone, Ecole Centrale des Arts et Manufactures, 2010.

[108] B. Lewis, G. Von Elbe, Bernard Lewis and Guenther von Elbe - Combustion, Flames and Explosions of Gases-Academic Press (1987), 1987.

[109] J. Oh, D. Noh, Laminar burning velocity of oxy-methane flames in atmospheric condition, Energy. 45 (2012) 669–675.

[110] R.M. Fristrom, C. Grunfelder, S. Favin, Methane-oxygen flame structure. I. Characteristic profiles in a low-pressure, laminar, lean, premixed methane-oxygen flame, J. Phys. Chem. 64

(1960) 1386–1392.

[111] B. Lewis, G. Von Elbe, Determination of the speed of flames and the temperature distribution in a spherical bomb from time-pressure explosion records, J. Chem. Phys. 2 (1934) 283–290.

[112] F. Halter, Z. Chen, G. Dayma, C. Bariki, Y. Wang, P. Dagaut, C. Chauveau, Development of an optically accessible apparatus to characterize the evolution of spherically expanding flames under constant volume conditions, Combust. Flame. 212 (2020) 165–176.

[113] F. Fiock, F. Marvin, R. Caldwell, FLAME SPEEDS AND ENERGY CONSIDERATIONS FOR EXPLOSIONS IN A SPHERICAL BOMB, (n.d.).

[114] M. Faghih, Z. Chen, The constant-volume propagating spherical flame method for laminar flame speed measurement, Sci. Bull. 61 (2016) 1296–1310.

[115] F. Halter, G. Dayma, Z. Serinyel, P. Dagaut, C. Chauveau, Laminar flame speed determination at high pressure and temperature conditions for kinetic schemes assessment, Proc. Combust. Inst. 38 (2021) 2449–2457.

[116] R. Addabbo, J.K. Bechtold, M. Matalon, Wrinkling of spherically expanding flames, Proc. Combust. Inst. 29 (2002) 1527–1535.

[117] Y.B. Zeldovich, The Theory of Combustion and Detonation, Publ. Academy of Sciences, USSR, 1944.

[118] G. Darrieus, Propagation d'un front de flamme, in: Congrès de Mécanique Appliquée, 1945.

[119] L. Landau, On the theory of slow combustion, in: Acta Physicochim. USSR, 1944.

[120] Z. Chen, M.P. Burke, Y. Ju, Effects of compression and stretch on the determination of laminar flame speeds using propagating spherical flames, Combust. Theory Model. 13 (2009) 343–364.

[121] C. Xiouris, T. Ye, J. Jayachandran, F.N. Egolfopoulos, Laminar flame speeds under engine-relevant conditions: Uncertainty quantification and minimization in spherically expanding flame experiments, Combust. Flame. 163 (2016) 270–283.

[122] A. Mouze-Mornettas, H. Keck, Y. Wang, Z. Chen, G. Dayma, C. Chauveau, F. Halter, Effect of wall heat transfer on the dynamics of premixed spherical expanding flames, Therm. Sci. Eng. Prog. 29 (2022) 101227.

[123] Z. Chen, M.P. Burke, Y. Ju, Effects of Lewis number and ignition energy on the determination of laminar flame speed using propagating spherical flames, Proc. Combust. Inst. 32 I (2009) 1253–1260.

[124] P. Dai, Z. Chen, Supersonic reaction front propagation initiated by a hot spot in n-heptane/air mixture with multistage ignition, Combust. Flame. 162 (2015) 4183–4193.

[125] L. Pizzuti, C.A. Martins, L.R. Dos Santos, D.R.S. Guerra, Laminar Burning Velocity of Methane/Air Mixtures and Flame Propagation Speed Close to the Chamber Wall, Energy Procedia. 120 (2017) 126–133.

[126] M.M. Elia M., Laminar burning velocity of methane-air-diluent mixtures, J. Eng. Gas Turbines Power. 123 (2001) 190–196.

[127] R.J. Kee, F.M. Rupley, J.A. Miller, Chemkin-Ii: a Fortran Chemical Kinetics Package for the Analysis of Gas-Phase Chemical Kinetics, J. Chem. Inf. Model. 53 (1989) 1689–1699.

[128] R.J. Kee, sss A FORTRAN COMPUTER CODE PACKAGE FOR THE EVALUATION OF GAS-

PHASE,MULTICOMPONENT TRANSPORT PROPERTIES, J. Chem. Inf. Model. 53 (2013) 1689–1699.

[129] Z. Chen, On the accuracy of laminar flame speeds measured from outwardly propagating spherical flames: Methane/air at normal temperature and pressure, Combust. Flame. 162 (2015) 2442–2453.

[130] R.R. Burrell, J.L. Pagliaro, G.T. Linteris, Effects of stretch and thermal radiation on difluoromethane/air burning velocity measurements in constant volume spherically expanding flames, Proc. Combust. Inst. 37 (2019) 4231–4238.

[131] Razus, Burning Velocity of Propane−Air Mixtures from Pressure−TimeRecords during Explosions in a Closed Spherical Vessel.pdf, (n.d.).

[132] A. Mouze-mornettas, M.M. Benito, G. Dayma, C. Chauveau, B. Cuenot, F. Halter, Laminar flame speed evaluation for CH 4 / O 2 mixtures at high pressure and temperature for rocket engine applications, Proc. Combust. Inst. 000 (2022) 1–8.

[133] B. Galmiche, Caractérisation expérimentale des flammes laminaires et turbulentes en expansion, Université d'Orléans, 2014.

[134] G. Bagheri, E. Ranzi, M. Pelucchi, A. Parente, A. Frassoldati, T. Faravelli, Comprehensive kinetic study of combustion technologies for low environmental impact: MILD and OXY-fuel combustion of methane, Combust. Flame. 212 (2020) 142–155.

[135] ANSYS CHEMKIN 20.0, ANSYS Reaction Design: San Diego, (2020).

[136] M. Fürst, A. Bertolino, A. Cuoci, T. Faravelli, A. Frassoldati, A. Parente, OptiSMOKE++: A toolbox for optimization of chemical kinetic mechanisms, Comput. Phys. Commun. 264 (2021) 107940.

[137] E. Hu, X. Li, X. Meng, Y. Chen, Y. Cheng, Y. Xie, Z. Huang, Laminar flame speeds and ignition delay times of methane-air mixtures at elevated temperatures and pressures, Fuel. 158 (2015) 1–10.

[138] Y. Wu, V. Modica, B. Rossow, F. Grisch, Effects of pressure and preheating temperature on the laminar flame speed of methane/air and acetone/air mixtures, Fuel. 185 (2016) 577–588.

[139] A. Mouze-Mornettas, G. Dayma, F. Halter, M. Martin Benito, Modelling and reduction of LOx-Methane chemical kinetics for rocket engine application, in: Proc. EUCASS Conf., 2022: pp. 1–10.

[140] A. Bertolino, OPTISMOKE++ crash course, 2021.

[141] D.L. Baulch, M.J. Pilling, C.J. Cobos, R.A. Cox, P. Frank, G. Hayman, T. Just, J.A. Kerr, T. Murrells, J. Troe, R.W. Walker, J. Warnatz, Evaluated Kinetic Data for Combustion Modeling. Supplement I, J. Phys. Chem. Ref. Data. 23 (1994) 847–848.

[142] D.L. Baulch, C.T. Bowman, C.J. Cobos, R.A. Cox, T. Just, J.A. Kerr, M.J. Pilling, D. Stocker, J. Troe, W. Tsang, R.W. Walker, J. Warnatz, Evaluated kinetic data for combustion modeling: Supplement II, J. Phys. Chem. Ref. Data. 34 (2005) 757–1397.

[143] M. Frenklach, H. Wang, M.J. Rabinowitz, Optimization and analysis of large chemical kinetic mechanisms using the solution mapping method-combustion of methane, Prog. Energy Combust. Sci. 18 (1992) 47–73.

[144] D.A. Sheen, H. Wang, The method of uncertainty quantification and minimization using polynomial chaos expansions, Combust. Flame. 158 (2011) 2358–2374.

[145] H.J.C. T. Turányi, T. Nagy, I. Gy. Zsély, M. Cserháti, T. Varga, B. T. Szabó, I. Sedyó, P. T. Kiss, A.

Zempléni, Determination of rate parameters based on both direct and indirect measurements, Int. J. Chem. Kinet. 44 (2012) 284–302.

[146] T. Varga, T. Nagy, C. Olm, I.G. Zsély, R. Pálvölgyi, Valkó, G. Vincze, M. Cserháti, H.J. Curran, T. Turányi, Optimization of a hydrogen combustion mechanism using both direct and indirect measurements, Proc. Combust. Inst. 35 (2015) 589–596.

[147] L. Elliott, D.B. Ingham, A.G. Kyne, N.S. Mera, M. Pourkashanian, C.W. Wilson, Genetic algorithms for optimisation of chemical kinetics reaction mechanisms, Prog. Energy Combust. Sci. 30 (2004) 297–328.

[148] JH Holland, Adaptation in natural and artificial systems: an introductory analysis with applications to biology, control, and artificial intelligence, The University of Michigan, 1975.

[149] W. Polifke, W. Geng, K. Döbbeling, Optimization of rate coefficients for simplified reaction mechanisms with genetic algorithms, Combust. Flame. 113 (1998) 119–134.

[150] L. Elliott, D.B. Ingham, A.G. Kyne, N.S. Mera, M. Pourkashanian, C.W. Wilson, Reaction Mechanism Reduction and Optimization Using Genetic Algorithms, Ind. Eng. Chem. Res. (2005) 658–667.

[151] E. El Rassy, A. Delaroque, P. Sambou, H.K. Chakravarty, A. Matynia, On the Potential of the Particle Swarm Algorithm for the Optimization of Detailed Kinetic Mechanisms. Comparison with the Genetic Algorithm, J. Phys. Chem. A. 125 (2021) 5180–5189.

[152] Matynia, Brookesia documentation, (2020).

[153] M. Fürst, Uncertainty Quantification and Optimization of kinetic mechanisms for non-conventional combustion regimes: Turning uncertainties into possibilities, 2020.

[154] A. Bertolino, M.B. Fürst, A. Stagni, A. Frassoldati, M. Pelucchi, C. Cavallotti, T. Faravelli, A. Parente, An evolutionary, data-driven approach for mechanism optimization: theory and application to ammonia combustion, Combust. Flame, under Rev. 229 (2021) 111366.

[155] B.M. Adams, W.J. Bohnhoff, K.R. Dalbey, M.S. Ebeida, J.P. Eddy, M.S. Eldred, R.W. Hooper, P.D. Hough, K.T. Hu, J.D. Jakeman, M. Khalil, K.A. Maupin, J.A. Monschke, E.M. Ridgway, A.A. Rushdi, D. Thomas, J.A. Stephens, L.P. Swiler, J.G. Winokur, Dakota, A Multilevel Parallel Object-Oriented Framework for Design Optimization, Parameter Estimation, Uncertainty Quantification, and Sensitivity Analysis: Version 6.15 User's Manual, (2021).

[156] https://dakota.sandia.gov/sites/default/files/docs/6.0/html-ref/method-coliny_direct.html, (n.d.).

[157] A. Cuoci, A. Frassoldati, T. Faravelli, E. Ranzi, OpenSMOKE++: An object-oriented framework for the numerical modeling of reactive systems with detailed kinetic mechanisms, Comput. Phys. Commun. 192 (2015) 237–264.

[158] Q. Cazères, Analysis and reduction of chemical kinetics for combustion applications, Université de Toulouse, 2021.

[159] P. Pepiot-Desjardins, H. Pitsch, An efficient error-propagation-based reduction method for large chemical kinetic mechanisms, Combust. Flame. 154 (2008) 67–81.

[160] F. Monnier, G. Ribert, Numerical simulations of supercritical CH4/O2 flame propagation in inhomogeneous mixtures following ignition, Proc. Combust. Inst. 000 (2022) 1–9.

[161] A. Pestre, Numerical simulations of aeronautical engine ignitions under realistic high altitude conditions Epaminondas, Institut National Polytechnique de Toulouse, 2023.

[162] T. Jaravel, Prediction of pollutants in gas turbines using Large Eddy Simulation, Institut National Polytechnique de Toulouse, 2016.

[163] R.B.B. Joseph O. Hirschfelder, Charles F. Curtiss, The Molecular Theory of Gases and Liquids, Wiley, 1964.

[164] J. Smagorinsky, General circulation experiments with the primitive equations, Science (80-.). (1963).

[165] F. Nicoud, F. Ducros, Subgrid-scale stress modelling based on the square of the velocity, Flow Meas. Instrum. 62 (1999) 183–200.

[166] F. Nicoud, H.B. Toda, O. Cabrit, S. Bose, J. Lee, Using singular values to build a subgrid-scale model for large eddy simulations, Phys. Fluids. 23 (2011) 0–12.

[167] T. Schönfeld, M. Rudgyard, Steady and unsteady flow simulations using the hybrid flow solver AVBP, AIAA J. 37 (1999) 1378–1385.

[168] N. Gourdain, L. Gicquel, G. Staffelbach, O. Vermorel, F. Duchaine, J.F. Boussuge, T. Poinsot, High performance parallel computing of flows in complex geometries: II. Applications, Comput. Sci. Discov. 2 (2009).

[169] G. Daviller, G. Oztarlik, T. Poinsot, A generalized non-reflecting inlet boundary condition for steady and forced compressible flows with injection of vortical and acoustic waves, Comput. Fluids. 190 (2019) 503–513.

[170] N. Lamarque, Schémas numériques et conditions limites pour la simulation aux grandes échelles de la combustion diphasique dans les foyers d'hélicoptère, Institut National Polytechnique de Toulouse, 2007.

[171] P. Lax, B. Wendroff, Systems of Conservation Laws, Commun. Pure Appl. Math. 13 (1960) 217–237.

[172] O. Colin, M. Rudgyard, Development of High-Order Taylor-Galerkin Schemes for LES, J. Comput. Phys. 162 (2000) 338–371.

[173] A.Z. Panagiotopoulos, Direct Determination of Fluid Phase Equilibria by Simulation in the Gibbs Ensemble : A Review EQUILIBRIA BY SIMULATION IN THE GIBBS, Mol. Simul. (2006) 1–23.

[174] N.K. Koutras, V.I. Harismiadis, D.P. Tassios, Equation of state for the Lennard-Jones fluid, Fluid Phase Equilibria,. 77 (1992) 13–38.

[175] W.A. Cañas-Marín, U.E. Guerrero-Aconcha, J.D. Ortiz-Arango, Comparison of different cubic equations of state and combination rules for predicting residual chemical potential of binary and ternary Lennard-Jones mixtures: Solid-supercritical fluid phase equilibria, Fluid Phase Equilib. 234 (2005) 42–50.

[176] K.G. Joback, R.C. Reid, Estimation of Pure-Component Properties from Group-Contributions, Chem. Eng. Commun. 57 (1987) 233–243.

[177] D.Y. Peng, D.B. Robinson, A New Two-Constant Equation of State, Ind. Eng. Chem. Fundam. 15 (1976) 59–64.

[178] G. Soave, Equilibrium constants from a modified Redlich-Kwong equation of state, Chem. Eng. Sci. 27 (1972) 1197–1203.

[179] M. Ghanbari, M. Ahmadi, A. Lashanizadegan, A comparison between Peng-Robinson and Soave-Redlich-Kwong cubic equations of state from modification perspective, Cryogenics (Guildf). 84

(2017) 13–19.

[180] T. Schmitt, D. Marchal, S. Ducruix, B. Cuenot, REST HF-10 test case : Large-Eddy Simulations using the AVBP solver, (2022) 1–15.

[181] A. Nicole, L. Dorey, REST HF10 test case : Simulation of combustion instabilities induced by flow rate modulations with diffuse interface modelling, (2022).

[182] R. Kaess, S. Köglmeier, R. Behr, O. Knab, REST HF-10 test case : URANS Simulations of Excited Methane Flames under Real Gas Conditions, (n.d.) 1–9.

[183] T. Schmitt, REST HF-10 test case : Synthesis of the Contributions for the Simulation of Excited Methane Flames under Real Gas Conditions, (n.d.) 1–15.

[184] R. Kaess, REST Testcase HF-10 - Test Case Description (ArianeGroup internal report), 2018.

[185] B. Cuenot, F. Shum-Kivan, S. Blanchard, The thickened flame approach for non-premixed combustion: Principles and implications for turbulent combustion modeling, Combust. Flame. (2021) 111702.

[186] L. Pons, N. Darabiha, S. Candel, Pressure effects on nonpremixed strained flames, Combust. Flame. 152 (2008) 218–229.

[187] L. Pons, N. Darabiha, S. Candel, T. Schmitt, B. Cuenot, The structure of multidimensional strained flames under transcritical conditions, Comptes Rendus - Mec. 337 (2009) 517–527.

[188] S.D. Cohen, A.C. Hindmarsh, CVODE, a stiff/nonstiff ODE solver in C, Comput. Phys. 10 (1996) 138–143.

[189] CVODE documentation - https://sundials.readthedocs.io/en/latest/cvode/index.html, (n.d.).

[190] T. Schmitt, D. Marchal, S. Ducruix, B. Cuenot, REST HF-10 test case : Large-Eddy Simulations using the AVBP solver, Proc. 9TH Eur. Conf. Aeronaut. Sp. Sci. (EUCASS. (2022) 1–15.

[191] X. Yang, W. Liang, T. Tan, C.K. Law, Reevaluation of the reaction rate of H + O2 (+M) = HO2 (+M) at elevated pressures, Combust. Flame. 217 (2020) 103–112.

[192] M.A. Turner, E.L. Petersen, Measurement and Kinetics Prediction of Undiluted Methane-Oxygen Laminar Flame Speeds, AIAA SciTech 2023 Forum. (2023).

[193] J. Liberatori, C. Palmese, R.M. Galassi, M. Valorani, P.P. Ciottoli, CSP-Driven Optimization of a 16-Species Skeletal Mechanism for Methane Ignition at High Pressure, AIAA SciTech 2023 Forum. (2023) 1–14.

[194] M. Furst, A.F. A. Bertolino, A. Cuoci, T. Faravelli, A. Parente, OptiSMOKE ++ User Manual, (2021).

Antoine MOUZE-MORNETTAS

Modélisation et réduction de la cinétique chimique LOx-Méthane pour des applications moteur-fusée

Le marché de l'espace étant de plus en plus compétitif, les lanceurs réutilisables sont considérés comme une technologie clé pour réduire de manière significative le coût de l'accès à l'orbite. Comme il représente le meilleur compromis coût-performance, le méthane est envisagé comme une solution pour de futurs moteurs réutilisables. Cependant, les conditions de fonctionnement des moteur-fusée sont extrêmes en termes de température et de pression, prohibitives pour la plupart des dispositifs expérimentaux existants. Il y a donc un manque fondamental de connaissances sur la cinétique de l'oxycombustion du méthane.
Pour obtenir un modèle cinétique, une base de données expérimentale de vitesse de flamme S_u représentative des conditions d'application est construite à l'aide de la chambre de combustion isochore OPTIPRIME développée à ICARE (CNRS). Une gamme variée de richesses, pression et température jamais explorée auparavant pour ces mélanges est construite. Une sélection de différents mécanismes chimiques récents est ensuite comparée aux résultats expérimentaux. Le mécanisme ayant l'écart le plus faible avec l'expérience (POLIMI C1-C3) est utilisé comme point de départ d'un processus d'optimisation sur la base de données expérimentale à l'aide de l'outil OPTISMOKE++. Un mécanisme adapté à la combustion CH_4/O_2 en conditions d'un moteur de fusée est ainsi obtenu. Pour finir, le modèle est testé dans une simulation LES 3D haute-fidélité d'une configuration moteur-fusée mono-injecteur à 100 bar (REST HF-10) avec le code AVBP développé au CERFACS. Les résultats obtenus sont comparés à des modèles existants. Les principales caractéristiques de la flamme sont retrouvées mais sa structure est plus complexe, soulignant ainsi l'intérêt d'une chimie optimisée.

Mots clés : Moteur fusées à ergols liquides, Oxycombustion du méthane, Haute pression, Mesures de vitesse de flamme, Cinétique chimique, Optimisation, Réduction, LES

Modelling and reduction of the LOx-Methane chemical kinetics for rocket engine applications

As the space market becomes increasingly competitive, reusable launch vehicles are seen as a key technology to significantly reduce the cost of access to orbit. As it represents the best cost-performance compromise, methane is considered as a solution for future reusable engines. However, the operating conditions of rocket engines are extreme in terms of temperature and pressure, hence prohibitive for most existing experimental devices. Thus, there is a fundamental lack of knowledge about the kinetics of methane oxycombustion.
To obtain a valid kinetic model, an experimental database of flame velocity S_u representative of the application conditions is built using the OPTIPRIME isochoric combustion chamber developed at ICARE (CNRS). A wide range of equivalence ratios, pressure and temperature never explored before for these mixtures is constructed. A selection of different recent mechanisms is then compared to the experimental results. The mechanism with the smallest deviation from experiment (POLIMI C1-C3) is used as a starting point for an optimization process on the experimental database using the OPTISMOKE++ tool. Hence, a kinetic model adapted to CH_4/O_2 combustion under rocket engine conditions is obtained. Finally, the model is tested in a high-fidelity 3D LES simulation of a single-engine rocket configuration at 100 bar (REST HF-10) with the AVBP code developed at CERFACS. The obtained results are compared to existing models. The main characteristics of the flame are recovered but with a more complex structure, thus underlining the interest of an optimized chemistry.

Keywords: Liquid Rocket Engine, Methane oxycombustion, High pressure, Flame speed acquisition, Chemical Kinetics, Optimization, Reduction, LES

CNRS - ICARE
(Institut de Combustion, Aérothermique, Réactivité et Environnement)
CERFACS
(Centre Européen de Recherche et de Formation Avancée en Calcul Scientifique)